Growth and Characterisation of Sputtered Transparent Conducting Oxides Targeting Improved Solar Cell Efficiency

---

by

Sonya Calnan

Doctoral Thesis
Submitted in partial fulfilment of the requirements
for the award of
Doctor of Philosophy of Loughborough University
3rd November 2008

Abstract

Transparent conducting oxides (TCO) are used to improve lateral current collection in thin film solar cells while allowing light into the absorber layers. Sputtering, an industrially mature coating technology, is potentially useful for low cost production of high quality TCO films. ZnO:Al films were grown by reactive MF (mid frequency) dual cathode magnetron sputtering from Zn:Al targets on glass with dynamic deposition rates up to 115 nm m min^{-1} compared to 6 nm m min^{-1} by RF sputtering from a single ceramic target. Adjusting the distribution of the oxygen influx improved the uniformity of the thickness and resistivity of ZnO:Al films grown on substrates measuring 30 cm x 30 cm. The ZnO:Al films were texture-etched for light trapping in micro-crystalline silicon (μc-Si:H) solar cells. Optimally textured ZnO:Al films were used as front contacts in 1cm² single junction μc-Si:H solar cells yielding an initial efficiency of 8.4 % which is comparable to cells on textured RF sputtered ZnO:Al films, despite the much higher deposition rate. High material utilisation target sputtering was used to grow thermally stable, highly transparent In_2O_3:Sn films on glass and polyimide substrates with resistivity below 2.0×10^{-4} Ω cm, while uniformly sputtering the In:Sn metallic target. A survey of high mobility impurity doped In_2O_3 and CdO indicated that transition metal dopants cause a resistivity ~ 10^{-4} Ω cm and transmission ≥ 80% in the spectral range from 400 nm to above 1500 nm. Studies on In_2O_3:Mo grown on glass by pulsed DC magnetron sputtering showed that interstitial oxygen inhibits the doping efficiency of Mo by forming neutral oxides. High mobility TCO contacts improved the NIR transmission of CdTe solar cells intended for use as the top cell in multi-junction solar cells. Further reductions in the resistivity of the high mobility TCO are required for enhanced solar cell efficiency. This thesis can contribute to transferring laboratory processes, for high quality TCO films, to industrial production and to improving TCO material properties for conventional as well as advanced solar cells and other opto-electronic devices.

Key words: solar cells, transparent conducting oxides, high mobility, sputtering, large area coatings, thin films

Contents

List of Figures

List of Tables

List of Publications

Some of the work described in this thesis has been published in the following articles:

I. S. Calnan, H.M. Upadhyaya, H. –L. Du, M.J. Thwaites, and A.N. Tiwari, Effects of substrate temperature on indium tin oxide films deposited using High Target Utilisation Sputtering, in Proc. 21st European Photovoltaic Solar Energy Conf., Dresden, Germany, September 2006, p. 1890.

II. S. Calnan, H.M. Upadhyaya, M.J. Thwaites and A.N. Tiwari, Properties of indium tin oxide films deposited using High Target Utilisation Sputtering. Thin Solid Films, Volume 515 (2007) p.6045.

III. S. Calnan, H. M. Upadhyaya, S. E. Dann, M. J. Thwaites, A..N. Tiwari, Effects of target bias voltage on indium tin oxide films deposited by High Target Utilisation Sputtering. Thin Solid Films, Volume 515 (2007) p.8500.

IV. S. Calnan, J. Hüpkes, B. Rech, H. Siekmann, A.N. Tiwari, High deposition rate aluminium doped zinc oxide films with highly efficient light trapping for silicon thin film solar cells. Thin Solid Films, Volume 516, Issue 6 (2008) p.1242.

V. S. Calnan, H.M. Uphadhyaya, S. Buecheler, G. Khrypunov, A. Chirila, A. Romeo, R. Hashimoto, T. Nakada and A. N. Tiwari, Application of high mobility transparent conductors to enhance long wavelength transparency of the intermediate solar cell in multi-junction solar cells. Revision submitted to Thin Solid August 2008.

VI. J.W. Bowers, H.M. Upadhyaya, S. Calnan, S. J.Watson, R. Hashimoto, T. Nakada, and A.N. Tiwari. Dye sensitised solar cells using high mobility, transparent conducting oxides for high efficiency tandem solar cell applications,. in Proc. 23rd European Photovoltaic Solar Energy Conf. 1 - 5 September 2008. Valencia. In press.

VII. J.W. Bowers, H.M. Upadhyaya, S. Calnan, R. Hashimoto, T. Nakada, and A.N. Tiwari, Development of nano-TiO_2 dye sensitised solar cells on high mobility transparent conducting oxide thin films,. Prog. in Photovolt. Res. Appl., 2008. Accepted for publication. October 2008.

VIII. S. Calnan and A. N. Tiwari, High mobility transparent conducting oxides for thin film solar cells. Submitted to Thin Solid Films October 2008.

Chapter 1 Introduction

The International Energy Agency predicts that the demand for energy will continue to rise as the world population increases and as the economies of developing countries grow [1]. Fossil fuels such as oil, coal and natural gas will be the main sources of energy in the 21st century [2]. However, as fossil fuels take millions of years to form, the current rates of consumption mean that reserves are being exploited faster than they can be replenished. Moreover, the damaging effects of emissions such as CO_2, SO_2 and NO_x from fossil fuels on the environment and the potential hazards associated with nuclear energy have hastened the need for alternative environmentally benign energy sources. Therefore, sustainable and renewable sources of energy will become increasingly important but their efficiency, long term stability, reliability and cost must be competitive if they are to provide a viable alternative to fossil fuels, especially in the short term.

Solar irradiation is a renewable energy source that could complement fossil fuels in the short term and eventually replace them. Solar cells are used to transform solar irradiation into electricity by means of photovoltaic (PV) conversion. The market share of terrestrial PV generation is dominated by mono crystalline silicon solar cells which require high purity raw materials [3, 4]. Currently, PV conversion is only economically competitive for stand alone generation in remote locations or through subsidies which cannot be sustained indefinitely. Since solar irradiation, the primary energy source for PV is free of charge, the cost of the generating system which includes the solar cells and peripherals such as DC-AC converters, battery banks, battery chargers and connecting cables, must be reduced. Nearly half the cost of the PV system cost comes from the PV modules such that there is scope to reduce the price per kWh by decreasing both the solar cell material and production costs. Some thin film materials have a higher absorption coefficient than mono-crystalline silicon and so layers thinner than 50μm, compared to a wafer typically >100 μm thick, are sufficient to absorb all incident photons. Besides, thin film PV materials can achieve reasonable photo-conversion efficiencies with less stringent requirements on material purity and crystalline quality [5]. From a research point of view, the material properties of thin film PV absorber layers can be easily varied by changing the chemical composition or the stoichiometry of the films or by combining layers of different components which is more difficult for mono-crystalline materials [6]. The thin film PV materials can be grown on cheap substrates allowing monolithic integration of multiple cells into large area modules without the need for additional material to interconnect individual cells as is required for mono-crystalline silicon wafer modules [7]. Additionally, thin films are easily adaptable to high throughput processes already well established for glass coating in industry which can substantially reduce the production costs compared to mono-crystalline silicon wafers [6, 8].

The semiconductor absorber materials in thin film solar cells are too resistive to allow efficient current collection of the generated charge carriers. Therefore, especially on the illuminated side of the solar cell, a transparent conductor is needed to act as an electrical contact while allowing incident photons through to the absorber layer. Metal oxide transparent conductors are preferred over ultra-thin pure metals because of their superior chemical stability, mechanical strength and optoelectronic properties [9] hence, the common reference to transparent conducting oxides (TCO). Since TCO films posses high optical transparency and near metal conductivity, they are used for a variety of applications including electrodes for solar cells, liquid crystal displays and thin film transistors, low emissivity coatings, transparent electrical heaters and gas sensors [10-14]. The most commonly used TCO materials are In_2O_3:Sn (ITO), SnO_2:F (FTO) and lately, ZnO:Al [12-14].

1.1 Aim and structure of thesis

1.1.1 Aims

The main objective of the work described in this thesis was to explore concepts for production of high quality TCO materials for solar cells, at low cost with good uniformity on large area substrates. Therefore, the research focused on improving both the film growth methods and the TCO material properties.

The best TCO materials obtained in research laboratories are prepared using film growth techniques which are not suitable for commercial production, such as pulsed laser deposition, which cannot uniformly coat large area substrates or RF magnetron sputtering, which is slow and requires complex equipment. Pulsed DC or MF dual cathode magnetron sputtering, both fast and potentially low cost deposition techniques, may be optimised to prepare high quality TCO materials on a large scale adaptable to industrial production. However, magnetron sputtering inefficiently uses the source material because of preferential sputtering of the target material in areas corresponding to the highest ion density such that a considerable proportion of the source material remains unused at the end of the sputter target life. This makes inventory costs, for expensive raw materials such as indium unnecessarily high. In this thesis, focus will be placed on the growth and characterisation of In_2O_3:Sn, ZnO:Al and In_2O_3:Mo films by these cost effective sputtering techniques.

Despite the high cost of indium, In_2O_3:Sn is the best commercially available TCO for opto-electronic device application because low resistivity can be obtained without intentional substrate heating. Therefore, in the short to medium term, In_2O_3:Sn is expected to remain an important component for the development of organic and hybrid solar cells grown on heat sensitive substrates. Thus the first aim of this thesis was to investigate the viability of high target utilisation sputtering (HiTUS) [15] to grow high quality In_2O_3:Sn while using as much as possible of the source material.

Textured TCO electrodes are beneficial to thin film silicon solar cells by causing multiple internal reflections of the weakly absorbed long wavelength light in the absorber layer, (also known as light trapping) which increases the photocurrent generation [16-18]. As a result, thinner absorber layers can be used, which reduce the processing time as well as the costs of materials and production. Aluminium doped zinc oxide is emerging as a low cost alternative to In_2O_3:Sn especially for various opto-electronic devices including solar cells [19]. Additionally, the electrical and optical properties of ZnO:Al are superior to natively textured SnO_2:F which is commercially available to enhance light trapping in thin film silicon solar cells [16]. However, the best light trapping properties of ZnO:Al for use in thin film silicon solar cells have been obtained by RF magnetron sputtering from ceramic targets which is unsuitable for large scale production [18]. Therefore, the second aim of this thesis was to prepare ZnO:Al, for thin film silicon solar cells, using reactive medium frequency (MF) reactive magnetron sputtering with light trapping properties after post deposition texturing, comparable to those of ZnO:Al films prepared by RF sputtering.

There is a preference in industry for coatings on larger substrates to benefit from economies of scale. The integration of thin film solar cells into modules on larger area panels, calls for reductions in the TCO film resistivity to values below $1 \times 10^{-4}\ \Omega$ cm. Materials that combine degeneracy with high mobility $> 62.5\ cm^2V^{-1}s^{-1}$ have been reported [20] opening possibilities to raise the conductivity without reducing the optical transparency by free carrier absorption [21]. However, the expected reductions in resistivity are yet to be achieved and thus the third aim of this thesis is to identify the factors limiting the conductivity of such TCO materials.

1.1.2 Thesis structure

The basic semiconductor physics which determines the properties of the TCO materials and the thin film solar cells that are relevant to this thesis are discussed in Chapter 2. The experimental and analytical techniques used to prepare and analyse, respectively, the TCO films and solar cells for this thesis are described in Chapter 3. The influence of the deposition parameters on the optical and electrical properties as well as the thermal stability of ITO films grown on glass and polyimide substrates using High target utilisation sputtering is investigated in Chapter 4. The effect of reactive gas inlet arrangement on the uniformity and light scattering quality of ZnO:Al films prepared by reactive MF sputtering from metallic targets is explored in Chapter 5. Also, the efficiency of thin film micro-crystalline solar cells prepared on a selection of the most promising textured ZnO:Al layers is related to the opto-electronic properties and light scattering ability of the TCO. A survey of high mobility impurity doped TCO films reported in literature is given in Chapter 6 and possible explanations for the charge transport behaviour of these films are suggested. Experiments which examine the relationship between the opto-electronic properties of In_2O_3:Mo and the chemical state of the molybdenum dopant are also described in Chapter 6. Also, the potential of high mobility TCO materials to improve solar cell efficiency is examined and the challenges and prospects in the development of high mobility TCO materials with improved conductivity are discussed.. Finally, in Chapter 7, general conclusions from the results presented are drawn and opportunities for future research are suggested.

Chapter 2 Physical properties and phenomena of TCO materials and solar cells

The opto-electronic properties of TCO materials and solar cell absorbers are explained by physical properties determined by the electronic band structure which in turn depends on the chemical composition of the materials. In this chapter, the basic physics of semiconductors is reviewed and correlated to opto-electronic phenomena observed in TCO films and solar cell devices.

2.1 Fundamental properties of TCO materials

The unique coincidence of high conductivity and visible light transparency in TCO materials is caused by their band structure [12, 22-24]. The band structure of a semiconductor depends on the chemical composition, the atomic arrangement and the presence of defects in the material as explained in semiconductor physics text books [25-27] . Most known TCO materials are n-type semiconductors where defects such as oxygen vacancies, impurity substitutions and interstitials donate electrons to the conduction band providing charge carriers for the flow of electric current.

2.1.1 Crystal structure and morphology

The arrangement of the atoms in a material contributes significantly to the physical and in some cases, the chemical properties of a material. The atoms in a material may be arranged either in an ordered or random manner leading to either a crystalline or amorphous structure, respectively. Amorphous materials have neither periodic symmetry nor crystalline structure. The atomic order is described as "short range" and is limited to the nearest neighbour.

Ideal crystals are quasi infinite periodic repetitions of an atomic arrangement. A unit cell is a volume in the lattice that is representative of the crystal's symmetry in 3-D space and which is repeated regularly throughout the crystal. Six lattice constants (or parameters) are necessary to define the size and shape of a unit cell. These are the lengths of the edges of the unit cell along its major axes, which are usually denoted as a, b, and c, and its inter-axial angles, which are usually denoted by α, β, and γ. Knowledge of the lattice constant values and the crystal structure is required to calculate the distances between neighbouring atoms in a crystal, as well as in determining the crystal's physical and electrical properties. Thin films of most materials generally retain the crystal structure of the bulk material with slight deviations in the size and orientation of the crystallites which give rise to variations in the film properties.

Disruptions in the periodic ordering of crystals form defects which trap the mobile electrons and holes thus impeding charge transport in the crystal. Several types of crystal defects exist namely, point defects, crystal dislocations, grain boundaries, stacking faults, disorder and antiphase domains.

Point defects are imperfections that occur at a site in the crystal lattice such as vacancies, substitutional defects, interstitial defects and Schottky defects. A vacancy describes an atom or an ion missing from its regular site in the crystal while a substitutional defect occurs where the site is occupied by an “incorrect” atom. Point defects are important especially in semiconductors as they can be used to alter the material properties by doping as will be discussed later.

Extended defects involve several lattice sites and occupy a finite volume of the crystal and include dislocations, stacking faults and surface defects. Dislocations are formed by line defects along which the crystal lattice is shifted. Dislocations can be caused by a lattice mismatch between the thin film and a substrate. In some cases, the addition of an impurity can significantly reduce the dislocation density in a material. Stacking faults are caused by disturbances in the stacking order of the planes in a crystal structure. An intrinsic stacking fault is formed by a missing plane whereas addition of an extra plane results in an extrinsic stacking fault. Surface defects are defects that form a two dimensional plane in the crystal. The actual external surface of a crystal is a surface defect because the atoms on the surface adjust their positions to accommodate the absence of neighbouring atoms. Also, surface defects may occur at the boundary between two grains within a larger crystal where the rows of atoms in two different grains run in different directions, leading to a mismatch across the grain boundary. Polycrystalline semiconductors consist of finite sized crystals (also known as grains) that are randomly oriented with respect to each other. The finite size of the crystal grains causes their boundaries to act as defects as they present discontinuities in the crystal periodicity. Small angle grain boundaries are arrays of dislocations causing small disorientations of the crystal across the surface of the imperfections. Grain boundaries are the most dominant extended defects in polycrystalline thin films.

Transparent conductors for solar cell applications are grown as thin films which exhibit polycrystalline and/or amorphous structure depending on the deposition conditions. Therefore, the presence of disorder and defects in TCO materials has an important influence on their properties. Thin films tend to develop large internal stresses which depend on the growth conditions and the nature of the substrate. The stress in films causes deviations in the lattice parameters which affect the material properties as reported for In_2O_3:Sn [28, 29]. Table 2.1 lists the structural, optical and electrical properties of intrinsic TCO thin film materials.

Table 2.1. Structural, optical and electrical properties of intrinsic TCO thin film materials compiled from [9, 11, 12].

TCO	Crystal structure	Lattice constant (Å)† a	c	Bandgap (eV)	Refractive index	Dielectric constant	Mobility ($cm^2 V^{-1}s^{-1}$)	Carrier density (cm^{-3})
CdO	Rock salt	-	-	2.3–2.7	-	-	≤120	10^{16}-10^{21}
ZnO	Wurzite	3.243	5.195	3.1-3.6	1.85–1.90	8.5	8-20	10^{16}-10^{21}
In_2O_3	Bixbyite	10.117	-	3.5-3.8	2.0–2.1	8.9	10-75	10^{16}-10^{21}
SnO_2	Rutile	4.737	3.186	3.7-4.6	1.8–2.2	12/9.4	5-30	10^{16}-10^{21}

† Bulk material property

2.1.2 Electronic band structure

The electronic band structure is the relationship between the energy E of a conduction electron and its momentum k in a solid state material. It can therefore be used to describe the behaviour of electrons under externally applied forces like light, heat and/or voltage. The detailed derivations of the mathematical expressions used to describe the electronic band structure are given in several textbooks [25-27].

The energy of an electron in free space is described as

$$E = \frac{\hbar^2 k^2}{2m_0} \qquad 2.1$$

where m_0 is the mass of the free electron and $\hbar$ is the reduced Planck's constant or $h/2\pi$.

The distribution of electrons in the crystal can be determined by Maxwell Boltzmann distributions provided that the carrier density is small compared to the effective density of states in both the conduction and valence band (non-degenerate semiconductors). In the crystal lattice, the electrons are only allowed to occupy to occupy specific discrete energy levels. As the number of atoms in the semiconductor increase, the allowed energy levels merge to form a continuous band of allowed states known as energy bands. Two bands of allowed energy states exist and they are separated by a forbidden gap known as the band gap. The lower band of allowed states is known as the valence band (VB) whilst the higher energy states make up the conduction band (CB). Since electrons fill the lowest available energy states, the valence band is always nearly completely filled with electrons at 0 K. The conduction band contains few or no electrons as energy is required to transfer electrons from the valence band to it. Electrons in the conduction band are free to move about in the crystal. As the temperature is increased or light is introduced, electrons in the valence band are energised and can be displaced from their positions. If the applied energy is greater than the band gap energy, the VB electrons can be transferred to the conduction band where they are free to move and become charge carriers which increases the conductivity of the semiconductor. When an electron leaves the valence band, a vacant site known as a hole is created which can also move about the crystal and add to the conductivity. The band gap thus represents the energy required to break a bond in a crystal and transfer an electron from the valence band to the conduction band. The width of the band gap determines the electrical character of the material at room temperature. Insulators are poor conductors as a lot of energy > 5 eV is needed to transfer electrons from the VB to the CB. Contrarily, metals are good conductors because the VB and the CB overlap and share electrons. Semiconductors lie between metals and insulators such that though the conduction band is empty, the energy band gap is narrow enough to allow promotion of electrons from the valence band to the conduction band on the application of a moderate amount of energy < 5 eV. Figure 2.1 shows the band diagrams corresponding to a metal, semiconductor and an insulator.

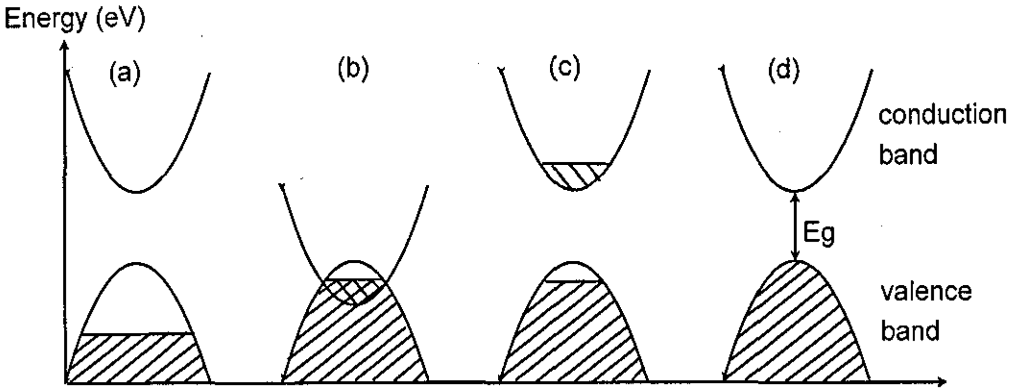

Figure 2.1. Possible energy band gaps in a crystal showing (a) a half filled valence band of a metal with one valence electron per atom (b) an overlap between conduction band and valence in a multivalent metal (c) a partially filled valence band separated by a small band gap from an

almost empty conduction band for a semiconductor and (d) a full valence band separated from an empty conduction band by a large band gap for an insulator. The hashed areas represent regions containing electrons.

The band gap of a TCO depends on its composition, the lattice constant (and bond length) and the ionicity. Typically, the lower the lattice constant, the higher the band gap. Similarly, the band gap increases with increasing ionicity of the bonds.

The electrons in semiconductors with energy close to the conduction band minimum (CBM) behave as free electrons since the *E-k* relation can be approximated by a parabola. These electrons accelerate in an applied electrical field just like a free electron in vacuum and experience an attractive force close to an atom which weakens as the electron moves through the crystal and out of the field of the atom. This process repeats itself as the electron moves through the lattice such that the crystal field can be approximated by a periodic array of potential wells. The presence of the periodic potential changes the properties of the electron such that the mass of the electron mass differs from m_0. To take account of the periodic nature of the crystal the electron mass is replaced an effective mass m_e * given by

$$m_e^* = \frac{\hbar^2}{d^2E/dk^2} \qquad 2.2$$

Most semiconductors can be described as having one band minimum at $k = 0$ and several other anisotropic band minima at $k \neq 0$. Because the effective mass depends on the direction of the external field and the presence of multiple equivalent band minima, two types of effective mass exist, one associated with the density of states and the other to the conductivity. The effective mass of a semiconductor is estimated by fitting the energy vs. wave-number diagram around the CBM or the valence band maximum (VBM) by a parabola.

To understand the conductivity mechanisms of semiconductors, the density of states close to the edges of the conduction and valence bands is important. Here, the discussion will be restricted to electrons as majority charge carriers as most TCO materials are n-type. Analogous relationships exist for p-type TCO materials in which holes are the majority carriers. The atomic structure of the constituent elements of a compound determines whether it will be simultaneously high conductivity and transparency [24]. Since the most common transparent conductors are oxides, the following discussion will be limited to the formation of bonds between oxygen and metals.

Oxygen has four 2p electrons in its outermost shell and if two electrons are added from a higher valence element, the oxygen atom will have a closed shell configuration with six 2p electrons. If the resulting cation has a completely filled outermost shell, the oxide will be transparent in the visible wavelength range since d-d transitions which require energy corresponding to light within the visible light spectrum will not be possible. The two closed shell configurations of cationic species are $d^{10}\ s^0$ and $d^{10}\ s^2$ as listed in Table 2.1.

Table 2.2. Possible cations for transparent conducting oxides [22, 24].

Valency	$3d^{10}\ s^0$	$3d^{10}\ s^2$	$4d^{10}\ 5s^0$	$4d^{10}\ 5s^2$
1		Cu^+	Ag+	In^+
2	Zn^{2+}		Cd^{2+}	Sn^{2+}
3		Ga^{3+}	In^{3+}	Sb^{3+}
4			Sn^{4+}	
5			Sb^{5+}	

Since, there should be no inter-band transitions for energy levels less than 3.1 eV, the host oxide must have a band gap greater than this value. However, for high electrical conductivity, two additional conditions have to be met. The oxide should be capable of being degenerately doped so that the Fermi level lies above the conduction band minimum. The material should also have a highly dispersed conduction band (for n-type) or valence band (for p-type) to promote a low effective charge carrier mass that would allow high mobility of the electrons and holes respectively [22, 24].

2.1.3 Doping mechanisms

Doping is the alteration of the properties of a semiconductor material by the introduction of defects into the crystal structure. The impurities may either be unintentional (intrinsic doping) or deliberately added (extrinsic doping) to provide free charge carriers in the semiconductors. Detailed explanations of the doping mechanisms in semiconductors can be found in various textbooks [30-32]. Also, some theoretical studies explaining the doping mechanisms of TCO materials [33, 34] have been published.

Intrinsic semiconductors have an equal number of electrons and holes under equilibrium conditions. If a bond is broken e.g. by raising the temperature, an electron is promoted to a higher energy level leaving a hole in the conduction band, however, when the system relaxes the electron will lose its energy and recombine with the hole in the valence band. In a band diagram, the Fermi level E_F (the energy at equilibrium at which the probability of the state being field with electrons is 0.5.) determines the majority carriers in the semiconductor. For an n-type material the Fermi level lies above the midpoint of the forbidden energy gap and the reverse is true for p-type semiconductors. In degenerate semiconductors, the Fermi level varies with temperature T, the carrier density in the conduction band N_C and the donor concentration N_D according to

$$E_F = E_C + kT \ln\left(\frac{N_D}{N_C}\right) \qquad 2.3$$

Where, E_C is the energy of the conduction band minimum.

As the temperature increases, the band gap energy decreases because the crystal lattice expands weakening the interatomic bonds. Weaker atomic bonds require less energy to be broken such that electrons are more easily transferred to the conduction band. Therefore the energy of formation of intrinsic defects depends on the chemical potential and the Fermi level position in the band gap. The intrinsic carrier density increases with temperature since more bonds can be broken creating additional electron-hole pairs. The number of holes generated is always equal to that of the electrons and if the temperature is reduced, the electrons in the conduction band lose their energy and fall back into the valence band where they recombine with the holes.

To avoid fluctuation of charge carrier density with temperature, semiconductor materials are doped by the introduction of impurities which form point defects. If the impurity is of the same valence as the rightful atom, it is an *isovalent impurity*. If an atom at a crystal site is replaced by an impurity with a higher valence, it will add at least one extra charge (positive or negative) to the crystal bond. An extra electron will introduce an energy state within the band gap close to the conduction band minimum but there will be no corresponding hole formed in the valence band. The donated electron(s) will require very little energy to be promoted to the conduction band and there will be an excess of negative charge carriers leading to *n*-type conductivity. Similarly, is if an atom in the crystal lattice is replaced by an impurity with a lower valence, the absence of an electron will introduce an energy state within the band gap close to the valence band maximum. The energy states near the valence band maximum can easily trap electrons from the valence band creating holes in the valence band. Since the acceptor impurities increase the number of holes but not electrons, the resulting semiconductor has a net positive charge and would be p-type.

When a semiconductor is doped with a donor or an acceptor, impurity energy levels are introduced in the forbidden band gap. Each specific impurity related to a given semiconductor has a unique ionisation (or activation) energy. Normally dopant impurities used to control the conductivity type of semiconductors have low ionisation energies and are often referred to as shallow impurities as they are similar to hydrogen. The ionisation energy E_i can be approximated using a hydrogen like model as follows

$$E_i = \frac{m_e^*}{m_0} \frac{1}{\varepsilon_r^2} \left(\frac{m_0 e^4}{2(4\pi\varepsilon_0 \hbar)^2} \right) \qquad 2.4$$

Where the factor in brackets represents the ionisation energy of a hydrogen atom. However, the average distance r from the electron to the donor ion is much larger than for a hydrogen proton, since the electron occupies one of the outer orbitals of the donor atom. Also, for shallow donors, r is much larger than the inter atomic spacing of the semiconductor crystal such that the radii of the neighbouring donor ions overlap at relatively low donor densities and an impurity band is formed from the donor states which enables electrons to hop from donor to donor. Thus an effective Bohr's radius a_B is used to approximate the extension of the wave-function of the electron bound to the fixed ion and is given by

$$a_B = \frac{\hbar^2 \varepsilon_0 \varepsilon}{\pi e^2 m_e *} \qquad 2.5$$

Where ε_0 is the permittivity of free space, and ε is the static dielectric constant of the host lattice. The critical carrier density N_{Cr} for the impurity band formation was defined by Mott as:

$$N_{C_r} = \left(\frac{0.26}{a_B} \right)^3 \qquad 2.6$$

The critical density of ZnO is estimated as 1.05 x 10^{19} cm^{-3} using $m_e{}^* = 0.38$ and $\varepsilon = 8.5$ [12] and that for In_2O_3 is about 4.51 x 10^{19} cm^{-3} using $m_e{}^* = 0.30$ and $\varepsilon = 8.9$ [12]. In general, the carrier density of TCO materials is much higher than this, typically ~$10^{21}cm^{-3}$ for In_2O_3:Sn and ~10^{20} cm^{-3} for ZnO:Al.

Deep impurities require an ionisation energy that is much higher than that for shallow impurities which is typically about *kT*. Thus deep impurities remain inactive at room temperature and may act as effective recombination centres in which electrons and holes are captured and neutralise each other. Though an element may have a low ionisation energy, other factors affect its suitability as a donor namely either the solid solubility, solid state diffusion or both in the semiconductor may be too low. Also, doping process may not be compatible with available device processing techniques. In practice, the carrier density is much less than the dopant concentration in the semiconductor as the impurity atom may provide a free carrier which spontaneously generates a defect which compensates and neutralises the charge of the intentional dopant. If the relative density of electrons exceeds that of holes the semiconductor is n-type, or p-type material under reverse conditions.

Normally point defects are described using the Kröger Vink notation which is explained using ZnO: Al as an example as follows

- Zn and O atoms reside in their proper locations i.e. at a Zn site and an O site, respectively (Zn_{Zn} and O_O),
- A Zn atom on an O site or an O atom on a Zn site (Zn_O or O_{Zn}) forming antisite defects,
- A Zn atom or an O atom in an interstitial site (which is a site that is not part of the crystal structure) ($Zn_i^{\bullet}$ or O_i'), where the ($^{\bullet}$) and (') the represent a positive and a negative charge, respectively, relative to the neutral lattice, forming interstitial defects
- A vacancy on a Zn site or on an O site (V_{Zn}' or $V_O^{\bullet}$),

- An Al atom on a Zn site ($Al_{Zn}^{\bullet}$) forming a substitutional defect,
- A special interstitial defect known as the Frenkel defect is caused by a pair of defects produced when an ion moves out of the lattice to create an interstitial site leaving a vacancy behind [V_{Zn}' +$Zn_i^{\bullet}$] or [$Vo^{\bullet}$+O_i'] and
- A Schottky defect is caused by a vacancy of an cation or anion at a lattice site but the missing atom/ion is not present as an interstitial. [V_{Zn}' +$Vo^{\bullet}$].

Using the definitions above, the types of defects can be classified, according to their doping effects as shown in Table 2.3 which considers intrinsic and Sn- doped In_2O_3.

Table 2.3. Possible defects in intrinsic and Sn- doped In_2O_3

Semiconductor	Donors	Acceptors	Neutral
Vacancies	V_O	V_{In}	
Interstitials	In_i, Sn_i	O_i	
Schottky defects			V_{In} + V_O
Frenkel defects			[V_{In}+ In_i] or [V_O+ O_i]
Substitutional atoms	In_O or Sn_{In}	O_{In}	In_O or O_{In} or Sn_O
Antisite defects			[In_O + O_{In}]

2.1.4 Electrical conduction in TCO materials

The conduction of current through a semiconductor is governed by the transport mechanisms of charged carriers. The principles of charge carrier transport in semiconductor films and electronic devices are discussed in detail in several texts [25-27, 35]. Charge carriers can flow from areas of high density to those of low density by diffusion as a result of random motion of the carriers caused by heat. On the other hand, drift motion is caused by an acceleration of charge carriers by an externally applied voltage. The total current in a semiconductor is therefore the sum of the drift and diffusion currents. When an external field is supplied, the random motion persists but the net effect is motion in the direction of the field. However, the velocity v of the charge carriers increases with applied field until a maximum as a result of scattering effects. The scattering events are described by an average relaxation time τ giving a maximum drift velocity v_d of

$$v_d = -\frac{e\overline{E}\tau}{m_e{}^*} \qquad 2.7$$

The current density *J* can be written as a function of the charge density N_e as:

$$J = N_e e v_d = \frac{N_e e^2 \overline{E}\tau}{m_e{}^*} \qquad 2.8$$

According to Ohm's law, the electrical conductivity σ is defined by

$$J = \sigma\overline{E} \qquad 2.9$$

Normally, the electrical properties of TCO materials are described by the resistivity ρ, the reciprocal of σ given by

$$\rho = \frac{1}{\sigma} = \frac{m_e{}^*}{N_e e^2 \tau} \qquad 2.10$$

The ratio of the drift velocity to electric field is known as the mobility μ given by

$$\mu = \frac{e\tau}{m_e{}^*} \qquad 2.11$$

Therefore the mobility can be increased by increasing τ or by decreasing $m_e{}^*$. Increasing τ requires films with fewer defects which may be achieved by reducing the charge carrier density, the grain boundaries and the neutral impurities. Decreasing $m_e{}^*$, requires semiconductors with a widely dispersed conduction band. The relaxation time in turn depends on the drift velocity and the mean free path of the charge carriers. These parameters further depend on scattering of the carriers by defects or by thermal vibrations of the lattice. The scattering mechanisms that govern the electron transport in semiconductors are described in detail in text books such as that by Lundstrom [35]. Of these, the scattering mechanisms relevant to n- type TCO thin films have been identified by other authors [12, 36-38]. Briefly, they are caused by ionised impurities, neutral impurities, grain boundaries and lattice vibrations. Scattering due to ionised impurity is significant for doped TCO materials as the electrostatic field of the impurities is effective at relatively wide distances. For degenerately doped semiconductors, the contribution of ionised impurities to the mobility is given by

$$\mu_{IIS} = \frac{4e}{h}\left(\frac{\pi}{3}\right)^{1/3} N^{-2/3} \qquad 2.12$$

Grain boundaries act as discontinuities in the crystal structure of a semiconductor causing electronic defects which are charged by carriers from the interior of the grains. If the carriers are n-type (p-type) a depletion (accumulation) zone is generated on both sides of a grain boundary. For TCO materials which are commonly n-type, the electrons have to overcome an energetic barrier height Φ_B which is related to the number of charge carriers in the grain and at the grain boundaries, designated by N_G and N_{GB}, respectively as

$$\Phi_B = kT \ln\left(\frac{N_G}{N_{GB}}\right) \qquad 2.13$$

The electrons can cross the grain barriers by thermionic emission and for very high electron densities, the depletion width narrows permitting tunnelling. Chemisorption of electrons by oxygen atoms at grain boundaries widens the potential barrier which also increases carrier scattering and thus reduces the mobility of TCO materials [39, 40]. The interface states at the grain boundaries form a space charge region around the grain boundaries causing band bending and the resulting potential barrier reduces the mobility according to

$$\mu_{GB} = \mu_0 \exp\frac{(-e\Phi_B)}{kT} \qquad 2.14$$

Where μ_{GB} is the grain boundary limited mobility. Grain boundary scattering only significantly affects the overall TCO mobility if the grain size is about the same as the mean free path of the charge carriers.

Neutral impurity scattering is caused by neutral dopants, interstitials and vacancies which interrupt the crystal symmetry. The interaction of neutral impurities with free carriers is weaker than that by ionised impurities because the former are not charged. The mobility by neutral impurities μ_{NI} is given by

$$\mu_{NI} = \frac{e^3 m_e^*}{A(T) 4\pi\varepsilon\varepsilon_0 \hbar N_{NI}} \qquad 2.15$$

Where $A(T)$ is the scattering cross section factor and N_{NI} is the density of neutral impurities. Under high neutral impurity density ($< 10^{19}$ cm^{-3}), this form of scattering becomes significant for example in ITO where neutral $(Sn_2O_4)^x$ complexes may be formed in such conditions [34].

Matthiesen's rule states that the contribution of different scattering processes to the mobility and thus carrier transport is additive provided that the scattering mechanisms are independent [35]. Therefore for the above scattering processes, the overall mobility can be determined as

$$\frac{1}{\mu} = \sum_{i=1}^{n} \frac{1}{\mu_i} \qquad 2.16$$

Where μ_i is the mobility due to the i^{th} scattering mechanism. In practice, the conductivity of TCO materials cannot be increased by simultaneously increasing the carrier density and the mobility. Usually, the mobility is observed to saturate and even start reducing as the carrier density is increased. Therefore, the dominant scattering mechanism on the carrier density N_e and as such, grain boundary scattering is dominant for $N_e \leq 10^{19}$ cm^{-3} while charge impurity scattering is more significant for $N_e \geq 10^{19}$ cm^{-3} for ITO and ZnO:Al [11, 12, 34, 37]. Ellmer et al. [37] also suggest that for $N_e > 10^{19}$ cm^{-3}, the nature of the scattering differs for both ITO and ZnO:Al as a result of the piezoelectricity of the latter material leading to higher trap densities. Also in degenerate TCO materials, defect scattering is typically more dominant than scattering due to thermal vibrations [12].

For amorphous semiconductors, the Fermi level is usually situated in the region of localized states in the band gap. At low temperatures, the electrical conductivity occurs by variable range hopping from occupied tail states to empty states close to the Fermi level and exhibits a non-activated temperature dependence. At higher temperatures, the electrons are excited from the Fermi level to the mobility edge in the conduction band, which leads to a thermally activated conductivity. Amorphous TCO materials have a significantly high mobility and thus conductivity compared to other amorphous semiconductors because of the possibility of degenerate doping and the long range s-band overlap of the metal cations [41]. Thus amorphous TCO material conduction is by band conduction which gives them a resistivity comparable to the polycrystalline form.

Combining equations 2.10 and 2.11, gives the well known relation between σ, N_e and μ as

$$\sigma = N_e \mu e \qquad 2.17$$

Another quantity which describes the quality of a TCO as a contact is the sheet resistance ρ_s which is independent of the area perpendicular to the flow of current

$$\rho = \rho_S \cdot d \qquad 2.18$$

2.1.5 Optical properties

TCO materials are required to be transparent over the visible wavelength and part of the near infra red region. Transparency is measured by transmission $T(\lambda)$ which is defined as the ratio of intensity of the incident light energy to that of the transmitted light at a given wavelength. Low transmission may be caused by either significant absorption $A(\lambda)$ or reflection $R(\lambda)$, or both where

$$T(\lambda) = 1 - R(\lambda) - A(\lambda) \qquad 2.19$$

These optical properties of a thin film can be determined from the refractive index n and the absorption coefficient α. For absorbing media, the refractive index is modified by adding a term known as the extinction coefficient κ to give a complex refractive index (n-$i\kappa$). The intensity of light passing through an absorbing film of thickness d is attenuated exponentially according to Beer Lambert's law,

$$T(\lambda) = \frac{I}{I_0} e^{-\alpha d} \qquad 2.20$$

Where, I_0 and I are the incident and transmitted light intensity, respectively. The absorption coefficient is related to the extinction coefficient as

$$\alpha = \frac{4\pi\kappa}{\lambda} \qquad 2.21$$

The refractive index and the absorption coefficient both determine a complex dielectric function ε given by

$$\varepsilon = \varepsilon_1 + i\varepsilon_2 \qquad 2.22$$

Where the real and imaginary dielectric functions are described as

$$\varepsilon_1 = n^2 - \kappa^2 \qquad 2.23$$

and

$$\varepsilon_2 = 2n\kappa \qquad 2.24$$

Figure 2.2 shows the typical transmission spectrum of a TCO, in this case In_2O_3:Sn, film indicating the bounds of the ultra violet (UV), the visible (VIS) and the near infra red (NIR) wavelength regions.

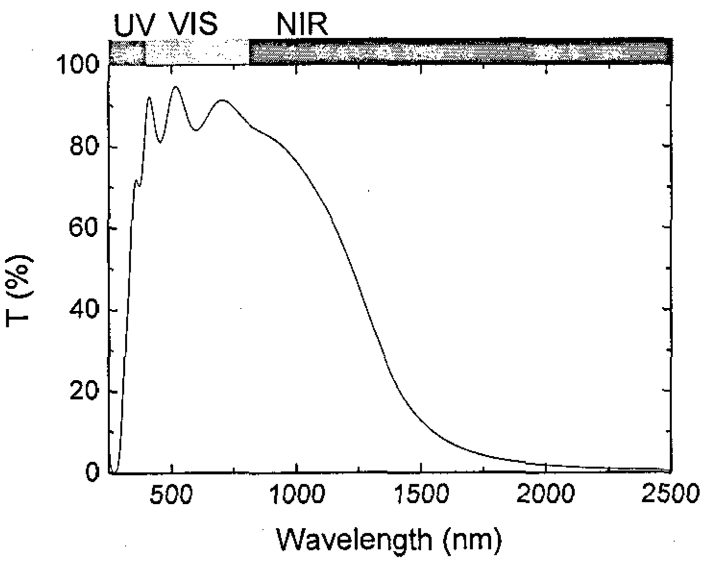

Figure 2.2. Typical transmission spectrum of a transparent conducting oxide. The bars labelled UV, VIS and NIR indicate the ultra violet, the visible and near infra red regions, respectively, of the electromagnetic spectrum.

The transmission of UV light through the TCO film is limited by electron-interband transitions from the valence band to the conduction band caused by absorption of photons with energies above the fundamental band gap around 3 eV. The band gap may be direct and indirect and both types are possible in TCO materials. Direct bandgap semiconductors in which the CBM and the VBM occur at the same wave number, have a strong absorption of light. An incident photon can be absorbed by a semiconductor, if an empty state in the conduction band is available for which the energy and momentum equals that of an electron in the valence band plus that of the incident photon. Photons have little momentum relative to their energy since they travel at the speed of light. The electron makes an almost vertical transition on the *E-k* diagram. Figure 2.3 (a) shows a schematic of a direct band gap transition. The absorption coefficient of a direct band gap material is related to the band gap energy as follows

$$\alpha \propto \sqrt{(E-E_g)} \qquad 2.25$$

If the CB minimum in a semiconductor is not vertically aligned to the VB maximum, a vertical transition of an electron is not sufficient to fill an empty state in the conduction band leading to an indirect band gap. A phonon of frequency ω_{ph} is required to supply additional energy $\hbar\omega_{ph}$ to transfer the electron from the VB to the CB. A phonon is a particle associated with lattice vibrations with a low velocity close to the speed of sound in the material, it has a small energy and large momentum compared to that of a photon. Figure 2.3 (b) and (c) show schematics of indirect band transitions. The minimum photon energy required is slightly below the CBM in the case of phonon absorption and is slightly above the CBM in case of phonon emission. The absorption coefficient for indirect band gap is determined as

$$\alpha \propto \left(E - E_g - \hbar\omega_{ph}\right)^2 \qquad 2.26$$

As the wavelength increases, the transmission increases (Figure 2.2) because band to band transitions corresponding to energy in the visible wavelength are absent since the conduction band lies ~ 3.5 eV above the VB maximum of the O 2p bond [22]. However, the transmission is less than 100% because of reflection, absorption, and/or scattering.

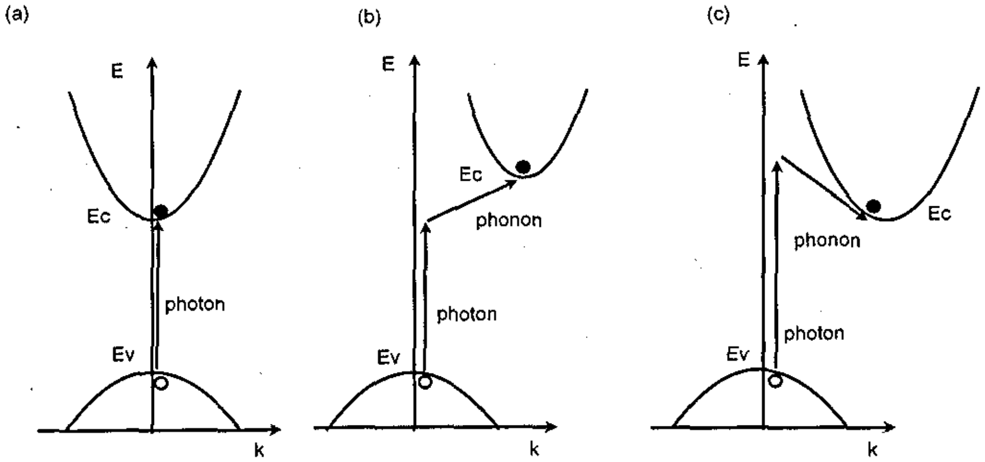

Figure 2.3: Energy E vs. wave number k showing the transition of an electron from the valence band to the conduction band as a result of (a) photon absorption in a direct band gap semiconductor (b) photon absorption accompanied by phonon absorption in an indirect band gap semiconductor and (c) photon absorption accompanied by phonon emission in an indirect band gap semiconductor.

The interference oscillations of the transmission spectrum for visible light are caused by reflections at the various interfaces since the TCO film is weakly absorbing. Visible light is also reflected from the TCO film through scattering from a rough surface which increases with the film thickness [11]. Low transmission of visible light may also be caused by absorption because of a poor crystal structure e.g. in In_2O_3:Sn [42] or by scattering from unreacted metal or neutral complexes of the dopant material as reported for ZnO:Al [43] and In_2O_3:Sn [34]. The transmission gradually reduces to zero as the wavelength increases towards the NIR region because of increased free carrier absorption and increasing reflection as the plasma edge is approached. The splitting of the s-band from the rest of the conduction band, keeps the plasma frequency of TCO materials in the IR range unlike metals, allowing visible light transmission despite the presence of free carriers [22].

2.1.6 Correlation of optical and electrical properties

The optical properties of TCO materials depend on the carrier density and thus are related to the electrical properties. When the carrier density increases, several other material properties are affected namely, (i) the fundamental absorption edge shifts towards shorter wavelengths, (ii) the effective carrier mass increases, (iii) the refractive index reduces, (iv) the plasma edge shifts towards shorter wavelengths and (v) the infra –red reflection increases.

In highly doped TCO thin films, the conduction band is partly filled such that the optical band gap is widened leading to a shift of the band edge toward shorter wavelength. This shift is commonly referred to as the Burstein Moss shift and its size increases with carrier density. Figure 2.4 illustrates band gap widening of a degenerate semiconductor which is typical of highly conductive TCO materials. Assuming that a parabolic CB and VB is maintained after doping the TCO material, the BM shift ΔE increases linearly with $(N_e)^{2/3}$

$$\Delta E = \frac{h^2}{8m_{vc}*}\left(\frac{3N_e}{\pi}\right)^{2/3} \qquad 2.27$$

Where $m_{vc}*$ is the reduced effective mass related to the CB and the VB. Above a critical value of N_e, the bandgap widening is compensated by a downward shift of the conduction band and a simultaneous upward shift of the valence band.

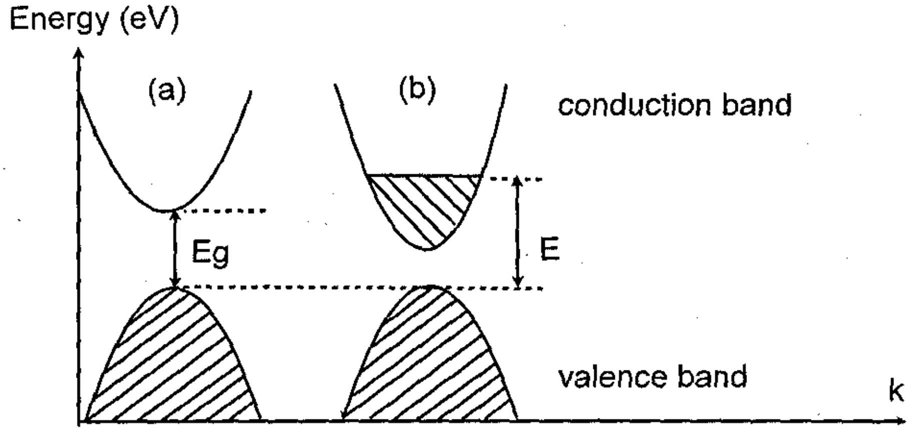

Figure 2.4: Electronic band structure of (a) an undoped and (b) a doped metal oxide semiconductor showing band gap widening ($E = E_g + \Delta E$) by increased carrier density causing degeneracy. The shaded areas represent occupied states.

This effect known as band gap narrowing is caused by merging of the dopant and host conduction bands and/or by electron-electron and electron-impurity scattering. Perturbation of the band edges caused by coulomb interactions with inhomogeneously distributed impurities forms "tails of states" known as Urbach tails. These tails are characterised by a linear relationship between the $\log_{10} \alpha$ versus. E(eV) and they are manifested by a gradual rather than an abrupt fundamental absorption edge. The slope of the Urbach tails generally increases with dopant concentration and thus carrier density as reported for ZnO:Al [43] and In_2O_3:Sn [42].

The dielectric function can be taken to consist of contributions of various frequency dependent susceptibilities

$$\varepsilon(\omega) = 1 + \chi^{VE}(\omega) + \chi^{FC}(\omega) + \chi^{PH}(\omega) \qquad 2.28$$

Where χ^{VE} (ω), χ^{FC}(ω), and χ^{PH} (ω) are contributions from valence electrons, free carriers and polar optical phonons, respectively. The term χ^{VE} (ω) accounts for interband transitions, which for TCO materials typically lie in the UV region but may extend into the visible region. χ^{FC}(ω) accounts for free carriers whose resonance lies at zero energy but damping of the resonance may lead to a complex susceptibility for energies lying in the near infra red region. Lastly, χ^{PH} (ω) is caused by optical phonons which couple to the transverse electromagnetic field. Undoped TCO materials can be described by $\chi^{VE}(\omega)$ and $\chi^{PH}(\omega)$ while doping with a donor impurity adds the effect of $\chi^{FC}(\omega)$. Since the resonance for optical phonons lies in the thermal infra red region, $\chi^{PH}(\omega)$ is not relevant to TCO materials for solar cell applications and is not considered hereafter. For regions well away from the optical band gap and phonon resonance, the dielectric function can be re-written as

$$\varepsilon(\omega) = \varepsilon_\infty + \chi^{FC}(\omega) \tag{2.29}$$

Where ε_∞ is the high frequency dielectric constant. $\chi^{FC}(\omega)$ can also be described by Drude's model where the free electrons behave as a plasma set into motion by the electric field component of the electromagnetic field, as

$$\chi^{FC}(\omega) = \frac{-\omega_N^2}{\omega^2 + i\omega\Gamma} \tag{2.30}$$

Where Γ is a damping term and

$$\omega_N^2 = \frac{e^2 N_e}{\varepsilon_0 m_c^*} \tag{2.31}$$

The condition where $\varepsilon_1 = 0$ describes the plasma frequency ω_p, at which the free electrons resonate, and for undamped oscillations, is given as

$$\omega_p^2 = \left(\frac{\omega_N^2}{\varepsilon_\infty}\right)^2 = \frac{e^2 N_e}{\varepsilon_\infty \varepsilon_0 m_c^*} \tag{2.32}$$

For undamped oscillations, $n = 0$ and $R(\lambda) = 1$ for $0 < \omega < \omega_p$. Above ω_p, κ is zero and the reflectance drops as n rises from zero to unity. Note that even for $\varepsilon_2 = 0$, κ and hence α is non zero. Introducing some damping causes $R(\lambda) < 1$ and the reflectance drop at ω_p is less severe.

For the application of TCO materials in solar cells, the transmission of the useable light spectrum must be higher than 80% and the sheet resistance lower than 10 Ω/□. The effect of N_e on the electrical and optical properties means that TCO materials are always optimised to balance high transparency with low resistivity. To compare different materials or even the same material but with differing thickness, a figure of merit Φ_{TC} derived by Haacke is used [44] which is described as

$$\Phi_{TC} = \frac{T(\lambda)^{10}}{\rho_s} \qquad 2.33$$

To improve Φ_{TC}, the sheet resistance has to be decreased without reducing the transmittance which can only be done by increasing the mobility [21].

2.2 Solar cell basics

The phenomena which have been described to explain the structural, electrical and optical properties of TCO thin films are applicable to the semiconductor materials used as solar cell absorber layer. The main difference is that the optical band gap of solar cell absorbers occurs in the visible wavelength region corresponding to wavelengths around 1.0 eV to 2 eV where the solar radiation is highest.

The first generation of solar cells are based on mono crystals of silicon and GaAs which are highly efficient but rather costly. In this section, descriptions are given for thin film solar cells based on silicon and semiconductor compounds (2nd generation), sensitised solar cells (3rd generation) and multi-junction solar cells (fourth generation), which all use TCO materials as contacts. Reviews comparing the relative advantages and disadvantages of different types of solar cells can be found in articles by Goetzberger *et al* [3, 45] and Waldau [4]. Record efficiency values for different types of solar cells have also been compiled by Green et al. [5].

The photovoltaic generation of electricity used by solar cells takes place in two steps. First, photons are absorbed from incident sunlight which generate electron-hole pairs in the semiconductor material which are then separated by an internal electric field. A special class of solar cells based on sensitized titanium dioxide separate the generation and charge separation as will be discussed later. In this section only the basic cell configuration and operation as well as the major research issues of the different types of solar cells are discussed. A summary of TCO specific issues regarding solar cell development will also be included.

2.2.1 Compound semiconductor solar cells

The simplest solar cell structure consists of two semiconductor regions with opposite doping type known as a pn junction. To reach thermal equilibrium, electrons/holes close to the junction diffuse across the junction into the *p*-type/*n*-type region, respectively where they are the minority charge carriers. This process leaves the ionized donors (or acceptors) behind, creating a depletion region around the junction, which is devoid of mobile carriers. The charge due to the ionized donors and acceptors induces an electric field across the depletion region, which in turn causes a drift of carriers in the opposite direction. The diffusion of carriers continues until the drift current balances the diffusion current, so that the Fermi energy is equal on both sides of the junction. When the pn junction is exposed to the light, only photons greater than the band gap energy generate electron hole pairs. The photo generated electrons and holes diffuse across the junction and are transported to the n- and p-type regions, respectively supplying an electric current to an external load. Figure 2.5 shows the band diagram of an illuminated pn junction solar cell.

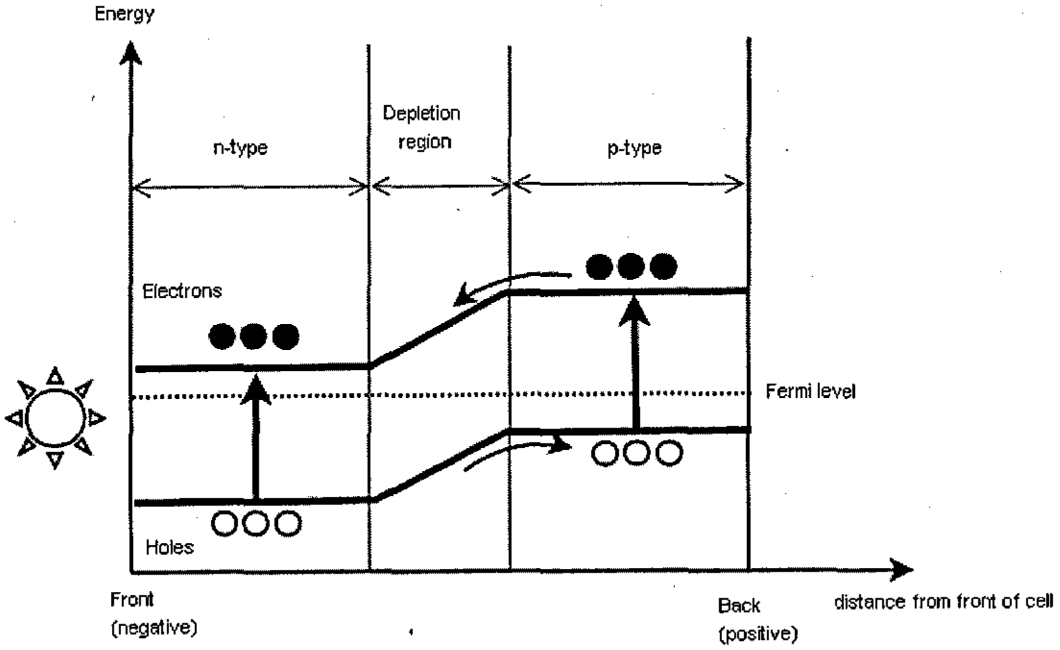

Figure 2.5. Energy band diagram of a pn junction solar cell under illumination. The arrows with solid heads indicate the direction in which the charge carriers flow.

Compound semiconductor solar cells are typically made up of a hetero-junction from two different materials. The front side semiconductor normally has a high energy band gap and is also very thin for high light transparency. The back side semiconductor of the junction has a low band gap and is normally relatively thicker than the front side semiconductor to absorb light for photo generation. Common examples of compound semiconductor solar cells are group II-VI and I-III-VI compounds.

Cadmium telluride (CdTe) is a II-VI compound semiconductor with a direct bandgap of 1.44 eV which is close to the optimum value for photo-conversion. Normally p-type CdTe is paired with n-type CdS to form a p-n hetero-junction. A maximum cell efficiency of about 16.5% has been reported [46] and though less than that for mono crystalline silicon, it is still significant because of the relative simplicity of processing CdTe cells. Reviews of the history and basic properties of CdTe solar cells have been published by several authors [47, 48]. Despite the potential hazards associated with cadmium, the simple preparation steps for CdTe solar cells make them attractive for commercial exploitation. It has been argued that CdTe solar cells rather than being hazardous, can be used to hold cadmium in an environmentally benign form [49]. Recycling of CdTe solar cells at the end of their lifetime may also ensure a continuous containment of cadmium which is not possible with most other forms of energy conversion [49]. The schematic structure of a typical CdTe/CdS polycrystalline thin film solar cell is shown in Figure 2.6.

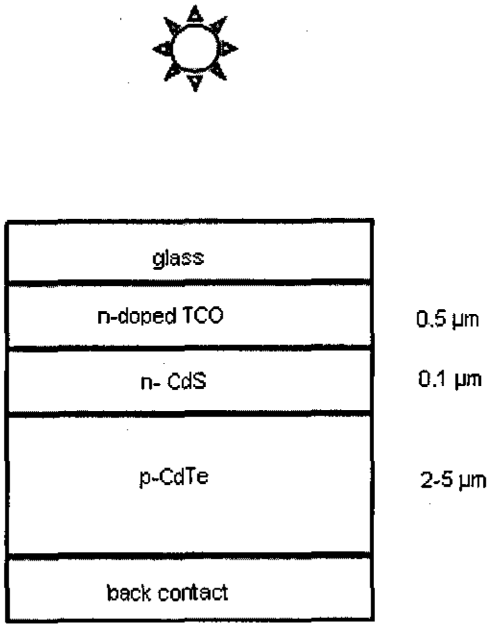

Figure 2.6: Schematic showing the different layers in a CdTe solar cell in the typical superstrate configuration.

Normally light enters the CdTe solar cell via the glass substrate. Just below the substrate comes the TCO layer which acts both as an electrode and a window to let light into the cell. The light then passes through a CdS window layer to the p-type CdTe where the incident photons are absorbed to generate electron-hole pairs. A thin layer of $CdS_{1-X}Te_X$ alloy is inserted between the CdTe and the back contact, to minimise the lattice mismatch which also reduces the defect density at the interface. The back contact is then made up of a metal [46] or a TCO film such as In_2O_3:Sn [50].

The structure presently used for CdTe solar cells suffers from two specific problems. First, the CdS window absorbs photons over 300-500nm reducing the photocurrent generated by the CdTe absorber but if the CdS layer is too thin, shunts arise. Secondly, it is difficult to form a back contact with CdTe solar cells which often leads to the formation of a schottky contact that would impede current flow in both directions near V_{OC}. Partial overlapping of the back contact and front junction could also lead to a reduction of the cell voltage. Current research includes finding alternatives to CdS as a window layer. Another area of research is to reduce the CdTe thickness and thus the amount of material required as the tellurium resources may be too low to sustain large scale production of such solar cells [51]. The role of copper in the formation of the back contact with CdTe still needs to be understood.

Another type of compound semiconductors are based on chalcogenide materials consisting of elements from Group VI of the periodic table. For PV applications, the most commonly used chalcogenides are the selenides, sulphides and tellurides of copper. A sub category of these are chalcopyrites based on copper, indium and selenium or sulphur which produce high efficiency cells. The discussion below is confined to the selenides. $CuInSe_2$ (CIS) is a semi-conducting compound of the I-III-VI2 family with a direct band gap of 1.0 eV and thus a high absorption coefficient compared to mono-crystalline silicon. Adding gallium to $CuInSe_2$ forms $CuGa_XIn_{1-X}Se_2$ (CIGS) and increases the band gap from 1.0 eV to 1.53 eV [52]. The highest laboratory efficiency just below 20%, which is the highest value reported for thin film solar cells, is obtained for a Ga: (Ga+In) atomic ratio of 0.3 [53]. CIS and CIGS are not easily n-doped and hence cadmium sulphide CdS, which improves current collection at short wavelengths, is often used to form a p-n hetero-junction.

The schematic structure of typical $CuGa_XIn_{1-X}Se_2|CdS$ polycrystalline thin film solar cell is illustrated in Figure 2.7. The solar cells can be prepared either in the superstrate or the substrate configuration. The light enters the cell through the front TCO contact which acts as a window layer and as an electrode for current collection.

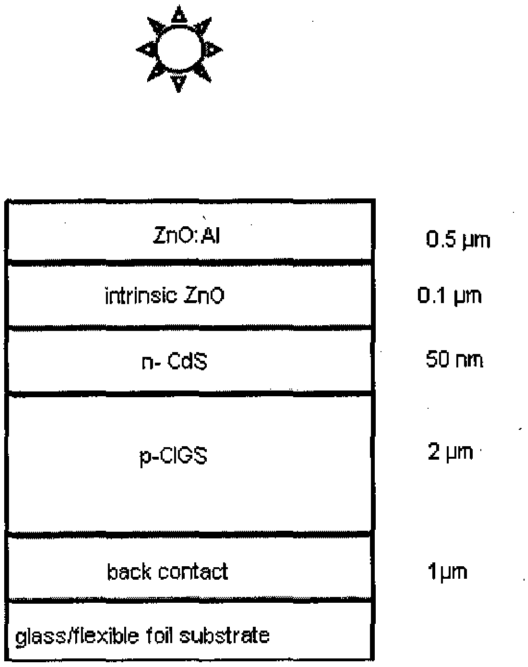

Figure 2.7. Schematic showing the different layers in a CIGS solar cell in the typical substrate configuration.

A thin highly resistive buffer layer consisting of intrinsic ZnO is used to prevent shunts. The PV action occurs in the CuGa$_X$In$_{1-X}$Se$_2$ absorber layers where the absorbed photons create the electron hole pairs responsible for the photo-current. The n-type window layer, typically CdS is used to create a depletion junction for charge separation. The back contact is usually molybdenum though other metals can be used. The device is completed by a metal contact grid on the front contact for current collection.

Current research for CuGa$_x$In$_{(1-x)}$Se$_2$ based solar cells is focussed on several issues. Firstly, n-type window layers other than CdS are being developed to improve the blue response and eliminate the use of Cd which is perceived to be toxic [54]. Secondly, research aimed at reducing the CuGa$_x$In$_{(1-x)}$Se$_2$ thickness is ongoing since indium is rather scarce and expensive. Light trapping schemes, that are used for thin film silicon have been investigated with the aim of reducing the CIGS thickness [55] Thirdly, a TCO material, at the front side, is required which has sufficient conductivity to act as an electrical contact while maintaining a high transparency in the wavelength region from 800 – 1200 nm. For CuGa$_x$In$_{(1-x)}$Se$_2$ solar cells, the development of such a

TCO material is challenging as the deposition temperatures should not exceed 200°C [56]. Other current research programmes are aimed at understanding the role of sodium in $CuGa_xIn_{(1-x)}Se_2$ growth, developing non vacuum preparation steps and/or low temperature deposition techniques to reduce manufacturing costs [57].

2.2.2 Thin film silicon solar cells

Thin film silicon is an attractive material for photovoltaic applications because silicon oxide is abundant and non-toxic and the films can be prepared using relatively inexpensive preparation techniques over large areas. Thin film silicon may be prepared in the amorphous state (a-Si:H) or the micro-crystalline state (μc-Si:H). Both types of thin film silicon materials incorporate small amounts of hydrogen. Small amounts of hydrogen are added to a-Si:H to bind with dangling bonds and reduce recombination centres in the material and for higher amounts of hydrogen, μc-Si:H synthesis is favoured.

The p-i-n structure rather than p-n junction is used for thin film silicon solar cells as the layer quality reduces with doping [58, 59] and charge carrier transportation by diffusion is not effective due to low carrier mobilities, short carrier lifetimes and thus low diffusion length of a-Si:H [58]. In a p-i-n solar cell, the charge carriers are generated in the intrinsic layer and are separated by an internal electric field. The electric field is caused by the depletion width which spans the whole intrinsic layer thus preventing recombination of the charge carriers along their path to the contacts. A schematic of the band diagram of an illuminated p-i-n solar cell is shown in Figure 2.8. The p-i-n solar cells are often designed to have the light entering through the p-layer for efficient hole collection because the holes have a lower mobility than electrons in thin film silicon.

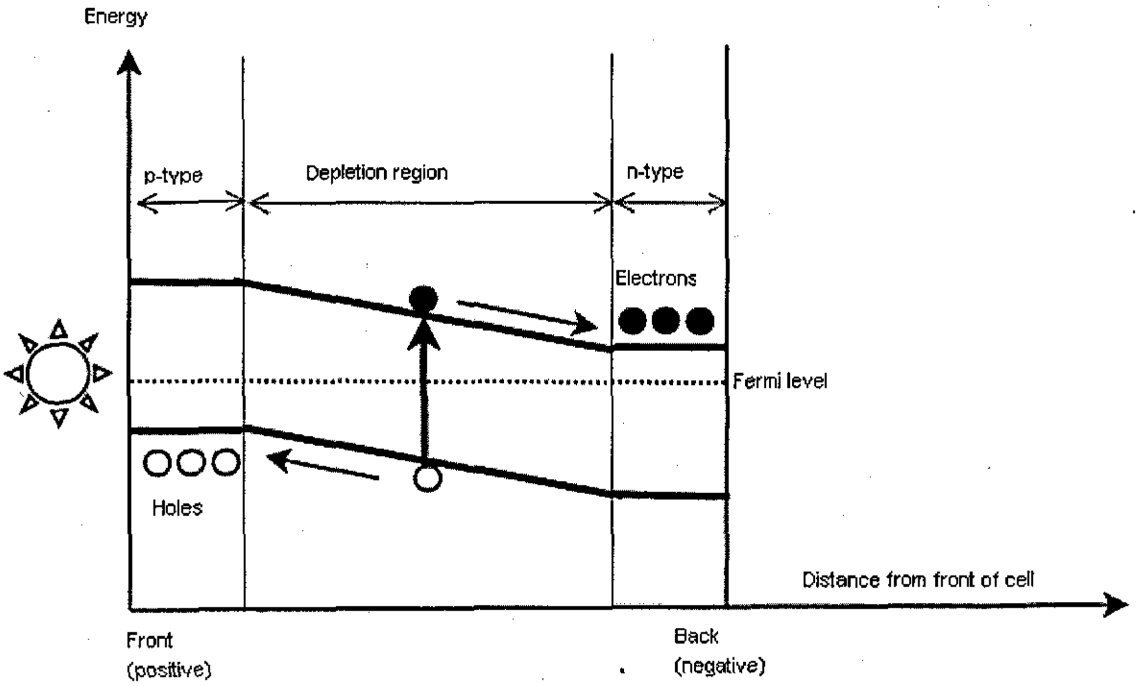

Figure 2.8. Energy band diagram of a p-i-n solar cell under illumination. The arrows with solid heads indicate the direction in which the charge carriers flow.

A schematic diagram of the typical components of a p-i-n solar cell is given in Figure 2.9. A transparent conductive oxide (TCO) film forms the front contact of the p-i-n solar cell.

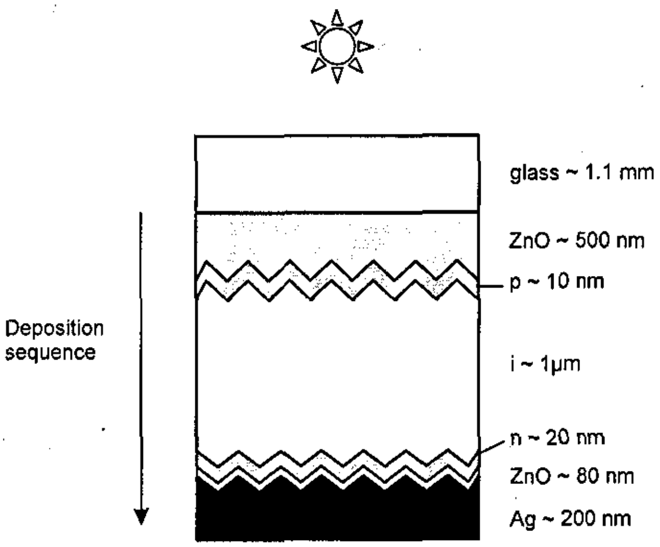

Figure 2.9. Schematic representation of a silicon thin film p-i-n solar cell.

Another ZnO:Al layer is inserted between the n -type thin film silicon and the metallic back contact to improve the reflection of the back contact [60]. At the rear of the cell, a metal film normally aluminium or silver, is used to serve both as an electrical contact and as a reflector. Amorphous silicon has a higher absorption coefficient than mono-crystalline silicon such that thin layers about 300 nm are sufficient to absorb visible wavelength light [61]. However, the a-Si:H solar cell efficiency degrades slightly after the first few hours of illumination to a lower stable value because of the Staebler Wronski (SW) effect whereby illumination during initial operation forms dangling bonds that reduce the carrier lifetime. Amorphous silicon solar cells have achieved stabilised efficiencies of 9.5 % in the laboratory [5]. Micro-crystalline silicon (μc-Si:H) solar cells which do not suffer from the SW effect have a typical laboratory efficiency of around 10% which is slightly higher than for a-Si:H [5].

Light trapping, a concept where a back contact with a rough surface is used to induce multiple reflections of weakly absorbed light within the absorber, is crucial to enhance the photo-current generation and thus the efficiency in thin film silicon solar cells. Light trapping may be induced by using rough metal back contact reflectors in the substrate configuration [62] or by using textured front contact TCO films in the superstrate configuration [63]. Amorphous silicon absorber layers thinner than 500 nm are desirable to minimise recombination because of the small drift length and to reduce the severity of light induced degradation [62]. Thicker i-layers in the range of 2–5 μm are necessary for μc-SiH absorber layers because the absorption coefficient is lower than a-Si:H. However, μc-SiH grows at relatively slow rates (a few angstroms per second) which hinders full commercial exploitation and a lot of research is currently dedicated to increasing the deposition rates and yield of μc-SiH. Light trapping allows the use of thinner μc-SiH absorbers ~ 1-2μm while maintaining high efficiency which minimises the actual thickness of material used and thus deposition time. Recent in light trapping techniques for thin film silicon cells use silver nano-particles [64] and carbon nanotubes [65] in the place of a rough TCO substrate.

2.2.3 Dye sensitised solar cells

Dye sensitized (DS) solar cells generate electricity via a photo-chemical process. A comprehensive review including the historical development of dye sensitized solar cells as well as the related technological challenges was made by Tributsch [66]. The first report of DS solar cells with significant efficiency ~ 11% was made in 1991 [67]. DS solar cell which are also known as Graetzel cells consists of a porous nanostructured anatase titanium dioxide (titania) film sensitized by a ruthenium complex in the presence of a iodide/triiodide redox couple. Figure 2.10 shows the schematic of a DS solar cell.

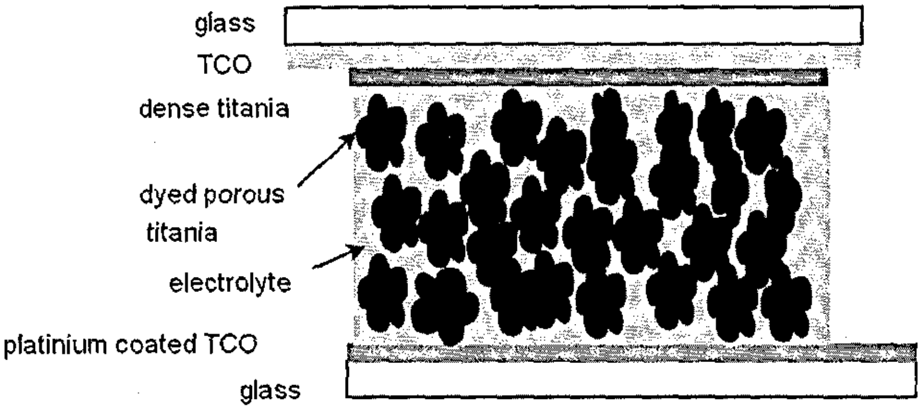

Figure 2.10. Components of a dye sensitised solar cell based on titania (TiO_2).

When a DS solar cell is illuminated, a photon is absorbed by the sensitizing dye which enters the excited state. The excited dye releases an electron which is then injected into the CB of the TiO_2. The electron percolates through the TiO_2 to the working electrode. At the same time, the electron given up by the dye is replaced by an electron from the iodide ions (I^-) in an electrolyte. The electrolyte also contains a triiodide (I^{3-}) which replenishes the electron lost by the iodide. Finally, the tri-iodide is reduced by addition of an electron by the platinum catalyst at the counter electrode. The iodide ion flows through the electrolyte to the working electrolyte ready to harvest the next photon and thus repeating the cycle. The voltage at the cell terminals under illumination is the difference between the Fermi level of the TiO_2 under illumination and the Nernst potential of the redox system in the electrolyte. Figure 2.11 shows a schematic of the charge separation and transfer mechanisms in a dye-sensitized solar cell. To ensure maximum charge transfer, a porous nano-structure is used to increase the surface area of the titanium dioxide. The electrolyte penetrates the porous TiO_2 matrix and reaches the front contact and reduces the electric field to zero. However, unlike p-n, p-i-n or MIS devices, the absence of the electric field is not important as charge separation is independent of an electric field and is kinetically driven.

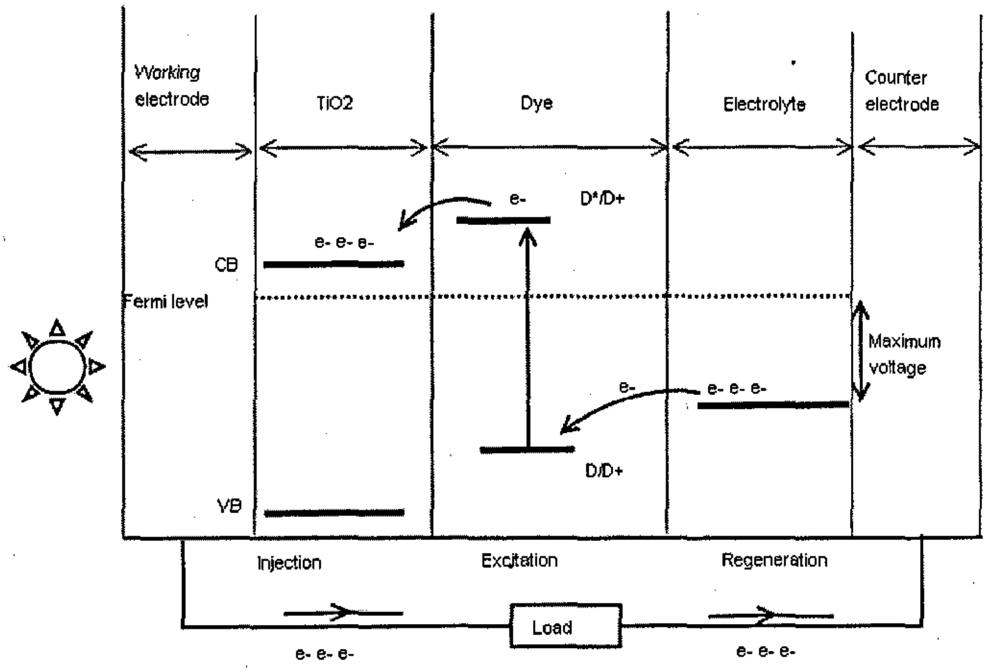

Figure 2.11. Schematic of the steps from dye excitation, to electron injection into the titanium dioxide layer to regeneration of the dye via the counter electrode.

The largely irreversible properties of the iodide/triiodide redox system mean that electrons can easily be donated but the reverse reaction to reduce triiodide is relatively slower. Thus, the reverse reaction of electrons from the front contact with triiodide is kinetically suppressed ensuring efficient charge transfer between the electrolyte and the TiO_2. However, an electrical field induced by the iodide/triiodide system at the front contact is critical for charge collection from the TiO_2 nano-structure.

Current research is aimed at improving the long term stability of DS solar cells, by replacing the liquid electrolyte with gels or solid electrolytes [66, 68]. Other research is aimed at reducing material costs by replacing the platinum catalyst with cheaper alternatives such as carbon [69] and at reducing the temperature required to sinter the porous TiO_2 layer [70].

2.2.4 Multi-junction solar cells and other solar cell configurations

The maximum achievable efficiency of single junction solar cells is limited by the inability for any known semiconductor material to utilise the entire solar light spectrum for photo-conversion. Multi-junction solar cell structures consist of stacks of different semiconductors with appropriately matched band gaps to increase the spectral response of the photovoltaic device over a wide wavelength range. The current of each solar cell in a series connected multi-junction cells must be matched since the overall photo-current is determined by the solar cell that generates the lower photo–current. However, optical losses from the front and back contacts, various inactive window layers of the cell as well as at interfaces between the layers in the stack may reduce the amount of light reaching the bottom cell causing a current mismatch. A microcrystalline silicon solar cell ($E_g \sim 1.12$ eV) can be combined with an amorphous silicon solar cell ($E_g \sim 1.8$ eV) to form a tandem solar cell in what is also referred to as the micromorph concept [59, 71, 72]. Tandem cells benefit from TCO materials with improved NIR transmission and efficient light trapping [63, 73, 74]. A stabilized efficiency exceeding 11% has been reported for small area micromorph tandem solar cells [5].

Bifacial solar cells in which photons incident on both faces of the solar cell contribute to photo current generation are a promising possibility to lower material costs by increasing the effective area used to harvest light. Also, for absorber layers that are transparent to long wavelengths, cells may operate at lower temperatures and thus attain higher efficiency than the equivalent single sided solar cells. The nature of bifacial solar cells means that their performance depends strongly on the transparency and conductivity of the TCO materials used as back and front contacts. Thin film bifacial solar cells with reasonable efficiency have been reported for CIGS [75] and CdTe [50].

Other types of solar cells such as concentrator, excitonic and organic solar cells are all being developed to increase solar cell efficiency while minimising material costs. These types of solar cells are outside the scope of this thesis and are not discussed here.

2.3 The role of TCO materials in the progress of solar cell development

The wide spread application of photovoltaic generation depends on research efforts to reduce the costs per kWh of PV generation while ensuring minimal damage to the environment. In this section, areas where high quality TCO materials may contribute to improving the solar cell efficiencies and/or to reducing material and production costs, are identified. More detailed discussions related to improvements in solar cell efficiency and lowering the production costs of thin film solar cells can be found in [7, 8, 45].

The large disparity between the PV efficiency of record small area research cells and record modules [5] has hindered the installation of large capacity PV systems. Differences in growth behaviour of small and large reactors typical of laboratories and industry, respectively, result in materials with different bulk and interface properties. Additionally, industrial production requires quicker deposition rates, simpler and cheaper processes and more environmentally benign process steps which would reduce the quality of the solar cell layers. The uniformity of layer thickness and other properties becomes more challenging as the substrate size and thus reactor size increases causing non uniform generation and collection of current across the module.

Since thin film solar modules consist of monolithic series connections of individual cells, area losses due to cell interconnect and contact areas further reduce the efficiency [7, 76, 77]. Therefore, to enhance the efficiency, I^2R losses caused by the TCO sheet resistance should be reduced. However, steps to reduce resistivity should not lower the TCO transmission since for example, $\rho_s < 4\ \Omega/\square$ and A $(\lambda) < 10\%$ over the range 400-1100 nm, have been proposed to increase the efficiency for CIGS modules [7]. The high resistivity of the SnO_2:F contacts in DS solar cells limits the cell width to values less than 1 cm^2 [69] but less resistive alternatives like In_2O_3:Sn and ZnO:Al are not stable to oxidation during the sintering step of the TiO_2 layer. Work is underway to replace the TiO_2 porous layer with different semiconductors such as ZnO nano rods [78] for better processing compatibility with existing TCO materials.

Solar cell efficiency must still be increased in order for PV generation to compete with other renewable energy technologies. Also, with higher efficiency, less surface area needs to be covered to generate a specific amount of energy. Solar cell efficiencies can be improved by developing absorbers with higher absorption coefficients over a wider range of the light spectrum and by understanding the fundamental properties of existing absorber materials. Increasing the spectral range of solar cell absorbers requires reductions in NIR absorption losses typical of TCO films.

Reducing the cost per kWh of PV generated electricity requires a further increase in solar cell efficiency and reductions in material costs, production costs and the balance of system (BOS) components. Andersson [79] projected that the rarity of certain materials may limit the large-scale deployment of photovoltaics. Moreover, the most efficient solar cells use rare metals as raw materials which makes their cost rather prohibitive - examples are:

- Indium used in the absorber layer of $CuGa_XIn_{1-X}Se_2$, as a cadmium free buffer in InS and in TCO materials such as In_2O_3:Sn.
- Tellurium used in CdTe solar cells
- Gallium used in $CuGa_XIn_{1-X}Se_2$, and as a dopant in emerging TCO materials such as ZnO:Ga and $InGaZnO_4$.

Since some metals are by-products of refinement of more abundant and thus cheaper metals e.g. Te from Cu, In from Zn and Ga from Al, better recovery techniques and new sources for production are imperative. Complementary solutions such as developing layer preparation processes with better material utilisation to improve production yields and to incorporate recycling of these materials during the manufacture and disposal of these cells are necessary. In_2O_3:Sn which has superior opto-electronic properties over ZnO:Al and SnO_2:F, is unsuitable for commercial solar cells because indium is expensive. Thus, the availability of high quality ZnO:Al substrates on large areas at low costs or an improvement of the even cheaper float line SnO_2:F substrates is imperative.

In cases where the cell efficiency is severely limited by substituting a costly material, efforts are being made to reduce the thickness of the layer e.g. light trapping has been considered for thinner CIGS solar cells [55]. The balance of system (BOS) components such as encapsulation, inverters and cabling, etc, contribute significantly to the overall module cost. Solar cells are required to have an operating lifetime exceeding 20 years but the TCO layers are susceptible to environmental degradation and thus the stability to heat and humidity, has to be improved. Therefore, the environmental stability of the TCO layers (and other layers in the solar cell) should be improved if low-cost module packaging is to be used for long-term reliability in the field.

Safety implications of the production and use of solar cells are important for their wide acceptance as a source of energy. The presence of potentially hazardous materials like Cd in CdTe absorbers, in CdS windows and in TCO materials such as $CdSnO_4$ in solar cells is objectionable to the public. While there is still no Cd free substitute for CdTe, window layers derived from TCO host materials such as ZnO:Mg, zinc oxy sulphide and zinc magnesium oxide are showing some success as reviewed by Siebentritt [54].

Lastly, PV is labelled as a "green" and sustainable energy source and thus it is important to use production process with minimal green house emissions and to have a relatively short energy payback period. In the first instance, this requires the use of processing steps that require a lower energy investment such as lower deposition temperatures, non vacuum processes and avoidance of annealing steps. The energy pay back time can also be further reduced if the solar cell efficiency is increased.

Additionally, several TCO materials have been reported with improved figures of merit, they have not resulted in better solar cell performance. Several factors contribute to this such as the influence of cell deposition processes, influence of TCO on growth of the absorber and inadequate understanding of the interface physics. TCO properties are often degraded when integrated into a solar cell. In the superstrate configuration, the growth and necessary treatment steps of the subsequently deposited absorber layers may chemically change the TCO material. Processes that require heating of the TCO substrate may further oxidise the TCO or form insulating layers at the interface of the absorber and the TCO material e.g. GaO in CIGS [80]. Additionally, in the substrate configuration, the TCO deposition parameters may be incompatible with previously deposited contacts or absorber layers thus the TCO material properties are adversely affected. Also the growth mechanism and thus the properties of the top TCO contact may be adversely affected by the underlying layers. Normally TCO materials grown under "soft" conditions such as low process temperature and/or higher sputter power, have a lower than optimum figure of merit. The TCO materials may themselves alter the structure of the photoactive layers. For instance, shunts may be introduced if the TCO surface is rough or crystallisation of materials such as CdTe and CIGS may be sub optimal. Alternative materials and better understanding of TCO thin films grown by various methods and the effect of the underlying substrate layers are topics being pursued in current research.

2.4 Recent developments and future directions in TCO research

Conventional TCO materials are typically n-type semi-conductors and whilst resistivity values approaching 10^{-4} Ω cm can be achieved in industry, values in the 10^{-5} Ω cm range are only achievable under controlled research conditions [19]. Therefore, there is still need to further reduce the resistivity. This section will only briefly discuss important recent developments and future directions in TCO research which are discussed in more detail elsewhere [14, 19, 81-85].

Presently, the most pressing issue is a means of reducing the TCO material and fabrication costs. Efforts are being made to develop indium free TCO host materials. The most promising alternative is ZnO:Al however improvements in large area processing are required [19]. Even with relatively low cost raw materials, there is still a need to reduce the TCO film thickness without reducing conductivity to allow faster processing rates and to further economise on the amount of raw materials required.

Further increments in the attainable conductivity of n-type TCO materials require the synthesis of new or improved materials with high mobility. High mobility > 50 $cm^2 V^{-1}s^{-1}$ is possible with CdO based TCO [86] but less hazardous alternatives are desirable. Also, mobility values above 70 $cm^2V^{-1}s^{-1}$ [87, 88] have been reported for degenerate In_2O_3 but cheaper more abundant host materials and dopants will be required for PV module production (see Chapter 6 for more details).

Intensive research in multicomponent oxides has led to the development of TCO materials with interesting properties and has also lead to a better understanding of the electronic transport mechanisms in TCO materials. Co-substitution of indium in In_2O_3 by low cost materials such as ZnO and/or SnO is now possible while maintaining reasonable conductivity [89]. TCO materials in the In_2O_3-ZnO-Ga_2O_3 system which are amorphous material but achieve relatively high charge carrier mobility ~ 40 $cm^2 V^{-1}s^{-1}$ for degenerate doping have been reported [41]. Highly conductive but amorphous In_2O_3-ZnO films at low temperatures with an atomically smooth surface have been developed [90], which will be useful for semi-conducting compound solar cells and OLEDs that are sensitive to spikes at interfaces with TCO contacts.

The discovery of p-type TCO materials may improve the quality of contacts to p-type absorber layers and also opens other possibilities for device applications [91, 92]. Examples of p-type TCO materials are delafossite oxides of the form AMO_2 which consist of alternate stacking of A cation layers with MO_2 layer e.g $CuAlO_2$ [93] as well as $CuGaO_2$ and $SrCuO_2$ [91]. Recent developments include the incorporation of chalcogenides to form LaCuOS and LaCuOSe and degenerate p-type conduction in Mg doped La CuOSe [83]. There have been reports of p-type conductivity in nitrogen doped zinc oxide typically with a hole density ~ 10^{17} cm^{-3} giving a resistivity ~ 10^{1} Ω cm. [94]. However since the high work function of ZnO makes p-type doping very difficult [33] there is much controversy surrounding this material as the doping effect is lost when the films are heated. At this stage, the resistivity and transmission of p-type TCO materials require further improvement as discussed in detail elsewhere [91, 92].

Other developments include deep-UV transparent TCO (β-Ga_2O_3) [95] and non-oxide compound transparent conductors such as single walled carbon nanotubes [96]. As further types of TCO materials are discovered, new areas of application become possible such as transparent opto-electronic devices [81]. In situ diagnosis will also be instrumental in studying the effect of defects states at interfaces between TCO materials and the other layers, on the performance of opto–electronic devices. For instance, in situ monitoring has been used to study the interface between SnO and the CdS window layer in CdTe solar cells [97] and the ZnO –CdS interface in CIGS solar cells [98].

2.5 Conclusion

TCO materials are unique semiconductors possessing simultaneous near metal conductivity and transparency to visible and near infra red light. Post transition metal oxides cations which have completely filled d-states fulfil these requirements and thus most of the known TCO materials fall in this group. Since the conductivity increases with charge carrier density whilst the transparency decreases, it is especially challenging to optimise both properties simultaneously. Moreover, for application of TCO materials as contacts in solar cells, it is important that the inclusion of the TCO does not degrade the device efficiency or unduly increase the production costs.

Extensive research is thus, still required to understand the fundamental properties of these materials and to develop processing techniques that are compatible to large scale application. The following chapters discuss the deposition techniques and characterisation techniques used to develop TCO materials for this thesis, with the aim of contributing incrementally to current solar cell research.

Chapter 3 Experimental methods

The method by which a thin film is prepared affects the material properties which in turn have to be measured to predict the suitability of the materials for a given application. TCO materials with desirable properties need to be assessed in solar cells to check their influence on the solar cell efficiency.

In this thesis, sputtering in one form or the other was used to prepare the TCO thin films under investigation. Sputtering allows a mostly independent variation of deposition parameters such that TCO thin films with a wide variety of properties could be prepared from the same source materials. In this chapter, the merits of sputtering over other common thin film preparation methods as well as challenges faced during the use of sputtering in practice, with special emphasis on TCO preparation, will be discussed. Additionally, other aspects relevant to TCO preparation such as the choice of substrate and post deposition treatments are described. Detailed characterisation of the TCO thin films was important to obtain information about the quality of the material (e.g. composition and structure) and the resulting properties (optical and electrical). An overview of the various methods used to characterise the TCO thin films is also included in this chapter. Finally, the steps used to prepare and characterise various types of solar cells using the TCO films are described.

3.1 Overview of thin film deposition methods

Several deposition techniques have been developed over the years in the production of thin film materials and the vast majority consist of either a physical or a chemical process [99-101]. Since the electrical and optical properties of TCO material depend on the microstructure and stoichiometric composition, the growth technique used may have an important influence. However, the choice of deposition technique is a compromise of the equipment and material cost, the deposition rate, the consistence and quality of the TCO films as well as the substrate area over which sufficient uniformity of film properties can be attained. The most common deposition methods for TCO thin films using chemical processes are spray pyrolysis and chemical vapour deposition (CVD) while the physical vapour deposition (PVD) processes include evaporation, sputtering and ablation.

In CVD, a mixture of gaseous compounds are allowed to chemically react and condense on a substrate to form a thin solid film. Careful control of the gas inlet layout and heating profile in the CVD reactor is required to avoid formation of powdery films and to achieve high uniformity over a large substrate area. CVD normally requires very high substrate temperatures, but if the reactant gases are ionised (plasma enhanced PE-CVD), substrate temperatures as low as 200 °C can be used. Several research groups have produced good quality TCO materials for solar cells using CVD [102, 103] while Pilkington Group Limited use atmospheric CVD to grow SnO_2:F on low emissivity glass panes on an industrial scale.

Spray pyrolysis involves the pyrolytic decomposition of droplets of a solution containing metal and other volatile agents sprayed onto a heated substrate. Normally a metal chloride is reduced by hydrogen to form the respective metal oxide. The disadvantages of spray pyrolysis include the requirement for very high substrate temperature and the film composition and structure depend on the droplet size and may vary from run to run. However, ultrasonic spray nozzles can be used to control droplet size and improve film consistency.

Chemical vapour deposition methods allow the stoichiometry of the starting materials and thus the end material, to be easily changed. However, there are three main disadvantages of both CVD and spray pyrolysis namely, the requirement for substrate heating during depositions which may preclude heat sensitive substrates, the relative difficulty in achieving TCO films with a smooth surface morphology and the inclusion of unwanted by-products e.g. chlorine, in the finished film.

Thin film preparation using PVD involves the generation of a vapour from a solid source by either evaporation, sputtering or ablation and allowing the vapour to condense onto a substrate as a solid thin film. With the exception of thermal evaporation, the source material does not require heating and a good quality of films is achievable by all these methods without intentionally heating the substrate. However, substrate heating or post deposition heat treatment might be required to improve specific TCO properties.

Evaporation involves heating a source material, in vacuum, to a temperature above its melting point and allowing the vapour phase to condense on a substrate facing the source. Thermal evaporation is often used for metallic source materials [87], though a reactive oxygen ambient is needed to prepare TCO films while electron beam evaporation is preferred for metal oxide sources [42]. Evaporation uses few process parameters and is easy to control but is limited to small area depositions because of high directionality.

Ablation involves the removal of material from a target as a result of absorbed light generated by either a laser or a high voltage spark. Pulsed laser deposition (PLD) is one example of ablation that has been used to prepare the highest quality TCO films on a laboratory scale e.g. for In_2O_3:Sn [104], for ZnO:Al [105], In_2O_3:Mo [106] and Cd_2SnO_4 [107]. In PLD, high-power laser pulses are used to raise the local temperature of the target above its vaporisation temperature releasing material that is ejected as a plume that eventually condenses on a substrate. The thin films are formed with very smooth surfaces suitable for epitaxial or multilayer coatings. Nevertheless, the films are uniform only over a small area, as the plume is highly directional, hindering the adaptation of PLD to mass production.

Sputtering is a PVD process based on a momentum transfer from accelerated energetic particles to the atoms of the target material [99, 101, 108, 109]. The arriving energetic particles eject material from the target which is allowed to condense on a suitably placed substrate. Sputtering can be used to produce high quality thin films on large substrates and is widely used in industry to coat architectural glass. The successful implementation of the industrially mature sputtering technology in solar cell fabrication would significantly reduce production costs. This thesis is mainly concerned with sputtering and a more detailed description of the aspects of sputtering follows in the next section.

3.2 Sputtering

Since sputtering requires low pressure conditions, prior to a deposition the coating chamber is evacuated to high vacuum to prevent contamination by residual gases and then it is back filled with an inert gas, usually argon, which provides the ions for sputtering. Other reactive gases such as oxygen may be included in reactive sputtering. The simplest form of sputtering is diode sputtering, in which a cathode is held at a high negative potential while the anode and the whole chamber are grounded. The high potential difference between the electrodes ionises the argon, contained therein according to the following equation:

$$e^- + Ar \rightarrow Ar^+ + 2e^- \qquad 3.1$$

The ionisation process forms a quasi-neutral plasma gas containing mainly neutral species as well as argon ions and electrons that are equally balanced in charge. The argon ions are then accelerated towards a target (cathode) by a negative potential where they sputter material from the target's surface as illustrated in Figure 3.1. The plasma is sustained by impact ionisation between neutral sputter gas atoms and secondary electrons emitted from the cathode. The low pressure environment maintains high ion energies and minimises collisions with the sputtered material after ejection from the target. Due to the highly energised bombarding ions, sputtered films are normally very compact and dense giving them good microstructures suitable for high conductivity and superior adhesion to most substrates. These aspects make sputtering suitable for coating large substrates while maintaining high film quality [110].

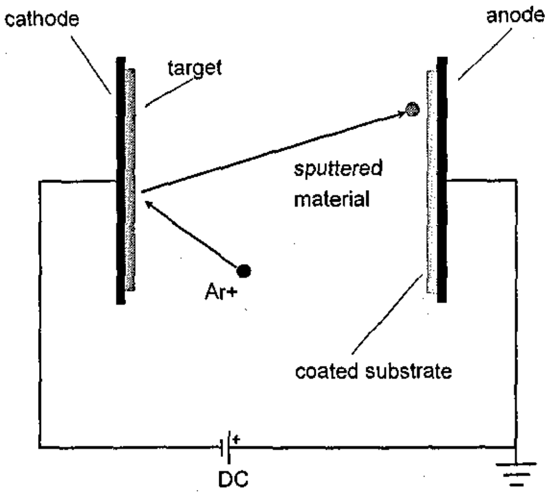

Figure 3.1. Schematic diagram showing the operating principle of diode sputtering.

The sputtering process can be characterised by the sputtering yield *S*, which is defined as the number of emitted atoms per incident ion, and determines the rate of erosion from the target and the growth rate of the film. The sputtering yield is enhanced by high cathode potential, high cathode current density, using heavier sputter gas ions and lower sputter pressure, all of which, increase the kinetic energy of the sputtering ions arriving at the target. Also, source materials with weaker bonds than compounds, such as metals, require less energy to dissociate leading to higher sputter yields.

Additionally, the presence of reactive gas in the sputtering ambient causes a reduction of deposition rate as will be discussed later in this chapter.

A direct current (D.C) voltage source may be used to energise the sputtering plasma provided that the cathode consists of metals or another conductive target material which can form part of the conductive path for the plasma discharge to the anode. Since most dielectric targets (e.g. metal oxides) have a relatively low conductivity, the accumulation of positively charged ions reduces the potential across the plasma discharge and may extinguish it.

A radio frequency (RF) power supply operating at 13.56 MHz can be applied to the dielectric target to prevent charge accumulation. The electrons, being very light, follow the polarity changes at radio frequency resulting in capacitive coupling such that the target surface need not be conductive. During the positive half cycle, the electrons negatively charge the target and in the negative half cycle; the much heavier argon ions are unable to reach the cathode under the influence of the electric field due to the RF-power. Thus, a net negative charge is maintained at the cathode regardless of the supply voltage polarity creating a self-biased electric potential between the electrodes. However, RF sputtering requires an impedance matching network to ensure that maximum power is transferred to the plasma making it more expensive than DC sputtering. It is therefore mainly used to sputter dielectric materials where the additional cost is justifiable. RF sputtering from ceramic targets is not often used for industrial purposes because of the low deposition rates which are further reduced by the need to limit the applied power to avoid over heating the targets [99-101].

3.2.1 Reactive sputtering

The problems with compound targets (especially for highly resistive materials) can be overcome by reactive sputtering from metallic targets. Reactive sputtering involves deposition from either a pure or an alloy metallic target and adding small amounts of a reactive gas e.g. oxygen, nitrogen or hydrogen to coat a substrate with the respective compound. Detailed descriptions of the mechanism of reactive sputtering exist [109, 111, 112] and several researchers have used reactive sputtering to prepare transparent conducting oxides [38, 113-125]. The reactive gas flow rate (or partial pressure) can be varied to adjust the stoichiometry of the deposited films without changing the target composition. The target may be biased using either DC or RF power, though the former is more common due to less complex equipment.

The reactive sputtering process stability is extremely sensitive to the condition of the target surface and a lot of research has been dedicated to understanding this phenomenon [109, 113, 114, 116, 119-121, 124]. When a metal target is sputtered in an inert gas ambient, the films deposited on the substrate are metallic and the target remains conductive. The case of reactive sputtering with oxygen addition will be considered in this work. If oxygen is added to the sputtering process, it combines with the sputtered metal to form an oxide which is deposited on the substrate. Small amounts of oxygen partially oxidise the films and as the oxygen flow rate increases, the degree of reaction in the films increases until full stoichiometry is reached. If the oxygen flow rate is further increased, the excess oxygen starts to react with the target surface coating it with a thin layer of oxide resulting in a sudden drop in discharge voltage as the plasma impedance is reduced. Reversal of the target surface back to pure metallic state is only possible by reducing the oxygen flow rate to a point where it can no longer maintain compound formation. This always happens at a significantly lower flow rate level than that which triggered the initial change. The reversal is also accompanied by a sudden increase in discharge voltage. This behaviour can be represented as a hysteresis curve where a high voltage indicates an exposed metallic surface in the metallic mode and a lower voltage indicating the state where the target surface is reduced in the oxide mode (Figure 3.2). Other film properties which depend on the condition of the target surface, such as film deposition rate, also show hysteresis effects as a function of oxygen flow rate. The hysteresis effect can be minimised once the process behaviour is known though several other factors need to be considered in this respect as proposed by several prediction models [111, 112]. Normally with reactive sputtering, the best film properties at high deposition rates can only be obtained either at the knee of the hysteresis curve, or in the transition mode which are highly unstable process conditions [112, 121, 126, 127]. Careful control of the process is required to operate under these conditions necessitating additional equipment for feed back control. The reactive sputtering process stability may be achieved by controlling the partial pressure of the reactive gas, the cathode voltage, or the discharge power. Detailed comparisons of the different methods used to control the reactive magnetron sputtering process have been discussed by Sproul in 1987 [126] and later in 2005 [127], however, here only brief descriptions are given.

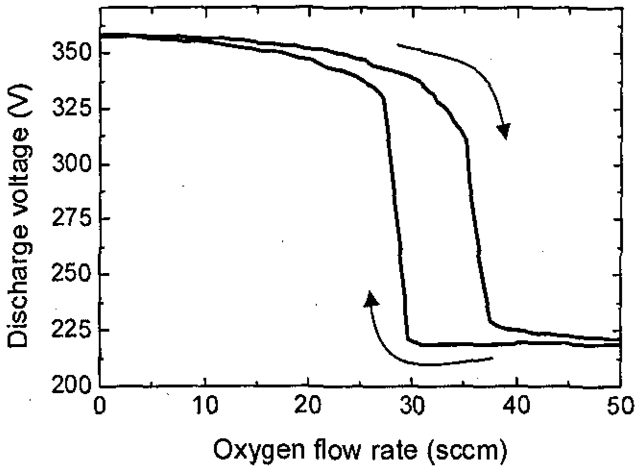

Figure 3.2. Hysteresis behaviour of the discharge voltage as oxygen flow rate is varied during reactive sputtering from a metallic target. The arrows indicate the direction in which the oxygen flow rate varies.

The simplest methods of maintaining the stability of the reactive sputter process, prevent poisoning of the target indirectly. For instance, a baffle can be placed between the substrate and cathode to reduce the oxygen partial pressure in the vicinity of the target [128]. Baffling is a simple method but is not widely used because of the reduced deposition rate and flaking which degrades the quality of the deposited film. Another simple method of preventing target poisoning is to pulse the reactive gas inflow into the sputter chamber so that only enough gas is admitted to the chamber to react with the sputtered metal [129]. More advanced methods of controlling the reactive sputter process make use of closed loop feedback using a monitored process parameter to adjust either the reactive gas flow or the power applied to the target. Since the target voltage reduces when the target is poisoned, it can be used as a signal to vary the reactive gas pressure and maintain a constant target power to avoid slipping out of the transition region [130]. The optical emission of one of the metal species in the plasma can also be used to control the reactive gas partial pressure [131]. A high intensity of the emission peak indicates the presence of unreacted metal in the plasma and if the peak intensity decreases, the oxygen flow is reduced to prevent the processes from slipping into the oxide mode. The response speed of this method has been significantly increased through the use of piezoelectric valves in a system known as Plasma Emission Monitoring (PEM®) which is widely used for TCO preparation [113, 114, 119-121, 124, 132]. Mass spectrometry of the reactive gas species can also be used to reduce the reactive gas flow or increase the discharge power (and thus deposition rate) if an excess of reactive gas is detected in the plasma [126]. Also, a λ-sensor can be used to monitor the reactive gas partial pressure and if it is higher or lower than the set point, the discharge power is reduced or increased, respectively [123, 133]. Lastly, *insitu* monitoring of the film properties by ellipsometry can be used to control the reactive gas partial pressure e.g. for silicon dioxide preparation whereby both the absorption coefficient and refractive index decrease significantly when the target is oxidised [134].

Another problem with reactive sputtering is arcing which spoils the film quality at the substrate, may extinguish the plasma and destabilises the reactive sputter process [109, 112]. Arcing is caused when a thin insulating coating over the target suffers dielectric breakdown as a high voltage is applied. Normally, the dc power supply is fitted with an arc suppressor that momentarily cuts off supply and quenches the arc with minimal interruption of the deposition process. Also, the gradual formation of a thin insulating film on the deposition chamber walls which form part of the anode causes long term drifts of the deposition process as the effective area of the anode changes. This phenomenon is known as the disappearing anode effect. Both arcing and the disappearing anode effect are prevented by using an RF- or pulsed DC- power source. During a positive half period, the target or chamber walls attract electrons, which prevent charge accumulation on insulating surfaces. The pulsed DC power can be alternately applied between two targets forming a dual cathode [113]. Both targets always have a conducting surface, because during every half cycle, any insulating coating is sputtered away so that the anode remains a conductive surface.

3.2.2 Magnetron Sputtering

The addition of a magnetic field perpendicular to the target surface as applied in magnetron sputtering, confines the secondary electrons close to the target surface such that the ionisation efficiency is substantially increased [101, 108, 135]. A high ionisation efficiency means that sputtering can be done at lower sputter pressure and thus lower gas consumption enabling sputtering at considerably lower voltages with high deposition rates. Additionally, magnetron sputtering is more desirable for semiconductor preparation than diode sputtering because unlike the latter, co-sputtering with impurity materials leads to their incorporation as active dopants [135].

The main challenges in magnetron sputtering are non uniformity of sputtered films and relatively low target material utilisation, both of which are caused by the enhanced erosion of the target in areas corresponding to the strongest magnetic field [136]. The greater ionisation efficiency near the strongest field lines enhances the ion current density increasing in the target erosion at these sites and particle bombardment of the growing film perpendicular to these sites. As a result, thin films prepared by magnetron sputtering without motion during deposition show non-uniformities along the substrate. The highest values of resistivity are observed in areas of the film corresponding to the erosion tracks especially at low deposition temperatures because of damage to the crystal structure [137]. Using elevated substrate temperatures may reduce this effect to a certain extent because of thermal induced healing of the crystal defects.

The non uniform erosion of the target surface requires that the target must be replaced before more than 30% of its volume has been used [13]. This is undesirable for expensive target materials like indium and for manufacturing plants where frequent shutdowns are unwanted. Dynamic methods that involve physical movement of the magnetic field source can further increase the target utilisation. For example, by scanning a magnetic array across the target surface using a step motor [115] or by using rotating cylindrical magnetrons [125], target utilisation of up to 90 % target utilisation can be achieved. Another technique named High Target Utilisation Sputtering (HiTUS^{TM}) completely eliminates the use of magnetrons giving an almost uniform erosion of the entire target surface [15]. Moreover, target material utilisation above 90% is achievable, without moving parts, while maintaining deposition rates comparable to magnetron sputtering. A 13.56 MHz RF source is used to ionise argon in a quartz tube remote from the target surface and the resulting plasma is then directed to the target surface using a series of magnets and a negative target bias voltage. Depending on whether the target material is metallic or ceramic, the bias voltage used is from a DC or an RF powered source, respectively.

3.2.3 Sputter deposition equipment used for this thesis

The ITO films discussed in this thesis were deposited using a HiTUS system, located at Plasma Quest Limited, UK in which the generation of the plasma and thus the ionisation current is remote and separate from the target bias. An external RF power supply is coupled by a coil to a quartz tube attached to the main chamber as illustrated in Figure 3.3. The sputter gas is then ionised in the quartz tube and not in the main chamber between the target and the substrate. A cylindrical electromagnet (launch magnet), located where the quartz tube joins the chamber wall, is used to intensify the ions and draw them towards the main chamber. Another magnet (steering magnet) placed concentric to the target, focuses the ions on to its surface. This layout of magnets eliminates the need for magnetrons and hence racetrack formation on the target is avoided. The ions are then accelerated towards the target by a voltage from an independent DC power supply to bring about sputtering from the target. HiTUS also allows high process stability during reactive sputtering without the need for active feed back control because the target voltage and ion current are independently controlled. This is possible because the degree to which the target is poisoned during reactive sputtering, is strongly correlated to the target voltage at a fixed current (or power) level [109, 111-113, 118, 132].

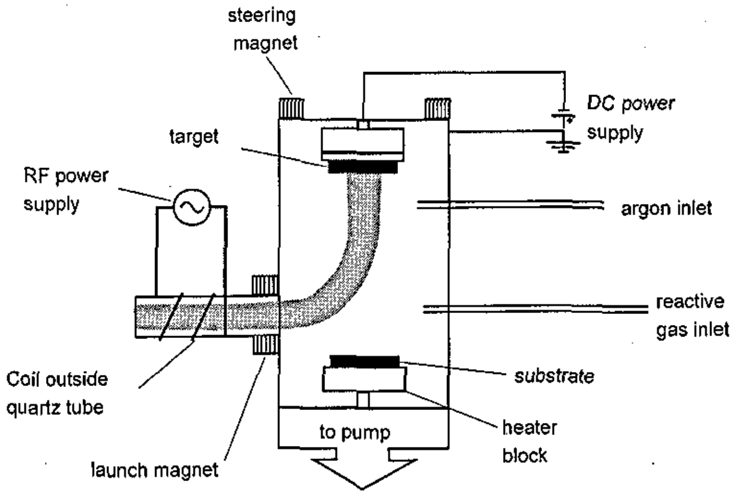

Figure 3.3. Schematic showing the basic set-up of a HiTUS system. Ionisation of argon occurs in the quartz tube and is independent of the applied voltage which accelerates the ions towards the target.

The base pressure in the HITUS system was typically 0.5 x 10^{-3} Pa as there was no load lock but this was sufficient for this work. A 108 mm diameter In:Sn (90:10 wt%) target was used for preparing the ITO thin films by reactive sputtering. The target to substrate distance was 160 mm so as to reduce interactions between the highly ionised and the growing thin film and as a result of this, the deposition rate was relatively low (20-45 nm/min). When required, the substrates were heated by a radial coil encased in a copper block fitted with a thermocouple. The temperature was maintained using simple on and off heating control. The actual temperature of the substrate was calibrated using a thermocouple attached to a bare glass substrate using silver epoxy and the heater temperature for subsequent depositions was adjusted to follow this calibration. The working pressure could be varied by adjusting the argon flow rate. The plasma was struck by applying a fixed RF power to the antenna coil outside the side arm to ionise the argon in the chamber via inductive coupling. During depositions, the DC power supply was operated in constant voltage mode to maintain the target at a fixed bias. The target current was monitored using the ammeter on the DC power supply while its value was controlled by adjusting the RF power supply to the quartz tube.

A vertical inline sputter system (VISS 300 manufactured by von Ardenne Anlagentechnik GmbH, Germany), located in Institute for Photovoltaics (now Institute of Energy Research (IEF-5)) at Research Centre Jülich, Germany, was used to prepare the ZnO:Al films for this thesis. This system can coat substrates measuring up to 30 cm x 30 cm but as smaller substrates were required for thin film characterisation, up to nine 0.7 mm thick pieces of Corning 1737 glass measuring 10 x 10 cm^2 were used for each run to prevent damaging the film by handling. The substrates were heated by elements controlled by PID and the substrate temperature was recorded using a pyrometer facing the growing film. The ZnO:Al films were deposited by mid frequency (40kHz) reactive magnetron sputtering from two Zn/Al (99.5/ 0.5 wt%) targets each measuring 10 x 75 cm^2 forming a dual cathode system. The chamber was evacuated to a base pressure of less than 2×10^{-5} Pa. Argon, used as sputter gas, enters the process chamber via two manifolds along the outer sides of the cathode system. The principal inlet for oxygen is a manifold situated between the two targets facing the substrate to allow reactive magnetron sputtering. The process stability was ensured by monitoring the PE intensity of zinc using a two channel PEM® device to adjust the oxygen flow appropriately. The PE intensity was calibrated such that a value of 50% corresponded to sputtering in the absence of oxygen (metallic mode) and lower values indicated more oxidic depositions [120]. After calibration, the working point at a fixed PE intensity was chosen in the transition region. The choice of working point was important as it has been found to have a considerable effect on the properties of the ZnO:Al films [116, 124].

The IMO thin films studied in this thesis were prepared using pulsed DC magnetron sputtering in an ATC Orion 8 UHV system (Aja International Inc., USA) for substrates up to 10 cm x 10 cm in size, located at CREST, Loughborough University. The sputtering power (2.8 – 3.4 W cm^{-2}) was supplied by a Pinnacle Plus source (Advanced Energy) as a DC signal pulsing at 150 kHz with a reverse time of 3 μs. The 75 mm diameter sputter target was composed of In_2O_3:Mo (98:2 wt%). A ceramic target was used in order to simplify the process control in the absence of an appropriate control facility for reactive sputtering. The sputter system is fitted with a load lock such that a base pressure about 5 x 10^{-6} Pa could be maintained in the deposition chamber. The desired sputter pressure could be adjusted and maintained by adaptive control of the gate valve in front of the high vacuum pump. If required, the substrates could be heated during film growth by two quartz lamps via an Inconel® holder. The heater temperature was controlled by PID using measurements by a thermocouple touching the surface of a quartz plate lying between the lamps and the Inconel® substrate holder. The actual substrate temperature was estimated to be ~10 % less than the indicated heater temperature.

3.3 Substrate materials

Thin film electronic devices such as solar cells require a substrate for mechanical support as well as protection from outside elements during the lifetime of the device. The type of substrate used always has an influence on the properties of the subsequently deposited material [99, 122, 138, 139].

Several physical and chemical properties must be considered when choosing substrates for solar cells and TCO thin films. For instance, if heating is required at any stage of the device process, the maximum temperature should be set below the softening point of the substrate to avoid deforming it. Also, the coefficient of thermal expansion *CTE* of the substrate and the subsequently applied thin film layers must closely match to prevent the development of stress which could cause cracking and/or de-lamination. If a substrate is flat at a given temperature then cooled, compressive strain results if the *CTE* of the film is smaller than that of the substrate and vice versa for tensile strain. A film under compressive strain has a concave curvature with respect to the outward normal in the direction of the film growth and the reverse is true for tensile strain.

The substrate should be chemically stable to prevent the diffusion of contaminant ions into the growing thin films. The substrate should also form an adequate barrier against the ingress of moisture or other detrimental gases into the device otherwise, an additional barrier layer is required and/or an appropriate encapsulation must be used. For solar cells in the superstrate configuration, a substrate with a high transmission of light ≥ 90% over a wide spectral range is mandatory to minimise optical losses of the device. The relative abundance of raw materials, the costs of handling and processing of a substrate may also be taken into consideration when choosing a substrate material. Using this criteria, though glass is derived from *silicon oxide which is widely abundant, the high thermal budget and careful handling* required during its production, significantly raise its cost. The substrates used for TCO preparation for this thesis were soda lime glass, boro-aluminosilicate glass and polyimide. Table 3.1 lists the typical properties of these substrates.

Table 3.1. Properties of substrates used for TCO preparation in this work.

Brand name	Menzel-Gläser Objektträger	Corning 1737	Upilex-S
Manufacturer	Gerhard Menzel Glasbearbeitungswerk GmbH & Co. KG (Germany)	Corning Incorporated (USA).	Ube Industries Ltd (Japan)
	Materials		
	Soda lime glass	Boro-aluminosilicate glass	Polyimide
Thickness (μm)	1100	700	25
Iron content (wt% Fe_2O_3)	0.09-0.1	>0.1	-
Alkali content (wt% Na_2O)	14.3	0.05	-
CTE (10^{-6}/°C)†	9.1	3.8	12
Softening point (°C)	720	975	-
Density (g/cm^2) at 20°C	2.45	2.54	-
Glass temperature	-	-	500
Visible light transmission (%)	~ 90	> 90	~65
References	[140]	[141]	[142]

† CTE - Coefficient of thermal expansion

Glass has conventionally been the substrate of choice for thin film solar cells because of its high transparency, mechanical strength, ability to prevent moisture and gas ingress as well as relatively high thermal stability (typically 600°C or more).

Usually, glass substrates are chosen according to their chemical composition as diffusion of different elements may affect either the film quality or the properties of the entire device. For instance, for solar cell applications, glass with a low iron (Fe_2O_3) content is desirable for high visible transparency. Also, soda lime glass which is commonly used for thin film preparation contains a relatively high amount of alkali (Na_2O) which may diffuse into the coating. While sodium from the soda containing glass may diffuse into the TCO materials and increase its resistance [143], it is beneficial for CIGS growth [144].

There is growing interest in replacing the more conventional wafer or thin films on rigid glass substrates with flexible plastic or metallic foils for solar cells and other electronic devices. Unlike glass, flexible substrates can be considerably thin while maintaining their mechanical strength resulting in cost savings as less raw materials are required. Thin flexible substrates are also desirable for solar cell applications such as in space or mobile electronics where weight is critical. Flexible devices can be applied to different shapes and can be handled in roll-to-roll processing which allows fast coating of large areas [110, 145, 146]. Metal foils provide flexibility, a CTE close to thin film semiconductors and high thermal stability. A wide variety of metals have been used as substrates for solar cells based on thin film silicon [147] and CIGS [148-151], but with less success for CdTe [152]. However, metals may diffuse into the device and degrade its performance or may form an unwanted conductive path in the device making plastic substrates preferable.

Plastic substrates have a low glass transition temperature (a few hundred degrees Celsius) and so are susceptible to deformation at the typical temperatures used for processing solar cells. Polyimide films such as Upilex and Kapton which are thermally stable to 500 °C have been developed and roll-to-roll coating on such substrates has been used to obtain efficiencies above 14 % [150] for CIGS compared with 19.9% on glass [53]. However, unlike glass, devices prepared on flexible foils are vulnerable to bending and stretching stresses while during process handling which may cause cracks or delamination of the device layers.

3.4 Post deposition treatment of TCO thin films

Post deposition treatment of the TCO thin films may be required to make them more suitable for application in solar cells or to study the stability of the film properties.

The following section discusses post deposition heat treatment and post deposition texture etching which were applied to some of the TCO films prepared for this thesis.

3.4.1 Heat treatment of TCO thin films

In most TCO related literature, the term annealing is used to describe heat treatment. Annealing refers to carefully controlled heat treatment of a material (often steel) followed by cooling at a predetermined rate to release strain and stress in the steel as well as to alter the structure to improve the material properties. In this thesis, limitations of the available equipment meant that the heat treatment procedures used cannot be referred to as annealing. However, the basic principles of annealing apply to some extent to the heat treatment processes used in this thesis.

Annealing comprises of three steps namely recovery, recrystallisation and grain growth. Recovery is the first stage of annealing whereby heating the material increases atomic diffusion which either heals or completely removes defects in the structure. However, the grains remain in a high strain state. Prolonged annealing of a previously amorphous film causes fine nuclei to form and grow into grains via short range diffusion until the previous strained grain structure is completely replaced by one with near zero strain. If annealing is continued beyond re-crystallisation, the grain size increases in order to reduce the grain boundary area and thus surface energy. Evidently, the temperature determines the material phase and structure during and after the treatment as it provides the energy for adatom diffusion while the heating duration determines whether or not significant changes in the film e.g. structural occur in the sample. The temperature required for post deposition heat treatment to achieve a given microstructure, always exceeds that required to grow the film with the same microstructure. Also the rate of heating and cooling affects the phase and structure of the film since rapid cooling may re-introduce stress and strain in the films.

Additional determinants come into play during heat treatment and these include the pressure and the composition of the processing environment. The ambient pressure affects the rate of chemical change as well as the temperature at which phase changes occur. Heat treatment of TCO thin films in vacuum often changes the preferred orientation of the grains and/or increases the grain size, both of which may increase the Hall mobility [153]. However, the changes in the TCO film structure after heat treatment may be modified according to the chemical composition of the ambient. For instance, heating a TCO thin film in an inert ambient may not only promote an increase in grain size, but also remove oxygen from the TCO surface. On the other hand, heating a TCO thin film in an oxidizing ambient such as steam, pure oxygen or air will oxidise the surface of the thin film. If the oxidative process is prolonged, oxygen may diffuse through the grain boundaries into the bulk of the films leading to increased grain boundary barrier height as well as oxidation of the film bulk. This reduces the conductivity of the TCO film as the increased grain boundary height reduces carrier mobility whilst oxidation of the film bulk fills oxygen vacancies and de-activates the impurity dopants and interstitial cations [39, 40]. On the other hand, heat treatment in a reducing atmosphere normally containing hydrogen or nitrogen or a mixture of both, removes oxygen from the TCO surface and may increase conductivity but reduce transparency of the TCO film [117, 154]. Lastly, the duration of the heat treatment determines whether the structural and or chemical change goes to completion or not.

In this thesis, post deposition heat treatment was carried out to study the thermal stability of the ITO films to examine their ability to withstand deterioration in conductivity and transmittance after the deposition of the active solar cell layers. Also, some In_2O_3:Mo films were heat treated in an attempt to understand the doping mechanism since the molybdenum content of the films had a strong dependence on the deposition temperature.

3.4.2 Modification of TCO surface morphology by etching

Thin film silicon cells require a TCO film with a rough surface in order to enhance absorption of long wavelength light. If the roughness of the TCO surface is of the same order of magnitude as the incident light, the scattered light undergoes total internal reflection within the cell which increases the probability of the light being absorbed in the cell since its optical length increases.

TCO thin films prepared by sputtering are generally smooth but by suppressing the ZnO film growth along the c-axis by using relatively high sputter pressure, and growing thick films, as-deposited textured ZnO films can be obtained [137, 155]. However, increasing the Al dopant content, which is necessary to improve the ZnO conductivity, reduces the haze of the films by hindering crystalline growth [155]. ZnO thin films with a rough surface structure can be prepared by either sputtering in the presence of water vapour [156]. or by CVD [102, 103]. In each of the afore-mentioned the processes, simultaneous optimisation of the transparency, the conductivity and the morphology of the TCO films is required, which is challenging. However, post deposition etching allows separation of the optimisation process allowing independent control of the ZnO conductivity as the etching process has minimal effect on the ZnO:Al carrier density and mobility [18]. The etching process can then be optimised by choice and/or composition of the etchant as well as the etching duration.

3.5 Analysis of TCO thin films

This section briefly describes the experimental techniques used to analyse the TCO films studied in this thesis. The thickness of the TCO films was measured and used to determine the deposition rate as well as some of the electrical properties. The opto-electronic properties of the TCO films were measured and further characterisation of the TCO surface morphology, structure and in some cases the chemical composition, was carried out for selected films. A more comprehensive discussion of the various techniques that could be used to characterise semiconductor materials and devices can be found in the text book by Schroder [157].

3.5.1 Thickness measurements

Since the sheet resistance of a TCO film reduces as the film is made thicker, while absorption increases, the determination of thickness is an important preliminary tool to correctly interpret any subsequent measurements. The thickness of the TCO films was measured at a step point on the film surface lying between the bare substrate and the edge of the film using a profilometer [1]. The step was created by masking the TCO surface and etching an exposed portion of the film with either 0.5 % HCl solution (for ZnO:Al) or a mixture of concentrated HCl and zinc powder for In_2O_3 and FTO films.

---

1. All ZnO:Al films were measured using a Dektak 3030 by Veeco Instruments Inc at IEF-5, Photovoltaics, Research Centre Jülich, Germany. Some ITO films were measured using a Talystep by Taylor Hobson at Plasma Quest Limited, UK. Some of the ITO and all other TCO films (IMO, FTO and ITiO) were measured using an XP-2 by Ambios Technology Inc. in CREST at Loughborough University.

3.5.2 Determination of electrical properties of TCO Films

The sheet resistance ρ_s, of the TCO films could be measured using a four-point probe which allows accurate measurements for thin films which normally have a resistance comparable to that of the measurement probes. A direct current I, is applied between the two outer probes while the voltage V, is measured across the two inner probes. Assuming an equal probe spacing on an infinite sheet, the sheet resistance is then given as

$$\rho_s = \frac{\pi}{\ln 2} \times \frac{V}{I} = 4.532\frac{V}{I} \qquad 3.2$$

This assumption was valid for all the films considered for this thesis as measurements were made on samples larger than 1cm². The film resistivity ρ was then determined using the film thickness. The van der Pauw method was used to determine the Hall effect properties of the TCO thin films[2,3]. Briefly, a 10mm x 10mm sample carrying a current I is placed perpendicular to a magnetic field B and then a Hall voltage is measured in the direction perpendicular to both I and B. The measurement is repeated with the magnetic field reversed and a computer programme provided with the equipment is used to calculate the carrier mobility, carrier density and resistivity, from the measured voltage and resistance using the van der Pauw method. The contacts onto the TCO films were made by using conductive silver paste that did not require heating to dry in order to avoid altering the conductivity of the films.

3.5.3 Optical measurements

The transmission $T(\lambda)$ and reflection $R(\lambda)$ spectrum measurements of TCO thin films and partially complete and complete solar cells were carried out using a spectrophotometer [4]. The $T(\lambda)$ and $R(\lambda)$ values were used to determine the absorption

---

[2] Keithley 926 located at IEF-5, Photovoltaics, Research Centre Juelich, Germany was used for ZnO:Al films.

[3] HMS 3000 (Ecopia) located at CREST, Loughborough University was used for all other TCO films.

[4] AvaSpec (UV-VIS) by Advantes B.V, Netherlands used for transmission measurements of some ITO thin films. The transmission and reflection of the rest of the TCO films were measured using UV-VIS-NIR spectrophotometers i.e. ZnO:Al thin films by a Lambda 19 by Perkin Elmer located at IEF-5,

$A(\lambda)$ according to equation 2.19. For transmittance measurements, the sample was clamped at a position just before the entry point of incident light to the sphere (see Figure 3.4a). Reflectance measurements were done by replacing the reference reflector (pressed barium sulphate disc) at the back of the sphere with the sample to be analysed as shown in Figure 3.4b.

The diffuse transmittance $T_{diffuse}$ of rough films was measured similarly to the transmission measurement described above, but without the reference reflector at the rear of the integrating sphere. Total transmittance, T_{total} of rough films was determined by using diiodomethane (CH_2I_2) as an index matching fluid between the rough TCO and an uncoated piece of corning glass to minimise losses due to internal light trapping inside the TCO.

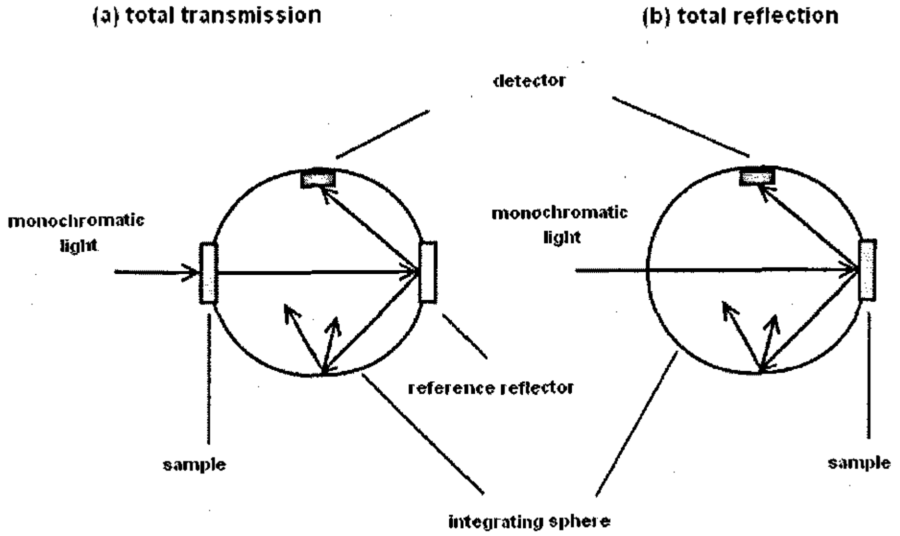

Figure 3.4. Schematic of the sample positions relative to the integrating sphere while measuring (a) the total transmission and (b) the total reflection of a sample.

The haze ratio of the etched films was determined as the fraction of diffuse (scattering angles exceeding 5°) transmittance with respect to the total transmittance. While transmission measurements are non-directional, reflection measurements are not, therefore care was taken in choosing the direction of illumination. For instance, for most TCO prepared as substrates for solar cells, the transmission was measured relative to air to measure the actual amount of light that would reach the cell and reflection measurements were taken with the sample illuminated via the substrate. For the

---

Photovoltaics, while a Cary 5000 by Varian at CREST, Loughborough University was used for all other TCO materials and solar cells.

reflection spectra under rear side illumination of bifacial solar cells and CIGS solar cells, the measurements were taken with illumination from the film side. In all the optical experiments, it was assumed that the sample is homogeneous though optical properties may, in practice, vary over a relatively small surface area.

3.5.4 Characterisation of TCO morphology

The morphology of selected TCO films was studied using Atomic Force Microscopy (AFM). Under operation in the tapping mode, a sharp tip, at the end of a flexible cantilever, is scanned over the thin film surface to form a high resolution image giving an indication of the thin film surface roughness and grain size. The tip-film interaction is monitored by detecting the reflection of a laser beam at the back of the cantilever. Differences in the height of the film surface give proportional changes in output voltage of a detector which are used to compile a three dimensional image of the scanned surface. The AFM images were generated for ITO on glass using a scanning probe microscope[5]. The ITO films on polyimide could not be analysed in the stylus mode as they were neither rigid nor flat enough and a more suitable acoustic scanning facility was not available on the instrument used.

Scanning Electron Microscopy (SEM)[6] was used to study the morphology of TCO thin film surfaces. SEM has a larger depth of field and lateral field of view making it more suitable than AFM for high resolution imaging of surface structures. In SEM operation, an electron beam is focussed and scanned across the sample by a series of electromagnetic lenses. When the electrons interact with the sample, some are either back scattered or cause the sample surface to emit secondary electrons. The electrons are attracted and collected by a detector and translated into a signal to create an image. The intensity of emitted electrons and thus brightness of the image produced, increases with the surface inclination and where sharp edges occur on the surface.

---

[5] Nanoscope IV, Digital Instruments of Veeco Metrology Group located at the Advanced Materials Research Institute, Northumbria University

[6] A Gemini1550, Leo SEM operated by E. Brauweiler and H.P. Bochem of the Institute of Thin Films and Surfaces at Research Centre Jülich, Germany was used to study the etched ZnO:Al films. The IMO thin film morphology was examined using a Leo 1530 VP located at Department of Materials, Loughborough University and was operated by J. Bates.

3.5.5 Analysis of TCO crystalline structure

X-ray diffraction (XRD) measurements are used to analyse the crystalline phases of crystals, powders and polycrystalline thin film materials. XRD can be further used to determine the structural properties of these phases such as the preferred orientation and grain size. XRD analysis operates on the principle that when an x-ray beam hits an atom, the electrons around the atom begin to oscillate at the same frequency as the incident beam. If the material is amorphous, the reflections of the x-ray will be randomly distributed in all directions and will cancel out. However, in a crystalline material, the regular arrangement of the atoms in the crystal will cause constructive interference in specific angles. Therefore a diffracted beam consisting of several coherent rays will be formed if Bragg's law of constructive interference is obeyed i.e.

$$n\lambda = 2d_{hkl} \sin\theta_{hkl} \tag{3.3}$$

Where n is an integer representing the order of reflection, λ is the x-ray wavelength in nm, d is the inter-planar spacing of atoms in the periodic lattice and θ is the angle of incidence of the x-rays.

For analysis, the intensity of the diffracted beam is plotted as a function of 2θ, which is related to the inter-planar spacing of the planes from which the peak is derived. The peak positions of the measured scans are used to identify phases in the thin film using a database compiled by the International Centre Diffraction Data (ICCD), formerly known as the Joint Committee on Powder Diffraction Standards (JCPDS). The microstructure or crystalline size can be determined from the full width at half maximum FWHM intensity of the peaks to determine the grain size according to the Debye-Scherrer's equation. Also, the intensities of the peaks can be compared to determine the preferred crystalline orientation. Crystalline phases of a material give sharp narrow diffraction peaks while amorphous phases give broad peaks. The crystallographic structure of some TCO films was analysed using a Bruker D8 Advance powder diffractometer in reflection mode. The instrument is fitted with a primary monochromator operating with Cu $K_{\alpha 1}$ radiation and uses a position sensitive detector[7].

3.5.6 Compositional analysis

X-ray photoelectron spectroscopy (XPS) was used to analyse the surface chemical composition of selected In_2O_3: Mo films. In XPS, a sample is placed under ultra high vacuum and irradiated with an x-ray beam which ejects inner shell electrons (photoelectrons) from the surface atoms of the sample. The kinetic energy measured by the XPS detector is made up of discrete energy levels emitted by the photoelectrons. Since the kinetic energy E_{KE} changes with photon energy $h\upsilon$ but the binding energy E_{BE} is independent of $h\upsilon$, XPS spectra are usually plotted in terms of E_{BE}. The binding energy of the electrons in the sample can be determined from the kinetic energy of electrons emitted from the sample as follows

$$E_{KE} = h\upsilon - E_{BE} - \Phi \qquad 3.4$$

Where Φ is the work function of the material under investigation. Each peak in the energy spectrum corresponds to the associated energy levels of the emitted photoelectrons which are characteristic of the atomic shell in the atoms and can thus be used to identify the chemical composition of the sample. By measuring the relative areas of peaks, the relative concentrations of specific elements in a sample can be determined. XPS is also used to identify the chemical state of the elements in the sample as the binding energy of an element increases as it becomes more oxidised.

XPS analysis of the IMO thin films was carried out using a Kratos AXIS ULTRA XPS system with a mono-chromated Al K_α X-ray source (1486.6eV) operated at 15mA emission current and 10kV anode potential[8]. The analysis chamber pressure was about 1.33×10^{-6} Pa. The ULTRA detector was used in fixed analyser transmission mode, with a pass energy of 80 eV for wide scans and a pass energy 20 eV for high resolution scans. Wide survey scans and high resolution scans were made for each

---

7. XRD data were collected by Dr. S.E Dann of the Department of Chemistry at Loughborough University.

8. XPS measurements were made by Ms. E. Smith, School of Chemistry at the University of Nottingham

sample and run thrice for a duration of 10 minutes and the resultant peaks were reproducible. Data analysis was carried out using CASAXPS software (Casa Software Ltd, UK) and the high resolution scans were charge corrected to the O 1s peak = 530 eV associated with In_2O_3 to determine atomic % values from the peak areas using Kratos sensitivity factors. The C 1s peak at 284.5 eV was not used for charge correction because it appeared to drift widely across the sample space. The chemical states of the different elements were identified by referring to numerical XPS databases [158-160]. A Guassian 70%– Lorentzian 30% product was used to model the component shapes of the Mo 3d peak with the full width half maximum constrained to less than 1.3eV.

3.6 Solar cell preparation and characterisation

The ultimate effectiveness of a TCO material in a solar cell can only be evaluated by the photovoltaic performance of the device. This section describes the preparation and characterisation methods of the solar cells used for this thesis.

3.6.1 Solar cell fabrication

The μc-Si:H solar cells were prepared on substrates comprising of texture etched ZnO:Al films on alumino-boroscilicate glass.[9] All the silicon layers of the solar cells were deposited in a PECVD system suitable for up to 30 x 30 cm² substrate size and eight different 5 x 10 cm² substrates were used at a time [74]. The PECVD process was energised by radio frequency power at 13.56 MHz and a predetermined silane and hydrogen mix was admitted into the deposition chamber to prepare the µc-Si:H. The PECVD system was fitted with two deposition chambers - one exclusively for the intrinsic layer and the other for doped silicon layers. During the deposition, the substrates were maintained at 200°C. First, a ~20 nm thick p-type layer was prepared by doping with trimethylboron on $B(CH_3)_3$ followed by a 1.1µm thick intrinsic layer and lastly the n-type layer with doping achieved by adding phosphine PH_3. To make the back contact, first an 80 nm thick ZnO:Al film was deposited over the thin film silicon using RF sputtering from a ceramic target without heating. This additional

---

[9] The µc-Si:H layers of the solar cells were prepared by J. Kirchoff and G. Schöpe at IEF-5 Phtovoltaics, Research Centre Jülich, Germany.

ZnO:Al layer is essential to improve the reflection of the silver back contact by preventing a reaction with the silicon layers [62]. Then several 1cm^2 silver back contacts of about 700 nm thick were applied via thermal evaporation through a mask to demarcate the individual cells. Next, the exposed back side ZnO:Al layers was etched away by a quick dip in a 5% HCl solution. An electrical contact to the front of the cells was created by masking the demarcated cells and scratching through the silicon layers in the spaces between the cells before evaporating silver into these channels. Finally, the entire cell was heated at 160 °C for 30 minutes and allowed to cool before being characterised.

The CdTe solar cells used in this thesis were prepared, on soda lime glass and consisted of the following layers, listed in order of deposition i.e. TCO|CdS|CdTe|Cu|back contact[10]. The CdS (window) and CdTe (absorber) layers were prepared using evaporation under high vacuum with the substrates kept below 450°C [161]. First, the CdS layers (300 nm – 500 nm) were deposited onto the TCO substrates, heated to 150°C, by evaporation and then annealed at 450 °C for re-crystallisation. Next, the CdTe layers (3 – 4.8 μm) were deposited with a substrate temperature of 300 °C. Though CdTe can be deposited at temperatures lower than 300°C, this was not investigated because of an anticipated reduction in efficiency as a result of poor structural quality [162, 163]. $CdCl_2$ was deposited onto the CdTe by evaporation without heating the substrate followed by heat treatment at 430 °C in air for 25 min. A post deposition $CdCl_2$ treatment is essential for the re-crystallisation of the CdTe regardless of the deposition method [163, 164] and the subsequent heat treatment increases the solar cell efficiency from about 2-3% to 10-12% for low temperature (330°C) grown CdTe. A tellurium rich layer required for a low resistance back contact was created by etching the exposed CdTe in a bromine-methanol solution. An ultra thin copper film was evaporated onto the etched CdTe to form Cu_xTe which was annealed at 200 °C for a short period. As the CdTe solar cells were required to be semi-transparent in the NIR region, the back contact was a sputtered TCO film and the cell area was defined by mechanical scribing.

The CIGS solar cells used for this work were prepared, at ETH-Zürich, in the substrate configuration on soda lime glass with the deposition order as follows:

---

[10] The deposition of the CdS, CdTe, CdCl and Cu layers as well as the intermediate treatment steps were carried out by S. Buecheler at Thin Films Physics Laboratory at ETH Zürich, Switzerland.

Mo|$CuGa_XIn_{1-X}Se_2$|CdS|ZnO|TCO[11]. The Mo back contact consisted of a bi-layer of a dense 100 nm film followed by a less compact 900 nm layer deposited using DC power set at 2kW and 0.3kW, respectively. The $CuGa_XIn_{1-X}Se_2$ stack was prepared by three-stage high vacuum evaporation with a 25% Cu-excess in the third stage. The total deposition time was 45 minutes giving a ~ 2μm thick stack. Afterwards, the CdS buffer was prepared by chemical bath deposition in a solution consisting of 200ml water, 10 ml of 0.024M thiourea, 15ml of 0.0018M cadmium acetate and 25 ml of 1.13M of ammonia solution. The deposition time was 15 minutes while the solution was maintained at 65°C to give a 60 nm thick film of CdS. The front electrode was made up of a ~50 nm thick RF sputtered ZnO film, followed by either an RF sputtered ZnO:Al film or a pulsed DC sputtered In_2O_3:Mo film. Finally, the solar cell was completed by a metal contact grid consisting of 50 nm Ni followed by 2μm of Al, both deposited by electron beam evaporation. Lastly, the cell area was defined by mechanical scribing.

The dye sensitised solar cells were prepared following a standard procedure to obtain high efficiency solar cells described elsewhere [165] [12]. First, the surface of the TCO film was pre-treated in a 40 mM $TiCl_4$ aqueous chemical bath maintained at ~65 °C and under constant stirring for about half an hour. Then a ~14 μm thick mesoporous layer of TiO_2 was screen printed (using Ti-Nanoxide HT/SP from Solaronix SA) and subsequently sintered at ~ 450 °C for 20 minutes. The large particle size TiO_2 scattering layer, which is generally deposited on top of HT/SP layers, was omitted to allow NIR light transmission through the DSC solar cell. A second $TiCl_4$ chemical bath treatment was applied to the sintered TiO_2 layer and then the whole stack was sintered again at ~ 450 °C for 15 minutes. The samples were then sensitised with a standard Ruthenium dye (N719 Ruthenium 535-bisTBA, Solaronix SA, Switzerland) in a solvent (1:1 ratio of acetonitrile and tert-butanol). The counter electrodes were made by applying a platinum precursor solution (hexachloroplatinic acid in propanol) on the TCO surface and then sintering for 15 min at ~400 °C. The cells were finished by sealing the counter-electrode on the top of the sensitised TiO_2 coated samples using a Surlyn™ spacer. The electrolyte consisting of a solution of 0.6M 1-propyl-3-methylimidazolium iodide, 0.03M I_2^-, 0.5M 4-tert-butylpyridine and 0.1M guanidine thiocyanate in a mixture of 85:15 acetonitrile to valeronitrile was prepared and filled

---

[11] The Mo,$CuGa_XIn_{1-X}Se_2$, intrinsic ZnO, ZnO:Al, Ni and Al layers were prepared by A. Chirila and S. Seyrling at the Thin Films Physics Laboratory at ETH Zürich, Switzerland.

[12] The DS solar cells were made by Jake Bowers at CREST, Loughborough University

through a pre-drilled hole in the counter electrode which was subsequently sealed with Surlyn™ and a glass cover-slip.

3.6.2 Solar Cell Characterisation

The performance of the solar cells was evaluated by measuring the current and voltage characteristics under illumination at standard test conditions (AM 1.5, 100mWcm^{-2} at 25°C) using a sun simulator[13]. The current generated in the illuminated solar cell varies in an exponential diode-like behaviour with an additional negative offset as shown in Figure 3.5.

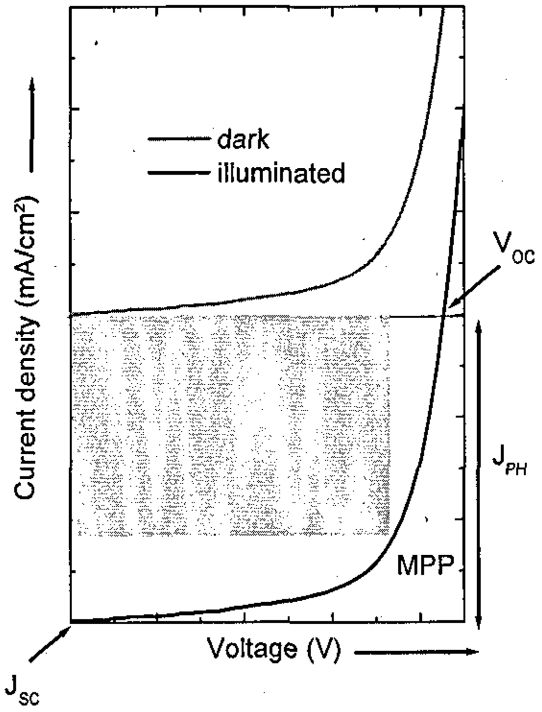

Figure 3.5. *J-V* characteristics of a solar cell under dark conditions and under illumination showing the short circuit current density J_{SC}, open circuit voltage V_{OC} and the maximum power point MPP. The grey area indicates the maximum power rectangle.

---

[13] For μc-Si:H thin film solar cells, a WXS-140S-Super (Class A) sun simulator by Wacom Ltd, Japan located at IEF-5, Research Centre Juelich, Germany was used. The DS solar cell J-V curves were obtained using a setup consisting of a Keithley 2425 source meter and a Xenon lamp (XBO, Osram) filtered (ScienceTech Inc. filter) to obtain AM1.5G.

The current at $V = 0$ is termed as the short circuit current I_{SC} . Normally, to compare cells of different surface area, the short circuit current density J_{SC} which is the short circuit current divided by the active surface area of the cell, is used. The voltage at $I = 0$ is termed as the open circuit voltage V_{OC}. The maximum power of the cell P_{MAX} is obtained at the maximum power point MPP where $dP/dV = 0$ and is the product of the current and voltage, at this point designated V_{MPP} and I_{MPP} , respectively. The quality of the cell is described by the fill factor FF, which is determined as follows

$$FF = \frac{J_{MPP} \times V_{MPP}}{V_{OC} I_{SC}} \tag{3.5}$$

The fill factor is important as solar cell operation with the highest possible current at the highest possible voltage is desirable. The power conversion η of the cells is related to the incident power P_{IN} and all the above parameters as

$$\eta = \frac{J_{MPP} \times V_{MPP}}{P_{IN}} = \frac{I_{SC} V_{OC}}{P_{IN}} FF \tag{3.6}$$

Details of solar cell performance and characterisation are discussed by Green [166]. The spectral response $SR(\lambda)$ of a solar cell compares the collected charge carriers to the number of incident photons over a specific wavelength spectrum and is described by the following relation

$$SR(\lambda) = \frac{I_{SC}(\lambda)}{E(\lambda)} = \frac{q \times \Phi_E}{h\upsilon \times \Phi_{PH}} \tag{3.7}$$

Where $E(\lambda)$ is the incident photon energy, Φ_E the electron flux and Φ_{PH} the photon flux. The spectral response can be used to derive the both the external and internal quantum efficiency. The external quantum efficiency $EQE\ (\lambda)$ shows how many electrons contribute to a current flowing into the external circuit under short circuit conditions. External quantum efficiency gives the net current available from the cell after optical losses through reflection, transmission or parasitic absorption and/or electrical losses caused by recombination of some of the photo-generated charge carriers. However, by measuring the reflection and transmission of the cell, *EQE (λ)* can be corrected to obtain the internal quantum efficiency *IQE (λ)* as follows

$$IQE(\lambda)=\frac{EQE(\lambda)}{1-R(\lambda)-T(\lambda)} \qquad 3.8$$

Spectral response measurements were used to evaluate the influence of optical losses on the performance of the solar cells [14]. For instance, the effect of light trapping caused by ZnO:Al in the solar cells could be quantified using these measurements. The extent to which a solar cell absorbs a particular wavelength of light depends on its reflectance, the absorption coefficient of the different materials and the path length; the light travels through the different layers. The differential spectral response (DSR), of selected solar cells was determined by illuminating the cell at zero bias, with monochromatic light of known irradiance, then measuring the resulting short circuit current. The procedure was repeated for each successive wavelength after a suitable interval between 300 nm and 1300 nm.

3.7 Summary

In this chapter the different methods available to prepare TCO thin films have been discussed, with particular emphasis on sputtering. All the TCO films prepared in this work were prepared by sputtering in one form or the other since sputtering offers a wide array of process parameters that can be independently adjusted. The advantages and disadvantages of each form of sputtering used have been discussed. The various methods used to characterise the TCO thin films and finished solar cells have also been discussed. Though, most of the preparation and characterisation methods used for these experiments were dictated mainly by the availability of suitable equipment, where there was a choice, an effort has been made to justify this.

---

[14] Spectral response measurements of μc-SiH solar cells on ZnO:Al were carried out by E. Bunte and W. Reetz of IEF-5, Photovoltaics, Research Centre Jülich, Germany.

Chapter 4 ITO prepared by High Target Utilisation Sputtering[15]

4.1 Introduction

Tin doped indium oxide (In_2O_3:Sn, ITO) is an n-type semiconductor widely used for optoelectronic applications requiring low electrical resistivity with high optical transparency. Despite the high cost of indium, In_2O_3:Sn is used in industry because low resistivity can be easily attained with low process temperatures making it applicable to heat sensitive substrates such as polymers. The low resistivity is a result of a high majority carrier density ~ 10^{21} cm^{-3} by tin doping [11, 12, 34, 42]. A relatively high mobility for such heavy doping is maintained by a highly dispersed s-state of the indium conduction band [167].

Intrinsic In_2O_3 thin films are n-type doped because of oxygen vacancies which result in a net positive charge. When Sn is added to In_2O_3, Sn^{4+} atoms substitute In^{3+} and provide an extra electron for conduction thus acting as an n-type donor. Electronic band structure calculations show that the conductivity of ITO is mainly attributed to 5s orbitals of Sn and the 2p- and 2s orbitals of O_2 [167]. Oxygen vacancies play a less significant role in doping when the Sn content exceeds a few percent [34]. Each Sn atom is assumed to contribute one electron but in practice, almost half the electrons introduced by Sn doping are trapped in the ITO. Several electron trapping defects have been put forward namely: excess oxygen interstitials which trap two electrons each at interstitial sites [34, 168], indium vacancies which trap three electrons each and divalent tin existing as Sn^{2+} instead of Sn^{4+}. At higher Sn contents, three other types of defects exist namely an ionisable tin oxide complex involving an interstitial O atom loosely bound to two Sn atoms, a non ionisable tin oxide complex consisting of two nearby Sn atoms strongly bound to three closest O atoms and an additional tin oxide associate [34, 168, 169].

In_2O_3:Sn thin films can be prepared using a variety of deposition methods such as sputtering from doped oxide targets [138, 170], reactive sputtering from indium –tin alloy targets [171], pulsed laser deposition [172], reactive evaporation [42] and spray pyrolysis [34]. Numerous studies have been carried out to investigate the influence of

---

[15] Most of the results presented in this chapter have been published in Papers I, II and III listed in the List of Publications.

deposition parameters on In_2O_3:Sn thin film properties in order to optimise the resistivity and transmittance. Generally, the optoelectronic properties of In_2O_3:Sn depend on the plasma excitation mode [29, 173], tin dopant concentration [174], oxygen content of films [170, 173], sputter pressure [173], substrate temperature [42, 171], and the target density [173, 175] during film growth and on the nature of the post deposition heat treatment [34, 153]. It is especially desirable to reduce the material and production costs of the In_2O_3:Sn layer for use in thin film solar cells. Material costs can be reduced by reactive sputtering from indium-tin (metal alloy) targets which are cheaper to fabricate than In_2O_3:Sn (ceramic) targets. Metallic targets also allow high rate deposition as their higher thermal conductivity allows application of elevated sputtering power. Additionally, there is growing interest in producing low resistivity In_2O_3:Sn films on plastic substrates to take advantage of their flexibility and light weight [13, 138].

This chapter presents the investigation of In_2O_3:Sn thin films prepared on either low iron soda lime glass or polyimide foils (Upilex) using High Target Utilisation Sputtering (HiTUS) in a small research system for substrates up to 50 x 50 mm^2 at Plasma Quest Limited. Since HiTUS allows target utilisation of up to 90%, this may potentially reduce the cost of large scale production of In_2O_3:Sn. The investigation was mainly concerned with the effect on the In_2O_3:Sn opto-electronic properties as a result of varying the target bias voltage, the total sputter pressure and the proportion of oxygen in the sputter gas mixture. A selection of the In_2O_3:Sn films deposited was subjected to heating in air and in vacuum to test their ability to survive degradation under high temperatures used for preparation of most solar cell absorbers.

4.2 Description and operation characteristics of the HiTUS system

The depositions were carried out in HiTUS system consisting of a cylindrical chamber fitted with a turbo molecular pump backed by a rotary pump giving a base pressure of about 0.5 x 10^{-3} Pa. The layout and principles of operation of the HiTUS system are discussed in chapter 3. The substrates for deposition were 1.1mm low iron soda lime glass and Upilex ^{TM} polyimide foils. The ammeter on the DC power supply unit (MDX5000, Advanced Energy) was used to monitor the target current level. The effective target power during HiTUS deposition was defined, here, as the product of the current measured at the target surface and the applied DC voltage. However, to compare conditions with reports by other workers, the target power density and target current density i_T which are calculated from the target power and target current, respectively divided by the target area are used. The applied voltage was assumed to be uniformly across the entire target surface. The current flow across the target surface was also assumed to be uniform. The target surface was cleaned by sputtering in a pure argon atmosphere for five minutes before oxygen was admitted into the chamber for reactive sputtering. When the process had stabilised as indicated by a stable target current, each deposition was run for twelve minutes. The details of the deposition conditions used to grow the various In_2O_3:Sn films are given in Table 4.1.

Table 4.1. Deposition conditions for In_2O_3:Sn film growth

Common parameters				
Sputter mode	High Target Utilisation Sputtering (HiTUS)			
Target composition	In:Sn (90:10 wt%)			
Target substrate separation (cm)	16			
Coating duration (min)	12			
Substrates	Soda lime glass, polyimide (Upilex^{TM})			
	Series			
	I	II	III	IV
RF ionisation power (W)	600-720	650-850	650	650- 720
Target power density (W cm^{-2})	1.36 – 2.18	2.18	2.18	2.18
DC target voltage (V)	500	300-500	500	500
Argon flow rate (sccm)	40	40	40	20-60
Oxygen flow rate (sccm)	4.0 – 4.2	4.2	4.2	4.0 – 4.4
Sputter pressure p_S (Pa)	0.3	0.3	0.3	0.15 – 0.45
Substrate temperature T_S (°C)†	460	460	25 - 460	460
Film thickness (nm)	370 - 420	312-408	380-408	380-424

† A substrate temperature of 25 °C designates no intentional heating of the substrate during deposition.

The target current density i_T during sputtering is comprised of the ion current density i_I and a contribution of secondary electrons emitted from the target associated with an emission coefficient γ. Thus target current density can be determined as

$$i_T = i_I(1+\gamma) \tag{4.1}$$

For sputtering, the film deposition rate D is related to the ion current i_I arriving at the target and the sputter yield S (defined as the number of sputtered atoms divided by the number of bombarding ions) by the following relation

$$D \propto i_I S \qquad 4.2$$

Also, S is directly proportional to the ion energy and thus the voltage applied to the target V_T. A film growth coefficient β, defined as the deposition rate normalised by target current density was used to correlate the sputter yield to the target voltage [176].

4.2.1 Influence of target power density

In order to study the influence of the target power density on In_2O_3:Sn films prepared by HiTUS, a set of In_2O_3:Sn films were prepared on glass and polyimide using the parameters listed under Series I in Table 4.1. All deposition parameters were fixed with the exception of the RF ionisation power (and thus target current and effective target power) and oxygen flow rate which were varied. The maximum values of I_T and V_T used were limited by the cooling ability of the system chiefly because the "sputter down" configuration was being used.

Increasing the target current while maintaining the voltage increases the effective target power. Figure 4.1 (a) shows the variation of target power density with RF ionisation power at a constant target voltage of 500 V and constant sputter pressure. The target power density increases almost linearly with the RF power used to ionise the argon sputter gas as a result of the increased target current . Figure 4.1 (b) shows a graph of the deposition rate against the target power density of the In_2O_3:Sn films. The deposition rate increases from about 20 nm/min to 35 nm/min as the target power density increases for both oxygen flow rates. Figure 4.1 (c) shows β as a function of the target power density. β increases slightly as the target power density is increased from 1.36 Wcm^{-2} then peaks for 1.64 Wcm^{-2} then reduces again for 2.18 Wcm^{-2}. Since the target bias voltage was constant for all the depositions considered here, the sputtering yield is not expected to vary much with increasing target power density. Therefore, the increase in deposition rate with target power density observed is caused by an increased ion flux.

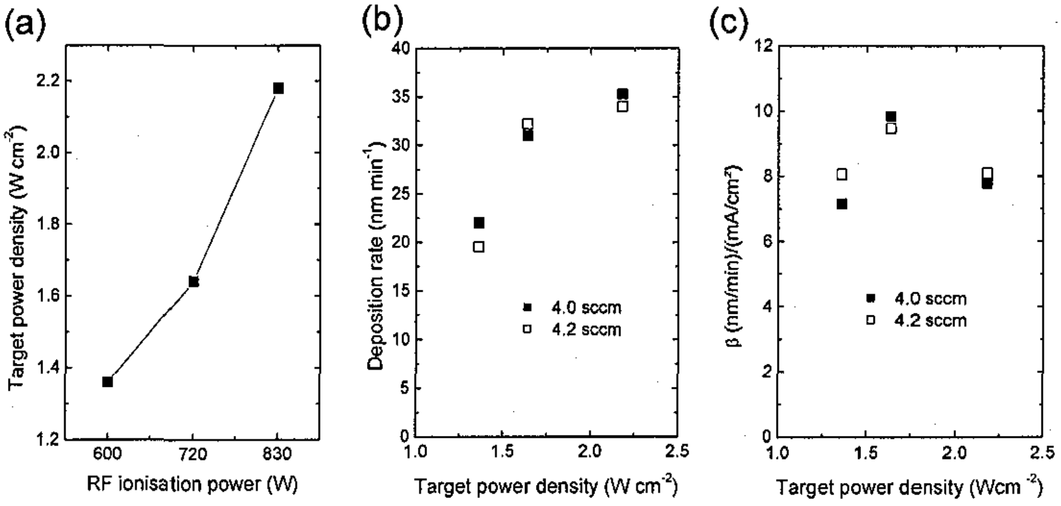

Figure 4.1. (a) Target power density as a function of RF ionisation power used to generate the target current and (b) deposition rate and (c) film growth coefficient (β) of In_2O_3:Sn on soda lime glass as a function of target power density. Deposition parameters are given under Series I in Table 4.1.

Figure 4.2 shows the resistivity as a function of the effective target power density for In_2O_3:Sn films on soda lime glass (left) and Upilex polyimide (right) for two different oxygen flow rates i.e. 4.0 sccm and 4.2 sccm.

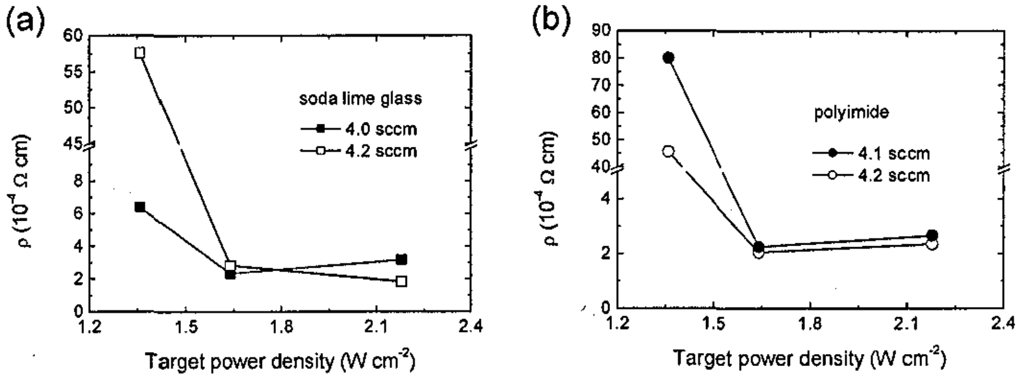

Figure 4.2. In_2O_3:Sn film resistivity as a function of target power density for (a) soda lime glass and (b) polyimide substrates. The filled and unfilled shapes in each graph correspond to an oxygen flow rate of 4.0 sccm and 4.2 sccm, respectively. Deposition parameters are given under Series I in Table 4.1. The lines are to guide the eye.

The In_2O_3:Sn resistivity on both soda lime glass and polyimide reduces as the target power density increases from 1.36 Wcm^{-2} to 1.64 Wcm^{-2} then appears to saturate at close to 2.0 x 10 $^{-4}$ Ω cm at 2.18 Wcm^{-2}. Also, at 1.36 Wcm^{-2}, with a lower oxygen flow rate, resistivity below 10 $^{-3}$ Ω cm is achievable for In_2O_3:Sn on glass whereas on the polyimide film, the corresponding resistivity is nearly ten times as much.

The In_2O_3:Sn film transmission is also considerably affected if target ionisation current and thus power is increased while oxygen flow rate is kept constant. Figure 4.3(a) shows the transmission spectra from 300 nm and 1000 nm for In_2O_3:Sn thin films deposited various target power densities at a fixed oxygen flow rate. The transmission edge of the In_2O_3:Sn thin films shifted to lower wavelengths as the target power density increases and the transmission spectra showed interference fringes from 400 – 1000 nm. Generally the average transmission from 400 nm to 1000 nm decreased as the target power density is increased. Figure 4.3(b) shows the figure of merit Φ_{VIS} (averaged over 400 – 800 nm) as a function of target power density for two oxygen flow rates of 4.0 sccm and 4.2 sccm. For a fixed oxygen flow rate of 4.0 sccm, Φ_{VIS} increased drastically as the target power density from 1.36 Wcm^{-2} to 1.64 Wcm^{-2} the reduced again. On the other hand for a slightly increased oxygen flow rate of 4.0 sccm, Φ_{VIS} increased as the target power density, with the magnitude of change reducing for higher target power densities.

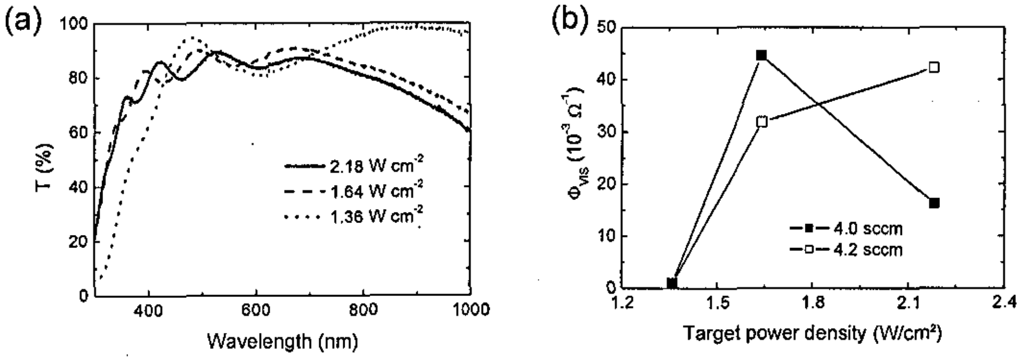

Figure 4.3. (a) Transmission spectra of In_2O_3:Sn on soda lime glass with various target power densities with a fixed oxygen flow rate of 4.2 sccm. (b) Average figure of merit Φ_{VIS} (400 nm to 800 nm) as a function of target power density. Deposition parameters are given under Series I in Table 4.1. The lines in (b) are to guide the eye.

Similar observations where increasing the target power density decreases the In_2O_3:Sn film resistivity and transmission, have been made by other workers [173, 175]. The observed influence of the target power density on the electrical and optical properties of the In_2O_3:Sn thin films is a result of the different oxygen content in the oxide. The varying stoichiometry in the In_2O_3:Sn thin films is a result of varying ratios of sputtered metal to oxygen atoms available at each target power density. With low target power, only a small amount of metal is sputtered from the surface. The oxygen added to the process either reacts with the target surface or further oxidises the sputtered particles on their way to the substrate. This results in highly oxidised films with higher resistivity and higher NIR transmission as less electrons from In and Sn are free to contribute to conduction and carrier enhanced absorption in the near infra red region. Increased target power with the same oxygen flow rate adds to the number of metallic atoms available for oxidation. This leaves insufficient oxygen to react with the metallic target surface, exposed by sputtering, which remains un-oxidised leading to more metallic In_2O_3:Sn films. Song et al. [174], also reported that In_2O_3:Sn films with an oxygen deficiency normally have low resistance and increased absorption in the long wavelength regions as observed here. Further increasing the target power density beyond 2.18 W cm^{-2} may lead to an excess of charge carriers that would increase the resistivity as a result of higher ionised impurity scattering of charge carriers but reduce the transmission as a result of impurity states forming in the band gap. Further elevation of the target power density would cause a further increase in resistivity and optical absorption as a result of re-sputtering of the materials from previously deposited layers of the In_2O_3:Sn films.

4.2.2 Influence of target voltage

Since polyimide films are rather delicate, the ion energy during deposition should be moderated to reduce the momentum with which the sputtered material arrives at the substrate. Also, in thin film solar cell fabrication steps that require a transparent conducting oxide (TCO) to be deposited onto the semi-conducting layers, moderate ion energy during the sputtering of In_2O_3:Sn thin film is desirable to minimise the ion damage. It is well known that the target voltage has the largest influence on ion energy during sputtering [112]. However, during dc reactive magnetron sputtering, the discharge voltage is constant for a given oxygen flow rate at a given target power level and in order to reduce the discharge(target) voltage, the target power density has to be lowered at the expense of the deposition rate [112, 177]. The sputter ion energy during magnetron sputtering can be controlled by either coupling both an RF and a DC power source directly to the target [176, 178] or by placing an RF powered coil in the space between a DC biased target and the substrate [179]. The HiTUS technology also allows the application of an independent DC voltage to the target for this purpose. Hence the work described in this section was aimed at investigating the effect of varying the target bias voltage on the properties of In_2O_3:Sn thin films grown on glass and polyimide foils.

It is known that film growth by reactive sputtering depends on deposition factors such as the total pressure, partial pressure of the reactive gas, and discharge power. In this work, all these factors are kept constant in order to study the influence of the target bias voltage only and the details of the deposition parameters are listed under Series II in Table 4.1. To maintain the target power, the RF ionisation power was varied to obtain the appropriate target current density with each DC target voltage considered. In the absence of a DC voltage bias, a voltage reading of about 25 V was recorded at the target regardless of the RF power level used for ionisation. Figure 4.4 shows the relationship between the RF ionisation power and the target current density in the voltage range of interest. The target current density increases linearly with the applied RF ionisation power.

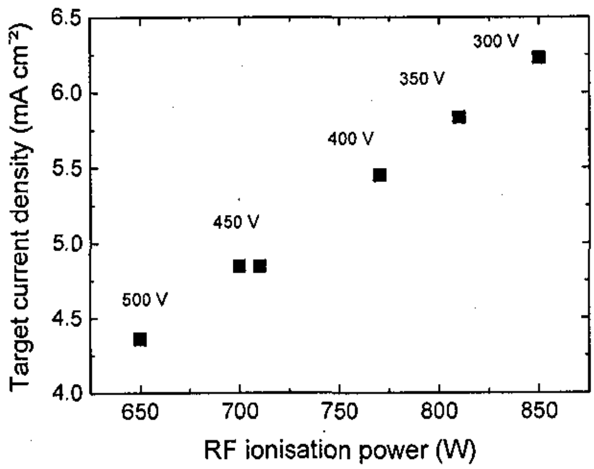

Figure 4.4. Target current density dependence on the RF ionisation power. Higher target current densities correspond to a lower target bias voltage in order to maintain the target power density at 2.18 W/cm². Deposition parameters are given under Series II in Table 4.1.

The dependence of both the deposition rate and the film growth coefficient (β) of the In_2O_3:Sn films, on glass, on the DC target voltage (V_T) is shown in Figure 4.5. The deposition rate increased from 26 nm min^{-1} to 34 nm min^{-1} as voltage was varied from 300 V to 500 V while β doubled when V_T was increased over the same range.

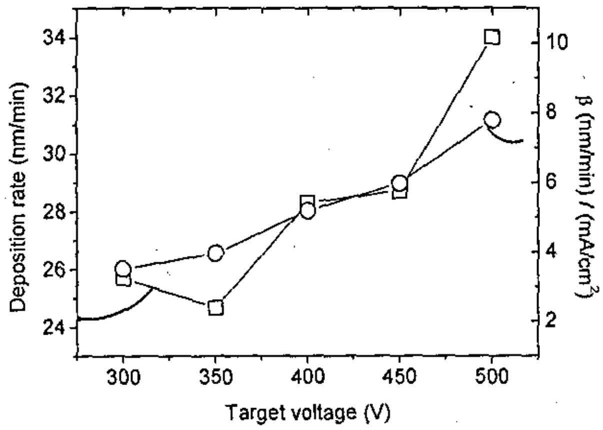

Figure 4.5. Deposition rate (squares) and film growth coefficient β (circles) as a function of target voltage. Deposition parameters are given under Series II in Table 4.1. Lines are to guide the eye.

Figure 4.6 shows the carrier density N, mobility μ and resistivity ρ, of the In_2O_3:Sn films on glass and polyimide, plotted against the target voltage.

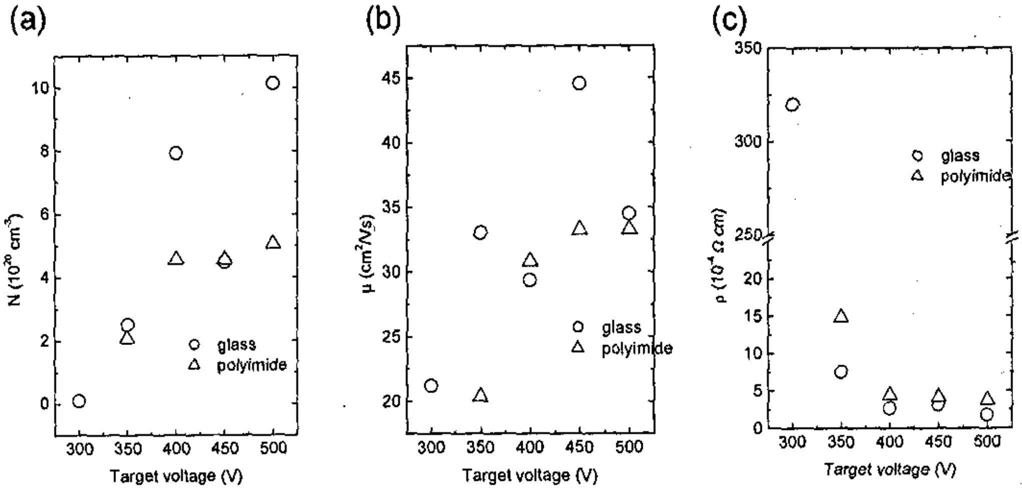

Figure 4.6. (a) Carrier density N, (b) carrier mobility μ and (c) resistivity ρ of In_2O_3:Sn films on glass (circles) and polyimide (triangles) as a function of target voltage. Deposition parameters are given under Series II in Table 4.1.

Both N and μ generally increase with DC target voltage for films on glass but the maximum value of mobility is 45 $cm^{-2}V^{-1}s^{-1}$ at 450 V as it is limited by an increased impurity concentration which leads to the highest carrier concentration of 10.1 x 10^{20} cm^{-3} at 500 V. However, for the In_2O_3:Sn films on polyimide, both N and μ initially sharply increased when V_T was raised from 350 V to 400 V then saturated as V_T was further increased to 500 V. For all films, ρ reduced as V_T increased to 500 V to values of 1.8 x 10 $^{-4}$ Ω cm and 2.4 x 10 $^{-4}$ Ω cm on glass and polyimide, respectively.

Figure 4.7 shows the XRD patterns of selected In_2O_3:Sn films on polyimide and glass deposited at different target bias voltages. The broad reflection at angles < 20° result from scattering from the Perspex sample holder caused by the small size of the sample in relation to the beam width. The deposition of a polycrystalline film of In_2O_3:Sn in each case was confirmed by comparison with the JCPDS card for In_2O_3:Sn (89-4597) that was derived from powder diffraction studies on In_2O_3:Sn by Nadaud and co-workers [180]. It is noticeable that the In2O3:Sn crystallinity is enhanced on the polyimide compared to the glass. As the target voltage increased, the relative intensities of the reflections changed particularly in the case of the (222) and (400) reflections.

At the lower voltage, the reflections are notably broader and less well defined indicating a lower crystallinity (crystallite size is inversely related to the reflection width at half maximum height according to the Debye-Scherrer equation). At 350 V on the polyimide substrate, a second phase of SnO is noticeable in the XRD pattern with clear additional reflections at 29° and 47° 2θ degrees.

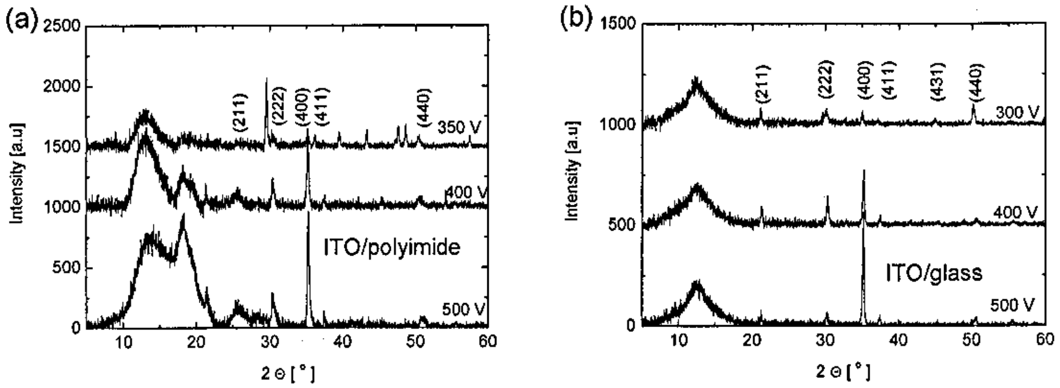

Figure 4.7. X-ray diffraction patterns of In_2O_3:Sn films deposited on (a) polyimide and (b) glass for different DC target voltage. The curves have been shifted by between 500 a.u to 1500 a.u for clarity. Deposition parameters are given under Series II in Table 4.1.

Figure 4.8. shows the transmission spectra of the In_2O_3:Sn films on glass and polyimide for the different target voltages, as well as the uncoated substrates. As the

target voltage increases, the optical band edge moves to lower wavelengths and the near infra-red wavelength transmission reduces for the In_2O_3:Sn films on glass.

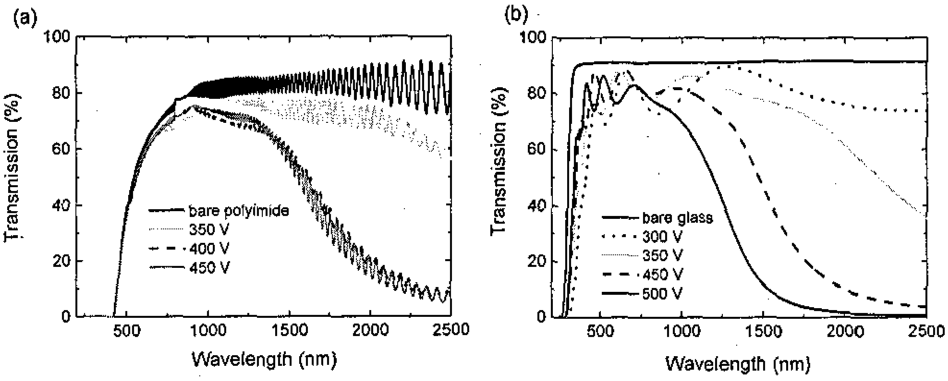

Figure 4.8. Transmission spectra for In_2O_3:Sn films on (a) polyimide and (b) soda lime glass (right) deposited at various target voltages. Deposition parameters are given under Series II in Table 4.1.

Information on the optical band-gap of the In_2O_3:Sn films on polyimide, cannot be deciphered as the substrate itself is only transparent to wavelengths greater than 420 nm. However, the In_2O_3:Sn film transmission in the infra-red region reduces as V_T is increased. Increasing V_T enhanced the momentum of ions arriving at the target sputtering more metal material leading to a higher deposition rate even though the ionisation current was reduced for higher voltage levels to keep the effective target power density of 2.18 W cm^{-2}. The reduction in deposition rate with V_T is in agreement with other authors using a combination of DC and RF excitation for sputtering SnN_x [176] and In_2O_3:Sn [178]. The In_2O_3:Sn film growth coefficient and thus sputtering yield reduce with V_T as observed by Kamei et al [176], despite increasing the RF ionisation power (and thus target current) to maintain the sputtering power level. This confirms that lowering the target voltage results in lower ion energies during sputtering which would minimise film damage during sputtering. Bender et al. [178] however observed that though the ion energy increased when the proportion of RF/ (RF +DC) excitation was increased, both the discharge voltage and deposition rate reduced. Nonetheless, since the argon-oxygen flow rate ratio was kept constant for the present study, less metal was sputtered from the target under lower DC bias which is an indication of a reduction in ion energy.

As a result, films deposited with higher target voltage had a lower oxygen content (and thus higher carrier density) leading to a lower resistivity. Also, the decline of the NIR transmission of the In_2O_3:Sn films and the transmission edge shift to lower energy with increasing V_T, are characteristic of enhanced free carrier absorption. The carrier density of In_2O_3:Sn films on polyimide was generally lower than that on glass possibly due to a higher degree of oxidation. The presence of an SnO phase in the In_2O_3:Sn film deposited on polyimide at $V_T = 350$ V which is not evident on glass even for $V_T = 300$ V, indicates a higher oxygen content for these films. One possibility is that moisture absorbed on the polyimide surface provides additional oxygen to the film during sputtering. At this stage, it is acknowledged that further studies are required to investigate why unlike on glass, the carrier concentration and NIR absorption for the In_2O_3:Sn films on polyimide appear to saturate for target voltages above 400 V.

The high energy of the particles arriving at the substrate under conditions of high V_T may increase the adatom mobility during film growth that promotes larger grains with higher mobility of carriers [181]. The carrier mobility also improved with increasing V_T up to 450 V due to better crystallinity of the films on both glass and polyimide. As the (400) reflection peaks became sharper, the film grain size increased as a result of enhanced adatom mobility while sputtering with higher with target voltage. However for $V_T > 450$V, the mobility was limited by scattering at ionised impurity centres which occurs at elevated carrier concentration and thus the resistivity starts to saturate. In this case, the better crystallinity on glass as compared to polyimide is the cause of the much lower μ on the latter.

Polycrystalline In_2O_3:Sn thin films retain the same bixybyte structure of bulk undoped In_2O_3. material [28, 180, 182]. XRD patterns for polycrystalline In_2O_3:Sn thin films generally show reflection peaks associated with In_2O_3 whilst those for SnO_2 are absent. The XRD patterns for polycrystalline In_2O_3:Sn exhibit strong (222), (400), (440) or (622) reflection peaks. Crystal growth along the <111> and <100> axes is resistant to re-sputtering and thus the corresponding reflection peaks along the (222) and (400) planes, respectively, are more prominent in the XRD patterns compared to the (440) and (622) peaks. The intensity of the peaks depends on the deposition method and on the deposition parameters. Since crystals growing along the <100> axis are more resistant to re-sputtering that those growing along the <111> axis, the former crystal orientation is favoured for films grown using higher energy particle energy [182]. Several authors have reported that thus preferred <100> orientation is prevalent in In_2O_3:Sn films deposited by DC magnetron sputtering which is characterised by higher target voltages than RF magnetron sputtering [29, 174, 183]. On the other hand, In_2O_3:Sn films with a preferred <111> orientation are mainly prepared by RF magnetron sputtering [29, 174]. Qiao et al. [29], attributed the relative increase in the intensity ratio of (222)/ (400) reflections to the increased proportion of reactive species of oxygen during sputtering with RF excitation compared to DC excitation. The <100> orientation is mainly attributed to high adatom mobility during film growth as a result of high particle energy as a result of higher kinetic energy or higher substrate temperature. Larger grain sizes in In_2O_3:Sn films are typical where preferential <100> crystallisation prevails over <111> orientation [184].

The XRD analysis showed that an increased intensity of the (400) reflection peak and thus preferred <100> orientation corresponded to a lower In_2O_3:Sn film resistivity than with a (222) reflection dominance for preferred <111> orientation. Other workers [174, 183, 185] have also observed that the ratio of the (222)/(400) reflection intensity increases with the oxygen content of the In_2O_3:Sn films. Kamei et al. [186] observed that In_2O_3:Sn films grown with yttria stabilised zirconia (YSZ) single <111> crystal orientation had a lower carrier density than those grown on <100> oriented YSZ despite containing similar amounts of Sn. They concluded that the <111> orientation accommodates more interstitial oxygen atoms than <100> which form defect clusters in the films that capture some of the free electrons available from interstitial Sn^{4+}. Interstitial oxygen atoms, result when there are insufficient metal atoms to react with the oxygen supplied when sputtering with low target voltage.

Increasing the target voltage, during HiTUS deposition, from 300 V to 500 V caused a reduction of both the In_2O_3:Sn thin film resistivity and NIR transmission but increased the film deposition rate. However though using a lower DC target voltage with constant sputtering power causes a change in preferred crystal orientation from the <100> to the <111> axis, varying V_T between 500 V to 400 V has minimal effect on In_2O_3:Sn film resistivity on either substrate. In short, where ion damage is to be avoided, moderate target voltage can be used during sputtering at the expense of only the deposition rate as the In_2O_3:Sn film resistivity saturates when the voltage is increased from 400 V to 500 V. Moreover the oxygen flow rate can be adjusted to achieve even lower values of resistivity than those reported here when the target bias is set below 500 V.

4.3 Post deposition heat treatment of In_2O_3:Sn films

This section presents and discusses the effects of various deposition parameters on the thermal stability of In_2O_3:Sn film resistivity and transmission, after heating in vacuum or air at 300 °C for 30 minutes. Selected In_2O_3:Sn samples were heated either in air or in vacuum at a constant substrate temperature of 300 °C for 30 min. Since it took 40 min to raise the substrate temperature from 25 °C to 300 °C in air, compared to 15 min in vacuum, the former ambient condition was considered equivalent to those typical for processing chalcogenide solar cell materials. The thermal stability of the various films was compared by calculating the relative change in film resistivity and transmittance, denoted as ($\Delta\rho/\rho$) and ($\Delta T/T$), respectively.

4.3.1 Influence of substrate temperature

A third set of In_2O_3:Sn films was grown on glass and polyimide substrates to study the influence of substrate temperature on the TCO properties. The details of the deposition parameters are listed under Series III in Table 4.1.

Figure 4.9 shows an SEM image of the surface of an In_2O_3:Sn film grown on polyimide heated 460 °C with the oxygen flow optimised for low resistivity. The film surface was densely packed with a uniform distribution of equally sized grains roughly 60 nm wide.

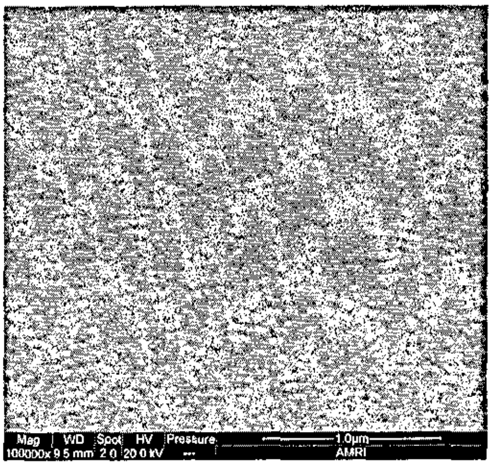

Figure 4.9. SEM image of an In_2O_3:Sn film on polyimide deposited at 460 °C.

The three dimensional AFM images of a selection of In_2O_3:Sn films on soda lime glass corresponding to substrate temperatures of 25 °C, 200 °C and 460 °C are shown in Figure 4.10. Increasing the substrate temperature increased the grain size and surface roughness of the In_2O_3:Sn films.

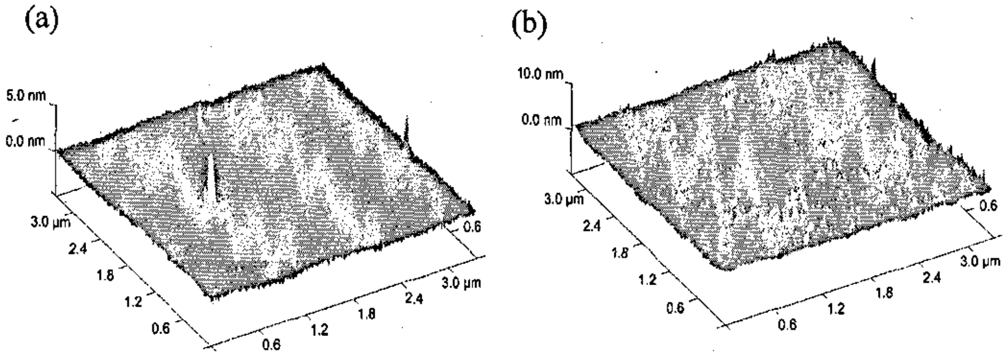

25 °C, 392 nm, 5.8 x 10^{-4} Ω cm, 0.34 nm

200 °C, 392 nm, 5.8 x 10 -4 Ω cm, 0.91 nm

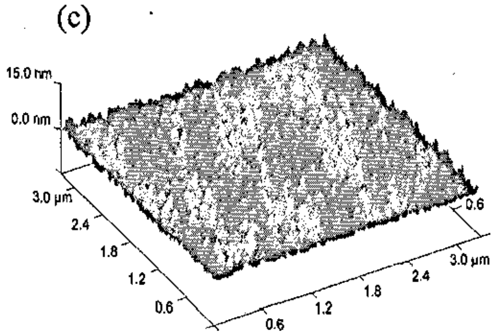

460 °C, 340 nm, 1.8 x 10 -4 Ω cm, 1.22 nm

Figure 4.10. AFM images of films deposited at a) 25°C, b) 200°C and c) 460 °C. Indicated below each image is the respective substrate temperature, film thickness, resistivity and rms roughness. Deposition parameters are given under Series III in Table 4.1.

Figure 4.11 shows a graph of film resistivity as a function of substrate temperature T_s. Though ρ of the films on soda lime glass, was independent of T_s between 25 °C and 200 °C remaining constant at 5.8 x 10^{-4} Ω cm, it dropped to 4.2 x10^{-4} Ω cm when T_s was raised to 250°C, and continued decreasing gradually to 1.8 x 10^{-4} Ω cm at 460°C. The resistivity of the ITO films on polyimide reduced in a fairly linear style from 6.0 x 10^{-4} Ω cm to 2.4 x10^{-4} Ω cm as T_s increased from 25 °C to 460°C, respectively. The only exception was the film deposited at 400°C which had a higher resistivity of 5.3 x 10^{-4} Ω cm.

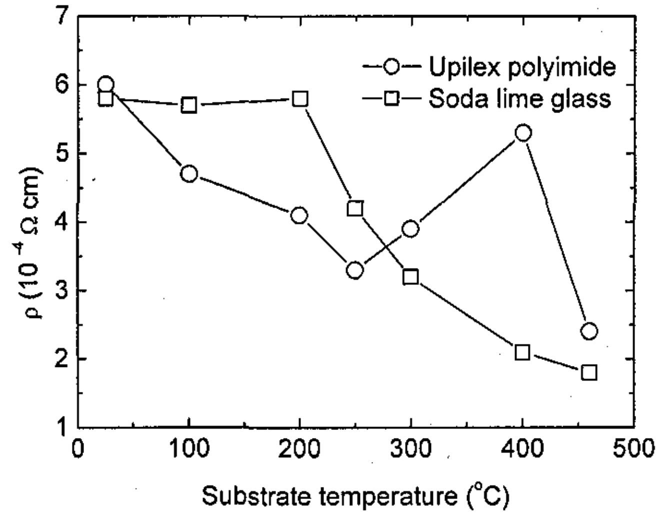

Figure 4.11. Resistivity of In_2O_3:Sn films on soda lime glass (squares) and on polyimide (circles) as a *function of substrate temperature. The lines are to guide the eye. Deposition* parameters are given under Series III in Table 4.1.

Figure 4.12(a) shows the variation of average transmission of In_2O_3:Sn thin films on glass as a function of substrate temperature. The In_2O_3:Sn film transmission generally increased as substrate temperature was raised from 25 °C to 300 °C then reduced for higher substrate temperatures. Figure 4.12 (b) shows a graph of the figure of merit Φ_{VIS} (400 – 800 nm) plotted as a function of substrate temperature. Φ_{VIS} increases with substrate temperature from 25 – 400 °C then increases slightly at 450 °C.

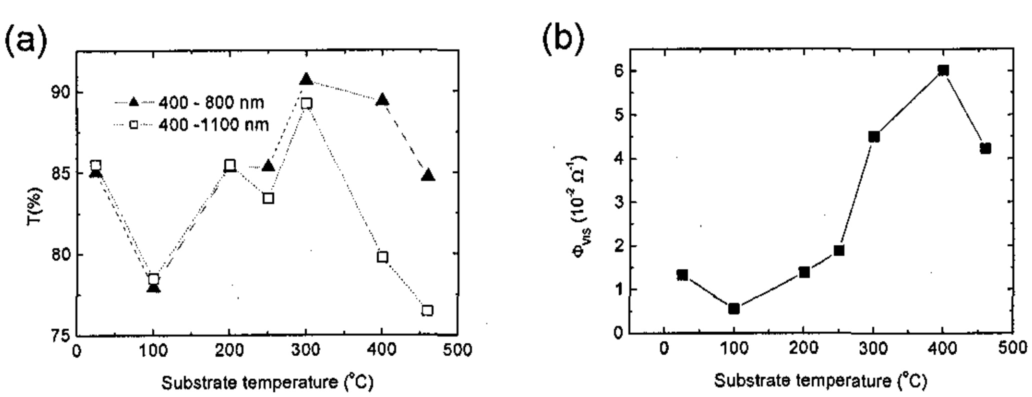

Figure 4.12. Average transmission *T* of In_2O_3:Sn thin films on soda lime glass (a) and figure of merit Φ averaged over 400 -800 nm (b) as a function of substrate temperature. Film thickness ranged from 380 nm to 408 nm. Deposition parameters are given under Series III in Table 4.1. Lines are to guide the eye.

Figure 4.13 shows the relative change in In_2O_3:Sn thin film resistivity (*Δρ/ρ*) after heating in air and vacuum as a function of substrate temperature for soda lime glass and polyimide substrates. Generally, the film resistivity, when heated in vacuum, either remained stable or increased by a factor of up to 15% for all on both soda lime glass and polyimide. Conversely, heating the In_2O_3:Sn films in air increased the resistivity by as much as 200% on glass and 20% on polyimide.

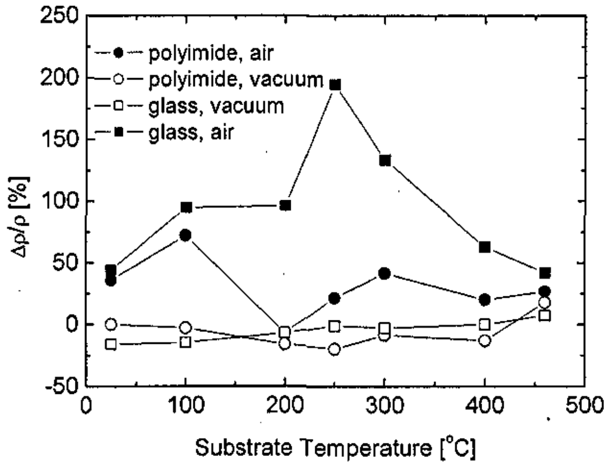

Figure 4.13. Relative change in resistivity *Δρ/ρ* as a function of substrate temperature for In_2O_3:Sn on soda lime glass (squares) and polyimide (circles). The substrate temperature was maintained at 300 °C during heat treatment. Deposition parameters are given under Series III in Table 4.1. Lines are to guide the eye.

A plot of *ΔT/T*, for In_2O_3:Sn thin films on glass after heat treatment in vacuum and air, against substrate temperature during deposition is presented in Figure 4.14. Generally heating in vacuum caused a reduction in transmission whereas heating in air increased the transmission. Increasing the substrate temperature reduces the In_2O_3:Sn film resistivity by increasing both the carrier density and the carrier mobility by the activating the tin dopant [171] and increasing the grain size [122], respectively. High substrate temperatures promote large grains in polycrystalline thin films by providing the activation energy for coalescence of nuclei formed [122]. Larger grain sizes of the In_2O_3:Sn films reduce the probability of recombination and scattering at grain boundaries resulting in higher carrier mobility and thus better resistivity. In_2O_3:Sn films grown with low process temperatures are amorphous [172, 174]. The change in resistivity at T_s =200 °C observed in Figure 4.11, may be explained by a transition between amorphous and polycrystalline In_2O_3:Sn films deposited on glass.

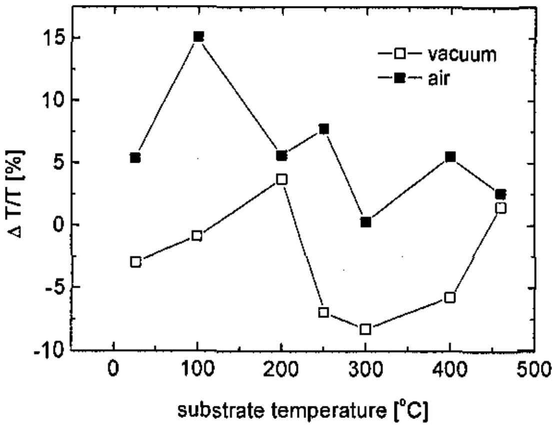

Figure 4.14. Relative change in transmission *ΔT/T* as a function of substrate temperature for soda lime glass. Substrate temperature maintained at 300 °C during heat treatment. Deposition parameters are given under Series III in Table 4.1. The lines are to guide the eye.

A transition from amorphous to polycrystalline structure has been reported to occur at 150°C [13, 172], 165 °C to 230°C [187] and 250°C for post deposition heat treatment of In_2O_3:Sn grown without intentional substrate heating [153]. Investigations of the initial growth modes of In_2O_3:Sn thin films prepared by pulsed laser deposition under varied substrate temperatures showed that the transition from amorphous to polycrystalline films coincides with the transition from 3- dimensional to 2-dimensional island growth, respectively [172]. The reported values of the transition temperature differ because of the different techniques used to record and/or determine the substrate temperature. The relatively lower visible range transmission for lower substrate temperatures between 25 °C to 250 °C could be a result of the presence of sub-oxides of In and Sn as well as free metal clusters [42]. On the other hand, high substrate temperature above 300°C could result in higher carrier density causing a reduction in NIR transmission.

The minimal effects on the In_2O_3:Sn thin film resistivity and transmission after heating in vacuum suggest negligible change in the film structure. Conversely, the greater changes in properties after heating in air indicate that the films were further oxidized by this treatment. The resistivity of films deposited with $T_s > 200$ °C on Upilex, was the most stable to heating in air possibly because additional oxygen from the substrate surface increased the oxygen content of these films compared to those on soda lime glass. The lowest resistivity value of In_2O_3:Sn on Upilex after heating in air was 3.3×10^{-4} Ω cm for 460 °C. The films deposited on soda lime glass must have been more metallic on the whole and thus could further be oxidised by heating in air. The lowest resistivity after heating in air on soda lime glass was 2.6 x 10 $^{-4}$ Ω which also occurred at 460 °C. Therefore, high substrate temperatures during deposition ensure high thermal stability to heating in air as also observed by Khrypunov et al. [181]. Heat treatment in air generally caused larger changes in transmission than in vacuum. Overall, thermal stability of transmission was worse for the In_2O_3:Sn films with a high metallic content as they underwent further oxidation in air thus losing some conduction electrons. This is validated by the accompanying increase in resistance for most films.

4.3.2 Influence of oxygen flow rate and sputter pressure

An additional set of In_2O_3:Sn thin films was prepared on soda lime glass and polyimide substrates to study the influence of the oxygen flow rate and the sputter pressure on the In_2O_3:Sn film properties. The deposition parameters used for this study are listed under Series IV in Table 4.1.

Figure 4.15 shows the In_2O_3:Sn film resistivity ρ plotted as a function of oxygen flow rate for three different total process pressure levels 0.15 Pa, 0.3 Pa and 0.45 Pa on (a) soda lime glass and (b) polyimide.

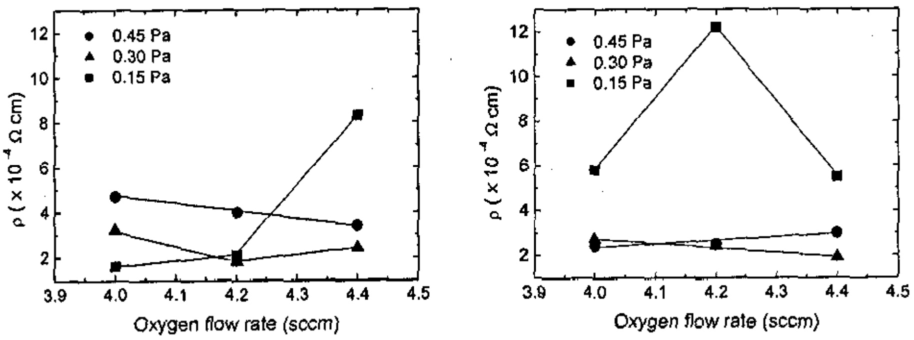

a) Soda lime glass

b) Upilex

Figure 4.15. Resistivity of In_2O_3:Sn films on a) soda lime glass and b) polyimide as a function of oxygen flow rate with varying process pressure. Deposition parameters are given under Series IV in Table 4.1. Lines are to guide the eye.

The influence of oxygen flow on ρ was pronounced at the lowest total pressure p_{tot} of 0.15 Pa. Considering films deposited on soda lime glass with p_{tot} = 0.15 Pa, resistivity increased with oxygen flow rate was increased from 4 sccm to 4.4 sccm but for the highest process pressure of 0.45 Pa, the resistivity instead slightly reduced over the same oxygen flow range. The resistivity of the In_2O_3:Sn films on polyimide was heavily dependent on process pressure. For the lowest pressure of 0.15 Pa, the In_2O_3:Sn film resistivity was at least three times greater than that for 0.3 Pa and 0.45 Pa over the considered range of oxygen flow rates. All the polyimide foils were curled with the In_2O_3:Sn coated side pushed outwards indicating compressive stress and this effect was strongest for the lowest process pressure of 0.15 Pa. These films grown at 0.15 Pa.also had wrinkles that were visible to the naked eye which could explain their much higher resistivity. A possible reason for this observation is that under extremely low pressure, the sputtered particles arrive at the substrate with such high energy that a very compact film is formed. The mismatch of the coefficient of thermal expansion between the film and substrate may have been enhanced at 0.15 Pa causing additional stress to the film. These effects were not immediately obvious for soda lime glass.

The average film transmission between 400 nm to 1100 nm was heavily dependent on oxygen flow rate. Figure 4.16 (a) shows the typical variation of the transmission spectra with oxygen flow rate for In_2O_3:Sn films deposited on soda lime glass with p_{tot} = 0.30 Pa.

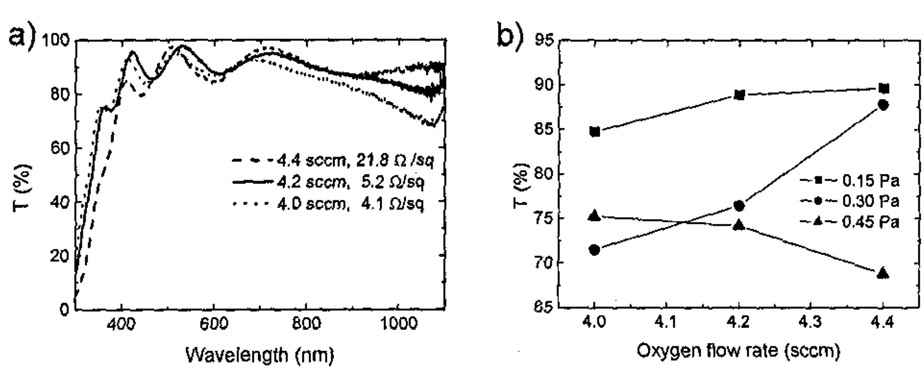

Figure 4.16. (a) Transmission spectra of In_2O_3:Sn on soda lime glass for various oxygen flow rates with a deposition pressure of 0.15 Pa . The legend also indicates the sheet resistance of the films. (b) Average transmission (400 nm to 1100 nm) of In_2O_3:Sn thin films on soda lime glass as a function of oxygen flow rates and sputter pressure. Deposition parameters are given under Series IV in Table 4.1. Lines in (b) are to guide the eye.

The onset of transmission moved to lower wavelengths as oxygen flow rate decreased from 4.4 sccm to 4.0 sccm. The transmission of visible light was independent of the oxygen flow rate and was over 80% for all films. However, in the NIR region, the film transmission increases as with the oxygen flow rate used during the In_2O_3:Sn thin film deposition. Figure 4.16 (b) shows the average transmission (400 nm – 1100 nm) as a function of oxygen flow rate for In_2O_3:Sn thin films for three different process pressures of 0.15 Pa, 0.3 Pa and 0.45 Pa on soda lime glass. In general, the films deposited at lower process pressure had the highest VIS-NIR transmission.

The effect of oxygen flow and sputtering pressure on the thermal stability of film resistivity when subjected to heat treatment in either air or vacuum was also investigated. Figure 4.17 shows the variation of $\Delta\rho/\rho$ after heating in either air or vacuum as a function of oxygen flow rate and sputtering pressure for In_2O_3:Sn films on (a) soda lime glass and (b) Upilex polyimide. Considering the In_2O_3:Sn films on glass, the oxygen flow rate had a minimal effect on the resistivity after heating in vacuum though at the higher pressure level of 0.45 Pa, $\Delta\rho/\rho$ increased slightly with the highest oxygen flow.

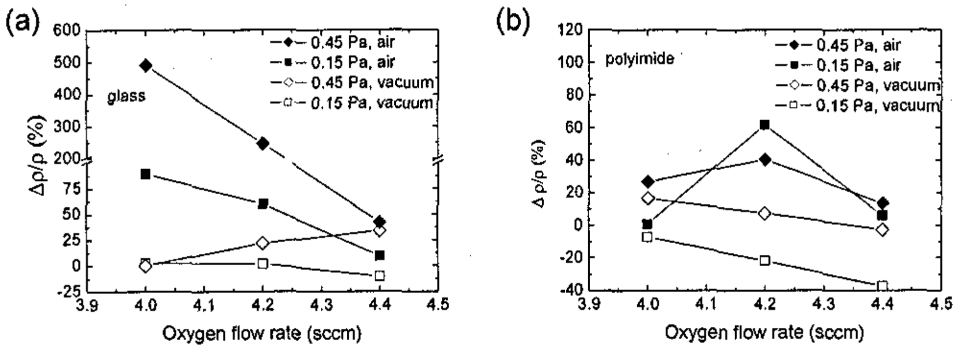

Figure 4.17. Relative change in resistivity $\Delta\rho/\rho$ against oxygen flow rate for total pressure of 0.15 Pa and 0.45 Pa on a) soda lime glass and b) Upilex polyimide. Substrate temperature maintained at 300 °C during heat treatment. Deposition parameters are given under Series IV in Table 4.1. Lines are to guide the eye.

Low oxygen flow rates during deposition caused the greatest increase in resistivity of In_2O_3:Sn on glass after heat treatment in air for both pressure levels. This effect was enhanced by higher sputter pressure where $\Delta\rho/\rho$ was as high as 500 % for p_{tot} = 0.45 Pa. After heat treatment in vacuum, ρ for the In_2O_3:Sn thin films on glass prepared at 0.15 Pa remained within 10% of the as deposited value whereas that of the films prepared at 0.45 Pa varied in the range from 0 – 40%. In contrast, the resistivity of films deposited on Upilex polyimide was less adversely affected by heat treatment in air and generally $\Delta\rho/\rho$ showed an increase of about 10%. On heat treatment in vacuum, the resistivity of the In_2O_3:Sn thin films on the polyimide reduced at 0.15 Pa but increased for 0.45 Pa under the same treatment.

The evolution of thermal stability of transmission of In_2O_3:Sn thin films, on soda lime glass, after heat treatment in air and vacuum with oxygen flow rate and process pressure is illustrated in Figure 4.18. Heat treatment regardless of the medium resulted in an increase in the In_2O_3:Sn film transmission. At a process pressure of 0.15 Pa, $\Delta T/T$ after heating in vacuum, is within ± 5% of the original value for F_O ranging from 4.0 sccm to 4.4 sccm. On the other hand, for a process pressure of 0.45 Pa, $\Delta T/T$ after heating in vacuum ranges from 2.5% to 15% for the investigated oxygen flow rates.

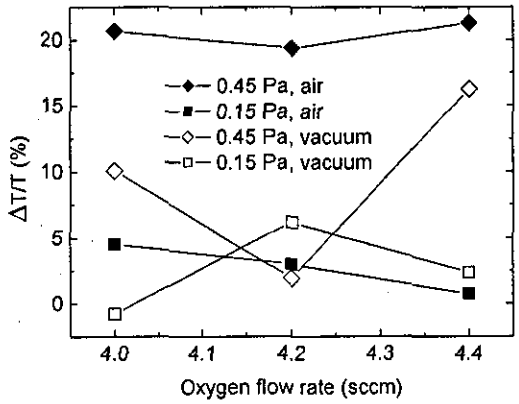

Figure 4.18. Relative change in transmission $\Delta T/T$ of In_2O_3:Sn films on soda lime glass after heat treatment in air or vacuum as a function of oxygen flow rate. Substrate temperature was maintained at 300 °C during heat treatment. Deposition parameters are given under Series IV in Table 4.1. Lines are to guide the eye.

The thermal stability of the In_2O_3:Sn film transmission in air heavily depends on sputtering pressure and increased by up to 5% for the films prepared at 0.15 Pa compared to above 20% for films prepared at 0.45 Pa. Increasing the oxygen flow rate (equivalent to the oxygen partial pressure) and thus the oxygen content of the films, results in a simultaneous increase in In_2O_3:Sn film resistivity and NIR transmission as a result of a reduced carrier density [42, 170]. Reducing the oxygen flow rate while keeping the sputter pressure constant results in less oxygen being available to react with the sputtered metal. Similarly, increasing the sputter pressure while keeping the oxygen flow rate constant results increases the rate at which the metal target is sputtered leading to more oxygen deficient films. When there is insufficient oxygen available to oxidize the sputtered metal, the In_2O_3:Sn thin film coating the substrate is oxygen deficient as a result of partial oxidation. Larger amounts of oxygen in the sputtering ambient fully oxidise the sputtered metal and thus In_2O_3:Sn coating and any excess oxygen reacts with the target surface.

Films prepared with relatively high oxygen flow rates are slightly In deficient and thus have a lower carrier density which increases the resistivity and optical transparency of the In_2O_3:Sn thin films. As the oxygen content in the In_2O_3:Sn films reduces, the optical transmission edge shifts to lower wavelengths as a result of the BM shift due to increased carrier density and the corresponding shift to higher energy levels of the Fermi level in heavily doped (degenerate) n-type semiconductors. Also, the transmission for wavelengths above 800 nm decreases with oxygen content of In_2O_3:Sn thin films owing to increased absorption by free charge carriers. The oxygen deficiency in In_2O_3:Sn thin films can be reversed by heat treatment in air which further oxidises the In_2O_3:Sn and thus increases both the resistivity and NIR transmission. Heat treatment in air can also increase the oxygen content of the In_2O_3:Sn thin films, if the film structure is porous e.g. as a result of re-sputtering during deposition at relatively high sputtering pressure. In such cases, the oxygen in the air can diffuse through the voids between the crystal grains and cause further oxidation at deeper levels of the film. Heat treatment in vacuum can also increase In_2O_3:Sn thin film transmission by improving the crystalline structure of the films.

4.4 Discussion

The relatively higher resistivity observed for the In_2O_3:Sn films on polyimide compared to that on soda lime glass with identical deposition conditions could have several causes:

I. The actual substrate temperature could have been less than that of glass as the polyimide sheets were not completely flat and thus uniform heating was not possible.

II. The difference in structure and /or orientation of the In_2O_3:Sn crystallites on polyimide was different from that on glass.

III. As it took considerably longer to achieve sufficiently low base pressure with polyimide substrates than with glass, it is possible that the presence of oxygen absorbed on the polyimide substrate contributed to the higher film resistivity.

Normally, a relatively higher In_2O_3:Sn resistivity is observed for amorphous polymer substrates compared to glass [122]. It is however possible to achieve a lower resistivity on polymers than on glass if the polymer is semi-crystalline e.g. PET [185].

The deposition parameters that favoured low resistivity ($\leq 2.0 \times 10^{-4}$ Ω cm) In_2O_3:Sn films prepared on glass and Upilex using HiTUS were high substrate temperature, moderate oxygen flow rate (4.0 sccm to 4.4 sccm) and film thickness exceeding 350 nm. Additionally, In_2O_3:Sn film deposition on Upilex required a process pressure of at least 0.3 Pa to obtain film low film resistivity. On the other hand, high transparency for the In_2O_3:Sn films on soda lime glass was promoted by high oxygen flow rate, high substrate temperature and low sputtering pressure during the deposition process.

4.5 Conclusion and outlook

HiTUS deposition is similar to magnetron sputtering with two exceptions. Firstly, separate control of the flux and energy of the argon ions used for sputtering is possible. Secondly, the absence of race track on the target surface as a result of a more uniform erosion of the target surface. These advantages make this method of sputtering attractive for large scale processing of In_2O_3:Sn films on delicate substrates while minimising material inventory costs.

In_2O_3:Sn films have been prepared on soda lime glass and Upilex polyimide foils using HiTUS deposition. The influence of deposition parameters such as sputter power density, target voltage, substrate temperature, oxygen flow rate (partial pressure), sputtering pressure and film thickness on the properties of tin doped indium oxide was also investigated. The target voltage can be varied to adjust the kinetic energy of the sputtered particles to reduce damaging the growing film without adversely increasing the In_2O_3:Sn film resistivity. A combination of high substrate temperature, medium oxygen flow rate and moderate pressure allowed the deposition of thermally stable In_2O_3:Sn films with high conductivity and transparency on both substrate materials. The results demonstrated that In_2O_3:Sn films deposited by HiTUS can be produced with good resistivity and transmission comparable to those prepared by the more conventional magnetron sputtering. The lowest resistivity for In_2O_3:Sn films prepared on soda lime glass was 1.6 x 10^{-4} Ω cm with a transmission of 85 % in the visible and near infra red regions. The lowest resistivity on Upilex polyimide was 1.9 x 10^{-4} Ω cm with optical transmission (including the substrate) exceeding 65% from 400 nm to 1500 nm. Thus fulfilling the requirements for device quality films suitable for use as substrates for compound semiconductor- and titanium oxide based dye-sensitized solar cells. The fact that the In_2O_3:Sn films were deposited in a very basic system without either substrate motion or active reactive process control, means that there is still much scope to improve their quality.

Chapter 5 High deposition rate ZnO:Al films with efficient light trapping for silicon thin film solar cells[16]

5.1 Introduction

Zinc oxide is gaining importance as a transparent contact for thin film silicon solar cells [16, 102, 103, 120, 124, 188-190]. Compared to fluorine doped tin oxide (SnO_2:F), which is commonly used in commercial production, zinc oxide is resistant to hydrogen rich plasmas used for chemical vapour deposition of thin film silicon layers [191]. Aluminium doped zinc oxide (ZnO:Al) also has better transparency and conductivity than commercial SnO_2:F coated glass substrates [16].

Micro-crystalline silicon μc-Si:H is a form of thin film silicon which is well passivated by hydrogen and thus does not undergo light induced degradation typical of amorphous silicon. Since the deposition rate of micro-crystalline silicon μc-Si:H is rather low ~ 5Å/s, it is desirable to restrict the film thickness to values below 1.5μm to reduce the deposition time [59]. However, in thin μc-Si:H layers, photons corresponding to wavelengths exceeding 800 nm are weakly absorbed because of the low absorption coefficient reducing the photo-generated current. Therefore an additional function of the front contacts in superstrate μc-Si:H solar cells, is the possibility to improve the performance, primarily through increased current density, by efficient light trapping. This requires the front contact to have a suitably rough surface to scatter the light under high angles into the thin silicon layer. By repeated total internal reflection within the silicon, the effective light path is strongly enhanced, leading to significant absorption of long wavelength light, though the corresponding absorption coefficient of silicon is quite low. The zinc oxide layer can be either directly grown with a rough surface by appropriately choosing deposition conditions [102, 103] or roughened after sputter deposition through wet chemical etching [188]. The latter technique is used in this study for films deposited by reactive medium frequency (MF) magnetron sputtering.

State of the art quality ZnO:Al films with low resistivity $\leq 3 \times 10^{-4}\ \Omega$ cm, high transparency > 80% and a surface morphology suitable for light trapping can be

---

[16] The results described in this chapter have been published in Paper IV in the List of Publications.

prepared using RF magnetron sputtering from ceramic targets. However, for industrial scale production of ZnO:Al, reactive magnetron sputtering from metallic Zn:Al targets is more attractive than RF sputtering owing to the higher deposition rate, cheaper target material and easier scalability to larger areas [116]. MF reactive sputtering has been proven to produce high quality ZnO:Al films at high deposition rates. Though the application of such ZnO:Al films as front contacts silicon thin film solar cells lead to high efficiency [120, 124], more work needs to be done to improve the quality of the surface morphology after etching to enhance the current density. This work therefore focused on improving the properties of MF sputtered ZnO:Al films with the goal that their performance in solar cells at least matches the current state of the art ZnO:Al films obtained by RF sputtering from ceramic targets [190].

5.2 Experimental details

The sputter system used to prepare the ZnO:Al films has been described in section 3.2.4. For this study, a fixed amount of oxygen was channelled via the argon manifolds around the peripheral edges of the cathodes to improve the uniformity of the oxygen distribution over the cathode system. In this case, the process was controlled by varying only the quantity of additional oxygen from the central inlet required to maintain a stable PEM® working point. Figure 5.1 shows a schematic of the modified oxygen inlet distribution from the point of view of the substrate side to be coated.

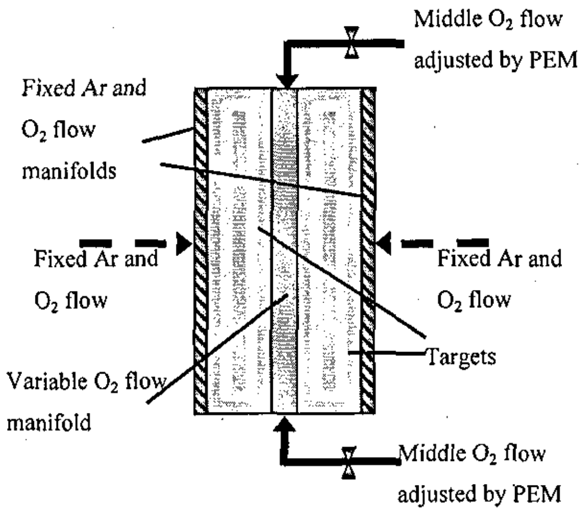

Figure 5.1. Schematic illustration of the modified oxygen inlet distribution with respect to the dual cathode system as "seen" by the substrate.

Several sets of films were deposited using different proportions of oxygen flowing through the two gas inlet configurations. The details of the deposition conditions of the films are summarised in Table 5.1.

Table 5.1: Summary of deposition parameters, discharge power *P*, total process pressure p_{tot}, substrate temperature T_S, plasma emission (PE) intensity, oxygen flow rate F_O from the outer sides and the as-deposited film thickness.

Film	P (kW)	p_{tot} (Pa)	T_s (°C)	F_O (sccm)	PE (%)	Thickness (nm)
A1	10	1.8	330	0	35	variable
A2	10	1.8	330	200	35	variable
B1	4	0.11	310	60	30	727
B2	4	0.11	310	60	32.5	806
B3	4	0.11	310	60	35	795
B4	4	0.11	310	70	35	799
B5	4	0.11	310	80	35	813
C1	10	0.5	310	100	25	1017
C2	10	0.5	310	100	27.5	959
C3	10	0.5	310	100	30	760
C4	10	0.5	310	150	30	910
C5	10	0.5	310	200	30	873
C6	10	0.5	310	250	30	963
C7	10	0.5	310	270	32.5	891

The middle oxygen flow was varied in the range of 34 - 42 sccm and 70 - 121 sccm for 4 kW and 10 kW, respectively. Multipass carrier velocity was 3.3 mm/s and 8 mm/s for 4 kW and 10 kW, respectively, for dynamically deposited films.

Relatively low process pressures were chosen as it has been established that such ZnO:Al films exhibit high electron mobility and thus low resistivity and higher transparency which are more suitable for solar cells [192]. Additionally, low deposition pressure leads to higher stability of ZnO:Al films under damp-heat conditions [193]. This damp heat test is a standard test to evaluate the long term performance stability of solar modules under accelerated conditions. Film growth by sputtering with static deposition, where both the target and substrate are stationary, is not suitable for large substrates as even on small area substrates, the films are non uniform. The film uniformity can be partially improved by sliding the substrate in front of fixed line targets during the deposition. The deposition system used for the ZnO:Al films is designed for inline dynamic depositions whereby the substrate can oscillate linearly in front of the cathode system so that the final film is made up of stacks of several layers. Such an arrangement is useful for large area depositions so that target dimensions, parallel to plane of motion during sputtering, can be smaller than the substrate, thus saving material costs. The thickness d, of the film, for a fixed sputter duration can then be varied by either adjusting the carrier speed v_C, or the number of oscillations N_O, or both. The rate of film growth can be expressed by a dynamic deposition rate R_{dyn}, as

$$R_{dyn} = \frac{dv_C}{N_O} \tag{5.1}$$

5.3 Results and discussion

5.3.1 Statically deposited films

Two films deposited in stationary mode under identical conditions except for the oxygen inlet configuration, were compared (see Table 5.1). Film A1 was deposited with oxygen let in from the middle only and for A2, additional oxygen was added from the side gas inlets. The sheet resistance ρ_S, of the films was measured using either the four-point or two-point method depending on the size of the film area. The thickness and resistivity profiles of both films are shown in Figure 5.2.

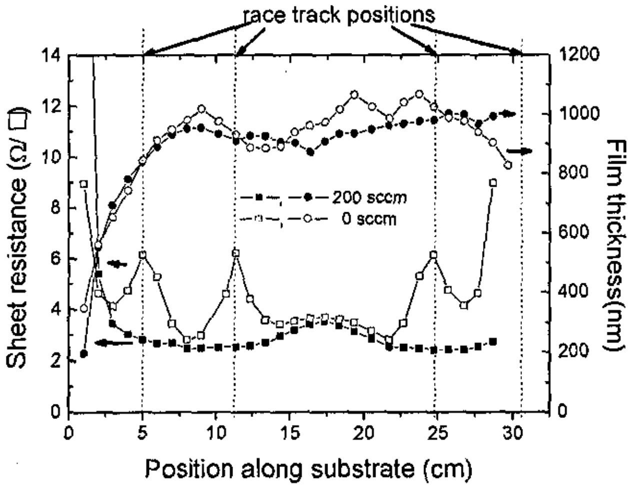

Figure 5.2. Sheet resistance (squares) and thickness (circles) of statically deposited ZnO:Al films as a function of position along the substrate. Film A1 with oxygen flow from the middle only is represented by unfilled shapes and film A2 with oxygen from both the middle and the sides of the targets by solid shapes. Lines are to guide the eye.

The thickness profile of film A2 was more uniform but slightly lower as compared to film A1. Sheet resistance was about 3 Ω/□ for both films but peaked to about 6 Ω/□ for film A1 at the positions on the substrate facing the racetracks of the targets. These distinct regions of high sheet resistance were significantly diminished in film A2 giving a lower and more uniform sheet resistance profile. The resistivity of films A2 and A1 deviated from the mean value by ±10.6% and ±23.9%, respectively, along the horizontal length of the substrate. The observed spatial distribution of ZnO:Al resistivity with high values peaking at the points corresponding to the target erosion tracks is in agreement with previous studies [194-196]. This effect has been attributed to inhomogeneous distribution of oxygen at the substrate surface [195] or to the increased bombardment of the ZnO:Al films by energetic oxygen atoms of the substrate at the target erosion sites [194, 196].

5.3.2 Electrical properties of dynamically deposited films

Figure 5.3 illustrates the dependence of the resistivity on the oxygen distribution for dynamically deposited films. Considering films B3 to B5, (see Table 5.1 for deposition details), an increase in the oxygen flow F_O through the outer inlet, from 60 to 80 sccm caused the resistivity to slightly rise from 3.5 x 10^{-4} Ω cm to 4.0 x 10^{-4} Ω cm.

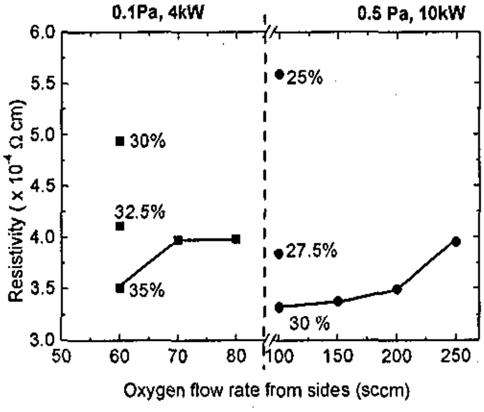

Figure 5.3. Resistivity as a function of oxygen flow rate from the sides. Squares and circles represent film types B and C, respectively. The percentage values represent the working point corresponding to a fixed plasma emission (PE) intensity. The lines are to guide the eye. Refer to Table 5.1 for details.

To check, if this effect is caused by a possibly different working point, though the plasma emission (PE) intensity was kept constant, films B1 to B3 (see Table 5.1) were prepared at different working points with F_O fixed at 60 sccm. The intentional shift of working point by a slight reduction of PE intensity from 35 % over 32.5% to 30% causes a larger rise in ρ from $3.5 \times 10^{-4}\ \Omega$ cm over $4.1 \times 10^{-4}\ \Omega$ cm to $5.0 \times 10^{-4}\ \Omega$ cm. Similar results were obtained for films C1 to C7 and are also included in Figure 5.3. All the ZnO:Al films were n-type and the changes in film resistivity were caused by variations in the both the hall mobility and density of the majority carriers. The slight rise in resistivity with increase of F_O is mainly caused by a slight decrease in majority carrier density of the films as can be seen in Figure 5.4. For instance, for films B3 to B5, the carrier density stays nearly constant around 4.9×10^{20} cm^{-3} when F_O was increased from 60 to 80 sccm. Considering films C3 to C6, the carrier density decreased slightly from 4.9×10^{20} cm^{-3} to 4.5×10^{20} cm^{-3} as the side oxygen flow rate increased from 100 to 250 sccm. On the whole, slight reductions in PE intensity resulted in large reductions of majority carrier density.

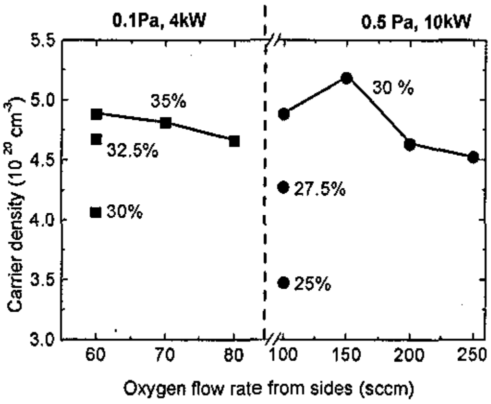

Figure 5.4. Majority carrier density as a function of oxygen flow rate parallel to the substrate surface. Squares and circles represent film types B and C, respectively. The percentage values represent the working point corresponding to a fixed plasma emission (PE) intensity. See Table 1 for details. Note: the lines are to guide the eye.

Figure 5.5 shows the variation of the carrier mobility as a function of F_O. The majority carrier mobility of films B3 to B5 reduces slightly from 38 to 35 cm^{2}V^{-1}s^{-1} as F_O is increased from 60 sccm to 80 sccm though it remains higher than if the PE intensity had been reduced. Similarly considering films C3 to C6, the mobility generally slightly reduces from 37 to 36 $cm^2V^{-1}s^{-1}$ for F_O between 100 and 250 sccm though there is an abrupt increase to 39 cm^2 $V^{-1}s^{-1}$ at $F_O = 200$ sccm. It should be noted that the variations of N and μ are still within the error limits of the Hall measurement (about 10%) making qualitative inference very difficult. All the same, the tendency of resistivity to increase with increasing F_O indicates a reduction of both N and μ.

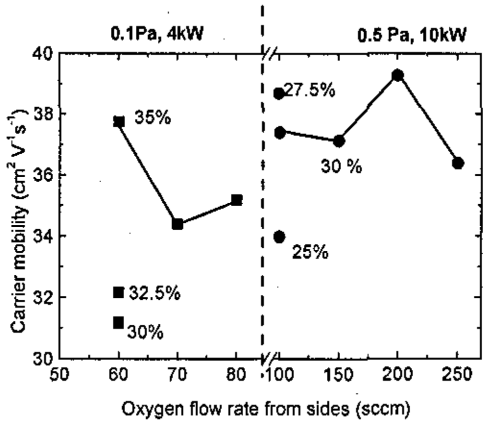

Figure 5.5. Majority carrier mobility as a function of oxygen flow rate from the sides. Squares and circles represent film types B and C, respectively. The percentage values represent the working point corresponding to a fixed plasma emission (PE) intensity. See Table 1 for details. The lines are to guide the eye.

In summary, the mobility and majority carrier density of the ZnO:Al films are only slightly affected by increasing the oxygen flow F_O, but tend to decrease, which results in slight increases in film resistivity. The comparison with the shift of the PE intensity indicates that the working point is at most, slightly affected by the different oxygen distribution at constant PE intensity.

5.3.3 Textured ZnO:Al thin films

All films deposited were smooth and had to be etched using 0.5% diluted hydrochloric acid to obtain a suitably rough surface for light scattering. Initially, all films in series B and C were etched for 30 seconds to compare the resulting surface texture. In general, the etch rate of the ZnO:Al films increased with F_O at constant PEM intensity from 2.5 nm/s to 3.5 nm/s and from 3 nm/s to 7.8 nm/s for films B3 to B5 and

C3 to C6, respectively. In both cases, the increase in etch rate with F_O is much less than if the working point is slightly shifted closer to the oxide mode. The moderate etch rates obtained demonstrate the relative ease of adjusting the etched film behaviour by varying the oxygen flow from the sides.

Scanning Electron Microscopy (SEM) was used to study the morphology of the etched films. Figure 5.6 (a) and (b) show SEM images of the surface of a state of the art RF sputtered ZnO:Al film after etching for 5s and 40s (optimised), respectively. The surface of the optimised film is well distributed with wide bottomed craters of diameters around 1μm. A previous study has indeed demonstrated that these features are well suited to good light trapping ability in solar cells [190]. Therefore, this type of film was subsequently used as a reference for this work.

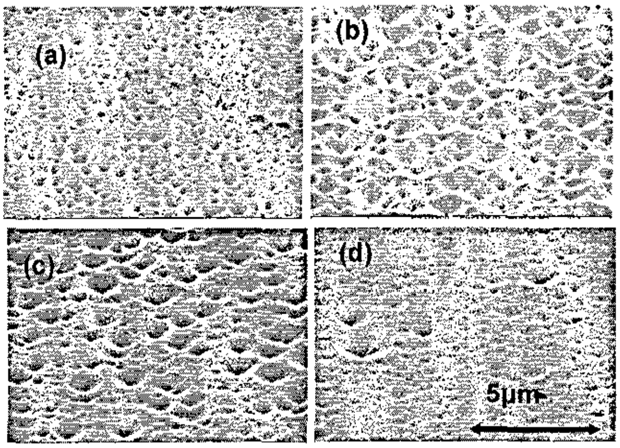

Figure 5.6. SEM images of ZnO:Al films after etching in 0.5% HCl. Images (a) and (b) show a reference RF sputtered ZnO:Al film etched 5 s and 40 s, respectively. Images (c) and (d) show MF sputtered ZnO:Al films B4 and B5, respectively both etched for 30 s. (See Table 5.1 for deposition details).

All films, when etched for a relatively short time duration of thirty seconds, under-went discernable surface texturing. Figure 5.6 (c) and (d) show the textured surface of MF sputtered ZnO:Al films B4 and B5 after etching. It can be seen that for film B4, with F_O = 70 sccm, the film surface has a fair coverage of deep craters with diameters close to 1μm, but when F_O is increased to 80 sccm for B5, craters of this size are considerably less in number. The oxygen distribution thus serves as tool to control the density of points of etch attack. Similar behaviour was observed for series C which confirms that F_O has an influence on the type of surface structure, after etching, of the ZnO:Al films. Figure 5.6 (a) and (b) also demonstrate that once a ZnO:Al film shows a tendency to develop craters of the right shape, their size and thus light scattering ability may be further adjusted within certain limits, by varying the etch duration. Film B2 (PE intensity = 32.5%, F_O = 60sccm) was etched for 30s, 50s and 70s and the corresponding SEM images of the surface morphology are shown in Figure 5.7, where it can be seen that the size and number of large craters increased with etching duration. Comparing the images in Figure 5.6 (b) and Figure 5.7 (c), it can be seen that they are remarkably similar in appearance, indicating that film B2 is suitable for light trapping in solar cells.

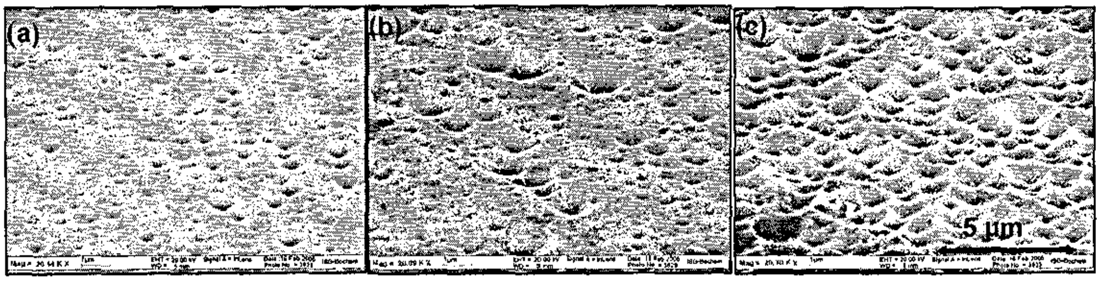

Figure 5.7. SEM images of ZnO:Al film type B2 after various etching durations in 0.5% HCl: (a) 30 s, (b) 50 s and (c) 70 s.

Another preliminary indication of the light trapping ability of an etched TCO film, is its haze ratio. The haze ratio defined as the diffuse transmission at a specific wavelength divided by the total transmission at the same wavelength can give an indication of the light scattering ability of a rough TCO surface. For conciseness, we consider the haze ratio at an intermediate wavelength (700 nm) to give us a general idea of the light scattering effect. Considering ZnO:Al film type B2, the haze was 20% after 30s etching and increased to a stable value of about 40% as the etching duration was increased to 50s and 70s. From earlier experiments, the haze ratio at 700 nm, H_{700}, of an etched ZnO:Al film increases as the working point is increased away from the oxide mode to a maximum then drops again as the metallic mode is approached [120]. Similar results were also found for series B and C in our experiments as shown in Figure 5.8, which illustrates a graph of H_{700} for selected films in series B and C after a 30s etch duration, as a function of the oxygen flow rate from the sides. H_{700} increased with F_O for series B and C up till 31 % and 27 %, respectively. These values are much higher, than the haze ratios obtained in the simple working point series.

The transmittance of the as-deposited films increases with PE intensity [7, 8] and reduces with the side oxygen flow, at constant PE intensity (not shown). The total transmission *T(λ)* and reflection *R(λ)* were measured, using di-iodomethane (CH_2I_2) as an index matching fluid to eliminate errors by light trapping within the ZnO:Al film.

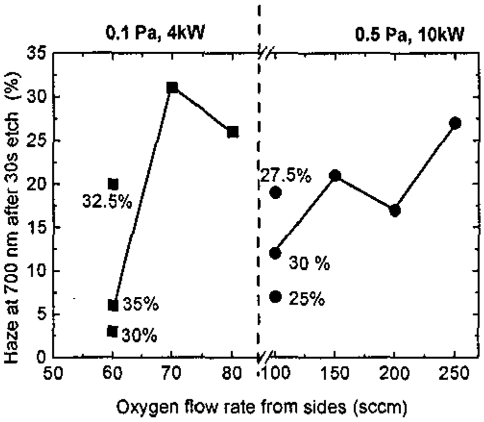

Figure 5.8. Haze ratio at 700 nm as a function of oxygen flow from the sides. Squares and circles represent film types B and C, respectively. All films were etched for 30 s in 0.5% hydrochloric acid. The percentage values represent the working point corresponding to a fixed plasma emission (PE) intensity. See Table 5.1 for deposition details. The lines are to guide the eyes.

The total transmittance and absorbance spectra of the etched films are shown in Figure 5.9. The discontinuities around 850 to 950 nm, in both types of spectra, are artefacts caused by the detector switch. The use of CH_2I_2 as an index matching fluid fixed the absorption edge at about 400 nm independently of the band gap energy of the respective ZnO:Al film. The optical reflectance is nearly the same (about 10 %) for all films over the wavelength range of 300-1300 nm considered and therefore has not been shown. However, over the visible wavelength, transmittance is close to 90% for all the films and only slightly reduces with decreasing F_O. As the wavelength approaches the NIR region, the reduction in *T(λ)* with decreasing F_O becomes more marked due to increasing absorption which raises to about 20% at 1100 nm for the lowest value of F_O considered for both film types. Free carrier absorption is the mostly likely cause of this optical behaviour since the increase in absorption shown in Figure 5.9 coincides with an increase in carrier density (see Figure 5.4).

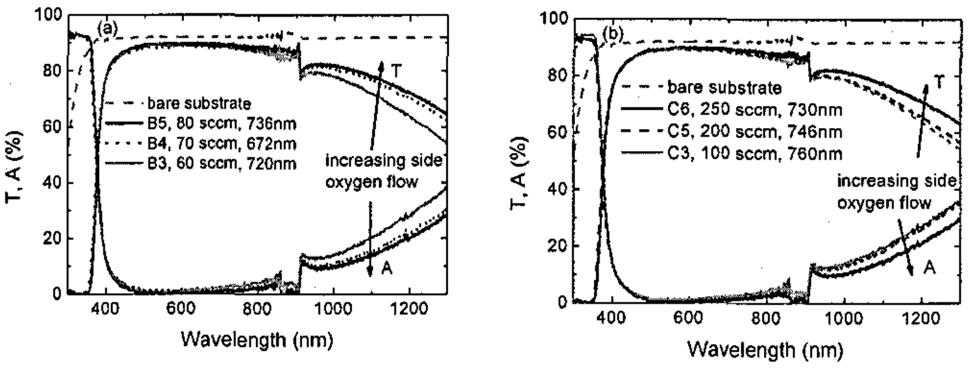

Figure 5.9. Total transmittance and total absorbance of etched films prepared with varying oxygen flow rates from the sides. All films were etched for 30s in 0.5% hydrochloric acid. The spectra for a bare substrate are included for comparison and the ZnO:Al film thickness in nm has also been included.

5.4 Solar cells

After further optimisation, selected ZnO:Al films were applied as front contacts in μc-Si:H solar cells of 1 cm² area. Details of the solar cell preparation are described in Chapter 3. An optimised RF-sputtered ZnO:Al film was included in each of the solar cell depositions for both group B and C MF sputtered films, as a reference. In all cases, the solar cells using the MF deposited ZnO:Al front contacts achieved higher values of J_{sc} (up to 24.3 mA/cm²) than the RF optimised ZnO:Al (23.2 mA/cm²). The most efficient cell based on MF-sputtered ZnO:Al had an efficiency of 8.4% which is similar to that of the cells on the RF sputtered ZnO:Al. The current gain however, could not enhance the efficiency due to the higher resistivity of the MF films which lead to lower fill factors of the cells. However, most of the other cells achieved efficiencies of at least 90% relative to the respective reference cell. Note, that the MF ZnO:Al films were deposited at dynamic deposition rates as high as 40 nm m/min and 115 nm m/min for low and high power films, respectively compared to 6 nm m/min for the reference RF ZnO:Al sputtered films using a single ceramic target.

Table 5.2 shows some solar cell parameters and haze values of the corresponding front contact, for solar cells prepared on the ZnO:Al films of series B and C. In general, the highest values of J_{sc} for the same set of ZnO:Al deposition parameters consistently occurred where the ZnO:Al films had developed a fairly good distribution of large sized craters similar to that of the reference (see Figure 5.6 (b)). However this is not reflected in the haze value. External quantum efficiency Q_E, spectra were determined for the best six cells presented in Table 5.2.

Table 5.2. Solar cell parameters for selected ZnO:Al films

ZnO:Al type	Etch duration (s)	H_{700} (%)	QE at 900 nm (%)	J_{sc} (mA/cm²)	η (%)
RF	40	45	26	23.2	8.4
B2	50	43	-	23.9	8.1
B2	70	39	27	24	8.2
B4	30	31	-	23.2	8.2
B4	50	61	27	24.3	8.3
RF	40	45	25	23.1	8.4
C6	50	30	28	24.1	8.2
C6	70	73	29	24.2	8.2
C7	50	24	28	24.3	8.4

Figure 5.10 shows the Q_E results for the μc-Si:H cells on the respective MF deposited ZnO:Al films with the reference cell on RF sputtered ZnO:Al included for comparison. The increase in J_{sc} was a direct result of improved light trapping leading to an enhancement of Q_E in the NIR wavelength region. All cells exhibited high *QE* in the blue and green wavelength region because of the high transmittance of the ZnO:Al films and good index matching of the rough interface. They also exhibited high Q_E in the red and NIR region, which was a strong indication of their good light trapping ability. The highest J_{sc} for each category of cells was due to a Q_E at 900 nm, equal to or exceeding 27% as can be seen in the fourth column of Table 5.2.

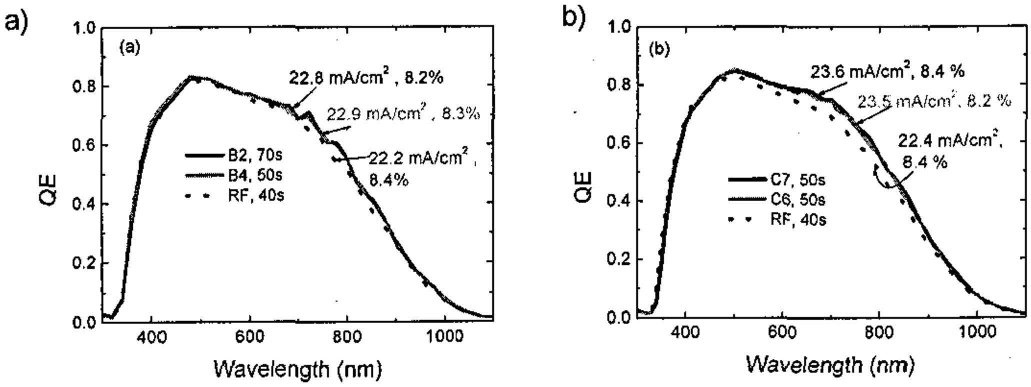

Figure 5.10. QE as a function of wavelength for μc-Si:H cells on low power (a) and high power (b) MF sputtered ZnO:Al films with the respective reference cells on RF sputtered ZnO:Al included. The labels indicate J_{sc} calculated from spectral response measurements and the solar cell efficiency.

5.5 Conclusion

The more uniform distribution of oxygen supply to the MF reactive magnetron sputtering process improves the average resistivity and the thickness uniformity of ZnO:Al films deposited in stationary mode. This also possibly contributes to a better structure of films deposited by multi-passes in the dynamic mode. By adjusting the oxygen distribution, favourable surface structure for light trapping could be achieved, after etching. The subsequent achievement of short circuit currents above 23 mA/cm^2 and an efficiency of up to 8.4% for a 1 cm^2 μc-Si:H single junction solar cell further illustrates the benefit of the oxygen inlet modification. These results would be useful when optimising large area reactors for TCO applications in industry.

Chapter 6 High mobility TCO materials for solar cells[17]

The efficiency of a solar cell can be improved by maximising the portion of the solar spectrum that is utilised to generate electron-hole pairs by grading the material band gap through the absorber layers as in $CuGa_XIn_{1-X}Se_2$ or by using multijunction solar cells. Additionally, if the stacked absorber layers of a multijunction solar cell, are connected in series, the overall efficiency can also be improved by increasing the terminal voltage of the solar cell provided that the current from all the individual device is closely matched and as high as possible. However, optical losses from the front and back contacts, various inactive window layers of the cell as well as at interfaces in the stack may reduce the amount of light reaching the bottom cell causing a current mismatch [197]. Figure 6.1(a) shows the J-V characteristics of a CIGS solar cell illuminated by AM1.5 light with or without a semi transparent solar cell (a 1μm thick CdTe absorber layer with ITO front and back contacts) filtering the incident light.

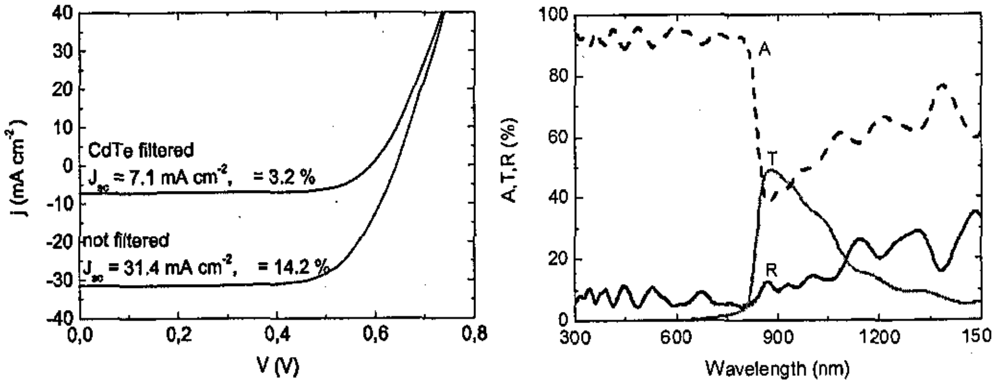

Figure 6.1. (a) J-V characteristics of a CIGS solar cell under AM1.5 global illumination (η= 14.2%, J_{SC} = 31.4 mAcm^{-2}) and with the illumination filtered through a semi-transparent CdTe solar cell (η= 3.2%, J_{SC} = 7.1 mA cm^{-2}). (b) Transmission *T*, reflection *R* and absorption *A* spectra of the semi-transparent CdTe solar cell used as a filter in (a). The solar cell "filter" consists of a 1μm thick CdTe absorber layer and uses ITO as the front and back contact.

---

[17] Part of the work described in this Chapter has been communicated in papers V to VIII in the list of publications.

As expected, the photo-generated current and thus efficiency of the CIGS cell reduces when the incident light is filtered through the CdTe cell. Figure 6.1(b) shows the transmission $T(\lambda)$, reflection $R(\lambda)$ and absorption $A(\lambda)$ spectra of the CdTe solar cell from which it can be seen that the NIR transmission is limited by considerable absorption losses exceeding 40%. Since CdTe does not absorb photons with wavelengths greater than 800nm, the absorption losses are mostly caused by the ITO contacts and therefore more transparent contacts are desirable. This problem may be solved by high mobility TCO (HMTCO) materials such as transition metal doped CdO and In_2O_3 films which possess low resistivity $\sim 10^{-4}\ \Omega$ cm and a high transmission > 80% over wavelengths from 300 nm to beyond 1500 nm. Table 6.1 compares the electrical properties of two high mobility TCO materials namely, In_2O_3:Ti (ITiO) and In_2O_3:Mo (IMO) with those of two conventional TCO materials i.e. ITO and FTO. The ITiO film was grown at Aoyama Gakuin University, Japan according to a method described in [198], the IMO film was grown at Loughborough University as will be discussed later in this chapter while the FTO and ITO films were obtained from a commercial vendor. It can be seen that the ITiO and IMO thin films have a high mobility > 77 $cm^2\ V^{-1}s^{-1}$ which results in low resistivity similar to ITO but with lower values of N comparable to the more resistive FTO thin film.

Table 6.1. Electrical properties of IMO, ITO, ITiO and FTO thin films on 1.1 mm thick low iron soda lime glass.

TCO	d (nm)	μ ($cm^2V^{-1}s^{-1}$)	N (10^{20} cm^{-3})	ρ (10^{-4} Ω cm)
ITiO	250	105	3.1	1.9
IMO	200	77	5.0	1.6
ITO	120	27	18	1.3
FTO	415	25	6.5	3.9

d – thickness; μ - majority charge carrier mobility; N - majority charge carrier density and ρ – resistivity.

Figure 6.2 (a) shows the transmission $T(\lambda)$, and reflection $R(\lambda)$ spectra of the TCO thin films on 1.1 mm soda lime glass while the related absorption $A(\lambda)$ spectra are shown in Figure 6.2 (b). The ITiO and IMO coated substrates are highly transparent over a wider spectral range than the other TCO materials, which adequately covers photons from 400 nm to 1300 nm required for a multi-junction solar cell using say, CdTe and CIGS. The IMO thin film has a slightly lower transmission of visible light than the ITiO thin film as a result of absorption close to 5%. The plasma edge moves towards higher wavelengths in the order ITO, FTO, IMO and ITiO. The NIR light transmission of the ITO is limited by high reflection for wavelengths above 1100 nm whilst that of the FTO is limited by the enhanced absorption, in both cases by a high carrier density and a low mobility. Though the gain in NIR transmission by replacing FTO and ITO with HMTCO thin films, is only about 5-10%, it becomes significant if a transparent contact is required on both sides of the solar cell as is shown later.

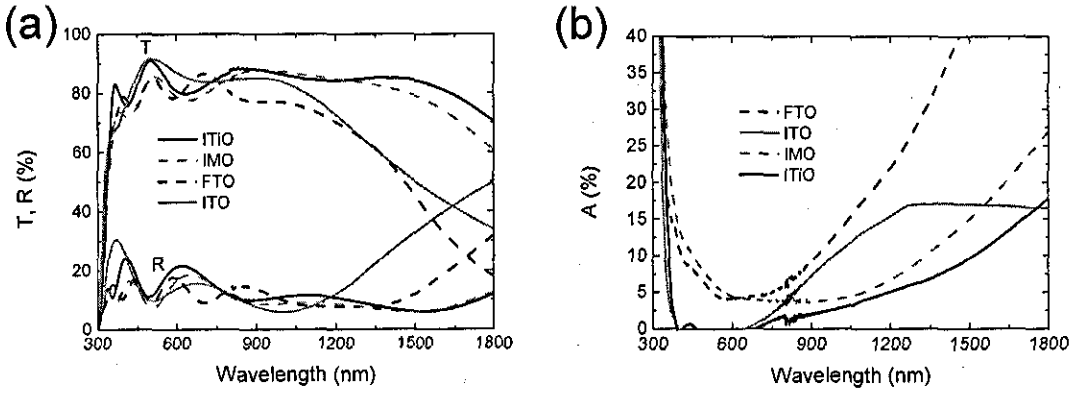

Figure 6.2. (a) Transmission *T* and reflection *R* as well as (b) absorption *A* spectra for ITiO, IMO, ITO and FTO thin films on glass with illumination from the glass side.

Therefore, this chapter is aimed at exploring how HMTCO properties may be improved by trying to understand the reasons for such high mobility values in degenerate films. Also, the use of HMTCO films in solar cells and the associated benefits and challenges are described.

6.1 Review of high mobility TCO materials

The exceptional coincidence of low resistivity and high transparency over the visible and NIR wavelength regions provides opportunities to improve the performance of opto-electronic devices and opens possibilities for new applications. However, it is imperative to understand the causes of these phenomena to maximise these benefits.

6.1.1 Strategies to attain high mobility in TCO materials

Various strategies have been used to increase the mobility of TCO thin films while maintaining high transparency and conductivity as reviewed by Exarhos etal. [20]. These and other methods that are perhaps less well known but show promise, are discussed in this section.

6.1.1.1 Post deposition heat treatment

Electron mobility in TCO thin films can be reduced to some extent by grain boundary and/or defect point scattering. Therefore, TCO films prepared in the amorphous state or with poor crystallisation are usually heated afterwards to improve the crystalline structure. This reduces point and/or dislocation defects thus increasing the grain size and improving the overall crystalline structure of the film which may enhance the electron mobility [12, 199]. However, effective heat treatment may require temperatures approaching 600°C, that are unsuitable for heat sensitive substrates such as polymers or soda lime glass which may soften and introduce undesirable impurities in the TCO films and so other methods have to be used.

6.1.1.2 Choice of deposition method

Deposition methods such as DC magnetron sputtering which use very energetic particles for film growth may damage the TCO film crystalline structure reducing the mobility [199]. During sputtering, the discharge voltage at the target surface repels both negative oxygen ions and neutral argon atoms, which arrive at the substrate with high kinetic energy ~ 100 eV and distort the TCO crystalline structure [200]. Since the discharge voltage is less for RF sputtering than for DC sputtering, it is usual for TCO films grown by the former method to have higher values of mobility [178, 200]. The kinetic energy of particles related to pulsed laser deposition varies from 1eV to a few 100 eV but is easier to control than in sputtering resulting in better TCO crystalline structures leading to higher mobility [201].

6.1.1.3 Control of crystal structure using mono-crystalline substrates

Control of crystal growth by using mono-crystalline substrates may enhance the mobility of TCO thin films by improving crystallinity. Thin films that are epitaxially grown on single crystals, consist of large crystallites which have nearly the same orientation which reduces the grain boundaries [99]. The highest reported mobility for highly conductive ZnO:Al ~ 70 $cm^2 V^{-1}s^{-1}$ at N> 10^{20} cm^{-3} has been reported for films grown on c-plane sapphire [201]. A study of Cd_2SnO_4 films grown on different substrates illustrates this point further, where the mobility of the films was measured as 609 $cm^2 V^{-1}s^{-1}$ (the highest reported value for a degenerate TCO material), 330 $cm^2 V^{-1}s^{-1}$ and 27 $cm^2 V^{-1}s^{-1}$ using MgO(111), MgO(100) and boro-silicate glass substrates, respectively [107]. The relatively high cost and limited suitability of these highly oriented substrates on large areas precludes the use of epitaxially grown TCO in a wide range of applications, especially displays and solar cells.

6.1.1.4 Controlling impurity concentration

Impurities are a source of ionised scattering centres as well as crystalline defects through distortion which can reduce the mobility of TCO film. Relatively high mobility in ZnO:Al up to 44.2 $cm^2 V^{-1} s^{-1}$ with N = 3.8 x 10^{20} cm^{-3} can be realized using a ZnO target with a low Al_2O_3 concentration of 0.5 wt % [202]. Also, by minimising intrinsic defects in thin film ZnO, a mobility of 440 $cm^2 V^{-1} s^{-1}$ but with a low N < 10^{16} cm^{-3} can be achieved [203].

6.1.1.5 Selective doping

Selective doping methods may increase the relaxation time τ in TCO materials by separating the doping and charge transport regions. The charge carriers are provided by the heavily doped regions while the lightly doped regions provide a high mobility path where scattering by ionised or neutral impurities is minimised. Zone confining is achieved by applying a (quasi) periodic temperature gradient across the surface of the substrate during deposition of the TCO material [204]. During film growth, the impurities tend to accumulate in the colder areas of the substrate surface. The impurity movement and temperature gradient are mutually parallel and are perpendicular to the growth direction. The result is a film consisting of alternate zones of heavily doped metal oxide and almost pure metal oxide as illustrated in Figure 6.3 a. Zone confining has been used to prepared ITO with a high mobility of 103 $cm^2 V^{-1}s^{-1}$ and an average carrier density of 1.4 x 10^{21} cm^{-3} giving a resistivity of 4.4 x 10^{-5} Ω cm [204, 205]. However, the visible transparency of ITO grown by this method was below 80% [205].

Selective doping using multilayered films composed of lightly- and heavily-doped semiconductors alternately stacked in the direction of the film growth as illustrated in Figure 6.3 (b), is also referred to as modulation doping [206].

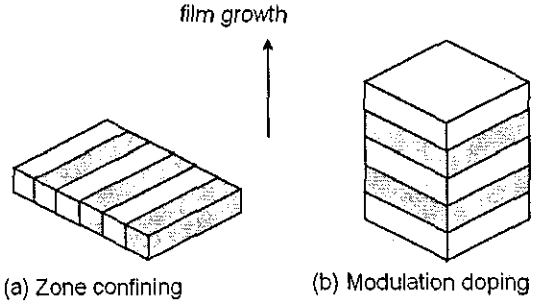

Figure 6.3. Schematic showing charge carrier distributions in relation to the direction of film growth of semiconductors prepared using selective doping by zone confining (a) and modulation (b). The dark and light sections denote regions of high and low carrier density, respectively.

Several studies predict that modulation doping may improve TCO mobility [207, 208]. Simulations on multi- layered films composed of $InGaO_3$ (relatively large electron affinity and low carrier density) alternately stacked with ZnO:Al layers (low electron affinity and high carrier densities) have predicted that high conductivity values $> 4.2 \times 10^4$ S cm^{-2} for carrier densities ~ 10^{20} are possible [207]. A mobility of 1560 cm $V^{-1}s^{-1}$ is possible if $N = 1 \times 10^{20}$ cm^{-3} at the bottom of a 5nm wide quantum well giving a resistivity of 4.0×10^{-5} Ω cm. Similarly, mobilities as high as 145 cm^2 V^{-1} s^{-1} were predicted for a modulation-doped ZnO|ZnMgO|ZnMgO:Al|ZnMgO structure and with the lowest resistivity was limited to 1.5×10^{-3} Ω cm for an average N of 3.8×10^{18} cm^{-3} [208]. The highest values of conductivity and mobility would require individual layers <5 nm thick with high crystalline quality and close lattice matching to avoid interface defects [207, 208].

Multi-layers consisting of ZnO|ZnO:Al and ZnO|$Zn_{1-X}Mg_XO$:Al have also been prepared on *a*- and *c*- plane sapphire substrates and though the crystal structure was comparable to that of single layers, the resistivity was quite high [209]. The authors attributed this effect to the high oxidation sensitivity of the thin films which passivated the donors and reduced the carrier density. Also, low resistivity multilayered films consisting of InO_x (2.0nm)|SnO_y (0.2nm) have been prepared despite a relatively low mobility of 17 cm^2 V^{-1} s^{-1} with a carrier density of 5×10^{20} cm^{-3} [210]. The predicted high mobility using modulation doping is yet to be reported in TCO films suitable for most applications because of the complex preparation required for very thin, closely lattice matched highly crystalline layers.

6.1.1.6 Hydrogen inclusion

First principles total energy calculations suggest that the bond length between hydrogen and the nearest host oxygen atom in a metal oxide is virtually the same regardless of the metal [211]. The hydrogen is "pinned" at a fixed energy level which introduces shallow defect states inside the conduction band of oxides, with a high electron affinity, causing n-type doping. The hydrogen may also passivate structural defects in TCO materials in the same way as is known for thin film silicon [212, 213]. Hydrogen inclusion in TCO materials is achieved either during film deposition or by post deposition annealing in a hydrogen atmosphere. One of the highest mobilities for ITO ($\mu \sim 145$ cm^2 V^{-1}s^{-1} for $N > 10^{20}$ cm^{-3}) has been achieved by post deposition treatment in a hydrogen plasma [213] whilst that for ZnO:Al ($\mu \sim 50$ cm^2 V^{-1}s^{-1} for $N > 10^{20}$ cm^{-3}) has been reported for films sputtered with a small amount of hydrogen added to the sputter gas [214]. A high value of $\mu = 130$ cm^2 V^{-1}s^{-1} for $N = 1.8 \times 10^{20}$ cm^{-3} has also been reported for hydrogen doped In_2O_3 [213].

6.1.1.7 Choice of appropriate dopants

The highest mobilities for conventional degenerate TCO thin films grown by sputtering are typically 40-50 cm² V^{-1}s^{-1} for In_2O_3:Sn [34, 199, 215] and ZnO:Al [89, 200]. However, specific elements have been used to prepare degenerate CdO and In_2O_3 thin films by sputtering or MOCVD with $\mu > 62.5$ cm² V^{-1}s^{-1} with transmission > 80% over wavelengths from 300 nm to 1500 nm. While undoped CdO thin films have a high mobility, the optical band gap is too low for use as a transparent conductor for visible light. Doping cadmium with several elements e.g. In [216], Sc [217], Y [218] and Ti [219] increases the band gap and can cause mobilities above 62.5 cm² V^{-1}s^{-1} while maintaining $N \geq x\ 10^{20}$ cm^{-3}. High mobility in In_2O_3 thin films can be achieved using elements such as Mo [220-222], Ti [198, 223-227], W [228-231], Zr [223, 224, 232-235], Gd [236]. Details of dopants elements leading to high mobility in CdO and In_2O_3 will be presented later in Table 6.3 and Table 6.4, respectively.

6.1.2 Deposition methods for high mobility degenerate In_2O_3:Mo films

Impurity doped In_2O_3 thin films can be grown with high mobility ($\mu > 62.5$ cm^{2}V^{-1}s^{-1}) using a variety of methods as listed in Table 6.2.

Table 6.2. Deposition methods used to prepare impurity doped In_2O_3 *thin films.*

Dopant	Method	N (10^{20} cm^{-3})	μ (cm^2 V^{-1}s^{-1})	ρ (10^{-4} Ω cm)	T_S (° C)	Ref
Mo	TRE	2.6	130	1.8	350	[87]
	RFMS	3.0	83	2.5	450†	[237]
	CSA	7.1	~18.3	4.8	350	[238]
	REHCS	4.1	80.3	1.9	290	[224]
	SP	4.98	~ 1.72	7.3	450	[239]
	Reactive DCMS	1.9	50	~ 5.0	350	[240]
	RFM co-sputtering	2.7	99	2.3	450†	[220]
	RFM co-sputtering	4.3	65.3	~2.22	550	[221]
	PLD	3.6	250	0.7	500	[222]
	Pulsed DCMS	5.0	77	1.6	500§	This work
Ti	SPD	1.0	120	5.2	500	[223]
	REHCS	4.3	80.6	1.8	300	[224]
	Combinatorial RFMS	2.9	83.3	2.6	500	[225]
	DCMS	2.0	89.5	3.5	300	[226]
	PLD (quartz)	0.8	199	0.98	500	[227]
	RFMS	3.1	105	1.95	530	[198]
Zr	SP	0.8	170	4.6	500	[223]
	ALD	2.2	76	3.7	500	[232]
	RHCS	4.3	63.3	2.3	250	[224]
	PLD, YSZ <111>	1.0	110	5.7	650	[233]
	RFMS	2.9	82	2.6	450	[234]
W	Reactive DCMS	4.0	57	2.7	380	[241]
	DCMS	2.9	73	3.0	300	[229]
	SP	2.4	26	10	525	[242]
	Reactive DCMS	2.8	67	2.8	320	[231]
	PLD (quartz)	~1.5	358	~1.1	500	[230]

N - majority charge carrier density; μ- majority charge carrier mobility; ρ- resistivity and d – thickness.

TRE – thermal reactive evaporation; RFMS - RF magnetron sputtering; CSA- Channel spark ablation; RHCS – Reactive environment hollow cathode sputtering; SP - Spray pyrolysis; DCMS - DC magnetron sputtering; PLD pulsed laser deposition and ALD – atomic layer deposition.

† Mobility enhanced by post deposition heat treatment.

§ Substrate temperature estimated to be within 10% of indicated heater temperature.

From Table 6.2 it is evident that though high mobility in impurity doped In_2O_3 can be achieved by a wide range of deposition techniques, the use of pulsed laser deposition (PLD) and/or post deposition annealing further enhances the Hall mobility. The lowest resistivity reported for IMO thin films to date is 6.7×10^{-5} Ω cm with a high mobility (250 cm^2V^{-1} s^{-1}) grown at 500°C by PLD on quartz [222]. However, the NIR optical transmission is not known as a high transmittance (~90%) was only presented for visible light.

6.1.3 Understanding the mechanisms of high mobility in impurity doped CdO and In_2O_3

The mobility μ of an electron in semiconductors depends on the relaxation time τ, the electronic charge e and the effective carrier mass m^* in the conduction band as given by Equation 2.11. Several factors may limit the electron mobility in impurity doped TCO films but often conflicting explanations are given for observed variations in the conductivity.

6.1.3.1 Role of crystalline quality and structure

Poor crystalline quality may cause a reduction in the relaxation time and thus mobility as a result of increased point defects, grain boundaries and lattice distortion. Charge transport in n-type semiconductor occurs when electrons drift from the conduction band of one cation in the crystal lattice to the other. Therefore shorter cation-cation bond length and a favourable cation distribution are believed to increase the electron mobility in the semiconductor. Studies by Shannon et al. [243] on single crystals in the CdO-SnO_2-In_2O_3 family suggest that oxide structures with continuous edge sharing of cation octahedra are essential for conductivity in metal oxides. Later work by Ingram et al. [244] on thin films of the same CdO-SnO_2-In_2O_3 family extends this rule to include structures where octahedra share corners. A means of classifying TCO materials according to the coordination of the cations was suggested, for example, ZnO has tetrahedral coordination whilst CdO, In_2O_3, SnO_2 and other Cd containing spinel oxides have octahedral coordination [244]. The decrease in both conductivity and mobility was also correlated to a decrease in the octahedral cation density in the structure in the order: CdO (rock salt)> In_2O_3 (bixbyite)> SnO_2 (rutile) [244]. Studies of $ZnSnO_4$ by Mossbauer spectroscopy and x-ray diffraction indicate that the unusually low mobility is a result of disorder on the cation octahedral sites which may disrupt transport between edge sharing cations [245]. Since high mobility with degenerate doping has only been reported for CdO and In_2O_3 based compounds with octahedrally coordinated cations, the associated cubic structure may also favour high mobility.

6.1.3.2 Role of the electronic band structure

The electronic band structure of TCO materials can be studied by theoretical modelling or by measurements of the relaxation time and effective mass as well as the Hall parameters. Owing to the simple structure of CdO, the majority of theoretical electronic band structure studies have been done on this material. Freeman et al. [167, 246] have identified three salient features of the electronic band structure of the conduction band of a TCO material which affect the charge carrier transport mechanisms namely, the curvature, the dispersion and the position. A parabolic conduction band minimum ensures a low effective carrier mass of the electrons which *promotes high mobility. A study of the* $Cd_{1+X}In_{2-2X}Sn_XO_4$ *system shows that both the* density of states effective mass and the relaxation time increase with N, resulting in a cancellation effect such that the mobility is less than expected [247]. In contrast, carrier mass of IMO was determined as 0.32 m_e and found to be independent of N implying a parabolic conduction band minimum [237]. A widely dispersed conduction band minimum allows electrons to drift unimpeded through the crystal structure resulting in a higher relaxation time and thus higher mobility. Electronic structure calculations of $In_xCd_{1-x}O$ thin films for which mobility up to 91.5 $cm^2\ V^{-1}s^{-1}$ with $N > 10^{20}\ cm^{-3}$ was measured, revealed an electron effective mass of 0.24-0.26 m_e and a broadening of the conduction band edge by hybridization of the Cd 5s and In 5s bands [216]. The calculated effective electron mass agrees with a value of 0.25 m_e determined by Seebeck measurements [248]. *Theoretical studies also suggest that the lowest conduction band* of In_2O_3 is split with Sn doping due to the strong hybridization with dopant s-type states and this splitting contributes to both the decrease of the plasma frequency and the mobility of the carriers [167]. In contrast, electronic band structure calculations suggest that high mobility is achievable in degenerate In_2O_3:Mo as the d-states of Mo do not hybridize with the s-states of In resulting in m* similar to undoped In_2O_3 [249].

6.1.3.3 Chemical character of dopant element

The review in the previous section illustrates that the discovery of elements that induce high mobility in TCO materials has largely been empirical. Few if any studies have been conducted to find the underlying mechanisms for high mobility caused by specific dopants. A series of studies predicted that the mobility of doped In_2O_3 would increase with the Lewis acid strength of the doping element and reported this effect for Ge^{4+}, Si^{4+} and Sn^{4+} [250] as well as for Cu, Ti and Zr [251]. However, the μ of the TCO films studied generally varied from 45 cm² V^{-1} s^{-1} to 55 cm² V^{-1} s^{-1} and in some cases, the films were non-degenerate. In this work, the Lewis acid strength principle is applied to known degenerately doped In_2O_3 and CdO thin films with mobility > 62.5 cm² V^{-1} s^{-1}. The Lewis acid strength L can be calculated according to a formula developed by Zhang [252] as follows

$$L = \frac{Z}{r^2} - 7.7\chi_Z + 0.8 \tag{6.1}$$

Where r is the ionic radius related to the electrostatic force due to the valence state Z of the ion and χ_z is the electronegativity of the element in the respective valence state. Using this formula, the Lewis acid strengths of elements that are now known to induce high mobility in CdO and In_2O_3 thin films were compiled in Table 6.3 and Table 6.4, respectively.

All these films are highly transparent in the visible and most (where reported) have a high near infra-red region transmission. It can be seen that the dopants that induce high mobilities are transition elements which have a higher Lewis acid strength than the host cation for example, whilst doping CdO by Sn^{4+} and In^{3+} leads to $\mu \sim$ 70 cm² $V^{-1}s^{-1}$, doping by the transition metal ions Y^{3+}, and Ti^{4+} drastically increases μ. The lists in Table 6.3 and Table 6.4 are not exhaustive and have been compiled, where possible, from TCO films prepared by MOCVD or sputtering, respectively on glass substrates to reduce the influence of the film deposition technique on the mobility values reported. Also, these films may not represent the highest possible mobility achieved by a given dopant.

Table 6.3. High mobility doped CdO films grown by MOCVD on glass substrates except where indicated. The elements are arranged in ascending order of group number and period. The host cation Cd^{2+} and the more common aliovalent dopants In^{3+} and Sn^{4+} are included for comparison.

Doping ion	Ionic radius (Å)§	Lewis Acid Strength §	N (10^{20} cm^{-3})	μ (cm^2 $V^{-1}s^{-1}$)	Reference
Sc^{3+}	0.89	1.697	~4.0	~80	[217]
Ti^{4+}	0.68	3.064	23.8	202	[219] †
Ga^{3+}	0.76	1.167	3	60	[253]
Y^{3+}	1.04	1,465	4.8~	110	[218]
Cd^{2+}	0.99	-0.108	1.5	146	[216]
In^{3+}	0.81	1.026	15	69.2	[216]
Sn^{4+}	0.71	0.228	2	65	[254] †

† RF magnetron sputtering.

§ The ionic radii and Lewis acid strengths are compiled from calculations by Zhang [252].

For instance , a value of μ = 609 cm^2 $V^{-1}s^{-1}$ and N = 4.74 x 10^{20} cm^{-3} for $Cd_{1-x}Sn_xO$, grown by pulsed laser deposition on MgO single crystals [107], is the highest mobility reported for a degenerately doped TCO material. However, most of the dopants listed that induce high mobility in CdO and In_2O_3 are strong Lewis acids compared to Cd^{2+} and In^{3+}, respectively. There are two exceptions in Table 6.4, namely H^+ and Gd^{3+}.

The Lewis acid strength for H^+ has not been calculated because of the difficulty in determining the ionic radius which is anyway expected to be much less than that of In3+. As mentioned previously, H^+ is a shallow donor in most TCO films and may passivate defects states in In_2O_3 thus increasing the τ and improving μ [213]. However, the optical properties of H-doped In_2O_3 have not yet been reported. On the other hand, Gd^{3+} has a much higher ionic radius and a lower Lewis acid strength than In^{3+} but corresponds to a high mobility of 128 cm^2 $V^{-1}s^{-1}$. Gadolinium is a Lanthanoid, a special group of metals, most with a partially filed 4f orbital lying below group three transition metals in the periodic table and hence may warrant further investigation [255].

Table 6.4. High mobility dopants in In_2O_3 films grown by sputtering on glass substrates except where indicated. The elements are arranged in ascending order of group number and period. The host cation In^{3+} and the more common aliovalent dopant Sn^{4+} are included for comparison.

Doping ion	Ionic radius (Å) §	Lewis Acid Strength §	N (10^{20} cm^{-3})	μ (cm^2 $V^{-1}s^{-1}$)	Ref
H^+	-	-	1.78	130	[213]
Ti^{4+}	0.68	3.064	3.06	104	[198]
Zr^{4+}	0.86	2.043	2.2	76	[232]†
Nb^{5+}	0.78	2.581	10	65	[256]#
Gd^{3+}	1.08	0.788	1.74	128	[236]#
Mo^{6+}	0.62	3.667	2.7	99	[220]
W^{6+}	0.68	3.158	2.9	73	[229]
In^{3+}	0.81	1.026	2.5	60	[257]
Sn^{4+}	0.71	0.228	10.3	43	[199]

§ The ionic radii and Lewis acid strengths are compiled from calculations by Zhang [252].
† atomic layer deposition ALD,
# pulsed laser deposition on quartz.

Sn^{4+} being a non transition metal ion with a lower Lewis acid strength than In^{3+} will induce a lower mobility in In_2O_3 than the transition elements listed in Table 6.4. On the other hand, mobility values <62.5 cm² $V^{-1}s^{-1}$ with $N > 10^{20}$ cm^{-3} have been reported for non–transition metal dopants with high enough Lewis acid strengths such as Sb^{5+} (3.559), Ge^{4+}(3.059), Si^{4+} (8.098) [250]. According to Wen et al. [250], high Lewis acid dopants polarise the electronic charge, away from the O^{2-} 2p valence band, more strongly than weaker Lewis acids, which screens the charge and weakens its activity as a scattering centre hence increasing the mobility. Similarly, the reason for higher mobility in In_2O_3:Mo compared to intrinsic In_2O_3 has been explained by Mo suppressing scattering by oxygen interstitials [237]. However, if the Lewis acid is too strong e.g. Ge in In_2O_3, the dopant has a greater affinity to oxygen and may incorporate an excess of oxygen in the lattice which would then limit μ by introducing scattering centres [250].

The high mobility of In_2O_3:Mo was originally attributed to the higher oxidation state of Mo^{6+} ions that would contribute three extra electrons to the In_2O_3 matrix [87]. Later studies by another group suggested that Mo in In_2O_3:Mo exists as both Mo^{4+} and Mo^{6+} for high carrier density and only as Mo^{6+} for films with lower carrier density though the mobility values were substantially lower than 62.5 cm² $V^{-1}s^{-1}$ [258]. However, a study comparing dopants with an oxidation state of +4 shows that both the electron mobility and the visible light transparency are higher for Ti-, Zr-, and Ge -doped In_2O_3 than for Sn-doped In_2O_3 for the same dopant atomic concentration [251]. A similar comparison of In_2O_3 doped by Sn, Ti and Zr also confirmed this result with even higher values of mobility than reported previously [235]. Though the role of possible multiple valency e.g. of Ti as Ti^{2+} was not considered, these studies assert that for high mobility in In_2O_3 the dopant need not donate more than one electron per atom but should be a transition metal ion.

6.2 Growth and analysis of In_2O_3:Mo films

As shown in Table 6.2, high mobility In_2O_3:Mo films can be grown by various deposition techniques. Also, several groups have investigated the influence of specific deposition parameters on the In_2O_3:Mo film properties including oxygen partial pressure [222, 237, 238, 240, 258-263], processing temperature [87, 220-222, 239, 258] as well as RF sputter power and thickness [264]. Also, the effect of post deposition heat treatment on In_2O_3:Mo films has been studied by some groups [220, 237, 265]. However, few of the studies have been aimed at understanding the high mobility observed. Therefore, this section will describe the structural, chemical and opto-electronic properties of In_2O_3:Mo films prepared by pulsed DC sputtering and use these properties to understand the role of molybdenum in the charge transport mechanism.

6.2.1 Growth of In_2O_3:Mo films by pulsed DC magnetron sputtering

The layout of the sputter system used to prepare the In_2O_3:Mo thin films was described in section 3.2.3. The deposition parameters used to prepare the In_2O_3:Mo films are listed in Table 6.5. Preliminary studies showed that the film resistivity and mobility did not vary much when the oxygen partial pressure was varied by adjusting the volume proportion of oxygen mixed with the argon. In contrast, the heater temperature T_H and the sputter pressure p_S had considerable influence on the In_2O_3:Mo film properties. Therefore, one set of films was prepared with T_H held at 450°C and p_S varied from 0.13 Pa to 1.67 Pa, while the other set was prepared with varying T_H with p_S maintained at 1.0 Pa.

Table 6.5. Parameters used to grow In_2O_3:Mo films in an ATC Orion 8 UHV sputter system

Target composition	In_2O_3: Mo (98:2 wt%)	
Applied target power density (W cm^{-2})	2.74	
Sputter mode	Pulsed DC magnetron sputtering	
Operating frequency (kHz)	150	
Pulsing duty cycle [= t_{ON} / T] (%)	55	
Oxygen proportion in sputter gas (vol.%)	0.53	
Substrate	Low iron soda lime glass	
	Series	
	A	B
Sputter pressure p_S (Pa)	0.13 – 0.17	1.00
Heater temperature T_H (°C)[a]	450	25-500
Coating duration (min)	30	45
Film thickness (nm)	200-290	311-383

[a] The substrate temperature is within 10% of the heater temperature. A heater temperature of 25 °C designates no intentional heating of the substrate.

6.2.2 Post deposition heat treatment of In_2O_3:Mo films

The In_2O_3:Mo films were heated under different ambient conditions namely in air, in vacuum and then in air followed by heating in vacuum. Table 6.6 gives the details of the heat treatment procedures. A heater temperature of 450 °C was chosen because it is typical for preparation of low temperature CdTe solar cells and dye sensitised solar cells (See Chapter 3). Heating in air (atmospheric pressure) was done on a hot plate whilst quartz lamps in an evacuated (~ 5 x 10^{-6} Pa) sputter chamber were used for vacuum heating hence the ramp duration differed slightly.

Table 6.6. Types of heat treatment used

Type	Treatment	Ambient	Heater temperature (°C)	Ramp duration (min)	Hold duration (min)
AD	as deposited	n/a	n/a	n/a	n/a
HA	heated	air	450	30	20
HV	heated	vacuum	450	40	20
HAV	heated	air then vacuum	450	30, 40	20, 20

6.2.3 Morphology and structural analysis

Figure 6.4 shows SEM images of the morphology of the IMO thin films prepared under different sputter pressure p_S conditions.

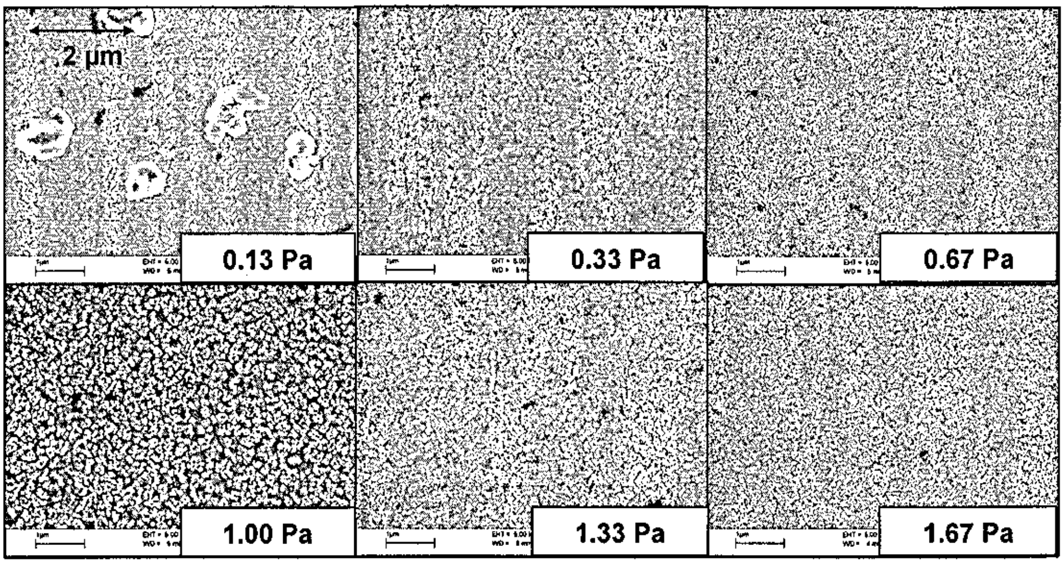

Figure 6.4: Evolution of the surface structure of In_2O_3:Mo thin films on soda lime glass as sputter pressure is increased over 0.13 – 1.67 Pa.

The surface of the In_2O_3:Mo thin film deposited at $p_S = 0.13$ Pa has triangular shaped grains interspersed with blister-like structures possibly caused by damage from re-sputtering. As p_S is increased to 0.3 Pa, the grains become smaller and the surface appears more uniform but porous. As p_S increases to 0.7 Pa, the grains become smaller with a denser packing. The grain size and surface porosity increase for the In_2O_3:Mo thin film prepared at 1.0 Pa and then reduces for films prepared at 1.3 Pa and 1.7 Pa.

Figure 6.5 shows the SEM micrographs of the surface of several In_2O_3:Mo thin films deposited with various heater temperatures. The film deposited without intentional heating (T_H indicated as 25°C) has very small needle-like grains that are inclined to the horizontal and the surface is interspaced with blister like features. At T_H = 150°C, the surface of the In_2O_3:Mo thin films consists of a mixture of triangular and cubic features. As T_H increases to 250 °C, the triangular features decrease relative to the cubic features and are eliminated for T_H = 350 °C. As T_H further increases to 500°C the width of the cubic grains gradually increases.

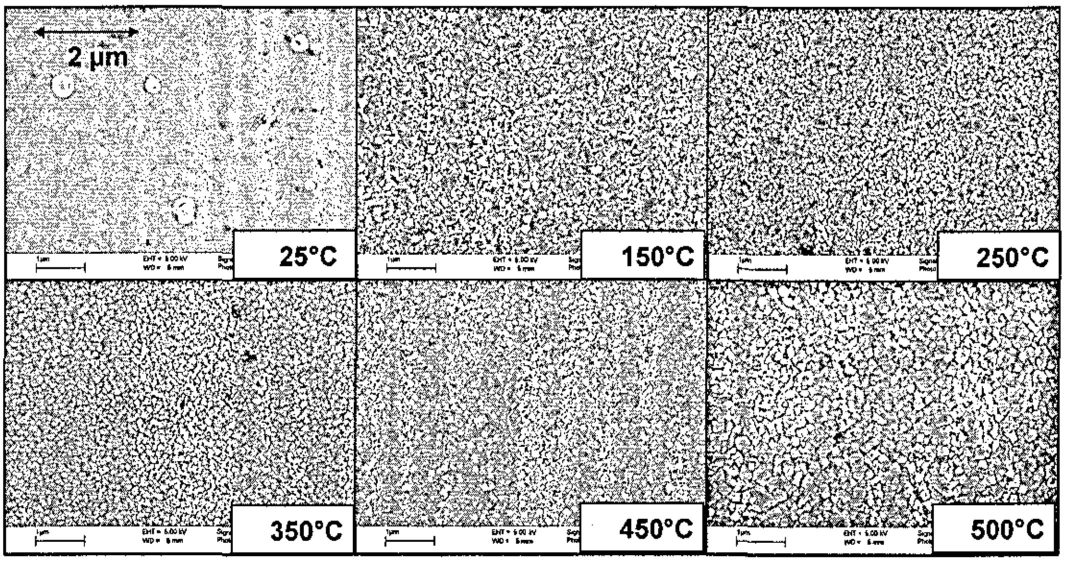

Figure 6.5. Evolution of SEM images of the surface of In_2O_3:Mo films on soda lime glass as the heater temperature is raised from 25 °C to 500 °C. Film thickness ranges from 311 -383 nm.

The left hand side of Figure 6.6 shows the XRD patterns of selected films prepared with varying p_S while the right hand side shows the related evolution of peak intensities of reflections along the (222), (440) and (622) planes normalised to those of the (400) plane.

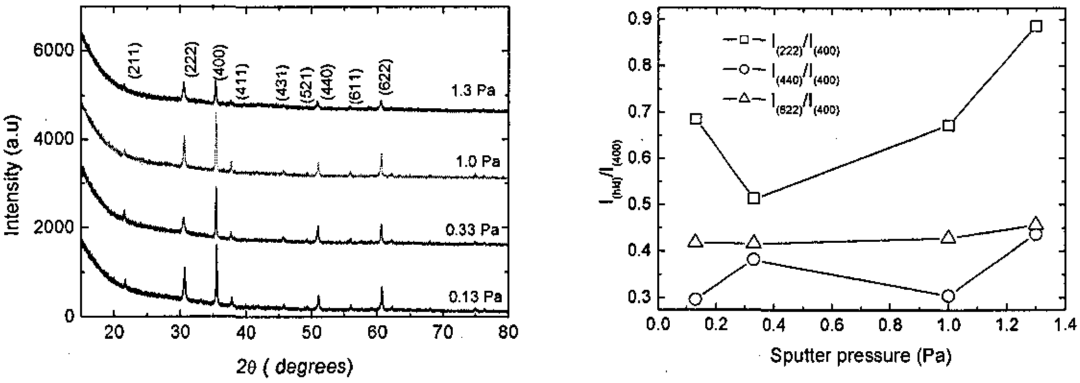

Figure 6.6. (Left) X-ray diffraction patterns for various IMO thin films prepared with different sputter pressures. (Right) Evolution of relative peak intensities with respect to the (400) diffraction plane of IMO thin films prepared with varied sputter pressure.

All the IMO films considered are polycrystalline showing most of the reflection peaks associated with bixbyite In_2O_3 (JCPDS Card 6-0416). The strongest reflection peak for all films coincides with the (400) plane. However as the sputter pressure is increased, the intensity of the reflection peak along the (222) and (622) planes increases slightly relative to that along the (400) plane.

The XRD reflection patterns corresponding to the films prepared at different heater temperatures are shown on the left hand side of Figure 6.7. The right hand side of Figure 6.7 shows the relative peak intensities of reflections along the (222), (440) and (622) planes with respect to those of the (400) plane. The (400) reflection peak has the highest intensity for all the IMO films except for that prepared without intentional heating where the (222) reflection is the most intense.

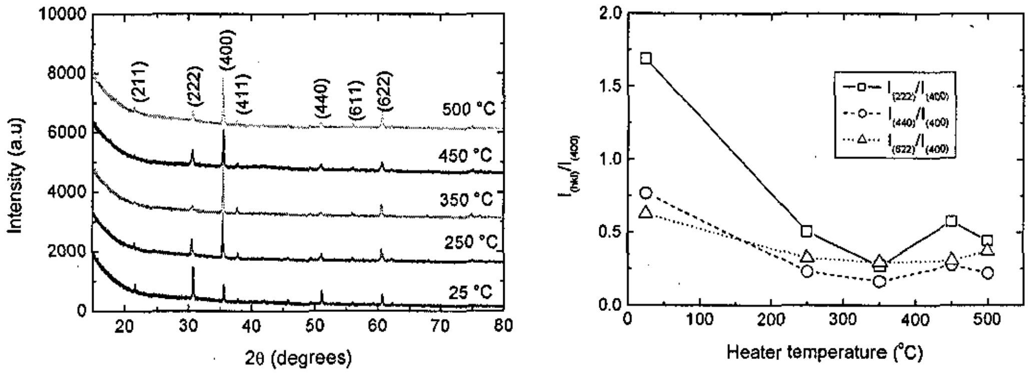

Figure 6.7. (Left) X-ray diffraction patterns for various IMO thin films prepared at different heater temperatures. (Right) Evolution of relative peak intensities with respect to the (400) diffraction plane of IMO thin films with varied heater temperature.

Some XRD studies show that In_2O_3:Mo films prepared without intentional heating are amorphous [259, 262, 265] while others, like the equivalent film shown in Figure 6.7, are polycrystalline with a relatively intense <111> texture [221, 264]. Elangovan et al. [264] reported that increasing the film thickness or the sputter power caused the formation of polycrystalline rather than amorphous films. On the other hand, for heated In_2O_3:Mo films the most intense XRD reflections are usually observed along the (222) planes [238, 239] unlike the In_2O_3:Mo films prepared in this section where the (400) reflection was the strongest. In some cases, the morphology of the substrate rather than the deposition method determines the In_2O_3:Mo texture. For instance, the strongest peak intensity corresponds to the (400) or the (200) plane, on YSZ (100) and glass, respectively, regardless of whether the films were grown by PLD or RF magnetron sputtering [266].

6.2.4 Electrical and optical properties of In_2O_3:Mo films

Figure 6.8 shows a graph of carrier density *N*, mobility μ and resistivity ρ as a function of sputter pressure. Increasing p_S from 0.13 Pa to 1.67 Pa, reduces *N* from 7.0 x 10^{20} to 2.0 x 10^{20} cm^{-3} while μ increases only slightly from 48 cm^2 $V^{-1}s^{-1}$ to 61 cm^2 $V^{-1}s^{-1}$ leading to an increase in ρ from about 3.0 x 10^{-4} to 6.9 x 10^{-4} Ω cm.

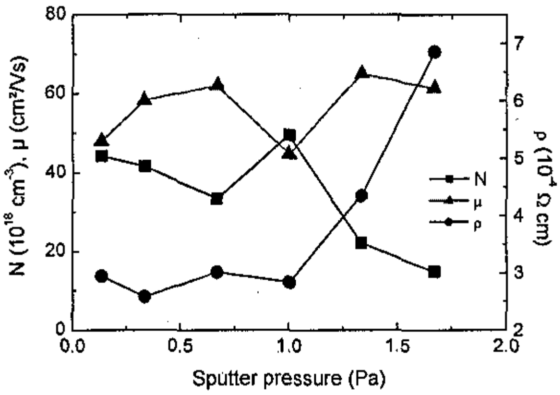

Figure 6.8. Charge carrier density *N* (squares), mobility μ (triangles) and resistivity ρ (circles) of IMO thin films as a function of sputter pressure. Film thickness ranges from 200 -290 nm. Lines are to guide the eye.

Figure 6.9 shows graphs of charge carrier density (a) and Hall electron mobility (b) of IMO thin films after different heat treatments as a function of T_H. The *N* and μ for the IMO film grown at room temperature and subsequently heated in air could not be detected by the Hall set up as the film became insulating. The charge carrier density is generally higher for films prepared with higher heater temperatures regardless of the treatment. Heating the as-deposited films in air reduces both *N* and μ. On the other hand, heating as-deposited films as well as those IMO films previously heated in air, in vacuum increases the values of both *N* and μ.

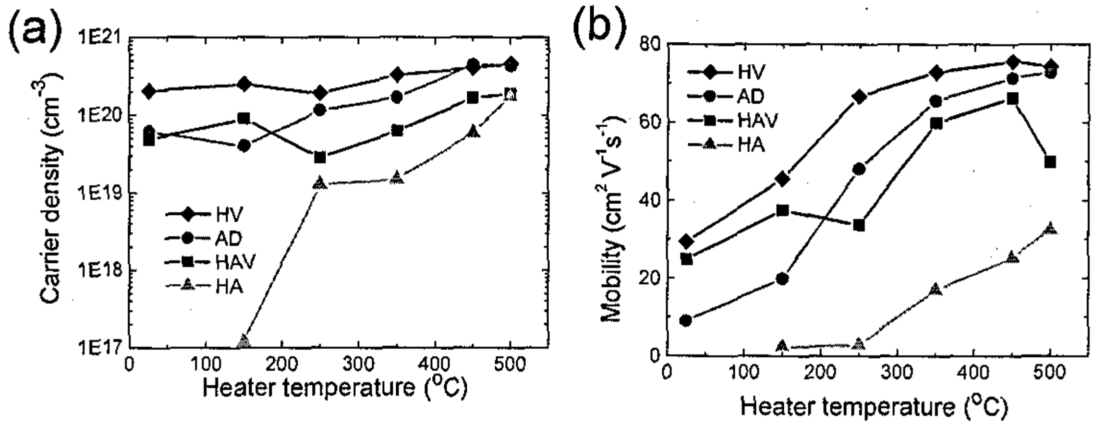

Figure 6.9. Charge carrier density (a) and mobility (b) of IMO films as a function of heater temperature for as-deposited IMO films *AD* (circles), as well as IMO films heated under different ambient conditions namely vacuum *HV* (diamonds), air *HA* (triangles) and air then vacuum *HAV* (squares). Lines are to guide the eye.

Figure 6.10 shows a graph of the resistivity ρ of IMO thin films after heat treatment in different conditions as a function of T_H.

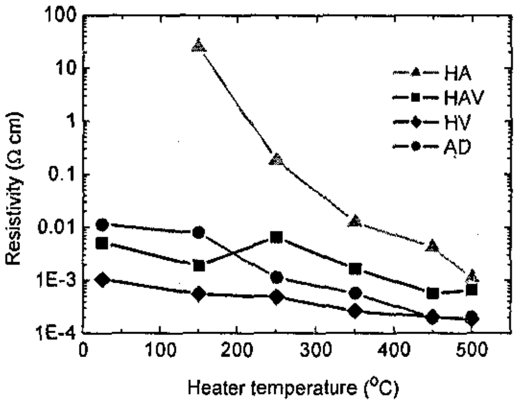

Figure 6.10: Resistivity of IMO films as a function of heater temperature for as-deposited IMO films *AD* (circles), as well as IMO films heated under different ambient conditions namely vacuum *HV* (squares), air *HA* (triangles) and air then vacuum *HAV* (diamonds). Lines are to guide the eye.

The resistivity generally reduces as T_H increases from 25°C to 450°C then saturates at about 2.0 x 10^{-4} Ω cm at 450°C and 500°C. The resistivity decreases because of a concurrent increase in N and μ from 0.6 x 10^{20} cm^{-3} to 4.5 x 10^{20} cm^{-3} and from 9 cm² V^{-1}s^{-1} to 73 cm² V^{-1}s^{-1}, respectively. The charge carrier density is generally higher for films prepared with higher heater temperatures regardless of the treatment.

Heating in air causes a significant reduction of both N and μ. On the other hand, heating in vacuum increases both N and μ of the as-deposited films as well as those IMO thin films previously heated in air.

Figure 6.11 (a) shows the spectral variation of the transmission $T(\lambda)$ and reflection $R(\lambda)$ of various IMO thin films grown with the sputter pressure varied between 0.1 Pa and 1.7 Pa on soda lime glass. Overall, the transmission over 300 nm to 1800 nm, increases with p_S. The reflection spectra exhibit interference fringes for wavelengths from 300 – 800 nm and for longer wavelengths, the reflection of the IMO increases with p_S. Figure 6.11 (b) shows the absorption spectra from 300 nm to 1800 nm for the IMO films.

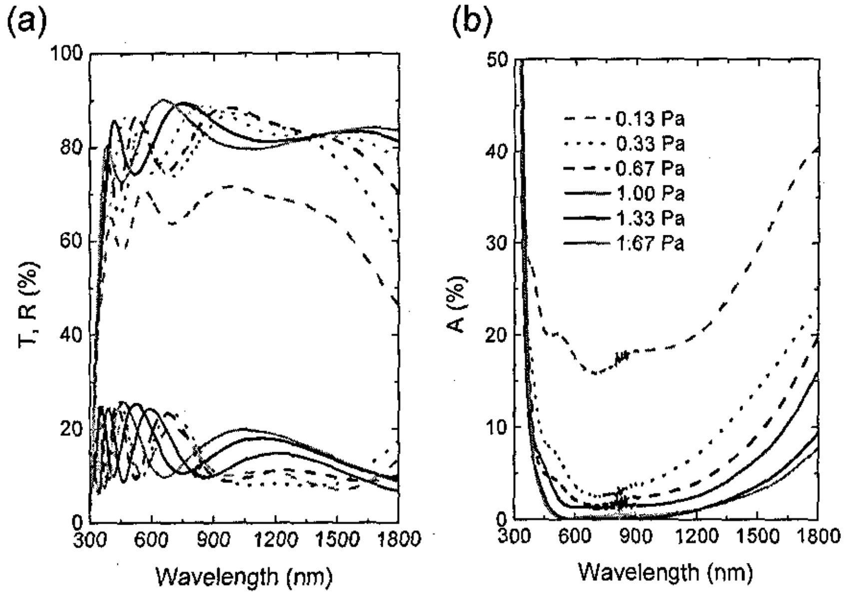

Figure 6.11. (a) Transmission T and reflection R spectra as well as (b) absorption A spectra of In_2O_3:Mo films grown with different sputter pressure on soda lime glass.

Over 300 nm to 1800 nm, the absorption increases with reducing sputter pressure as a result of increasing carrier density (Figure 6.8). The relatively low absorption of the IMO films prepared with sputter pressure exceeding 0.1 Pa results in interference fringes in the transmission spectra as a result of multiple internal reflections. The IMO film prepared at 0.1 Pa is highly absorbing compared to the other films because of a very rough surface that appeared hazy to the unaided eye.

The transmission $T(\lambda)$ and reflection $R(\lambda)$ spectra of IMO films sputtered with different T_H are shown in Figure 6.12 (a) and the associated absorption spectra are shown in Figure 6.12 (b).

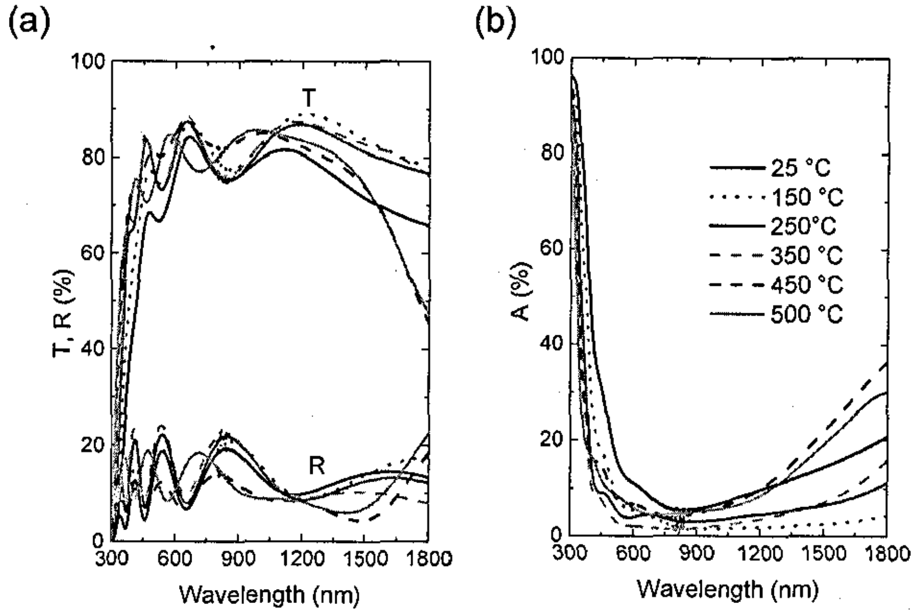

Figure 6.12. (a) Transmission T and reflection R spectra as well as (b) absorption A spectra of In_2O_3:Mo films grown with different heater temperature on soda lime glass.

The onset of transmission moves to lower wavelengths as T_H increases as a result of the Burstein Moss effect caused by increasing N (refer to Figure 6.9). Also, the Urbach band tailing indicates the presence of secondary oxide phases. The visible light transmission from 300 nm to 800 nm increases as T_H increases from 25°C to 350°C then reduces as T_H increases to 450°C then 500°C. In the NIR region, the transmission increases as T_H rises from 25 – 150°C then progressively reduces as T_H increases to 450 and 500 °C. The visible light reflection increases as T_H rises from 25 – 350°C, reduces at 450°C then rises again at 500°C. From 800 – 1500 nm, reflection increases as T_H increases from 25 – 150°C then reduces as T_H further increases to 500°C. For wavelengths from 1500 – 1800 nm, $R(\lambda)$ increases as T_H increases from 25 -150°C and then reduces as T_H increases from 250 – 500°C. The In_2O_3:Mo visible light absorption reduces as the temperature increases from 25 °C to 350°C while, from 350°C to 500°C, the visible light absorption increases. The NIR light absorption also reduces as T_H increases from 25 °C to 150°C then progressively increases as T_H rises from 250°C to 500°C because of increasing free carrier absorption.

6.2.5 Correlating electrical and optical properties of In_2O_3:Mo films

Figure 6.13. shows a graph of the average figure of merit for visible (Φ_{VIS}) and near infra-red (Φ_{NIR}) light of the IMO films, as a function of the sputter pressure. Initially Φ_{VIS} and Φ_{NIR} increase as p_S increases from 0.1-0.3 Pa then saturate for $p_S >$ 0.3 – 1.7 Pa. The value of Φ_{VIS} is more than thrice that of Φ_{NIR} for a given film at the same sputter pressure.

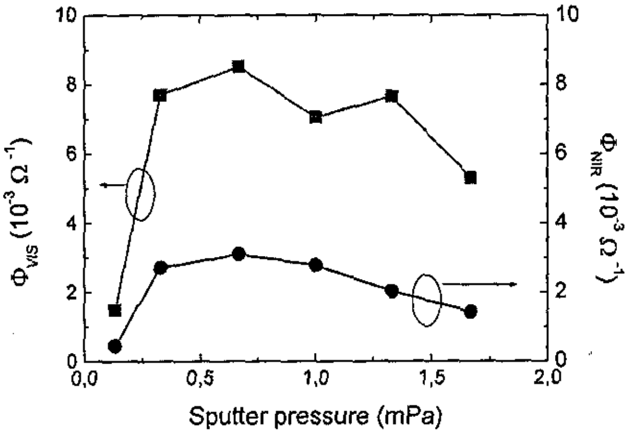

Figure 6.13. Average figure of merit (Φ) over 400 – 800 nm (squares) and 800 – 1200 nm (circles) of In_2O_3:Mo thin films versus sputtering pressure. Lines are to guide the eye.

The variation of Φ_{VIS} and Φ_{NIR} with heater temperature is shown in Figure 6.14. As T_H increases from 25°C to 450°C, both Φ_{VIS} and Φ_{NIR} increase from below 1 x 10^{-3} Ω^{-1} to 27.3 x 10^{-3} Ω^{-1} and 32.7 x 10^{-3} Ω^{-1}, respectively, then reduce slightly for T_H = 500°C. The range of values of Φ reported here are similar to those of In_2O_3:Mo films with a maximum mobility ~ 25 $cm^2\ V^{-1}\ s^{-1}$ and higher resistivity values reported elsewhere [259].

6.2.6 Nature of Mo impurities in In_2O_3

Since the temperature variation caused more significant changes in the In_2O_3:Mo mobility, compared to pressure variation, the films in the former series were analysed using XPS. Knowledge of the atomic composition as well as the chemical species of Mo present in the films was expected to clarify the observed opto-electronic properties.

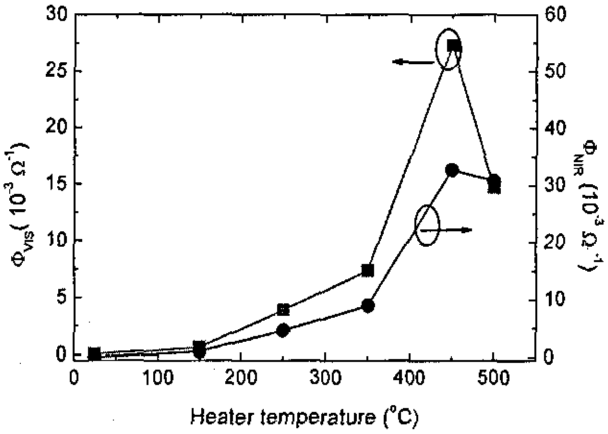

Figure 6.14. Average figure of merit (Φ) over 400 – 800 nm (squares) and 800 – 1200 nm (circles) of In_2O_3:Mo thin films as a function of heater temperature. Lines are to guide the eye.

The survey spectrum of the In_2O_3:Mo film prepared at 500°C is shown in Figure 6.15 and since it is similar to all the other films, they are omitted here. The wide scan spectra indicates the presence of indium (In 3d), molybdenum (Mo 3d) and oxygen (O 1s) as expected. Also, a significant amount of carbon (C1s), as a result of surface contamination by exposure to the environment during the interval of film growth and XPS analysis.

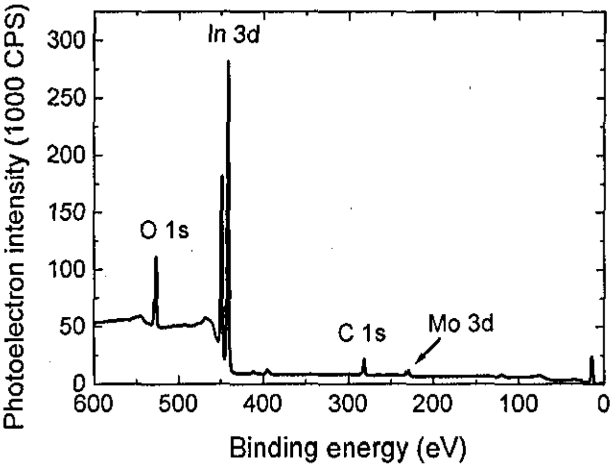

Figure 6.15. Typical XPS survey spectrum of an In_2O_3:Mo film.

Figure 6.16 shows higher resolution spectra of the O1s, In 3d and Mo 3d peaks for the IMO thin films prepared with T_H varied from 25°C to 500°C.

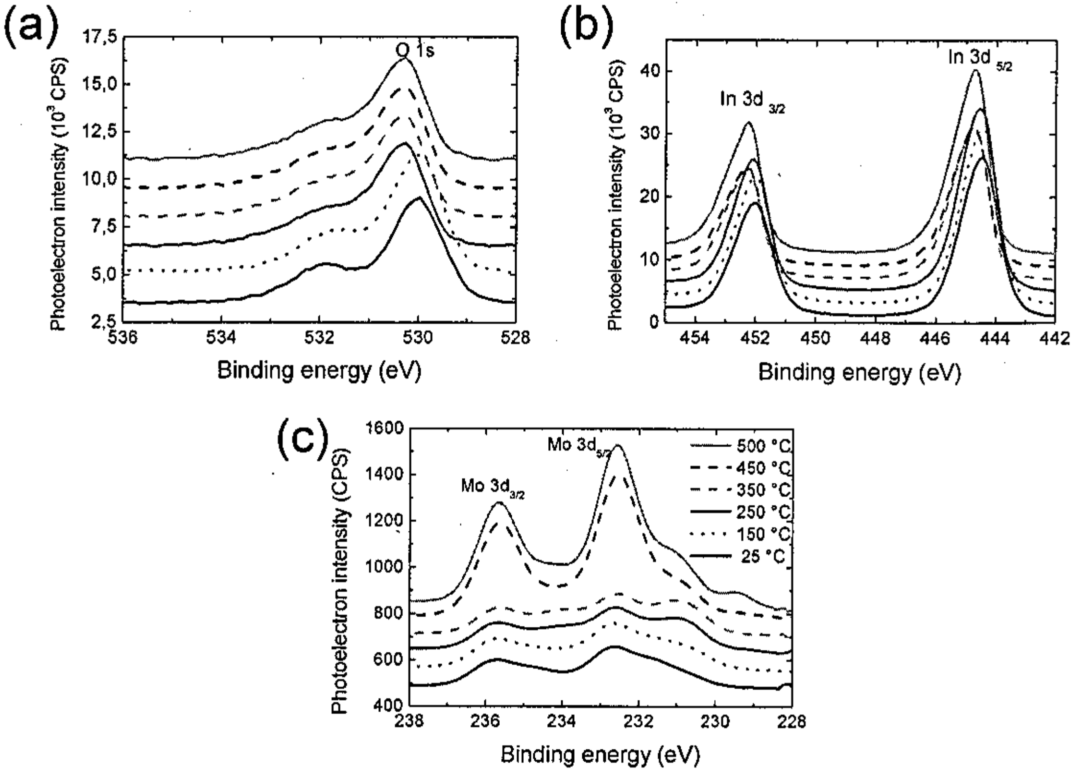

Figure 6.16. XPS spectra in the In 3d region (upper) and the O 1s region (lower) for IMO thin films prepared with different heater temperature.

The $3d_{5/2}$ peak positions for In metal and In_2O_3 are quite close at 443.8 eV and 444.4eV, respectively [158]. However, a slight shift of the In3d peaks towards higher binding energy was detected in all the films indicating that indium is exclusively present in the oxide state. The O1s spectra exhibit a peak about 530 eV which corresponds to oxides i.e. In_2O_3 (529.8 eV) [267] and MoO_3 (530.6 eV) [158]. The slight shift of the O 1s peak towards higher energies with increasing heater temperature indicates an increase in the MoO_3 content of the films. There is a shoulder on the high energy side of the O1s peaking around 531.7±0.3 eV which broadens as T_H increases. In the case of In_2O_3: Sn, this peak has been assigned to O^{2-} species in oxygen deficient regions [170], oxygen in amorphous In_2O_3 [268], or oxygen species of hydroxyl groups or water [268, 269] and so could also apply for In_2O_3:Mo. Other possible species with peaks close to 531.7 ± 0.1 eV include $Mo(OH)_X(Mo)$, $In(OH)_3$, $In(OH)_3 . nH_2O$ and molybdenum oxide complexes such as Mo_4O_{11} [267].

The Mo3d spectra of all the films could be resolved into several peaks indicating that the molybdenum exists in the elemental form, in the oxidation states of +6 and +4 as well as an intermediate oxidation state $+4 < x <+6$ [158, 267]. In Figure 6.17, only the resolved Mo 3d spectra for IMO films prepared without intentional substrate heating and with heating to 500°C are shown, for clarity. The concentration of the different Mo species could then be determined from the intensities of the peak areas and the instrument dependent factors (see Chapter 3).

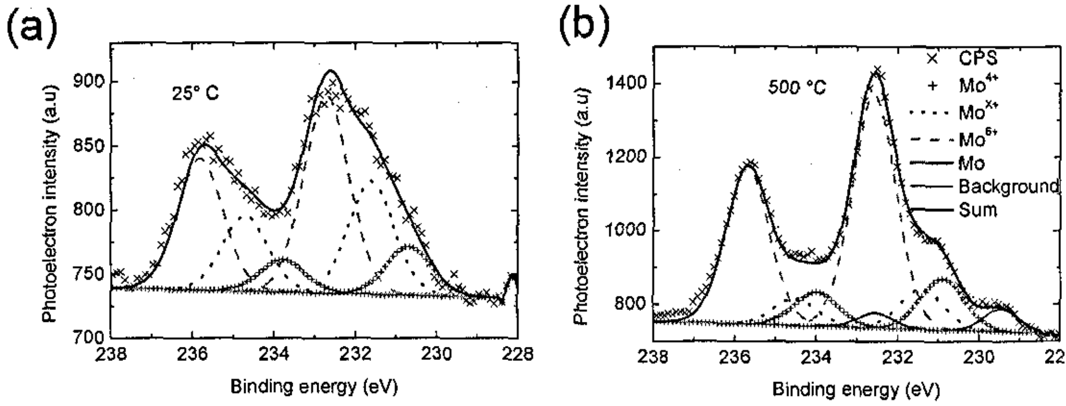

Figure 6.17. Mo 3d spectra for In_2O_3:Mo films prepared without intentional heating (25 °C) and with a heater temperature of 500 °C.

Figure 6.18 shows the evolution of the oxidation state of molybdenum in the IMO films as the heater temperature during deposition is raised. For all films, the Mo^{6+} state is the most prevalent while the metallic Mo content is less than 5%. However, as T_H is increased from 25 – 250 °C, both the Mo^{6+} and Mo^{X+} contents decrease whilst the Mo^{4+} state increases.

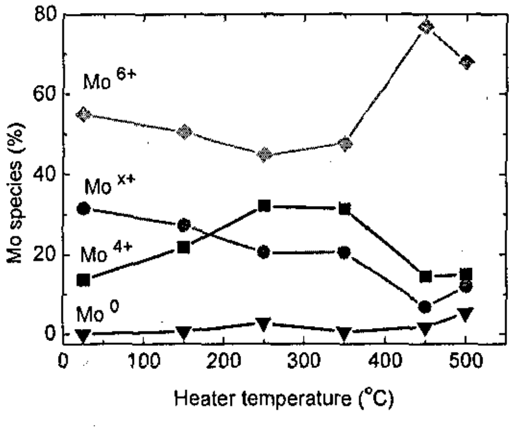

Figure 6.18. Evolution of the molybdenum species in IMO thin films prepared with different heater temperature. Lines are to guide the eye.

From 250- 450 °C, the Mo^{6+} content increases whilst the Mo^{4+} and Mo^{X+} content reduces. At 500 °C, the Mo^{6+} reduces slightly because of a slight increase in metallic molybdenum and Mo^{X+}.

Though for In_2O_3:Mo films, a reduction of the (222) XRD peak intensity relative to that of the (400) reflection, coincides with an increase in mobility, the correlation is not very strong as also reported for other studies e.g. [264]. Therefore, other factors such as defects introduced by the molybdenum dopant may have a more significant influence on the mobility of the In_2O_3:Mo films. The doping efficiency η_D of the donor impurity indicates whether it also contributes to the creation of both charged and uncharged defects. For this reason, the doping efficiency η_D due to Mo impurities was estimated using the following formula [270]

$$\eta_D = \frac{100 \times N \cdot A}{1.2(\rho_m \cdot a \cdot N_A)} \qquad 6.2$$

Where N is the charge carrier (electron) density in cm^{-3}, A is the atomic weight of In_2O_3 (= 277.63 g), ρ_m is the mass density of In_2O_3, a is the Mo:In atomic ratio, and N_A is Avogadro's number. The factor 1.2 is a product of the atomic ratio of indium in an ideal In_2O_3 unit cell containing 80 atoms with a stoichiometric oxygen content (= 0.4) and the maximum number of electrons each molybdenum atom can donate (= 3). Also, all the Mo atoms are assumed to reside at In sites in the In_2O_3 lattice without changing the lattice parameter and the contribution of oxygen vacancies to the charge carrier density is neglected. Table 6.7 lists the atomic ratios of molybdenum to indium, oxygen to metal and the Mo doping efficiency in the In_2O_3:Mo films prepared at different heater temperatures. The dopant ratio (Mo:In) of the IMO films increased with heater temperature but remained less than that of the target for all the films possibly because of preferential sputtering. The doping efficiency corresponds to a donation of less than 1 electron per Mo atom for all the films, but generally increases with heater temperature (with the exception of the film prepared at 150°C). For the films prepared with $T_H \leq 250$°C, it is likely that a significant portion of the carriers is contributed by Mo^{4+} and not Mo^{6+} as suggested in another study of In_2O_3:Mo films corresponding to maximum $N \sim 2 \times 10^{20}$ cm^{-3} and $\mu \sim 44$ cm $V^{-1}s^{-1}$ [258].

Table 6.7. Relative atomic composition and doping efficiency η_D of IMO thin films prepared with different heater temperature.

Heater temperature (°C)	Mo:In (at.%)	O: metal (at.%)†	η_D
25	2.44	146.1	0.14
150	2.95	146.6	0.07
250	3.40	135.9	0.18
350	3.24	145.4	0.28
450	8.32	147.5	0.29
500	8.17	147.5	0.29
Target§	14.82	130.6	n/a
In_2O_3 #	0	150	n/a

† Metal refers to In only or to (In+Mo).

§ The target compositions were calculated from values quoted by the supplier i.e. In_2O_3:Mo (98:2 wt.%).

The In_2O_3 composition is a theoretical calculation from the chemical formula.

However, since η_D, N and μ increase noticeably when the heater temperature is raised above 250°C, the contribution of the Mo^{6+} species to the charge transport system becomes dominant since the oxygen content of the films does not vary significantly. Additionally, N increases as expected, from theory, since the Mo^{6+} content exceeds the sum of the remaining Mo species in the films in agreement with groups [87]. Further, an analogy with In_2O_3:Sn films where a strong <111> texture relative to the <100> texture accommodates more interstitial oxygen which deactivate the tin dopant by forming neutral oxide complexes [186], is observed. Since the Mo^{X+} species in the In_2O_3:Mo films presented here reduced in favour of the Mo^{4+} and Mo^{6+} species when the <100> texture increased relative to the <111> texture, it can be concluded that the Mo^{X+} species suppressed both N and μ for films prepared at low temperature. These Mo^{X+} species are associated with hydroxyls and other complex oxides, such as Mo_4O_{11} [267] which may exist as neutral impurities in the film and thus reduce the mobility by scattering as has also been reported for In_2O_3:Sn films [34, 271]. Nevertheless, since the dopant efficiency in all the films was lower than 100% some of the charge carriers could be attributed to oxygen vacancies. Though the as-deposited IMO films were slightly more oxidized than target as a result of oxygen addition during the sputtering process, they were still oxygen deficient compared to pure In_2O_3.

To understand more about the activation mechanism of Mo in the films, the influence of post deposition heat treatment in different ambient conditions, on IMO films grown without intentional substrate heating, was studied by XPS analysis. Figure 6.19 shows the O1s, In 3d and Mo 3d XPS spectra of the IMO thin films after heat treatment in different conditions.

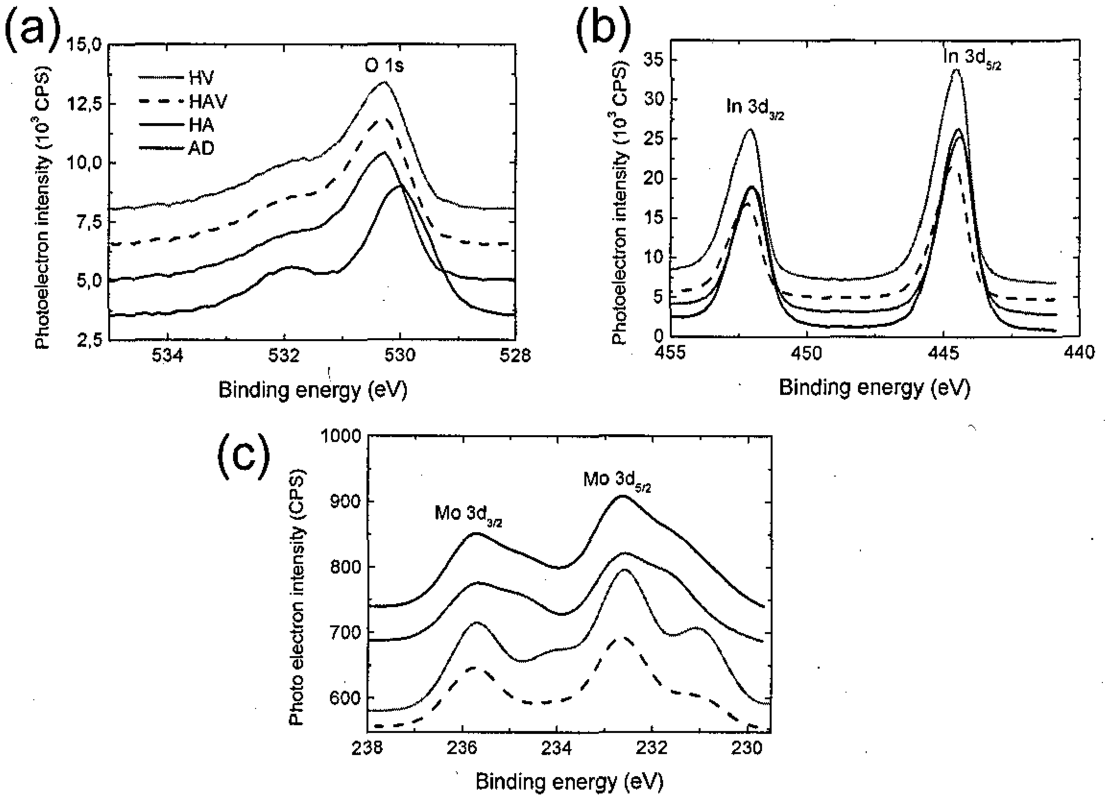

Figure 6.19. XPS spectra in the In 3d region (upper) and the O 1s region (lower) for IMO thin films after different heat treatments i.e. in vacuum *HV*, in air *HA* and in air then vacuum *HAV*. The spectra for an as-deposited IMO film *AD* are included for comparison.

The results are similar to those reported in the previous section whereby the shoulder on the high energy side of the O1s peak around 532 eV may indicate the existence of hydroxides and/or oxy-hydroxides of molybdenum and indium. The slight shift of the main O 1s peak towards higher energies after heating indicates an increase in the MoO_3 content of the films compared to the as-deposited film. The In3d peaks of the films shifted slightly towards higher binding energy after heating in vacuum indicating an increase in the oxidation state. Also, indium exists entirely in the oxide state, while molybdenum exists in several chemical states from the metallic state right through to a oxidation state of +6 as before.

Figure 6.20 shows the evolution of the oxidation state of molybdenum in the IMO films after heat treatment in different ambient conditions. Heating in vacuum increases Mo^{4+} and to a lesser extent, the metallic molybdenum whilst the Mo^{X+} content reduces. Heating in air increases the Mo^{X+} content while the Mo^{4+} content is decreased. Heating the as-deposited In_2O_3:Mo in air or vacuum appears to have little influence on the Mo^{6+} content. However, subsequently heating the film that had been heated in air, under vacuum, increases the Mo^{6+} content significantly. Since this increase in Mo^{6+} occurred with a less intense increase in Mo^{4+}, it is possible that heating in vacuum dissociated the hydroxyl and sub-oxide bonds associated with the Mo^{x+} species.

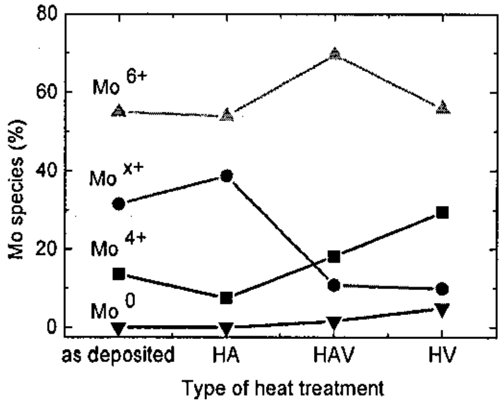

Figure 6.20. Evolution of the molybdenum species in IMO thin films after different heat treatments i.e. in vacuum *HV*, in air *HA* and in air then vacuum *HAV*. The species for an as-deposited IMO film *AD* are included for comparison. Lines are to guide the eye.

Table 6.8 lists the relative composition of the molybdenum dopant and the oxygen in the IMO films, η_D for molybdenum, as well as the related electrical properties of the IMO films after different heat treatments.

As mentioned earlier the electrical properties of the IMO thin film heated in air, could not be measured and are thus are not shown. Both N and μ of the IMO thin films could be increased by heating in vacuum. Heating in air caused a slight reduction in the Mo:In ratio but a considerable increase of about 18 at.% absolute in the O:metal ratio. Subsequent heating in vacuum did not significantly change the Mo:In ratio though the O:metal ratio was reduced by about 7 at. % in absolute terms though the film remained over oxidised. Heating the as-deposited In_2O_3:Mo thin film in vacuum decreased the O:metal ratio by 22 at.% absolute and increased the Mo:In by 75% relative.

Table 6.8. Relative atomic composition of molybdenum and oxygen, the molybdenum doping efficiency η_D and electrical properties of IMO thin films after different heat treatments.

Type	Treatment	Mo:In (at.%)	O: metal (at.%)†	η_D	N (10^{19} cm^{-3})	μ (cm^2 V^{-1}s^{-1})	ρ (10^{-3} Ωcm)
AD	as deposited	2.44	146.1	0.14	6.2	9.0	11.7
HA	heated	2.41	164.1	-	-	-	-
HAV	heated	2.39	157.2	0.11	4.9	24.8	5.1
HV	heated	4.27	123.8	0.26	20.5	29.3	1.0
Target §	n/a	14.82	130.6				
In_2O_3 #	n/a	0	150				

† Metal refers to In only or to (In+Mo).

§ The target compositions were calculated from the wt% quoted by the supplier i.e. In_2O_3:Mo (98:2 wt.%).

The In_2O_3 composition is a theoretical calculation from the chemical formula.

Such a large increase in the Mo:In ratio is probably caused by reduction of In_2O_3 to indium (melting point ~ 156.6 °C) which desorbed from the film. Heating the In_2O_3 film in air de-activated the dopant but subsequent heating in vacuum recovered the dopant efficiency to about 80 % of the original value and judging by the high oxygen content of this film, a large proportion of the charge carriers may be attributed to doping by Mo^{6+} (see Figure 6.20). A relatively higher doping efficiency of 0.26 was calculated for the IMO film heated in vacuum only, indicating that N arises from contributions from both the Mo^{6+} and Mo^{4+} species as well as oxygen vacancies. The heat treatment of the TCO layer in vacuum, desorbs the loosely bound oxygen at the surface creating vacancies and oxygen residing along grain boundaries (if the TCO is slightly porous) thus lowering the depletion barrier along the grain boundaries, increasing the charge carrier density while improving the electron mobility, respectively. This "conduction recovery" phenomenon is used for gas sensor application and has been reported for $CdIn_2O_4$ [243], SnO_2 films [39] and In_2O_3 [40].

Though the heat treatment in vacuum increased the mobility of the IMO thin films, the maximum mobility was limited to values around 25-30 cm² V^{-1} s^{-1}. This is still much lower than that of the In_2O_3:Mo films prepared with heater temperatures of 350°C. Reasons for this would be the excess oxygen content of the film heated in air causing increased scattering at grain boundaries and at the other extreme, the severe oxygen deficiency of the In_2O_3:Mo film heated in vacuum increasing the scattering by ionised impurities. Larger improvements in μ were not achieved since the post deposition heat treatment conditions were not optimised to ensure complete removal of both crystalline and impurity defects.

6.2.7 Conclusions on In_2O_3:Mo film growth and analysis

The influence of sputter pressure and heater temperature on In_2O_3:Mo films prepared by pulsed dc magnetron sputtering has been investigated. Decreasing the sputter pressure increases both the sputtering and deposition rates which results in either an excess of metal ions or oxygen vacancies hence N is high and thus the resistivity and transmission are low. The sputter pressure appears to have a minimal influence on the mobility except for the In_2O_3:Mo thin film grown at 0.13 Pa whose surface is blistered indicating damage from re-sputtering. On the other hand, increasing the heater – and thus substrate temperature reduced the resistivity. XPS analysis showed that low mobility occurs when Mo in the films exists as Mo $^{X+}$ in relatively high concentrations (20 % or more). Though the molybdenum dopant is active in both the 4+ and 6+ states, high mobility above 60 $cm^2\ V^{-1}\ s^{-1}$ under degeneracy, is only possible when the Mo^{4+} species are substantially less than the Mo^{6+} species. The minimum resistivity achieved was $2.0 \times 10^{-4}\ \Omega$ cm corresponding to an electron density of $4.3 \times 10^{20}\ cm^{-3}$ and a mobility of 73 $cm^2\ V^{-1}s^{-1}$. All films had a wide window of transparency stretching from 300 nm to 1800 nm and the plasma wavelength was greater than 1800 nm in agreement with other reports [87, 106, 220, 221]. The highest optical transparency could be achieved at intermediate temperatures where optimal oxidisation of the metal minimises the presence of both absorbing sub-oxides and unreacted molybdenum. Only two films, which also have the highest values of mobility (71 and 73 $cm^2\ V^{-1}s^{-1}$) in this study, have a figure of merit above $10 \times 10^{-3}\ \Omega^{-1}$ ($\rho_s \leq 10\ \Omega/\square$ and $T(\lambda) \geq 80\%$) and therefore, further optimisation is required.

6.3 High mobility TCO contacts for solar cells

High mobility TCO materials are desirable where a high transparency > 80% is required over a wide spectral range (400 – 1200 nm) such as in micro-crystalline silicon, CIGS and multi-junction solar cells. Therefore, the work described in this section was aimed at investigating the effect of using HMTCO materials as contacts in the top or middle solar cell in a triple junction solar cell.

6.3.1 Single junction solar cells

HMTCO layers can be used as front contacts for single junction solar cells in the superstrate configuration because the highest possible process temperatures can be used to optimise the resistivity and transparency. A record efficiency of 16.5% for CdTe solar cells has been achieved using $CdSnO_4$ coated glass in the superstrate configuration [46]. Also, an improved light trapping structure for nano-crystalline silicon solar cells using In_2O_3:Mo layers with a textured ZnO layer can increase the QE for wavelengths exceeding 900 nm compared to cells using ZnO:Al [272].

The high optical transmission from 300 nm to values over 1300 nm, implies that HMTCO films could also be suitable front contacts for CIGS solar cells in the substrate configuration. Various In_2O_3:Mo depositions were run using similar deposition parameters to those listed in Table 6.5, with the heater temperature ranging from 25 °C to 200 °C. Heating of CIGS solar cells to temperatures above 200°C should be avoided to prevent interdiffusion of selenium and sulphur across the CdS|CIGS interface which causes a reduction in the open circuit voltage and thus reduces the solar cell efficiency [56]. The resistivity reduced from ~ 10^{-2} Ω cm^2 to ~10^{-3} Ω cm^2 with increasing heater temperature since both N and μ increased. Figure 6.21 shows representative T and R spectra of selected In_2O_3:Mo films prepared with $T_H \leq 100$ °C on soda lime glass, and it can be seen that the plasma edge extends beyond 1200 nm as required for CIGS solar cells. One should note that the properties of the In_2O_3:Mo films prepared on a CIGS|i-ZnO stack may differ from those grown on glass because of differences in the morphology and chemical nature of the surfaces to be coated even though similar deposition parameters are used.

In order to test the low temperature In_2O_3:Mo films, identical Mo|CIGS|iZnO stacks were prepared on 1.1 mm thick soda lime glass at ETH Zürich, Switzerland as described in Chapter 3. Energy dispersive X-Ray analysis of the CIGS stacks revealed a Ga:(Ga+In) ratio of 0.32. A selection of low temperature In_2O_3:Mo layers were then sputtered over the absorber stacks at Loughborough University. The stacks were sent back to Zürich where, the cells were scribed to an area ~ 0.6 cm^2 and metal grids were applied prior to J-V measurements under AM 1.5 global illumination.

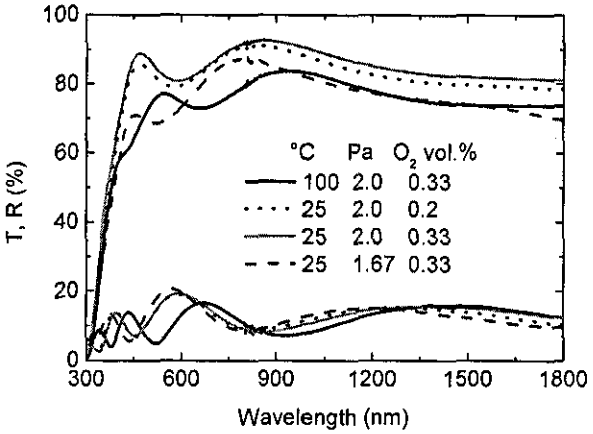

Figure 6.21. Transmission and reflection spectra of IMO thin films on glass. The legend gives the heater temperature, the sputter pressure in Pa and the oxygen content of the sputter gas (vol.%). Film thickness was in the range of 200 – 250 nm.

The photo conversion efficiency *η*, reduced as the heater temperature, during the In_2O_3:Mo deposition, increased and the best cells were obtained for the In_2O_3:Mo films grown with $T_H \leq 100°C$. Table 6.9 lists the device parameters of representative CIGS cells made using In_2O_3:Mo films grown without intentional substrate heating (IMO25) and with a heater temperature of 100°C (IMO100).

Table 6.9. Device parameters of CIGS solar cells using In_2O_3:Mo front contacts.

Front TCO	Cell	X†	Area (mm²)	η (%)	Jsc (mA cm $^{-2}$)	FF(%)	Voc (mV)	Rp (Ω cm²)	Rs (Ω cm²)
IMO25	A	0.320	551	11.1	26.5	66.1	636	1568	0.9
IMO100	B	0.320	578	10.0	29.0	57.6	594	763	1.2

† X represents the atomic ratio [Ga]/[Ga+In]

Figure 6.22 shows the EQE spectra and J-V characteristics of cells A and B. According to Figure 6.21, the IMO25 (2 Pa and 0.2 vol% O_2) film is more transparent than IMO100 ((2 Pa and 0.3 vol% O_2) but being more resistive, causes larger current losses in cell A than in cell B. In contrast, the efficiency of cell B is low because of a relatively low voltage and fill factor which indicates that heating during the deposition of the In_2O_3:Mo front contact degraded the CdS|CIGS interface reducing the shunt resistance. A similar value of efficiency of 10.7% was reported for CIGS solar cells using In_2O_3:Ti as front contacts in the substrate configuration, (glass|Mo|CIGS|ZnO|ITiO) [273].

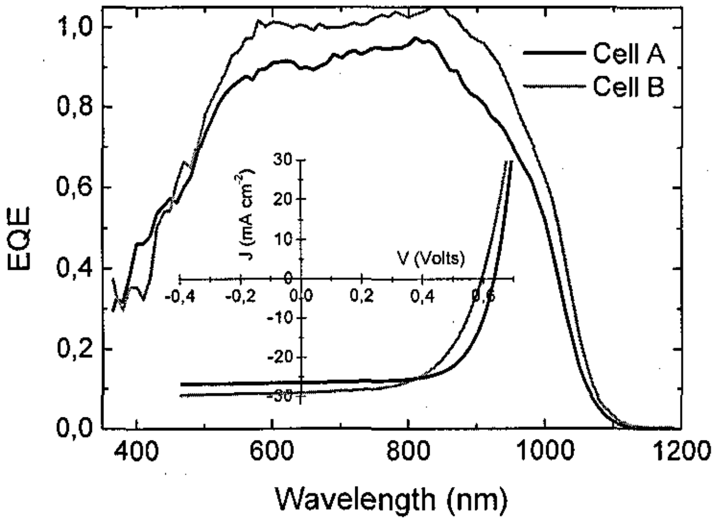

Figure 6.22. EQE of CIGS cells using In_2O_3:Mo films prepared at different temperatures of 25°C and 100 °C for cell A and B, respectively. The J-V curves of the respective cells are included as an inset.

6.3.2 Bifacial solar cells

The rear side illumination of bifacial CIGS thin film solar cells can be improved by using ITiO coated substrates because of reduced NIR light absorption [274]. The benefits of using HMTCO contacts for CdTe based bifacial solar cells are illustrated in Figure 6.23 which shows the absorption *A* spectra of different TCO|CdTe stacks and one complete TCO|CdS|CdTe|TCO stack under (a) front- and (b) rear side illumination. The visible wavelength absorption under illumination from either side, is less than 100% because of reflection losses. Also over the NIR wavelength range up to 1500 nm, the absorption decreases when the ITO front contact of the CdS|CdTe treated stack is replaced by ITiO. However when an ITO back contact is added to complete the cell on the ITiO front contact, the NIR absorption increases significantly under illumination from either side. Under front side illumination, the high absorption and/or reflection by either the front TCO and/or the ITO back contact cause significant optical losses over 1100 nm to 1500 nm. For visible light, under rear side illumination, higher reflection losses by CdTe in the complete cell are dominant.

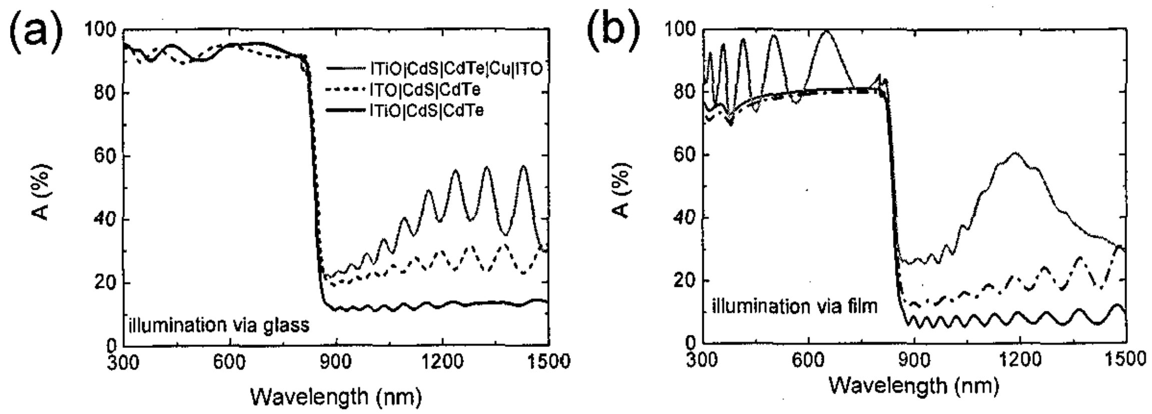

Figure 6.23. Absorption A spectra for(a) front and (b) rear side illumination of different TCO|CdS|CdTe stacks and a complete ITiO|CdS|CdTe|ITO solar cell. The CdS thickness is 300nm while the CdTe thickness is 3 μm.

Again, here it is clear that using an HMTCO as the back contact could substantially reduce the NIR optical losses. However, for single CIGS solar cells junction and all types of bifacial solar cells, a means of preparing the HMTCO layer at low temperature with reasonably low resistivity must be developed to realise their full potential.

6.3.3 Multi-junction solar cells

The top and intermediate solar cells in a multi-junction configuration also require a transparent conducting contact at both the front and back of the cell to ensure efficient transmission of unused light to the underlying lower band gap solar cell. CdTe with an optical band gap ~ 1.45 eV and amorphous silicon are examples of solid state absorber materials suitable for upper junctions in multi-junction solar cells. Also, dye sensitised solar cells whose spectral response can be adjusted by varying the TiO_2 nano-particle size or the sensitising dye, are promising candidates for the top junction in a multi-junction solar cells. Current matching can then be achieved by using solar cells with thinner absorbers or smaller area than the bottom cell to transmit some of the lower energy photons to the bottom cell. Alternatively, the transmission of unused NIR photons through the upper absorber may be employed as it is simpler to realise in terms of current collection and solar cell fabrication, and so was considered for this work.

CdTe solar cells with a significant efficiency of 13.9% have been developed on Cd_2SnO_4 coated glass (μ ~ 53.2 cm^2 V^{-1} s^{-1}, resistivity ρ~ 1.8 x 10^{-4} Ω cm) while maintaining a NIR transparency of 50% for the entire device [275]. While a high efficiency of a top solar cell is desirable, its full impact on the entire multi-junction solar cell efficiency cannot be realised unless the NIR transparency is improved to ensure adequate current matching with the bottom cells [197]. Figure 6.24 shows the transmission spectra of CdTe solar cells, at various stages of completion, with an ITiO front contact and the *T* spectrum of a |CdS|CdTe stack on an ITO front contact, for comparison. The NIR wavelength transmission of the ITiO|CdS|CdTe is much higher than that of the ITO|CdS|CdTe. When the ITO back contact is added to complete the CdTe solar cell on the ITiO front contact, the NIR transmission drops steadily with increasing wavelength.

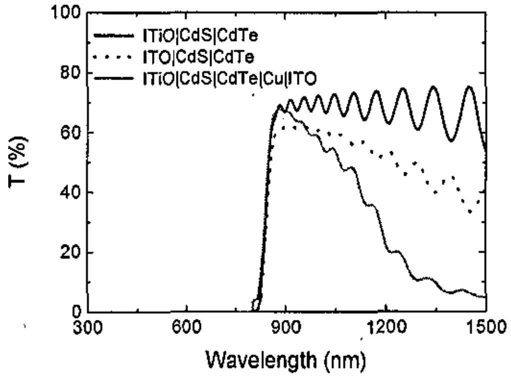

Figure 6.24. Transmission *T* spectra of a complete and various incomplete CdTe solar cells on ITiO and one additional stack, consisting of ITO|CdS|CdTe, for comparison. The CdS thickness is 300 nm while the CdTe thickness is 3 μm.

Figure 6.25 (a) shows *T(λ)* and *A (λ)* spectra of CdS|CdTe stacks on IMO, ITO and FTO coated soda lime glass under front side illumination (via the glass).

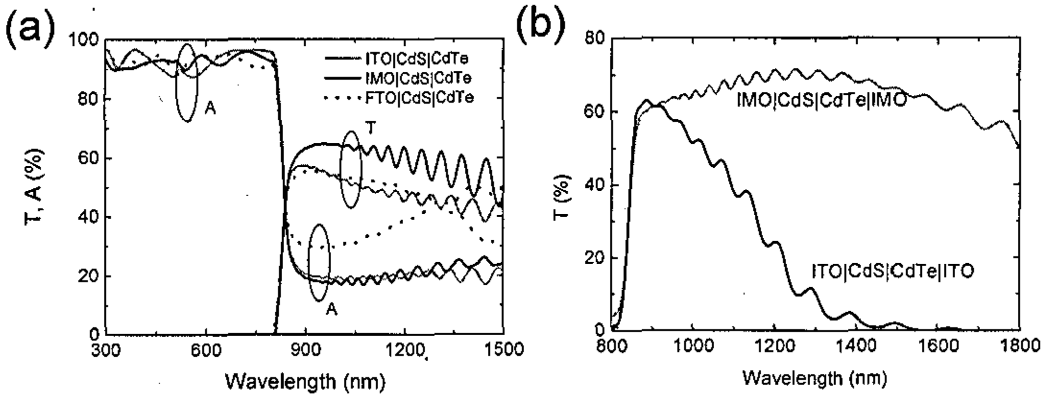

Figure 6.25. (a) Transmission *T* and absorption *A* spectra of TCO|CdS|CdTe stacks and (b) transmission spectra of TCO|CdS|CdTe|TCO stacks under illumination via the substrate. The

CdS thickness is 500 nm for all samples while the CdTe thickness is 2.8 μm, 4.3 μm, and 4.5 μm for FTO, ITO and IMO coated soda lime glass respectively.

The CdS thickness is 500 nm for all samples while the CdTe thickness is 2.8 μm, 4.3 μm, and 4.5 μm for FTO, ITO and IMO coated substrates, respectively. The stack on the IMO substrate has a total NIR transmission which exceeds that of the stacks on ITO and FTO by more than 10% absolute. The absorption in the visible wavelength range is less than 100% because of reflection losses of about 10% for all the TCO coated substrates. Over the NIR wavelength range, the stack absorption increases with that of the corresponding bare TCO thin film (see Figure 6.2b). The NIR transmission of the stacks on ITO and FTO is limited by the high reflection and/or absorption, respectively of the related TCO materials over the same wavelength range. The relatively high NIR transmission of the stack on the IMO substrate is caused by a comparatively lower absorption and reflection in this wavelength region. Figure 6.25 (b) shows the NIR transmission spectra of identical CdTe solar cells using all IMO or all ITO contacts. There is a significant gain in NIR transmission when using IMO contacts for a CdTe solar cell that would act as either a top or an intermediate absorber in a multi-junction solar cell. However, such a stack requires that the rear side TCO which has to be prepared at low temperatures over the absorber layers, is sufficiently conductive to prevent losses in the total cell voltage and fill factor which would limit the overall photo-conversion cell efficiency. High mobility TCO films have also been used to improve the total current of a tandem solar cell consisting of Ag(In,Ga)Se_2 and Cu(In,Ga)Se_2 junctions [276].

On the other hand, the TCO layers applied at both the front and rear of a dye sensitised solar cell, can be prepared using high process temperatures without the danger of destroying the absorber layers. Taking advantage of this fact, semi transparent dye sensitised solar cells were prepared using ITiO coated glass. While the NIR transparency increased to 60% compared to DS solar cell devices using FTO coated glass, the efficiency was somewhat lower i.e. 5.8% compared to 8.2%, respectively. The reason for the lower efficiency was the different growth conditions of the TiO_2 interfacial layer on the smoother ITiO films (compared to FTO) and on the elevated resistivity of the ITiO after a sintering step at 450°C in air required to prepare the porous TiO_2 absorber. A slight improvement in the DS solar cell efficiency to 6.8% could be achieved by adjusting the growth conditions of the dense TiO_2 interfacial layer and by heating the entire stack in vacuum after the sintering step in air.

6.3.4 Discussion

Several factors contribute to the NIR transmission losses of the CdS|CdTe stacks under illumination from either side namely, free carrier absorption, various scattering processes and reflection at interfaces. However, the results presented show that at least in the NIR wavelength range 800 nm to 1300 nm, the TCO material used either as a front or rear side contact can contribute significantly to these losses. Therefore, the development of transparent conducting oxides where both the reflection and absorption in the NIR wavelength region are minimal is desirable to improve the performance of multi-junction- and bifacial solar cells. In order to maximise the benefits of using HMTCO materials in both multi-junction and bifacial solar cells, several issues still remain to be investigated and addressed, namely:

- the temperature compatibility of HMTCO films during deposition of subsequent layers in the superstrate (absorber layers deposited on the TCO) configuration,
- the influence of the HMTCO layer on the growth mechanism of the absorber layers in the superstrate configuration,
- the development of an HMTCO back contact with good electrical contact with the absorber materials,
- the need to develop a low temperature process for growing conductive HMTCO films,
- and in the long term, a HMTCO based on cheaper materials than indium.

6.4 Challenges and prospects

Coutts et al. [277] identified key areas of basic research required to develop improved TCO materials for industrial production. While the HMTCO materials reviewed in this work can be prepared with mobility $\mu > 62.5\ \text{cm}^2\ \text{V}^{-1}\ \text{s}^{-1}$ using sputtering and MOCVD, which are mature deposition techniques for industrial fabrication, some challenges remain.

6.4.1 Low mobility in TCO films grown with low processing temperature

It is desirable to prepare thin films at low temperatures to coat plastic substrates or pre-deposited layers of an optoelectronic device with minimal damage, to reduce the energy input into the manufacturing process and to avoid diffusion of undesirable impurities from the substrate into the TCO films. All the low resistivity TCO materials with μ > 62.5 cm^2 V^{-1} s^{-1} in Table 6.3 and 1.4 were prepared with deposition temperatures of at least 300°C. The observed suppression of mobility to values below 62.5 cm $V^{-1}s^{-1}$ at low process temperature > 300°C in Figure 6.9, has also been observed by other groups for In_2O_3:Mo [198, 220, 224, 226, 258], In_2O_3:Ti [226], In_2O_3:Zr and In_2O_3:Wo [229]. Table 6.10 lists the electrical and optical characteristics of IMO, IWO, ITiO thin films prepared without intentional substrate heating.

Table 6.10. A survey of transition element doped In_2O_3 thin films prepared without intentional substrate heating.

N (10^{20} cm^{-3})	μ (cm^2/ Vs)	ρ ($10^{-4}\Omega\cdot cm$)	d (nm)	T_{VIS} (%)	Target material (wt%)	Method	Ref
0.6	9.0	112	383	75	In_2O_3:Mo 98: 2)	PDCMS	This work
5.5	22	6.1	~140	80	In_2O_3:MoO_3 (95: 5)	HDPE	[260]
14.3	14.6	3.6	~140	80	In_2O_3:MoO_3 (99: 1)	HDPE	[261]
5.2	20.2	5.9	~ 130	80	In:Mo (98:2)	Reactive DCMS	[259]
5.2	20.2	5.9	~120	80	"	Reactive DCMS	[262]
1.08	13.6	42.0	300	75	In_2O_3:Mo 95: 5)	RF MS	[278]
0.16	19.5	195	~100	80	"	"	[264]
4.16	5.7	26.5	305	18	"	"	[264]
15	10	5.0	500	-	In_2O_3:TiO_2*	DCMS	[226]
0.92	21	3.2	~400	-	In_2O_3:WO_3*	DCMS	[229]

N - majority charge carrier density; μ- majority charge carrier mobility; ρ- resistivity; d – thickness; DCMS - DC magnetron sputtering; HDPE – high density plasma evaporation; RFMS - RF magnetron sputtering.

*target composition not indicated.

Regardless of the deposition technique, the mobility of the impurity doped indium oxide films does not exceed 25 cm^2 V^{-1} s^{-1} which is slightly less than that for degenerate films of ITO [279, 280] and ZnO:Al [200, 281] and intrinsic In_2O_3 [257, 282], all deposited on unheated substrates. The cause for low μ for films prepared at low temperatures is not yet fully understood. This is a major challenge that precludes the growth of these high mobility films onto heat sensitive substrates.

An interesting development is the lower but still significant mobility ($50 \leq \mu \geq 60$ cm^{2}V^{-1}s^{-1}) that can be obtained in degenerate amorphous Zn-doped In_2O_3 (IZO) films prepared without intentional substrate heating [90, 283]. These films have a relatively high optical transmission in the NIR wavelength region and thus may be an alternative to high mobility TCO materials for coating heat sensitive substrates. Also, since oxygen vacancies contribute significantly to the conductivity of the IZO thin films, Zn^{2+} substitution on In^{3+} sites does not decrease the carrier density of In_2O_3 films and thus a degenerate carrier density is maintained [90, 282]. Further, Zn may increase the density of oxygen vacancies by reducing some of the In-O bonds [282] or by passivating defects caused by interstitial oxygen. The above reports indicate that the electronic band structure rather than crystalline structure determines the maximum attainable high mobility in TCO materials.

6.4.2 Inadequate characterisation and analysis methods

One of the major problems in studying the limitations of mobility in TCO films is the difficulty in obtaining sufficiently accurate values of the effective mass and relaxation times which would be used to determine the dominant scattering mechanisms. Data extracted from optical analysis using Drude's model and the Burstein Moss shift has to be treated with caution because of the difficulties in measuring the film thickness to a high enough accuracy and assumptions that the conduction band is parabolic, respectively [21, 42]. However, though Hall measurements are widely used to analyse high mobility TCO materials, few are complemented with the experimental determination of the Seebeck and Nernst coefficients and thus the exact scattering mechanisms limiting the mobility can only be estimated or speculated. Young et al. [284] describe a four coefficient method used to measure the Hall, Seebeck and Nernst coefficients of TCO thin films that can be used to determine the charge carrier density, mobility, the effective electron mass, the scattering mechanisms and relaxation time but it is still not widely used.

Studies on the electronic transport mechanisms reported for HMTCO films so far seem to be empirical. Theoretical modelling using either computational chemistry or physics methods, is a useful tool for calculating and understanding the structure and properties of materials and may even predict hitherto unknown transparent conducting materials. Specifically, more insights into the influence of dopant chemistry, dopant concentration, and film structure on the charge carrier transport mechanisms would aid further increments in the conductivity of these high mobility TCO materials. Developments in electronic band structure calculations may also predict the material behaviour and can help to elucidate limitations to mobility and doping efficiency. For example, a combination of electronic structure calculations and Seebeck measurements have been used to determine an electron effective mass of Cd_2SnO_4 around 0.25 m_e [216, 248] which is higher than values of 0.08-0.11 m_e and 0.04 m_e, determined from the Burstein Moss shift in the 1970s by Nozik [285] and Haacke [286], respectively. Most of the reported theoretical electronic band structure calculations for HMTCO have focused on CdO which has a simpler crystalline structure (cubic) than In_2O_3 (bixbyite). More theoretical calculations of the electronic band structure and properties of In_2O_3, which is less hazardous than CdO and thus more technologically important, are needed to develop TCO materials with improved conductivity.

6.4.3 Lack of alternative low cost and environmentally benign materials

The high mobility with low resistivity ~ 10^{-4} Ω cm values described in the previous sections have only been observed in materials based on In_2O_3 which is rather costly and CdO which is potentially hazardous and may not be acceptable for environmental reasons. Efforts to dope cheaper and environmentally benign materials with transition elements have not yet resulted in a higher mobility e.g. ZnO doped with Zr [287], Ti [288], Mo [214], Ta doped SnO_2 [289] and Nb- doped TiO_2 [290]. Also, doping ZnO with hydrogen [291] gives a mobility of ~ 40 $cm^2\ V^{-1}s^{-1}$ which is comparable with values for Al doping and much less than the value of 130 $cm^2\ V^{-1}s^{-1}$ for H-doped In_2O_3 [213]. It is possible that the wurtzite structure of ZnO with tetrahedral coordination is less favourable for electron transport than the cubic structure of CdO and In_2O_3 both of which have an octahedral coordination [244]. In general, for the same dopant element e.g. tin, the mobility of the films increases going from ZnO to In_2O_3 to CdO as Sn inclusion in ZnO causes disorder in the octahedral causing short relaxation times despite the low effective electron mass [245]. Evidently, to achieve high mobility but cheap and non-hazardous TCO materials, alternative dopants or ternary compounds of ZnO, SnO_2 and possibly TiO_2 need to be developed, and alternative materials that may not necessarily be oxides should be investigated. Single walled carbon nano-tubes are an emerging p-type transparent conducting material that have low resistivity ~ 10^{-4} Ω cm with transparency > 80% over the near infra-red region [96]. Promising solar cell efficiencies have been achieved on CIGS [292] and on CdTe [293] using SWNT as transparent contacts. Improvements in SWNT for application in PV should be aimed at reducing the relatively high visible light absorption in films thicker than 100 nm [96, 292, 293].

6.4.4 Insignificant reductions in resistivity despite higher mobility

Lastly, despite the elevated values of mobility reported, the resistivity of the In_2O_3 and CdO thin films has remained similar to that of state of the art ITO thin films. A lower than expected dopant activation as well as an upper limit for carrier density above which the mobility begins to reduce have been reported for In_2O_3:Mo [106, 237, 258, 266], In_2O_3:W [228, 242], In_2O_3:Zr [232, 234], In_2O_3:Ti [225, 226] CdO:Sc [217, 218] and CdO:Y [218]. For the case of In_2O_3:Mo, it is possible that the reduced dopant activation efficiency of Mo is caused by interstitial oxygen forming neutral complexes with some of the Mo at specific sites as inferred by some authors [106] and as demonstrated by XPS measurements described earlier in this chapter. Examination of heavily W-doped In_2O_3 thin films by Energy-Filtered Transmission Electron Microscopy revealed segregation of tungsten at the grain boundaries where it is ineffective as a donor [242]. This implies that the transition element dopants limit the mobility through formation of neutral and impurity scattering centres in much the same way as observed for In_2O_3:Sn [34, 186]. Theoretical modelling and band structure calculations may be used to understand the limitations to the conductivity of HMTCO films and to predict other eligible dopants. However, for accurate and realistic results, the required calculation time as well as the hardware resources increase with the complexity of the host oxides (especially In_2O_3) and the (transition metal) dopant ions, making accurate theoretical calculations difficult.

6.5 Conclusions on high mobility TCO films

Several high mobility TCO materials based on In_2O_3 and CdO which combine low resistivity with a high visible and near infra red optical transmission, exist, and the highest mobilities attainable continue to be exceeded. These materials can be prepared using industrially mature deposition technologies such as sputtering and chemical vapour deposition without significant degradation of the opto-electronic properties. Several explanations have been given for the high mobility in specific In_2O_3 and CdO based materials but none wholly explain this phenomenon. Studies on In_2O_3:Mo films show that the conductivity is limited by neutral impurities which limit both the charge carrier density and mobility. The application of high mobility TCO layers in various types of thin film solar cells has demonstrated their potential to improve the efficiency of single junction, multi-junction and bifacial solar cells. However, additional aspects such as thermal stability, formation of suitable interfaces with solar cell absorbers and low temperature growth of low resistivity HMTCO films, need to be considered. For large scale production and regardless of the end use, high mobility TCO using alternative cheaper and less hazardous host cation elements, than indium and cadmium respectively, are being sought Additionally, despite the enhanced mobility of HMTCO materials, the achievement of resistivity below 10^{-4} Ω cm is still challenging. Therefore, in the short to medium term, new analysis techniques are required to learn more about underlying mechanisms in high mobility In_2O_3- and CdO- based TCO films. In the long term, both empirical and theoretical studies are crucial to discover hitherto unknown high mobility transparent conductors.

Chapter 7 Conclusions and outlook

Several issues related to the processing and materials properties of various TCO films suitable for solar cells have been tackled in this thesis. However, additional questions have been raised that need to be investigated outside the scope of this thesis as discussed below.

7.1 Conclusions

The influence of the deposition parameters on the optical and electrical properties as well as the thermal stability of the In_2O_3:Sn films grown on glass and polyimide substrates using High target utilisation sputtering (HiTUS) has been investigated. The deposition rate increased to a maximum of 40 nm min^{-1} when the power and discharge voltage where increased or when the sputter pressure was reduced. The HiTUS system layout allows one to vary the target voltage and thus the influence of the kinetic energy of the sputtered particles on the In_2O_3:Sn films could be indirectly investigated. The resistivity reduced with increasing discharge voltage values around 2.0 x 10^{-4} Ω cm as a result of an increase in both the carrier density and mobility while the NIR transmission reduced monotonically.

The crystallite size and surface roughness of the In_2O_3:Sn films increased with increasing substrate temperature while the film resistivity reduced. Unlike the In_2O_3:Sn films grown on glass, the films grown on polyimide were sensitive to the sputter pressure and had micro-cracks, visible to the un-aided eye, on the surface when deposited at low sputter pressure. The resistivity of In_2O_3:Sn films grown on polyimide increased by more than 100% when the pressure was set at 0.15 Pa instead of either 0.30 Pa or 0.45 Pa. Increasing the target current and thus the sputter power density, reduced the resistivity to a minimum value around 2.0 x 10^{-4} Ω cm for power densities above 1.6 Wcm^{-2}. The visible and near infrared light transmission increased with reducing power density indicating a decrease in carrier density as was corroborated by an accompanying shift of the band gap edge towards longer wavelengths.

Heat treatment in either air or vacuum was also used to investigate the thermal stability of the opto-electronic properties of the In_2O_3:Sn films. The resistivity of the In_2O_3:Sn films on glass was more stable to heating treatment in vacuum, but less stable to heating in air than the In_2O_3:Sn samples on polyimide. For In_2O_3:Sn films on glass, heating in air increased the transmission by up to 20% as a result of incorporation of excess oxygen which reduced the charge carrier density. Heat treatment in vacuum generally caused the film transmission to increase or reduce change by about 5%.

The ability to control the kinetic energy of sputtered particles while growing In_2O_3:Sn films is useful to vary the strain in the films for coatings on a substrates with varying coefficients of expansion. The lowest resistivity values achieved in this study for In_2O_3:Sn films on soda lime glass and polyimide substrates were 1.6×10^{-4} Ω cm and 1.9×10^{-4} Ω cm, respectively. The stability of In_2O_3:Sn film properties after heating in air could improved by using relatively high oxygen flow rates, high substrate temperatures and low process pressures during film deposition. These studies show that HiTUS deposition can be used to reduce the costs of solar cell fabrication by minimising the amount of unused material in the target.

The uniformity of the resistivity and thickness profile of ZnO:Al films across the substrate could be improved by adjusting the oxygen inlet distribution to allow a portion of the oxygen influx along the edges of the substrate instead of exclusively from the centre of the substrate. This arrangement did not interfere with the plasma emission intensity monitoring system that was used to maintain the reactive sputter process stability. Re-directing part of the oxygen influx along the edges of the substrate improved the uniformity of the oxidation across the substrate and may have also reduced the energy of the oxygen atoms bombarding the ZnO:Al films. This arrangement also enhanced the surface roughness of the layers after post deposition wet-etching, which is beneficial for light trapping in thin film silicon solar cells allowing the use of thinner absorber layers. A higher haze than that of the optimised RF sputtering reference was realised for some of the MF sputtered ZnO:Al which increased the quantum efficiency of the related microcrystalline silicon (μc-Si:H) solar cells. Despite the higher haze and photocurrent generation, the best μc-Si:H solar cells on MF sputtered ZnO:Al achieved reproducible efficiency values of 8.2% to 8.4 % which are comparable to values for the reference solar cell on RF sputtered ZnO:Al. The relatively higher sheet resistance of the MF sputtered ZnO:Al films reduced the cell voltage and fill-factor and thus there is still scope for improvement. Nevertheless, this work is an important step towards transferring technologies used to prepare high efficiency thin film silicon solar cells from the laboratory to industrial production.

Choosing an appropriate donor impurity is the simplest method to attain high mobility > 62.5 $cm^2 V^{-1} s^{-1}$, which allows low resistivity ~ 10^{-4} Ω cm with optical transmission > 80 % over wavelengths from 400 nm to over 1500 nm by reducing free carrier absorption. Transition metal dopants fulfil the requirements for optimal Lewis acid strength and electronic band structure, which suppress scattering by oxygen interstitials thus enhancing the mobility, for example in In_2O_3 and CdO. Experiments were carried out to examine the influence of the chemical state of molybdenum on the opto-electronic properties of In_2O_3:Mo. The influence of several deposition parameters on the structural, morphological, and opto-electronic properties of In_2O_3:Mo films grown by pulsed DC magnetron sputtering from a ceramic target was also studied. The NIR was also limited by increasing free carrier deposition typical for In_2O_3:Mo films grown with higher heater temperature or lower sputter pressure.

No significant difference in the In_2O_3:Mo film crystallite size and mobility was observed when the sputter pressure was increased, though the majority carrier density reduced thus increasing the resistivity. Varying the substrate temperature had a stronger effect on both the crystallite size and carrier mobility of the In_2O_3:Mo films. X-ray diffraction (XRD) measurements revealed that while most of the grains in the In_2O_3:Mo film, prepared without intentional substrate heating, were oriented along the <111> axis, the majority of grains in the heated films were oriented along the <100> axis. This transition in crystallite orientation was accompanied by a gradual change in surface structure from triangular grains to cubic grains which expanded as the heater temperature was raised. Although, the mobility and conductivity also increased with substrate temperature, there was no systematic correlation with the evolution of the texture of the films. While the electrical properties of the In_2O_3:Mo films obtained here, were similar to other groups, the lowest resistivity and highest mobility coincide with the strongest <100> orientation as opposed to <111> orientation reported by most groups. This disparity in crystalline texture indicates that the electrical properties in In_2O_3:Mo films are dominated by the doping efficiency. The In_2O_3:Mo films were heated at 450°C (i) in air, (ii) in vacuum and (iii) in air followed by a second heat treatment in vacuum to further examine the doping mechanism of molybdenum. Though the conductivity of the In_2O_3:Mo samples declined drastically after heat treatment in air as a result of excessive oxidation, it could be partially recovered by subsequent heat treatment in vacuum.

Other workers have used studies on the charge transport mechanisms and electronic band gap calculations to identify the factors that limit the conductivity in In_2O_3:Mo as well as other high mobility TCO materials. The work in this thesis reports for the first time, a detailed study by X-ray electron spectroscopy, of the chemical state of the individual elements in In_2O_3:Mo films over a wide variety range of carrier density and mobility values. Increasing the atomic ratio of Mo:In in the In_2O_3:Mo films and the doping efficiency of Mo, increases both the mobility and carrier density by reducing the Mo^{X+} species which are related to neutral complexes formed by interstitial oxygen. Both the visible and near infra-red transmission reduced with increasing amounts of elemental Mo in the films. Heat treatment of the In_2O_3:Mo films in vacuum increased the Mo^{4+} and Mo^{6+} species at the expense of the Mo^{X+} species thus reducing the resistivity.

Therefore, interstitial oxygen is the main inhibitor of the charge transport mechanism in In_2O_3:Mo films. These results corroborate the prediction in literature that high mobility in degenerate systems can be achieved provided that the dopant ion, by virtue of an optimal Lewis acid strength, suppresses the scattering effects of interstitial oxygen. Finally, the potential of high mobility TCO materials to improve solar cell efficiency was examined which emphasized the need for HMTCO materials that could be prepared at low temperatures with low resistivity ~ 10^{-4} Ω cm.

7.2 Outlook

The promising results of low resistivity In_2O_3:Sn prepared on polyimide foils should be extended to other low cost materials such as ZnO:Al. The feasibility of preparing flexible solar cells based on dye sensitized titania or organic materials should be tested on In_2O_3:Sn coated Upilex polyimide. An alternative to RF excitation used to ionise the plasma should be developed to simplify the equipment used for HiTUS deposition.

A better understanding of the correlation of the textured ZnO:Al morphology, the light trapping effect and the solar cell performance is still required. The effect of distributing a portion of the reactive gas via the edges of the substrate on the uniformity of ZnO:Al films prepared by reactive sputtering should be tested on substrates larger than 30 cm x 30 cm, for realistic industrial coatings. The resistivity of the ZnO:Al films should be further reduced to enable the use of thinner layers to save on material costs and to minimise I^2R losses in larger modules. The high deposition rates for the ZnO:Al layers by reactive MF magnetron sputtering from metallic targets for large area depositions should be complemented by faster deposition rates for the μc-Si:H solar cells.

The wide spectral range of transparency of high mobility TCO materials is desirable but more reductions in the resistivity to values below 10^{-4} Ω cm are essential. Also, the full potential of high mobility TCO for PV applications still has to be proven for films coated onto solar cell absorbers at low substrate temperatures. HMTCO films based on low cost, non hazardous materials such as ZnO, SnO_2 or TiO_2 are urgently required for wide spread application of thin film solar cells. More experimental studies on HMTCO films using techniques such as scanning tunnelling microscopy to investigate segregation of impurities or spectroscopic ellipsometry to analyse the optical properties are needed to better understand the charge transport properties.

General developments required for diverse TCO films have also been identified. First, in situ diagnostic techniques that are cheap, robust and easy to interpret, should be developed to control the oxidation of TCO films during deposition. Secondly, the chemical and thermal stability of the TCO properties to the processing steps used for the subsequent absorber layers of solar cells in the substrate configuration, must be improved. Thirdly, the nature of the interfaces formed between the different TCO films and the absorber materials for solar cells requires further investigation to improve solar cell efficiency. Lastly, the search for higher quality transparent conductors should not be limited to oxides but extended to other compounds.

7.3 Closing remarks

Deposition methods that are fast, use simple equipment and minimise material waste are desirable to reduce the cost of fabricating thin film solar cells on an industrial scale. This thesis has demonstrated that HITUS deposition and reactive MF magnetron sputtering from metallic targets as well as pulsed DC magnetron sputtering from ceramic targets fulfil most of these criteria. It should be noted that though the optimised deposition parameters in one sputter system cannot be replicated in others, the general trends are still useful in determining viable process windows. Finally, though the concepts described in this thesis have focused on PV applications, the outcomes are applicable for TCO materials used for opto-electronic devices as well as other semi-conducting thin films.

References

1. International Energy Agency, *World Energy Outlook.* 2006 http://www.iea.org/textbase/nppdf/free/2006/weo2006.pdf.
2. International Energy Agency, *Key World Energy Statistics.* 2008 http://www.iea.org/textbase/nppdf/free/2008/key_stats_2008.pdf.
3. A. Goetzberger, C. Hebling, and H.-W. Schock, *Photovoltaic materials, history, status and outlook.* Materials Science and Engineering, 2003. **R40**: p. 1.
4. A. Jaeger-Waldau, *Status of thin film solar cells in research, production and the market.* Solar Energy, 2004. **77**: p. 667
5. M. A. Green, K. Emery, Y. Hishikawa, and W. Warta, *Solar Cell Efficiency Tables (Version 31).* Prog. in Photovolt. Res. Appl., 2008. **16**: p. 61.
6. K. L. Chopra, P. D. Paulson, and V. Dutta, *Thin-film solar cells: An overview.* Prog. in Photovolt. Res. Appl., 2004. **12**: p. 69.
7. S. Hegedus, S. Albright, F. Jeffrey, T.J. McMahon, and S. Wiedeman, *Substrates, contacts and monolithic Integration.* Progress in Photovoltaics: Research and Applications, 1997. **5**: p. 365.
8. S. Hegedus, *Thin film solar modules:The low cost, high throughput and versatile alternative to Si wafers.* Prog. in Photovolt. Res. Appl., 2006. **14**: p. 393.
9. G. Haacke, *Transparent conducting coatings,.* Ann. Rev. Mater. Sci., 1977. 7: p. 73.
10. J.C. Manifacier, *Thin metallic oxides as transparent conductors.* Thin Solid Films, 1982. **90**: p. 297.
11. K. L. Chopra, S. Major, and D.K. Pandya, *Transparent conductors - A status review.* Thin Solid Films, 1983. **102**: p. 1.
12. H. L. Hartnagel, A. L. Das, A. K. Jain, and C. Jagadish, *Semiconducting transparent thin films.* 1995, Bristol: Institute of Physics Publishing.
13. B. G. Lewis and D. Paine, *Applications and processing of transparent conducting oxides.* Material Research Society Bulletin, 2000. **25**: p. 22
14. C. G. Granqvist, *Transparent conductors as solar energy materials: A panoramic review.* Sol. Energy Mater. & Sol. Cells, 2007. **91**: p. 1529.
15. M. J. Thwaites, *High Density Plasmas,*, in *Patent No. 646387.* 2002: USA.
16. J. Müller, G. Schöpe, B. Rech, H. Schade, P. Lechner, R. Geyer, H. Stiebig, and W. Reetz. *Role of glass/TCO substrate in thin film silicon solar cells.* in *3rd World Conf. Photovolt. Sol. En. Conversion,*. 11 - 18 May 2003. Osaka, Japan 1839
17. N Beck, J. Meier, J. Fric, Z. Remeš, A. Poruba, R. Flückiger, J. Pohl, A. Shah, and M. Vanecek, *Enhanced optical absorption in microcrystalline silicon.* Journal of Non-crystalline Solids, 1996. **198 -200**: p. 903
18. O. Kluth, A. Löffl, S. Wieder, C. Beneking, W. Appenzeller, L. Houben, B. Rech, H. Wagner, S. Hoffman, R. Waser, J.A.A. Selvan, and H. Keppner. *Texture etched Al-doped ZnO: A new material for enhanced light trapping in thin film solar cells.* in *26th IEEE Photovoltaic Specialists Conference.* 30 September - 3 October 1997. Anaheim, CA. 715
19. T Minami, *Transparent conducting oxide semiconductors for transparent electrodes.* Semiconductor Science and Technology, 2005. **20**: p. 35
20. G. J. Exarhos and X. -D. Zhou, *Discovery-based design of transparent conducting oxide films.* Thin Solid Films, 2007. **515**: p. 7025.
21. T. J. Coutts, D.L. Young, and X. Li, *Characterisation of transparent conducting oxides*, in *MRS Bulletin.* 2000. p. 58 August (2000).
22. A J Freeman, K.R. Poeppelmeier, T.O. Mason, R.P.H. Chang, and T.J. Marks, *Chemical and thin film strategies for new transparent conducting oxides*, in *MRS Bulletin.* 2000. p. 45 August 2000.
23. O.N. Mryasov and A.J. Freeman, *Electronic band structure of indium tin oxide and criteria for transparent conducting behaviour.* Phys. Rev. B, 2001. **64**: p. 233111.
24. B J Ingram, G.B. Gonzalez, D.R. Kammler, M.I. Bertoni, and T.O. Mason, *Chemical and Structural Factors Governing Transparent Conductivity in Oxides.* Journal of Electroceramics, 2004. **13**: p. 167.
25. S. M. Sze, *Semiconductor devices.* 2002, New York: Wiley & Sons, Inc.
26. K. Seeger, *Semiconductor physics: An introduction.* 2004: Springer Verlag.
27. M. Grundmann, *The physics of semiconductors: An introduction including devices and nanophysics.* 2006, Berlin Heidelberg: Springer.

28. M. Quaas, C. Eggs, and H. Wulff, *Structural studies of ITO thin films with the Rietveld method.* Thin Solid Films, 1998. **332**: p. 277.

29. Z. Qiao and D. Mergel, *Comparison of radio-frequency and direct-current magnetron sputtered thin In_2O_3 :Sn films.* Thin Solid Films, 2005. **484**: p. 146.

30. Sze S.M., *Semiconductor Devices.* 2002: Wiley & Sons, Inc., New York.

31. K Seeger, *Semiconductor physics: An introduction.* 2004: Springer Verlag.

32. Grundmann, M., *The physics of semiconductors: An introduction including devices and nanophysics.* 2006, Berlin Heidelberg: Springer.

33. S. B. Zhang, S.-H. Wei, and A. Zunger, *Intrinsic n-type versus p-type doping asymmetry and the defect physics of ZnO.* Phys. Rev. B, 2001. **63**: p. 075205.

34. G. Frank and H. Köstlin, *Electrical properties and defect model of tin-doped indium oxide layers.* Appl. Phys. A, 1982. **27**: p. 197.

35. M. Lundstrom, *Fundamentals of carrier transport.* 2nd ed. 2000, Cambridge: Cambridge University Press.

36. R. Clanget, *Ionised impurity scattering in degenerate In_2O_3.* Appl. Phys., 1973. **2**: p. 247.

37. Ellmer, K. and R. Mientus, *Carrier transport in polycrystalline ITO and ZnO:Al II: The influence of grain barriers and boundaries.* Thin Solid Films, 2008. **516**: p. 5829.

38. K Ellmer, *Resistivity of polycrystalline zinc oxide films: current status and physical limits.* J. Phys. D: Appl. Phys., 2001(34): p. 3097.

39. E. Shanthi, A. Banerjee, V. Dutta, and K. L. Chopra, *Annealing characteristics of tin oxide films prepared by spray pyrolysis,.* Thin Solid Films, 1980: p. 237.

40. A. Gupta, P. Gupta, and V.K. Srivastava, *Annealing effects in indium oxide films prepared by reactive evaporation.* Thin Solid Films, 1985. **123**: p. 325.

41. H. Hosono, *Ionic amorphous oxide semiconductors: Material design, carrier transport, and device application.* J. Non-Cryst. Solids, 2006. **352**: p. 851.

42. I. Hamberg and C.G. Granqvist, *Evaporated Sn-doped In_2O_3 films: Basic optical properties and application to energy efficient windows.* J. Appl. Phys., 1986. **60**(11): p. R123.

43. Jin, Z.C., I. Hamberg, and C.G. Granqvist, *Optical properties of sputter deposited ZnO:Al thin films.* Journal of Applied Physics, 1988. **64**: p. 5117.

44. G. Haacke, *New figure of merit for transparent conductors.* J. Appl. Phys., 1976. **47**(9): p. 4086.

45. A. Goetzberger, J. Luther, and G. Willeke, *Solar cells: past, present, future.* Solar Energy Materials & Solar Cells, 2002. **74**: p. 1.

46. X. Wu, J. C. Keane, R. G. Dhere, C. DeHart, A. Duda, T. A. Gessert, S. Asher, D.H. Levi, and P. Sheldon. *16.5%-efficient CdS/CdTe polycrystalline thin-film solar cell.* in *17th European Photovoltaic Solar Energy Conference.* 22-26 October 2001. Munich, Germany 995.

47. B.M. Basol. *Thin film CdTe solar cells - A review,.* in *21 IEEE PV Specialists Conference.* 1990 588.

48. G Khyrpunov, A. Romeo, F. Kurdesau, D.L. Bätzner, H. Zogg, and A.N. Tiwari, *Recent developments in evaporated CdTe solar cells.* Solar Energy Materials and Solar Cells, 2006. **90**: p. 664

49. V. M. Fthenakis, *Life cycle impact analysis of cadmium in CdTe PV production.* Renewable and Sustainable Energy Reviews, 2004. **8**: p. 303.

50. A. Romeo, G. Khrypunov, S. Galassini, H. Zogg, and A.N. Tiwari, *Bifacial configurations for CdTe solar cells.* Sol. Energy Mater. Sol. Cells, 2007. **91**: p. 1388.

51. A. Gupta, V. Parikh, and A. D. Compaan, *High efficiency ultra-thin sputtered CdTe solar cells.* Solar Energy Materials & Solar Cells, 2006. **90**: p. 2263.

52. J. T. Heath, J. D. Cohen, W. N. Shafarman, D. X. Liao, and A. A. Rockett, *Effect of Ga content on defect states in $CuIn_{1-x}Ga_xSe_2$ photovoltaic devices.* Appl. Phys. Lett., 2002. **80**(24): p. 4540.

53. I. Repins, M. A. Contreras, B. Egaas, C. DeHart, J. Scharf, C. L. Perkins, B. To, and R. Noufi, *19.9%-efficient ZnO/CdS/$CuInGaSe_2$ solar cell with 81.2% fill factor.* Prog. in Photovolt. Res. Appl., 2008. **16**: p. 235.

54. S. Siebentritt, *Alternative buffers for chalcopyrite solar cells.* Solar Energy, 2004. **77**: p. 767.

55. J. Malmström, O. Lundberg, and L. Stolt. *Potential for light trapping in $Cu(In,Ga)Se_2$ solar cells.* in *3rd World Conference on Photovoltaic Energy Conversion.* 11-18 May 2003. Osaka, Japan 344.

56. M. Ruckh, D. Hariskos, U. Ruhle, H.W. Schock, R. Menner, and B. Dimmler. *Applications of ZnO in $Cu(In,Ga)Se_2$ solar cells.* in *25th IEEE Photovoltaic Specialists Conference.* 13-17 May 1996. 825

57. M Kaelin, D. Rudmann, and A.N. Tiwari, *Low cost processing of CIGS thin film solar cells.* Solar Energy, 2004. **77**: p. 749.

58. A.V. Shah, R. Platz, and H. Keppner, *Thin-film silicon solar cells: A review and selected trends.* Sol. Energy Mater. & Sol. Cells, 1995. **38**: p. 501.

59. A. V. Shah, J. Meier, E. Vallat-Sauvain, N. Wyrsch, U. Kroll, C. Droz, and U. Graff, *Material and solar cell research in microcrystalline silicon.* Sol. Energy Mater. Sol. Cells, 2003. **78**(469 - 491).
60. W. W. Wenas, A.Y. A. De, M. Konagai, and K. Takahashi, *Optimization of ZnO for front and rear contacts in a-Si solar cells.* Sol. Energy Mater. & Sol. Cells, 1994. **34**: p. 313.
61. B Rech and H. Wagner, *Potential of amorphous silicon for solar cells.* Applied Physics A, 1999. **69**: p. 155.
62. A. Banerjee and S. Guha, *Study of back reflectors for amorphous silicon alloy solar cell application.* J. Appl. Phys., 1991. **69**(2): p. 1030.
63. J Müller, G. Schöpe, B. Rech, H. Schade, P. Lechner, R. Geyer, H. Stiebig, and W. Reetz. *Role of glass/TCO substrate in thin film silicon solar cells.* in *3rd World Conf. Photovolt. Sol. En. Conversion,*. Osaka, Japan 1839
64. S. Pillai, K. R. Catchpole, T. Trupke, and M.A. Green, *Surface plasmon enhanced silicon solar cells.* J. Appl. Phys., 2007. **101**: p. 093105.
65. H. Zhou, A. Colli, T. Butler, N. Rupesinghe, A. Mumtaz, G. Amaratunga, and J.I.B. Wilson, *Carbon nanotube arrays for optical design of amorphous silicon solar cells.* Int. J. Mater Form, 2008. **1**: p. 113.
66. H.Tributsch, *Dye sensitization solar cells: a critical assessment of the learning curve.* Coordination Chemistry Reviews, 2004. **248**: p. 1511.
67. B. O' Regan and M. Grätzel, *A low cost high efficiency solar cell based in dye sensitized colloidal TiO_2 films.* Nature, 1991. **353**(24): p. 737.
68. B. Li, L. Wang, B. Kang, P. Wang, and Y. Qi, *Review of recent progress in solid-state dye-sensitized solar cells.* Solar Energy Materials & Solar Cells, 2006. **90**(549).
69. A. Kay and M. Graetzel, *Low cost photovoltaic modules based on dye sensitized nanocrystalline titanium dioxide and carbon powder.* Solar Energy Materials & Solar Cells, 1996. **44**: p. 99.
70. L. N. Lewis, J. L. Spivack, S. Gasaway, E. D. Williams, J. Y. Gui, V. Manivannan, and O. P. Siclovan, *A novel UV-mediated low-temperature sintering of TiO_2 for dye-sensitized solar cells.* Solar Energy Materials & Solar Cells, 2006. **90**: p. 1041.
71. J. Meier, S. Dubail, R. Fluckiger, D. Fischer, H. Keppner, and A. Shah. *Intrinsic microcrystalline silicon (μc-Si:H) - a promising new thin film solar cell material.* in *Proceedings of the First World Conference on Photovoltaic Energy Conversion.* 5-9 December 1994. Hawaii, USA 409.
72. H Keppner, J. Meier, P. Torres, D. Fischer, and A. Shah, *Microcrystalline silicon and micromorph tandem solar cells.* Appl. Phys. A: Materials Science and Processing, 1999. **69**(2): p. 169
73. N. Beck, J. Meier, J. Fric, Z. Remeš, A. Poruba, R. Flückiger, J. Pohl, A. Shah, and M. Vanecek, *Enhanced optical absorption in microcrystalline silicon.* J. Non-Cryst. Solids, 1996. **198 -200**: p. 903
74. T. Repmann, B. Sehrbrock, C. Zahren, H. Siekmann, J. Müller, and B. Rech. *Thin film solar modules based on amorphous and microcrystalline silicon.* in *3rd World Conference on Photovoltaic Energy Conversion.* 11- 18 May 2003. Osaka, Japan 1574.
75. T. Nakada, Y. Hirabayashi, T. Tokado, D. Ohmori, and T. Mise, *Novel device structure for $Cu(In,Ga)Se_2$ thin film solar cells using transparent conducting oxide back and front contacts.* Solar Energy, 2004. **77**: p. 739.
76. M. Powalla and B. Dimmler, *Scaling up issues of CIGS solar cells.* Thin Solid Films, 2000. **540**: p. 361
77. M. Powalla, D. Hariskos, E. Lotter, M. Oertel, J. Springer, D. Sellbogen, B. Dimmler, and R. Schaeffler, *Large-area CIGS modules: processes and properties.* Thin Solid Films, 2003. **431 - 432**: p. 523.
78. T. Yoshida, M. Iwaya, H. Ando, T. Oekermann, K. Nonomura, D. Schlettwein, D. Wöhrle, and H. Minoura, *Improved photoelectrochemical performance of electrodeposited ZnO/EosinY hybrid thin films by dye re-adsorption.* Chem. Commun., 2004: p. 400.
79. B. A. Andersson, *Materials availability for large-scale thin-film photovoltaics.* Prog. in Photovolt. Res. Appl., 2000. **8**: p. 61.
80. F. -J. Haug, Z.S. Geller, H. Zogg, A.N. Tiwari, and C. Vignali, *Influence of deposition conditions on the thermal stability of ZnO:Al films grown by rf magnetron sputtering.* J. Vac. Sci. Technol. A, 2001. **19**(1): p. 171.
81. H. Ohta, K. Nomura, H. Hiramatsu, K. Ueda, T. Kamiya, M. Hirano, and H. Hosono, *Frontiers of transparent oxide semiconductors.* Solid-State Electron., 2003. **47**: p. 2261.
82. H. Hosono, *Recent progress in transparent oxide semiconductors: Materials and device application.* Thin Solid Films, 2007. **515**: p. 6000.

83. H. Hosono. *Novel transparent conductive oxides.* in *3rd World Conference on Photovoltaic Energy Conversion.* May 11-18. 2003. Osaka, Japan. 31.

84. C G Granqvist and A. Hultaker, *Transparent conducting ITO films: new developments and applications.* Thin Solid Films, 2002. **411**: p. 1

85. G. J. Exarhos and X. -D. Zhou, *Discovery-based design of transparent conducting oxide films.* Thin Solid Films, 2007. **515**: p. 7025.

86. X. Wu, R.G. Dhere, J. Zhou, A. Duda, C. Perkins, Y. Yan, and H.R. Moutinho. *High-quality cadmium stannate transparent conductive oxide film for tandem thin-film solar cells,.* in *3rd World Conference on Photovoltaic Energy Conversion.* 11-18 May 2003. Osaka, Japan 507.

87. Y. Meng, X. Yang, H. Chen, J. Shen, Y. Jiang, Z. Zhang, and Z. Hua, *A new transparent conductive thin film* $In_2O_3:MO$. Thin Solid Films, 2001. **394**: p. 219.

88. A E Delahoy and S.Y. Guo, *Transparent and semitransparent conducting film deposition by reactive environment hollow cathode sputtering.* J. Vac. Sci. Technol., 2005. **A23**(4): p. 1215.

89. T. Minami, *Transparent conducting oxide semiconductors for transparent electrodes.* Semicond. Sci. Technol., 2005. **20**: p. 35

90. R. Martins, P. Barquinha, A. Pimentel, L. Pereira, and E. Fortunato, *Transport in high mobility amorphous wide band gap indium zinc oxide films,.* Phys. Stat. Sol., 2005. **A202**(9): p. R95.

91. H. Kawazoe, H. Yanagi, K. Ueda, and H. Hosono, *Transparent p-type conducting oxides: Design and fabrication of p-n heterojunctions.* Material Research Society Bulletin, 2000. **25**: p. 28.

92. Banerjee, A.N. and K.K. Chattopadhyay, *Recent developments in the emerging field of crystalline p-type transparent conducting oxide thin films.* Progress in Crystal Growth and Characterization of Materials, 2005. **50**: p. 52.

93. H. Kawazoe, M. Yasukawa, M. Hyodou, M. Kurita, H. Yanagi, and H. Hosono, *p-type electrical conduction in transparent thin film of* $CuAlO_2$. Nature, 1997. **389**: p. 939.

94. D.C. Look, D.C. Reynolds, C.W. Litton, R.L. Jones, D.B. Eason, and G. Cantwell, *Characterization of homoepitaxial p-type ZnO grown by molecular beam epitaxy.* Appl. Phys. Lett., 2002. **81**: p. 1830.

95. M. Orita, H. Ohta, and M. Hirano, *Deep-ultraviolet transparent conductive* β-Ga_2O_3 *thin films.* Appl. Phys. Lett., 2000. 77(25).

96. Z. Wu, Z. Chen, X. Du, J. M. Logan, J. Sippel, M. Nikolou, K. Kamaras, J. R. Reynolds, D. B. Tanner, A. F. Hebard, and A. G. Rinzler, *Transparent Conductive Carbon Nanotube Films.* Science, 2004. **305**: p. 1273.

97. J. Fritsche, T. Schulmeyer, A. Thißen, A. Klein, and W. Jaegermann, *Interface modification of CdTe thin film solar cells by* $CdCl_2$*-activation.* Thin Solid Films, 2003. **431-432**(267).

98. F. Säuberlich, J. Fritsche, R. Hunger, and A. Klein, *Properties of sputtered ZnO films and its interfaces with CdS.* Thin Solid Films, 2003. **431 - 432**: p. 378.

99. K. L. Chopra, *Thin Film Phenomena.* 1979, New York: Robert E. Krieger Publishing Company.

100. H. K. Pulker, *Thin films science and technology 6: Coatings on glass.* 1984: Elsevier Publishers B.V.

101. S. M. Rossnagel, *Magnetron plasma deposition processes*, in *Handbook of plasma processing technology*, S. M. Rossnagel, J. J. Cuomo, and W. D. Westwood, Editors. 1999, Noyes Publications. p. 160.

102. J. Meier, U. Kroll, S. Dubail, S. Golay, S. Fay, J. Dubail, and A. Shah. *Efficiency enhancement of amorphous silicon p-i-n solar cells by LP-CVD ZnO.* in *28th IEEE Photovoltaic Specialists Conf.,.* 2000. Anchorage, Alaska. 746

103. R. Groenen, J. Löffler, P.M. Sommeling, J.L. Linden, E.A.G. Hamers, R.E.I. Schropp, and M.C.M.v.d. Sanden, *Surface textured ZnO films for thin film solar cell applications by expanding thermal plasma CVD.* Thin Solid Films, 2001. **392**: p. 226.

104. H. Ohta, M. Orita, M. Hirano, H. Tanji, H. Kawazoe, and H. Hosono, *Highly electrically conductive indium-tin-oxide thin films epitaxially grown on yttria-stabilized zirconia (100) by pulsed-laser deposition.* Appl. Phys. Lett., 2000. 76(19): p. 2740.

105. H. Tanaka, K. Ihara, T. Miyata, H. Sato, and T. Minami, *Low resistivity polycrystalline ZnO:Al thin films prepared by pulsed laser deposition-.* J. Vac., Sci. Technol A, 2004. **22**(4): p. 1757.

106. C. Warmsingh, Y. Yoshida, D. W. Readey, C. W. Teplin, J. D. Perkins, P. A. Parilla, L. M. Gedvilas, B. M. Keyes, and D. S. Ginley, *High-mobility transparent conducting Mo-doped* In_2O_3 *thin films by pulsed laser deposition.* J. Appl. Phys., 2004. **95**(7): p. 3831.

107. M. Yan, M. Lane, C. R. Kannewurf, and R. P. H. Chang, *Highly conductive epitaxial CdO thin films prepared by pulsed laser deposition,.* Appl. Phys. Lett., 2001. **78**(16): p. 2342.

108. S Swann, *Magnetron sputtering.* Phys. Technology, 1988. **19**.

109. W. D: Westwood, *Reactive sputter deposition,*, in *Handbook of plasma processing technology*, S. M. Rossnagel, J. J. Cuomo, and W. D. Westwood, Editors. 1999, Noyes Publications. p. 233

110. S. Schiller, G. Beister, M. Neumann, and G. Jaesch, *Vacuum coating of large areas.* Thin Solid Films, 1982. **96**: p. 199.

111. Y. Mastuda, K. Otomo, and H. Fujiyam, *Quantitative modelling of reactive sputtering process for MgO thin film deposition.* Thin Solid Films, 2001. **390**(1-2): p. 59.

112. S. Berg and T. Nyberg, *Fundamental understanding and modelling of reactive sputtering processes.* Thin Solid Films, 2005. **476**: p. 215

113. J. Strümpfel, G. Beister, D. Schulze, M. Kammer, and S. Rehn. *Reactive dual magnetron sputtering of oxides for large area production of optical multi-layers.* in *40th Annual Technical Conference of the Society of Vacuum Coaters.* 12-17 April 1997. New Orleans, USA, . 179.

114. R. Menner, M. Oertel, M. Powalla, M. Dimer, S. Rehn, J. Strümpfel, and B. Dimmler. *Reactive sputtering from dual magnetron Zn:Al targets for TCO in CIGS solar modules on an industrial scale.* in *19th European Photovoltaic Solar Energy Conference.* 7-11 June 2004. Paris.

115. N. S. Panwar, K.D. Vargheese, and G.M. Rao, *Design and performance study of a scanning magnetron sputtering target.* Review of Scientific Instruments, 1997. **68**(4): p. 1858

116. B. Szyszka, *Transparent and conductive aluminum doped zinc oxide films prepared by mid-frequency reactive magnetron sputtering.* Thin Solid Films, 1999. **351**: p. 164

117. I. Baia, M. Quintela, L. Mendes, P. Nunes, and R. Martins, *Performances exhibited by large area ITO layers produced by RF magnetron sputtering.* Thin Solid Films, 1999. **337**: p. 171.

118. J -L Huang, Y.-T. Jah, B.-S. Yau, C.-Y. Chen, and H.-H. Lu, *Reactive magnetron sputtering of indium tin oxide films on acrylics - morphology and bonding state.* Thin Solid Films, 2000. **370**(1-2): p. 33.

119. C. May, R. Menner, J. Strümpfel, M. Oertel, and B. Sprecher, *Deposition of TCO films by reactive magnetron sputtering from metallic Zn:Al alloy targets.* Surface and Coatings Technology, 2003. **169 -170**: p. 512.

120. J. Hüpkes, B. Rech, B. Sehrbrock, O. Kluth, J. Müller, H.P. Bochem, and M. Wuttig. *Development of surface textured zinc oxide for thin film silicon solar cells by high rate sputtering.* in *19th European Photovoltaic Solar Energy Conference.* 7- 11 June 2004. Paris. 1415

121. J. Hüpkes, B. Rech, O. Kluth, T. Repmann, B. Sehrbrock, J. Müller, R. Drese, and M. Wuttig. *Surface textured mf-sputtered ZnO films for microcrystalline silicon based thin-film solar cells.* in *14th Int. Photovoltaic Science and Engineering Conference.* 26-30 January 2004. Bangkok, Thailand. 379

122. J. Lee, H. Jung, D. Lim, K. Yang, W. Song, and J. Yi, *Effects of bias voltage on the properties of ITO films prepared on polymer substrates.* Thin Solid Films, 2005. **480-481**: p. 157.

123. V. Sittinger, F. Ruske, W. Werner, B. Szyszka, B. Rech, J. Hüpkes, G. Schöpe, and H. Stiebig, *ZnO:Al films deposited by in-line AC magnetron reactive sputtering for a-Si:H thin film silicon solar cells.* Thin Solid Films, 2005. **496**: p. 16.

124. J. Hüpkes, B. Rech, S. Calnan, O. Kluth, U. Zastrow, H. Siekmann, and M. Wuttig, *Material study on reactively sputtered zinc oxide for thin film silicon solar cells.* Thin Solid Films, 2006. **502**: p. 286.

125. S. J. Nadel, P. Greene, J. Rietzel, M. Perata, L. Malaszewski, and R. Hull, *Advanced generation of rotatable magnetron technology for high performance reactive sputtering.* Thin Solid Films, 2006. **502**: p. 15

126. W. D. Sproul, *High rate reactive sputtering process control.* Surface and Coatings Technology, 1987. **33**: p. 73.

127. W.D. Sproul, D.J. Christie, and D.C. Carter, *Control of reactive sputtering processes.* Thin Solid Films, 2005. **491**: p. 1.

128. S. Maniv, C. Miner, and W.D. Westwood, *High rate deposition of transparent conducting films by modified reactive planar magnetron sputtering of Cd_2Sn alloy.* Journal of Vacuum Science and Technology, 1981. **18**(2): p. 195.

129. A. J. Aronson, D. Chen, and W.H. Class, *Preparation of titanium nitride by a pulsed D.C. magnetron reactive deposition technique using the moving mode of deposition.* Thin Solid Films, 1980. **72**: p. 535.

130. K. Koski, J. Hölä, and P. Juliet, *Voltage controlled reactive sputtering process for aluminium oxide thin films.* Thin Solid Films, 1998. **326**: p. 189.

131. S. Schiller, U. Heisig, K. Steinfelder, J. Strümpfel, R. Voigt, R. Fendler, and G. Teschner, *On the investigation of d.c. plasmatron discharges by optical emission spectrometry.* Thin Solid Films, 1982. **96**: p. 235.

132. J. Strümpfel and C. May, *Low Ohm large area ITO coating by reactive sputtering in DC and MF mode.* Vacuum, 2000. **59**: p. 500.

133. N. Malkomes, M. Vergöhl, and B. Szyszka, *Properties of aluminum-doped zinc oxide films deposited by high rate mid-frequency reactive magnetron sputtering.* Journal of Vacuum Science and Technology, 2001. **A19**(2): p. 414.

134. M. Vergöhl, N. Malkomes, T. Staedler, T. Matthée, and U. Richter, *Ex situ and in situ spectroscopic ellipsometry of MF and DC-sputtered* TiO_2 *and* SiO_2 *films for process control.* Thin Solid Films, 1999. **351**: p. 42.

135. K. Wasa and S. Hayakawa, *Some features of magnetron sputtering.* Thin Solid Films, 1978. **52**(3143).

136. T. Fukami, F. Shintani, and M. Naoe, *Observations on the operation of a planar magnetron sputtering system by target erosion patterns.* Thin Solid Films, 1987. **151**: p. 373.

137. H. Sato, T. Minami, S. Takata, T. Mouri, and N. Ogawa, *Highly conductive and transparent ZnO:Al thin films prepared on high-temperature substrates by d.c. magnetron sputtering.* Thin Solid Films, 1992. **220**: p. 327.

138. J. Herero and C. Guillen, *High quality ITO on polymer on a laboratory scale.* Vacuum, 2002. **67**(3-4): p. 611

139. F Kessler and D. Rudmann, *Technological aspects of flexible CIGS solar cells and modules.* Solar Energy, 2004. **77**: p. 685.

140. Menzel gläser. 2008 http://www.menzel.de/Produkte.655.0.html?id=687&L=1. 27 August 2008.

141. Corning Incorporated, *Corning 1737 AMLCD Glass Substrates-Material Information.* 2003.

142. Ube Industries Limited, *Upilex-S Data Sheet.* 2000.

143. R. G. Gordon, *Criteria for choosing transparent conductors*, in *MRS Bulletin.* 2000. p. 52 August 2000.

144. D. Rudmann, D. Brémaud, A.F.d. Cunha, G. Bilger, A. Strohm, M. Kaelin, H. Zogg, and A.N. Tiwari, *Sodium incorporation strategies for CIGS growth at different substrate temperatures.* Thin Solid Films, 2005. **480-481**: p. 55

145. P. Sommeling, M. Späth, J.A.M.v. Roosmalen, T.B. Meyer, A.F. Meyer, and O. Kohle. *Dye sensitized nanocrystalline* TiO_2 *solar cells on flexible substrates.* in *2nd World Conference on Photovoltaic Solar Energy Conversion.* 6-10 July 1998. Vienna, Austria. 288

146. R. Birkmire, E. Eser, S. Fields, and W. Shafarman, *Cu(InGa)*Se_2 *Solar Cells on a Flexible Polymer Web.* Prog. Photovolt. Res Appl., 2005. **13**: p. 141.

147. I. Masat and T. Ellison, *Roll-to roll manufacturing of amorphous silicon alloy solar cells with in situ cell performance diagnostics.* Solar Energy Materials and Solar Cells, 2003. **78**(1 - 4): p. 613

148. J. Penndorf, M. Winkler, O. Tober, D. Röser, and K. Jacobs, *Cu*InS_2 *thin film formation on a Cu tape substrate for photovoltaic applications,.* Solar Energy Materials and Solar Cells, 1998. **53**: p. 285.

149. J.R. Tuttle, A. Szalaj, and J. Keane. *A 15.2% AM0/1433 W/kg thin-film Cu(In,Ga)*Se_2 *solar cell for space applications.* in *Twenty-Eighth IEEE Photovoltaic Specialists Conference.* 15-22 Sept. 2000,. Anchorage, Alaska 1042

150. D. Rudmann, D. Brémaud, H. Zogg, and A. N. Tiwari, *Na incorporation into CuInGa*Se_2 *for high-efficiency flexible solar cells on polymer foils.* J. Appl. Phys., 2005. **97**: p. 084903:1.

151. D. Brémaud, D. Rudmann, M. Kaelin, K. Ernits, G. Bilger, M. Döbeli, H. Zogg, and A.N. Tiwari, *Flexible Cu(In,Ga)*Se_2 *on Al foils and the effects of Al during chemical bath deposition.* Thin Solid Films, 2007. **515**: p. 5857.

152. X. Mathew, G. W. Thompson, V.P. Singh, J.C. McClure, S. Velumani, N.R. Mathews, and P.J. Sebastian, *Development of CdTe thin films on flexible substrates-A review.* Solar Energy Materials & Solar Cells, 2003. **76**: p. 293.

153. A. Rogozin, N. Shevchenko, M. Vinnichenko, F. Prokert, V. Cantelli, A. Kolitsch, and W. Möller, *Real-time evolution of the indium tin oxide film properties and structure during annealing in vacuum,.* Appl. Phys. Lett., 2004. **85**(2): p. 212.

154. R. X. Wang, C.D. Beling, S. Fung, A.B. Djurisic, C.C. Ling, and S. Li, *Influence of gaseous annealing environment on the properties of indium tin oxide thin films.* J. Appl. Phys., 2005. **97**(033504): p. 1.

155. H. Sato, T. Minami, Y. Tamura, S. Takata, T. Mouri, and N. Ogawa, *Aluminium content dependence of milky transparent conducting ZnO:Al films with textured surface prepared by d.c. magnetron sputtering.* Thin Solid Films, 1994. **246**: p. 86.

156. T. Nakada, Y Ohkubo, and A. Kunioka, *Effect of water vapour on the growth of textured ZnO-based films for solar cells by DC-magnetron sputtering.* Jpn. J. Appl. Phys., 1991. **30**(12A): p. 3344.

157. D.K. Schroder, *Semiconductor material and device characterization.* 3rd ed. 2006, Hoboken, New Jersey: John Wiley and Sons, Inc.

158. C.D. Wagner, *Photoelectron and Auger energies and the Auger parameter: A data set, Appendix 5.*, in *Practical Surface Analysis: Auger and X-ray photoelectron Spectroscopy*, D. Briggs and M.P. Seah, Editors. 1990, John Wiley & Sons, Ltd. p. 595.

159. NIST, *NIST X-ray Photoelectron Spectroscopy Database,*. 2003: National Institute of Standards and Technology, Gaithersburg, http://srdata.nist.gov/xps/ Accessed on 12 August 2008.

160. CNRS, *LaSurface Web Site Database for XPS*. 2008: Centre National de la Recherche Scientifique (CNRS) http://www.lasurface.com/database/spectrexps.php Accessed on 12 August 2008.

161. A. Romeo, H. Zogg, and A.N. Tiwari. *Influence of transparent conducting oxides on the properties of CdTe/CdS solar cells.* in *Proceedings of Second World Conference and Exhibition on Photovoltaic Solar Energy Conversion.* 6-10 July 1998. Vienna, Austria 1105.

162. U. Hiroshi, I. Seiji, and S. Hajimu, *Effect of substrate temperature on the photovoltaic properties of a CdS/CdTe solar cell.* Jpn J. Appl. Phys., 1990. **29**: p. 2003.

163. A. Romeo, D.L. Bätzner, H. Zogg, C. Vignali, and A.N. Tiwari, *Influence of CdS growth process on structural and photovoltaic properties of CdTe/CdS solar cells.* Solar Energy Materials & Solar Cells, 2001. **67**: p. 311.

164. T. Potlog, L. Ghimpu, P. Gashin, A. Pudov, T. Nagle, and J. Sites, *Influence of annealing in different chlorides on the photovoltaic parameters of CdS/CdTe solar cells.* Sol. Energy Mater. Sol. Cells, 2003. **80**: p. 327.

165. S. Ito, T.N. Murakami, P. Comte, P. Liska, C. Grätzel, M.K. Nazeeruddin, and M. Grätzel, *Fabrication of thin film dye sensitized solar cells with solar to electric power conversion efficiency over 10%.* Thin Solid Films, 2008. **516**(14): p. 4613.

166. M. A. Green, *Solar cells: Operating principles, technology and system applications.* 1998: University of New South Wales.

167. O. N. Mryasov and A.J. Freeman, *Electronic band structure of indium tin oxide and criteria for transparent conducting behavior.* Phys. Rev. B, 2001. **64**: p. 233111.

168. T. Omata, H. Fujiwara, S. Otsuka-Yao-Matsuo, and N. Ono, *Electron trapping center and SnO_2-doping mechanism of indium tin oxide.* Appl. Phys. A, 2000. **71**: p. 609.

169. G. B. González, T. O. Mason, J. P. Quintana, O. Warschkow, D. E. Ellis, J.-H. Hwang, J. P. Hodges, and J. D. Jorgensen, *Defect structure studies of bulk and nano-indium-tin oxide.* J. Appl. Phys., 2004. **96**(7): p. 3912.

170. J. C. C. Fan, F. J. Bachner, and G.H. Foley, *Effect of O_2 pressure during deposition on properties of rf sputtered Sn-doped In_2O_3 films.* Appl. Phys. Lett., 1977. **31**(11): p. 773.

171. L.-J. Meng and M.P. dos Santos, *Properties of indium tin oxide films prepared by rf reactive magnetron sputtering at different substrate temperature.* Thin Solid Films, 1998. **322**: p. 56.

172. X. W. Sun, H. C. Huang, and H. S. Kwok, *On the growth of indium tin oxide on glass.* Appl. Phys. Lett., 1996. **68**(19): p. 2663

173. R. Mientus and K. Ellmer, *Reactive magnetron sputtering of tin-doped indium oxide ITO : influence of argon pressure and plasma excitation mode,*. Surface and Coatings Technology, 2001. **142-144**: p. 748.

174. P.K. Song, Y. Shigesato, I. Yasui, C.W. Ow-Yang, and D.C. Paine, *Study on crystallinity of tin-doped indium oxide films deposited by DC magnetron sputtering.* Jpn J. Appl. Phys., 1998. **37**: p. 1870.

175. P. Canhola, N. Martins, L. Raniero, S. Pereira, E. Fortunato, J. Ferreira, and R. Martins, *Role of annealing environment on the performances of large area ITO films produced by RF magnetron sputtering.* Thin Solid Films, 2005. **487**: p. 271

176. R. Kamei, T. Migita, T. Tanaka, and K. Kawabata, *Effect of D.C bias on the deposition rate using R.F -D.C. coupled magnetron sputtering for SnN_x thin films.* Vacuum, 2000. **59**: p. 764.

177. W. D. Sproul, D.J. Christie, and D.C. Carter, *Control of reactive sputtering processes.* Thin Solid Films, 2005. **481**: p. 1.

178. M. Bender, J. Trube, and J. Stollenwerk, *Deposition of transparent and conducting indium-tin-oxide films by R.F.-superimposed DC sputtering technology.* Thin Solid Films, 1999. **354**: p. 100.

179. T. Nakamura and K. Okimura, *Ti ion density in inductively coupled plasma enhanced DC magnetron sputtering.* Vacuum, 2004. **74**: p. 391.

180. N. Nadaud, N. Lequeux, M. Nanot, J. Jove, and T.Roisnel, *Structural studies of tin-doped indium oxide (ITO) and $In_4Sn_3O_{12}$.* J. Solid State Chem, 1998. **135**: p. 140.

181. G. Khyrpunov, A. Romeo, F. Kurdesau, D.L. Bätzner, H. Zogg, and A.N. Tiwari, *Recent developments in evaporated CdTe solar cells.* Sol. Energy Mater. Sol. Cells, 2006. **90**: p. 664

182. M. Kamei, Y. Shigesato, and S. Takaki, *Origin of characteristic grain-subgrain structure of tin-doped indium oxide films.* Thin Solid Films, 1995. **259**: p. 38.

183. Y. S. Jung, D.W. Lee, and D.Y. Jeon, *Influence of dc magnetron sputtering parameters on surface morphology of indium tin oxide thin films.* Appl. Surf. Sci., 2004. **221**: p. 136

184. D. Mergel, M. Schenkel, M. Ghebre, and M. Sulkowski, *Structural and electrical properties of* In_2O_3*:Sn films prepared by radio-frequency sputtering.* Thin Solid Films, 2001. **392**: p. 91.

185. C. Guillen and J. Herero, *Comparison study of ITO thin films deposited by sputtering at room temperature onto polymer and glass substrates.* Thin Solid Films, 2005. **480 - 481**: p. 129.

186. M. Kamei, H. Enomoto, and I. Yasui, *Origin of the crystalline orientation dependence of the electrical properties of tin-doped indium oxide films.* Thin Solid Films, 2001. **392**: p. 265.

187. F. O. Adurodija, L. Semple, and R. Bruening, *Crystallization process and electro-optical properties of In2O3 and ITO thin films,.* J. Mater. Sci., 2006. **41**: p. 7096.

188. A. Löffl, S. Wieder, B. Rech, O. Kluth, C. Beneking, and H. Wagner. in *14th European Photovoltaic Solar Energy Conference.* 30 June - 4 July 1997. Barcelona, Spain 2089.

189. B. Rech, J. Müller, T. Repmann, O. Kluth, T. Roschek, J. Hüpkes, H. Stiebig, and W. Appenzeller, MRS Proc., 2003. **762**: p. A3.1.

190. B. Rech, G. Schöpe, O. Kluth, T. Repmann, T. Roschek, J. Müller, J. Hüpkes, and H. Stiebig. in *Proceedings of the 3rd World Conference on Photovoltaic Energy. Conversion.* 11-18 May. Osaka, Japan, 2783.

191. T. Minami, H. Sato, H. Nanto, and S. Takata, *Heat treatment in hydrogen gas and plasma for transparent conducting oxide silms such as ZnO, SnO and indium tin oxide.* Thin Solid Films, 1989. **176**: p. 277.

192. O. Kluth, G. Schöpe, J. Hüpkes, C. Agashe, J. Müller, and B. Rech, *Modified Thornton model for magnetron sputtered zinc oxide: film structure and etching behaviour.* Thin Solid Films, 2003. **442**: p. 80

193. T. Tohsophon, J. Hüpkes, S. Calnan, W. Reetz, B. Rech, W. Beyer, and N. Sirikulrat, *Damp heat stability and annealing behaviour of aluminium doped zinc oxide films by magnetron sputtering.* Thin Solid Films, 2006. **516**(14): p. 4628.

194. K. Tominga, K. Kuroda, and O. Tada, Jpn. J. Appl. Phys., 1988. **27**: p. 1176.

195. T. Minami, T. Miyata, T. Yamamoto, and H. Toda., J. Vac. Sci. Technol.,, 2000. A(18): p. 1584.

196. R.J. Hong, X. Jiang, B. Szyszka, V. Sittinger, S.H. Xu, W. Werner, and G. Heide, *Comparison of the ZnO:Al films deposited in static and dynamic modes by reactive mid-frequency magnetron sputtering,.* J. Cryst. Growth, 2003. **253**: p. 117.

197. T.J. Coutts, J.S. Ward, D.L. Young, K.A. Emery, T.A. Gessert, and R. Noufi, *Critical issues in the design of polycrystalline, thin-film tandem solar cells.* Prog. in Photovolt: Res. Appl., 2003. **11**: p. 359

198. R. Hashimoto, Y.Abe, and T. Nakada, *High mobility titanium-doped* In_2O_3 *thin films prepared by sputtering/post-annealing technique,.* Appl. Phys. Express, 2008. **1**: p. 015002.

199. Y. Shigesato, S.Takaki, and T.Haranoh, *Electrical and structural properties of low resistivity tin-doped indium oxide films.* J. Appl. Phys., 1992. **71**: p. 3356.

200. K. Ellmer, *Magnetron sputtering of transparent conductive zinc oxide: Relation between the sputtering parameters and the electronic properties,.* J. Phys. D: Appl. Phys., 2000. **33**: p. R17.

201. M. Lorenz, E. M. Kaidashev, H. von Wenckstern, V. Riede, C. Bundesmann, D. Spemann, G. Benndorf, H. Hochmuth, A. Rahm, H.-C. Semmelhack, and M. Grundmann, *Optical and electrical properties of epitaxial* $(Mg,Cd)_XZn_{1-X}O$*, ZnO, and ZnO:(Ga,Al) thin films on c-plane sapphire grown by pulsed laser deposition,.* Solid-State Electron., 2003. **47**: p. 2205.

202. C. Agashe, O. Kluth, J. Hüpkes, U. Zastrow, B. Rech, and M. Wüttig, *Efforts to improve carrier mobility in radio frequency sputtered aluminium doped zinc oxide films.* J. of Appl. Phys., 2004. **95**(4): p. 1911.

203. A. Tsukazaki, A. Ohtomo, and M. Kawasaki, *High-mobility electronic transport in ZnO thin films.* Appl. Phys. Lett., 2006. **88**: p. 152106:1.

204. I. A. Rauf, *A novel method for preparing thin films with selective doping in a single evaporation step.* Journal of Materials Science Letters, 1993. **12**: p. 1902.

205. I.A. Rauf, *Low resistivity and high mobility tin-doped indium oxide films.* Mater. Lett., 1993. **18**: p. 123.

206. R. Dingle, H.-L. Störmer, A.C. Gossard, and W. Wiegmann, *Electron mobilities in modulation-doped semiconductor heterojunction superlattices.* Appl. Phys. Lett., 1978. **33**(7): p. 665.

207. J. J. Robbins and C.A. Wolden, *High mobility oxides: Engineered structures to overcome intrinsic performance limitations of transparent conducting oxides.* Appl. Phys. Lett., 2003. **83**(19): p. 3933.

208. D. J. Cohen and S.A. Barnett, *Predicted electrical properties of modulation-doped ZnO-based transparent conducting oxides.* J. Appl. Phys., 2005. **98**: p. 053705.

209. K. Ellmer and G. Vollweiler, *Electrical transport parameters of heavily-doped zinc oxide and zinc magnesium oxide single and multilayer films heteroepitaxially grown on oxide single crystals.* Thin Solid Films, 2006. **496**(1): p. 1104.

210. T. Suzuki, T. Yamazaki, and H. Oda, *Properties of indium oxide/tin oxide multilayered films prepared by ion-beam sputtering,.* Journal of Materials Science Letters, 1988. **23**: p. 3026.

211. Ç. Kiliç and A. Zunger, *N-type doping of oxides by hydrogen,.* Appl. Phys. Lett., 2002. **81**(1).

212. S.H. Keshmiri, M. Rezaee-Roknabadi, and S. Ashok, *A novel technique for increasing electron mobility of indium-tin-oxide transparent conducting films Thin Solid Films 413/1-2 (2002) 167. -* . Thin Solid Films, 2002. **413**(1-2): p. 167.

213. T. Koida, H. Fujiwara, and M. Kondo, *Structural and electrical properties of hydrogen-doped In_2O_3 films fabricated by solid-phase crystallization,.* J. Non-Cryst. Solids, 2008. **354**: p. 2805.

214. J.N. Duenow, T.A Gessert, D.M.Wood, T. M. Barnes, M. Young, B. To, and T.J. Coutts, *Transparent conducting zinc oxide thin films doped with aluminium and molybdenum.* J. Vac. Sci. Technol., 2007. **A 25**(4): p. 955.

215. K. Utsumi, H. Iigusa, R. Tokumaru, P.K. Song, and Y. Shigesato, *Study on In_2O_3-SnO_2 transparent and conductive films prepared by d.c. sputtering using high density ceramic targets.* Thin Solid Films, 2003. **445**: p. 229.

216. A. Wang, J.R. Babcock, N.L. Edelman, A. W. Metz, M. A. Lane, R. Asahi, V.P. Dravid, C.R. Kannewurf, A.J. Freeman, and T.J. Marks, *Indium-cadmium -oxide films having exceptional conductivity and optical transparency: Clues for optimising transparent conductors.* Proc. Natl. Acad. Sci. USA, 2001. **98**(13): p. 7113.

217. S. Jin, Y. Yang, J. E. Medvedeva, J. R. Ireland, A.W. Metz, J. Ni, C. R. Kannewurf, A. J. Freeman, and T. J. Marks, *Dopant ion size and electronic structure effects on transparent conducting oxides. Sc-doped CdO thin films grown by MOCVD.* J. Am. Chem. Soc, 2004. **126**: p. 13787.

218. Y. Yang, S.Jin, J. E. Medvedeva, J. R. Ireland, A. W. Metz, J. Ni, M. C. Hersam, A. J. Freeman, and T. J. Marks, *CdO as the archetypical transparent conducting oxide. Systematics of dopant ionic radius and electronic structure effects on charge transport and band structure,.* J. Am. Chem. Soc, 2005. **127**: p. 8796.

219. B. Saha, R. Thapa, and K.K. Chattopadhyay, *Bandgap widening in highly conducting CdO thin film by Ti incorporation through radio frequency magnetron sputtering technique,.* Solid State Commun., 2008. **145**: p. 33.

220. N. Yamada, T. Tatejima, H.Ishizaki, and T. Nakada, *Effects of post deposition annealing on electrical properties of Mo-doped indium oxide (IMO) thin films deposited by RF magnetron co-sputtering.* Jpn. J. Appl. Phys., 2006. **45**(44): p. L1179.

221. M.F.A.M. van Hest, M.S. Dabney, J.D. Perkins, and D.S. Ginley, *High-mobility molybdenum doped indium oxide.* Thin Solid Films, 2006. **496**: p. 70.

222. R.K. Gupta, K. Ghosh, S.R. Mishra, and P.K. Kahol, *Structural, optical and electrical characterization of highly conducting Mo-doped In_2O_3 thin films.* Appl. Surf. Sci., 2008. **254**: p. 4018.

223. R. Groth, *Unterschungen an halbleitenden Indiumoxydschichten.* Phys. Stat. Sol., 1966. **14**: p. 69.

224. A. E. Delahoy and S.Y. Guo, *Transparent and semitransparent conducting film deposition by reactive environment hollow cathode sputtering.* J. Vac. Sci. Technol., 2005. **A23**(4): p. 1215.

225. M. F. A. M. van Hest, M. S. Dabney, J. D. Perkins, D. S. Ginley, and M. P. Taylor, *Titanium-doped indium oxide: A high-mobility transparent conductor.* Appl. Phys. Lett., 2005. **87**: p. 032111:1.

226. Y. Abe and N. Ishiyama, *Titanium-doped indium oxide films prepared by d.c. magnetron sputtering using ceramic target.* J. Mater. Sci., 2006. **41**: p. 7580.

227. R.K. Gupta, K. Ghosh, S.R. Mishra, and P.K. Kahol, *Opto-electrical properties of Ti-doped In_2O_3 thin films grown by pulsed laser deposition.* Appl. Surf. Sci., 2007. **253**: p. 9422.

228. P. F. Newhouse, C.-H. Park, D. A. Keszler, J. Tate, and P. S. Nyholm, *High electron mobility W-doped In_2O_3 thin films by pulsed laser deposition.* Appl. Phys. Lett., 2005. **87**: p. 112108:1.

229. Y. Abe and N. Ishiyama, *Polycrystalline films of tungsten-doped indium oxide prepared by d.c. magnetron sputtering,.* Mater. Lett., 2007. **61**: p. 566.

230. R.K. Gupta, K. Ghosh, S.R. Mishra, and P.K. Kahol, *High mobility W-doped In_2O_3 thin films: Effect of growth temperature and oxygen pressure on structural, electrical and optical properties,.* Appl. Surf. Sci., 2008. **254**: p. 1661.

231. M. Yang, J. Feng, G. Li, and Q. Zhang, *Tungsten-doped In_2O_3 transparent conductive films with high transmittance in near-infrared region,.* J. Cryst. Growth, 2008. **310**: p. 3474.

232. T. Asikainen, M. Ritala, and M. Leskelä, *Atomic layer deposition growth of zirconium doped In_2O_3 films,.* Thin Solid Films, 2003. **440**: p. 152.

233. T. Koida and M. Kondo, *High-mobility transparent conductive Zr-doped In_2O_3,*. Appl. Phys. Lett., 2006. **89**: p. 082104:1.
234. T. Koida and M. Kondo, *Improved near-infrared transparency in sputtered In_2O_3-based transparent conductive oxide thin films by Zr-doping.* J. Appl. Phys., 2007. **101**: p. 063705:1.
235. T. Koida and M. Kondo, *Comparative studies of transparent conductive Ti-, Zr-, and Sn-doped In_2O_3 using a combinatorial approach.* J. Appl. Phys., 2007. **101**: p. 063713:1.
236. R.K. Gupta, K. Ghosh, S.R. Mishra, and P.K. Kahol, *High mobility, transparent, conducting Gd-doped In_2O_3 thin films by pulsed laser deposition.* Thin Solid Films, 2008. **516**: p. 3204.
237. Y. Yoshida, D. M. Wood, T. A. Gessert, and T.J. Coutts, *High- mobility, sputtered films of indium oxide doped with molybdenum.* Appl. Phys. Lett., 2004. **84**(12): p. 2097
238. L. Huang, X.-F. Li, Q. Zhang, W.-N. Miao, L. Zhang, X.-J. Yan, Z.-J. Zhang, and H. Z. -Y., *Properties of transparent conductive In_2O_3: Mo thin films deposited by channel spark ablation.* J. Vac. Sci. Technol., 2005. **A23**(5): p. 1350.
239. D. J. Seo and S.H. Park, *Structural, electrical and optical properties of In_2O_3:Mo films deposited by spray pyrolysis.* Physica, 2005. **B 357**: p. 420.
240. X. Li, W. Miao, Q. Zhang, L. Huang, Z. Zhang, and Z. Hua, *Preparation of molybdenum-doped indium oxide thin films using reactive direct-current magnetron sputtering.* J. Mater. Res., 2005. **20**(6): p. 1404
241. X. Li, Q. Zhang, W. Miao, L. Huang, and Z. Zhang, *Transparent conductive oxide thin films of tungsten-doped indium oxide.* Thin Solid Films, 2006. **515**: p. 2471.
242. D. R. Acosta and A. I. Martínez, *Electron microscopy and physical studies of a new tungsten doped indium oxide transparent conductor.* Thin Solid Films, 2007. **515**: p. 8432.
243. R. D. Shannon, J. L. Gillson, and R. J. Bouchard, *Single crystal synthesis and electrical properties of $CdSnO_3$, Cd_2SnO_4, In_2TeO_6 and $CdIn_2O_4$,*. J. Phys. Chem. Solids., 1977. **38**: p. 877.
244. B. J. Ingram, G.B. Gonzalez, D.R. Kammler, M.I. Bertoni, and T.O. Mason, *Chemical and structural factors governing transparent conductivity in oxides.* Journal of Electroceramics, 2004. **13**: p. 167.
245. D. L. Young, D. L. Williamson, and T. J. Coutts, *Structural characterization of zinc stannate thin films,*. J. Appl. Phys., 2002. **91**(3): p. 1464
246. A. J. Freeman, K.R. Poeppelmeier, T.O. Mason, R.P.H. Chang, and T.J. Marks, *Chemical and thin film strategies for new transparent conducting oxides*, in *MRS Bulletin.* 2000. p. 45 August 2000.
247. D. R. Kammler, T. O. Mason, D. L. Young, T. J. Coutts, D. Ko, K. R. Poeppelmeier, and D. L. Williamson, *Comparison of thin film and bulk forms of the transparent conducting oxide solution $Cd_{1-x}In_{2-2x}Sn_xO_4$,*. J. Appl. Phys., 2001. **90**(12): p. 5979
248. T. Pisarkiewicz, K. Zakrzewska, and E. Leja, *Preparation, electrical properties and optical characterisation of Cd_2SnO_4 and $CdIn_2O_4$ thin films as transparent and conductive coatings.* Thin Solid Films, 1987. **153**: p. 479.
249. J. E. Medvedeva, *Magnetically mediated transparent conductors: In_2O_3 doped with Mo.* Phys. Rev. Lett., 2006. **97**: p. 086401.
250. S. J. Wen, G. Campet, J. Portier, G. Couturier, and J. B. Goodenough, *Correlations between the electronic properties of doped indium oxide ceramics and the nature of the doping element,*. Mater. Sci. Eng., 1992. **B14**: p. 115.
251. S. J. Wen and G. Campet, *The textural effect of Cu doping and the electronic effect of Ti, Zr and Ge dopings upon the physical properties of In_2O_3 and Sn-doped In_2O_3 ceramics,*. Active and Passive Electronic Components, 1993. **15**: p. 79.
252. Y. Zhang, *Electronegativities of elements in valence states and their applications. 2. A scale for strengths of Lewis acids,*. Inorg. Chem., 1982. **21**: p. 3889.
253. S. Jin, Y. Yang, J. E. Medvedeva, L. Wang, S. Li, N.Cortes, J. R. Ireland, A.W. Metz, J. Ni, M.C. Hersam, A.J. Freeman, and T. J.Marks, *Tuning the properties of transparent oxide conductors. Dopant ion size and electronic structure effects on CdO -based transparent conducting oxides. Ga- and In-doped CdO thin films grown by MOCVD,*. Chem. Mater., 2008. **20**: p. 220.
254. X. Wu, W.P. Mulligan, and T.J. Coutts, *Recent developments in RF sputtered cadmium stannate films,*. Thin Solid Films, 1996. **286**: p. 274.
255. IUPAC Periodic Table of the Elements. 22 June 2007. p. http://www.iupac.org/reports/periodic_table/.
256. R.K. Gupta, K. Ghosh, R. Patel, S.R. Mishra, and P.K. Kahol, *Effect of oxygen partial pressure on properties of Nb-doped In_2O_3 thin films.* Mater. Chem. Phys., 2008. **112**: p. 136.
257. H. Nakazawa, Y. Ito, E. Matsumoto, K. Adachi, N. Aoki, and Y. Ochiai, *The electronic properties of amorphous and crystallized In_2O_3 films,*. J. Appl. Phys., 2006. **100**: p. 093706:1.

258. Y. Yoshida, T. A. Gessert, C. L. Perkins, and T. J. Coutts, *Development of radio-frequency magnetron sputtered indium molybdenum oxide.* J. Vac. Sci. Technol.A, 2003. **21**: p. 1092.

259. X. Li, W. Miao, Q. Zhang, Li Huang, Z. Zhang, and Z. Hua, *The electrical and optical properties of molybdenum-doped indium oxide films grown at room temperature from metallic target.* Semicond. Sci. Technol., 2005. **20**(8): p. 835

260. S. -Y. Sun, J. -L. Huang, and D.-F. Lii, *Effects of H_2 in indium-molybdenum oxide films during high density plasma evaporation at room temperature.* Thin Solid Films, 2004. **469-470**(6 -10).

261. S. - Y. Sun, J.-L. Huang, and D.-F. Lii, *Properties of indium molybdenum oxide films fabricated via high-density plasma evaporation at room temperature.* J.Mater. Res., 2005. **20**(1): p. 248.

262. W. -N. Miao, X. -F. Li, Q. Zhang, L. Huang, Z. -J. Zhang, L. Zhang, and X. -J. Yan, *Transparent conductive In_2O_3:Mo thin films prepared by reactive direct current magnetron sputtering at room temperature.* Thin Solid Films, 2006. **500**: p. 70

263. E. Elangovan, R. Martins, and E. Fortunato, *Effect of base pressure and oxygen partial pressures on the electrical and optical properties of indium molybdenum oxide thin films.* Thin Solid Films, 2007. **515**: p. 8549

264. E. Elangovan, A. Marques, A.S. Viana, R. Martins, and E. Fortunato, *Some studies on highly transparent wide band gap indium molybdenum oxide thin films rf sputtered at room temperature.* Thin Solid Films, 2008. **516**: p. 1359.

265. E. Elangovan, A. Marques, F.M. Braz Fernandes, R. Martins, and E. Fortunato, *Preliminary studies on molybdenum-doped indium oxide thin films deposited by radio-frequency magnetron sputtering at room temperature.* Thin Solid Films, 2007. **515**: p. 5512.

266. Y. Yoshida, C.Warmsingh, T.A Gessert, D.L. Young, D.M.Wood, J.D. Perkins, D.S. Ginley, and T.J. Coutts. *Molybdenum doped indium oxide deposited by radio frequency magnetron sputtering and pulsed laser deposition.* in *Third World Conference on Photovoltaic Energy Conversion.* 11-18 May 2003. Osaka, Japan. 34.

267. NIST X-ray Photoelectron Spectroscopy Database. 2003: National Institute of Standards and Technology, Gaithersburg,. p. http://srdata.nist.gov/xps/ http://srdata.nist.gov/xps/ Accessed on 12 August 2008.

268. T. Ishida, H. Kobayashi, and Y. Nakato, *Structures and properties of electron-beam-evaporated indium tin oxide films as studied by x-ray photoelectron spectroscopy and work function measurements,.* J. Appl. Phys., 1993. **73**: p. 4344

269. N. Mori, S. Ooki, N. Masubuchi, A. Tanaka, M. Kogoma, and T. Ito, *Effects of post deposition annealing in ozone environment on opto-electrical properties of Sn-doped In_2O_3 thin films.* Thin Solid Films, 2002. **411**: p. 6

270. Y. T. Levitskii and V. I. Palazhchenko, *Polytropy of Group IV and VI Dopants in Bismuth Crystals.* Inorganic Materials, 2000. **36**(7): p. 665.

271. O. Warschkow, D. E. Ellis, G. B. González, and T. O. Mason, *Defect cluster aggregation and nonreducibility in tin-doped indium oxide.* J. Am. Ceram. Soc., 2003. **86**(10): p. 1707.

272. J.A. Anna Selvan, A. E. Delahoy, S. Guo, and Y. -M. Li, *A new light trapping TCO for nc-Si:H solar cell,.* Sol. Energy Mater. & Sol. Cells, 2006. **90**: p. 3371.

273. A. E. Delahoy, L. Chen, M. Akhtar, B. Sang, and S. Guo, *New technologies for CIGS photovoltaics,.* Solar Energy,, 2004. 77: p. 785.

274. T. Nakada, T. Miyano, R. Hashimoto, Y. Kanda, and T. Mise. *Impact of high - mobility ITiO back contacts on the cell performance of bifacial CIGS thin films solar cells.* in *22nd European Photovoltaic Solar Energy Conference.* Milan, Italy 1870

275. X. Wu, J. Zhou, A. Duda, J.C. Keane, T.A. Gessert, Y. Yan, and R. Nouli, Prog. Photovolt: Res. Appl., 2006. **14**: p. 471.

276. T. Nakada, S.K., Y. Kuromiya, R. Arai, Y. Ishii, N. Kawamura, H. Ishizaki, N. Yamada. *Chalcopyrite thin-film tandem solar cells with 1.5 V open-circuit-voltage.* in *Conference Record of the 2006 IEEE 4th World Conference on Photovoltaic Energy Conversion,.* 7-12 May 2006. Hawaii 400

277. T.J. Coutts, J.D. Perkins, D.S. Ginley, and T.O. Mason. *Transparent Conducting Oxides: Status and Opportunities in Basic Research,.* in *195th Meeting of the Electrochemical Society.* May 2-6. Seattle, Washington August 1999.

278. E. Elangovan, R. Martins, and E. Fortunato, *Effect of base and oxygen partial pressures on the electrical and optical properties of indium molybdenum oxide thin films.* Thin Solid Films, 2007. **515**: p. 8549

279. C. Guillén and J. Herrero, *Structure, optical, and electrical properties of indium tin oxide thin films prepared by sputtering at room temperature and annealed in air or nitrogen.* J. Appl. Phys., 2007. **101**: p. 073514.

280. J.R. Bellingham, W.A. Phillips, and C.J. Adkins, *Electrical and optical properties of amorphous indium oxide,.* J. Phys.: Condens. Matter.,, 1990. **2**: p. 6201.

281. M. Berginski, J. Hüpkes, M. Schulte, G. Schöpe, H. Stiebig, B. Rech, and M. Wuttig, *The effect of front ZnO:Al surface texture and optical transparency on efficient light trapping in silicon thin-film solar cells,*. J. Appl. Phys., 2007. **101**: p. 074903:1.

282. B. B. Yaglioglu, Y.-J. Huang, H.-Y. Yeom, and D. C. Paine, *A study of amorphous and crystalline phases in In_2O_3-10 wt.% ZnO thin films deposited by DC magnetron sputtering,*. Thin Solid Films, 2006. **496**: p. 89.

283. E. Fortunato, A. Pimentel, A. Gonçalves, A. Marques, and R. Martins, *High mobility amorphous/nanocrystalline indium zinc oxide deposited at room temperature,*. Thin Solid Films, 2006. **502**: p. 104.

284. D. L. Young, T. J. Coutts, and V. I. Kaydanov, *Density-of-states effective mass and scattering parameter measurements by transport phenomena in thin films,*. Rev. Sci. Instrum., 2000. **71**(2): p. 462.

285. A.J. Nozik, *Optical and electrical properties of Cd_2SnO_4: A defect semiconductor.* Phys. Rev. B, 1972. 6(2): p. 453.

286. G. Haacke, W.E. Mealmaker, and L. A. Siegel, *Sputter deposition and characterisation of $CdSnO_4$ films.* Thin Solid Films, 1978. **55**: p. 67.

287. H. Kim, J. S. Horwitz, W. H. Kim, S. B. Qadri, and Z. H. Kafafi, *Anode material based on Zr-doped ZnO thin films for organic light-emitting diodes,*. Appl. Phys. Lett., 2003. **83**(18): p. 3809.

288. Y.-M. Lu, C.-M. Chang, S.-I. Tsai, and T.-S. Wey, *Improving the conductance of ZnO thin films by doping with Ti,*. Thin Solid Films, 2004. **447-448**: p. 56.

289. H. Toyosaki, M. Kawasaki, and Y. Tokura, *Electrical properties of Ta-doped SnO2 thin films epitaxially grown on TiO2 substrate,*. Appl. Phys. Lett., 2008. **93**: p. 132109: 1.

290. Y. Furubayashi, T. Hitosugi, Y. Yamamoto, Y. Hirose, G. Kinoda, K. Inaba, and T.H. T. Shimada, *Novel transparent conducting oxide: Anatase $Ti_{1-X}Nb_XO_2$,*. Thin Solid Films, 2006. **496**: p. 157.

291. L. -Y. Chen, W. -H. Chen, J.-J. Wang, F. C. -N. Hong, and Y. -K. Su, *Hydrogen-doped high conductivity ZnO films deposited by radio-frequency magnetron sputtering,*. Appl. Phys. Lett., 2004. **85**(23): p. 5628.

292. M.Contreras, T.B., J. van de Lagemaat, G. Rumbles, T.J. Coutts, C. Weeks, P. Glatkowski, I. Levitsky, J. Peltola,. *Application of Single-Wall Carbon Nanotubes as Transparent Electrodes in Cu(In,Ga)Se2-Based Solar Cells.* in *Conference record of the 2006 IEEE 4th World Conference on Photovoltaic Energy Conversion.* 7-12 May 2006. Hawaii 428

293. T. M. Barnes, X. Wu, J. Zhou, A. Duda, J. van de Lagemaat, T. J. Coutts, C. L. Weeks, D. A. Britz, and P. Glatkowski, *Single-wall carbon nanotube networks as a transparent back contact in CdTe solar cells.* Appl. Phys. Lett., 2007. **90**: p. 243503:1.

Summary

The cost per kW of generating electricity by photovoltaic (PV) conversion can be substantially reduced by using low cost materials and/or processing techniques for thin film solar cells. Transparent conductive oxides (TCO) are important components of thin film solar cells because they minimise losses in lateral current collection while allowing light into the solar cell absorber. Therefore, if high quality TCO films, for solar cell applications, can be grown using industrial methods, the cost of PV generation can be reduced without decreasing the photo-conversion efficiency. Three different areas which are important for the fabrication of TCO films for PV applications have been investigated in this thesis, namely:

- (i) Improving the spatial uniformity and optimising the light scattering properties of ZnO:Al films grown at high rates on large area substrates.
- (ii) Studying the influence of deposition parameters on the opto-electrical properties and thermal stability of In_2O_3:Sn films grown, with minimal waste of the source material, by high target utilisation sputtering on polyimide and glass substrates.
- (iii) Understanding the reasons for high mobility > 62.5 $cm^2 V^{-1} S^{-1}$ in degenerately doped In_2O_3 and CdO films and identifying the factors that limit the conductivity.

Sputtering is an industrially mature deposition technology that would be useful for low cost production of high quality TCO films on a large scale. In this thesis, different sputtering methods which are potentially low cost and allow high film growth rates, were investigated. After deposition, some of the TCO films were further subjected to heat treatment in different conditions or to surface texturing by wet chemical etching. The TCO films were characterised using various techniques including four point probe measurements, Hall effect measurements, optical spectrophotometry, x-ray diffraction, scanning electron microscopy (SEM), atomic force microscopy (AFM) and x-ray photoelectron spectroscopy. Also, the role of the TCO films prepared in this work in improving solar cell efficiency was analysed.

Despite the high cost of indium, In_2O_3:Sn is important for the development of flexible solar cells because a low resistivity $< 10^{-3}$ Ω cm can be obtained without intentional substrate heating. A process known as High Target Utilisation Sputtering

(HiTUS), which eliminates the use of magnetrons and thus race track formation on the target, and increases the source material utilisation to above 90%, was used to grow In_2O_3:Sn films on soda lime glass and polyimide foils. Reactive sputtering from a metallic In/Sn target increased the scope for reductions in the fabrication costs. Deposition rates of up to 40 nm/min were possible for a target to substrate separation of 160mm and a target power density of 2.2 Wcm^{-2}. The influence of various process parameters on the material properties of the In_2O_3:Sn films was investigated. Increasing the target voltage caused the film texture to shift from predominantly <111> orientation to <100> orientation. The charge carrier density increased with increasing voltage but at higher voltages, the resistivity was limited to values close to 2.0×10^{-4} Ω cm because the mobility reduced. High substrate temperature, medium oxygen flow rate and moderate pressure gave the best compromise of low resistivity and high transmittance. The lowest resistivity values on glass and polyimide substrates were 1.6×10^{-4} Ω cm and 1.9×10^{-4} Ω cm, respectively. Substrate temperatures above 100° C were required to obtain visible light transmittance exceeding 85% for ITO films on glass. The In_2O_3:Sn film resistivity was either unaffected or reduced after heating in vacuum but generally increased for oxygen deficient films when heated in air. The greatest increase in transmittance of oxygen deficient films occurred for heat treatment in air while that of the highly oxidised films was largely unaffected by heating in both media.

Aluminium doped zinc oxide is a low cost alternative to In_2O_3:Sn for various opto-electronic devices including solar cells. Also, the conductivity and transparency of ZnO:Al are superior to natively textured SnO_2:F which is commercially available to enhance light trapping in thin film silicon solar cells. Light trapping increases the effective thickness of the thin film silicon absorber by multiple internal reflections of long wavelength light, which increases the photocurrent generation. Since thinner absorber layers can be used with textured TCO layers, the processing time as well as the material and production costs of solar cells can be reduced. The best light trapping properties of ZnO:Al are usually obtained by RF magnetron sputtering from ceramic targets which is unsuitable for large scale production because of low deposition rate (6 nm m min^{-1}, in dynamic mode) for a single cathode target. Therefore, the ZnO:Al films were grown on glass substrates using reactive mid frequency (MF) reactive magnetron sputtering from low cost metallic targets at deposition rates as high as 115 nm m min^{-1}. The oxygen influx along the middle and sides of a dual cathode arrangement in the in-line sputter system used, could be varied. Increasing the oxygen influx from the sides improved the resistivity profile of static prints on a 30 cm x 30 cm glass substrate and gave highly conductive and transparent films in dynamic deposition mode. The etched films developed rough surface textures with effective light scattering which could be controlled by the oxygen balance between the middle and sides. Textured ZnO:Al films were used as front contacts in 1cm² single junction μc-Si:H solar cells yielding an initial efficiency of 8.4 % which is comparable to that for cells on RF sputtered ZnO:Al films.

As thin film solar cells are integrated to make modules on larger area panels, the TCO film resistivity must reduce below 1 x 10^{-4} Ω cm to reduce I^2R losses. The only avenue to improve both the conductivity and transmittance, is by increasing the mobility since increasing the charge carrier density reduces the near infra red transmission. A survey of TCO materials based on In_2O_3 and CdO that combine degeneracy with high mobility > 62.5 $cm^2V^{-1}s^{-1}$ showed that the highest values of mobility occurred where transition metals, with a higher Lewis acid strength than the host cation, were used as dopants. However, resistivity values below 10^{-4} Ω cm are rare and thus some experiments were done to identify the factors which limit the conductivity in In_2O_3:Mo films.

Pulsed DC magnetron sputtering from ceramic targets was used to prepare In_2O_3:Mo films as it allows faster deposition rates than RF magnetron sputtering but with less complex equipment. The influence of sputter pressure and heater temperature on the structure, morphology and the opto-electronic properties of the In_2O_3:Mo films was investigated. Decreasing the sputter pressure increased the deposition rate and the carrier density but had minimal influence on the mobility. Increasing the substrate temperature increased the molybdenum to indium ratio, the molybdenum doping efficiency, the carrier mobility and the carrier density, and thus the electrical conductivity of the In_2O_3:Mo films. All films were transparent to wavelengths from 300 nm to 1800 nm and the plasma wavelength was greater than 1800 nm. The highest optical transparency could be achieved at intermediate temperatures where optimal oxidisation of the metal minimises the presence of both absorbing sub-oxides and un-reacted molybdenum. The minimum resistivity value achieved an optimised In_2O_3:Mo film was 1.6 x 10^{-4} Ω cm with a carrier density of 5 x 10^{-4} cm^{-3} and a mobility of 77 cm^2 $V^{-1}s^{-1}$. Heating the In_2O_3:Mo films in air reduced both the carrier density and mobility because of increased oxygen incorporation in the films, which could be partially reversed by subsequent heating vacuum. A detailed study of the chemical composition of the In_2O_3:Mo films revealed that when the atomic content of Mo^{X+} ($4+ < x < 6+$) species increases, both the carrier density and mobility decrease. The Mo^{X+} species are related to sub-oxides, formed between molybdenum and interstitial oxygen, which do not contribute electrons to the In_2O_3 and act as neutral impurity scattering centres.

This thesis can contribute to transferring laboratory processes for high quality TCO films to industrial production and to improving TCO material properties for conventional as well as advanced solar cells and other opto-electronic devices.

Acknowledgement

I am greatly indebted to Professor A. N. Tiwari for supervising this thesis and giving me many opportunities to learn more about the field of photovoltaics.

I gratefully acknowledge the Engineering and Physical Science Research Council, UK for financing this studentship.

I wish to thank Professor J.I.B Wilson of School of Engineering and Physics, at Herriot-Watt University and Professor S. Rastogi of Department of Materials, Loughborough University for agreeing to examine this thesis.

I thank Dr S.J. Watson of CREST, Loughborough University for acting as my supervisor in the last months of this thesis. Dr. R. Gottschalg of CREST, Loughborough is also acknowledged for being my an "unofficial" mentor.

Special thanks to the PV-Materials and Devices group for their help around the laboratory as well as to all other members of CREST, Loughborough University for the pleasant working atmosphere. I am also thankful to the technical and administrative staff in the Department of Electronic and Electrical Engineering, Loughborough University, who were helpful in organizing the logistics for this work, and handling the paper work associated with this thesis, respectively.

Many thanks to the Management, Group Leaders, and members of staff at the laboratories and companies, where I made some of the experiments for this work, especially

- Professor B. Rech (now at Helmholtz Centre Berlin for Materials and Energy, Germany) and Dr. J. Hüpkes at Institute of Photovoltaics (now Institute of Energy Research, IEF-5 Photovoltaics) at Research Centre Jülich, Germany.
- Professor M.J. Thwaites at Plasma Quest Limited UK.
- Dr. H. Zogg at Thin Film Physics Laboratory, ETH-Zürich, Switzerland.

I am very grateful to the many people who have prepared samples or carried out measurements on my behalf, they are,

- Dr. S.E. Dann of the Department of Chemistry, Loughborough University for carrying out the XRD measurements.
- E. Brauweiler and H.P. Bochem of Research Centre Jülich, Germany for taking the SEM micrographs of the ZnO:Al samples.

- J. Kirchoff and G. Schöpe of IEF-5 Photovoltaics, Research Centre Jülich for preparing the micro-crystalline silicon absorber layers.
- Dr. E. Bunte and W. Reetz of IEF-5 Photovoltaics, Research Centre Jülich for taking the spectral response measurements of the micro-crystalline silicon solar cells.
- Professor T. Nakada of Aoyama Gakuin University for providing the In_2O_3:Ti films.
- Mr. J. Bates of Department of Materials at Loughborough University for taking the SEM micrographs of the In_2O_3:Mo samples.
- E. Smith of School of Chemistry at the University of Nottingham for XPS measurements.
- S. Buecheler for preparing the CdTe absorber layers at Thin Film Physics Laboratory, ETH-Zürich, Switzerland.
- A. Chirila and S. Seyrling for preparing and characterising the CIGS solar cells at Thin Film Physics Laboratory, ETH-Zürich, Switzerland.
- J. Bowers of CREST, Loughborough University for preparing and characterising the dye-sensitized solar cells.

Dr. H.-L. Du of Advanced Materials, Research Institute, Northumbria University is also acknowledged for giving me access to an AFM system.

Finally, I would like to thank my friends and family, especially my parents, for their support during all my studies.